Deciphering processes of the early solar system with silicon isotopes

Delphine Losno


Numéro National de Thèse : **2021LYSEN087**

THESE DE DOCTORAT DE L'UNIVERSITE DE LYON

opérée par

L'École Normale Supérieure de Lyon

Ecole Doctorale N° 52
Physique et Astrophysique de Lyon (PHAST)

Discipline : Sciences de la Terre

Soutenue publiquement le 17/12/2021, par :

Delphine LOSNO

Deciphering processes of the early solar system with silicon isotopes

Déchiffrer les processus du système solaire précoce avec les isotopes du silicium

Devant le jury composé de :

BECKER Harry	Professor	Université de Berlin	Rapporteur
LEYA Ingo	Associate Professor	Université de Berne	Rapporteur
MEHEUT Merlin	Maître de conférences	Université de Toulouse	Examinateur
MICHAUT Chloé	Professeure des Universités	LGL-TPE, ENS de Lyon	Examinatrice
BOURDON Bernard	Directeur de recherche CNRS	LGL-TPE, ENS de Lyon	Directeur de thèse
FITOUSSI Caroline	Chargée de recherche CNRS	LGL-TPE, ENS de Lyon	Co-encadrante

Remerciements

Je remercie l'ensemble des membres du jury d'avoir accepté d'évaluer mon travail de thèse, mes deux rapporteurs Harry Becker et Ingo Leya ainsi que Merlin Méheut et Chloé Michaut respectivement en termes d'examinateur et examinatrice. Merci Chloé d'avoir accepté d'être la présidente du jury pour ma thèse dans ces circonstances particulières.

Merci à mes directeurs de thèse Bernard et Caroline pour m'avoir encadrée pendant ces quatre années de thèse. Caroline, merci pour ta bonne humeur, ta disponibilité 365 jours par an à toute heure du jour et de la nuit et pour m'avoir dit un jour « peu importe l'heure et le jour de la semaine, pendant les vacances scolaires et les jours fériés, tu peux m'appeler n'importe quand ! ». Merci aussi pour ton implication sans faille et tes conseils avisés et toujours très justes dans mon travail de thèse, si j'ai eu la chance d'analyser autant d'échantillons super cool c'est grâce à toi ! Je ne te remercierai jamais assez d'avoir accepté certains de mes défauts comme mon obstination, mon étourderie et ma propension à ne pas répondre à tes appels (j'ai vraiment essayé de changer sur ce point …). Bernard, merci pour tes blagues mythiques et pour ton soutien inébranlable pendant les périodes les plus difficiles de ma thèse. Jamais je n'aurais pensé pouvoir rédiger une thèse dont je serais aussi fière et effectuer une soutenance totalement en anglais. Enfin merci à tous les deux pour votre patience et pour tout ce que vous m'avez transmis, j'ai beaucoup d'admiration pour vous deux et suis extrêmement fière d'avoir été votre stagiaire puis votre thésarde pendant ces années.

Je remercie chaleureusement toutes les personnes du laboratoire qui m'ont épaulé pendant ma thèse : Florent, Manue, Philippe, Eléonore, Clémentine, Marie-Jeanne, Hervé, Gilles D., Gilles M., Fred, Jéremy, Bruno, Guillemette, Yanne, Francis, Stéphane, Aline et Mathieu. Je te remercie Philippe pour les heures passées ensemble au téléphone et au spectro pour essayer de faire fonctionner cette grosse machine capricieuse qu'est le Neptune 2 (ce n'était qu'une histoire de faux contact dans un câble finalement !). Marie-Jeanne, je ne te remercierai jamais assez pour ta gentillesse, ta franchise et surtout pour ta patience infinie avec une tête en l'air comme moi … Merci de m'avoir rappelé les deadlines, les procédures à effectuer pour mes réinscription en thèse, mes renouvellements de contrat et surtout tous les chocolats, bonbons et autre gourmandise !

Il est temps de remercier toutes les personnes avec qui j'ai passé plus de temps qu'avec ma propre famille ces dernières années : Momo, Auguste, Anaïs, Damian, Thibaut, Priyanka, Chloé, Héloïse, Marianne, Salomé, Fanny, Samuel, Jean, Mélie, Quentin, Elsa, Xueying, Nadège, Pierre-Jean, Marwane, Alexandra, Valentine, Valentin, Laetitia, Asma, Nathalie, Victor, Cédric, Farid, Pauline, Romain, Ophélie, Marie, Robin et tous les autres. Merci à toutes et à tous pour votre écoute, vos conseils et votre soutien tout au long de ma thèse. Merci Nadège de m'avoir réconfortée plusieurs fois, tu es une amie précieuse. Quentin et Mélie, vous avez été beaucoup plus que mes cobureaux pendant toutes ces années et occuperez toujours une petite place particulière dans mon cœur. Mélie, je te remercie pour ta patience, ta bienveillance, et surtout pour cette tendresse que tu donnes sans retenue qui te caractérise tant. Merci aussi pour toutes ces conversations enrichissantes et épanouissantes autour d'une bière ou d'un thé. Merci aussi pour toute cette énergie positive qui m'a aidée à ne pas baisser les bras dans les moments les plus décourageants de ma thèse. Quentin, merci pour ton soutien inébranlable pendant les grosses galères de spectro, les baisses de moral et surtout pour toutes ces heures passées en compagnie du ranger d'argon de 180L caréné et bien sûr livré avant midi (pas avant 9h pour les matières dangereuses, ouf !). Je garde un souvenir doux de nos pauses théééééé et de ses nombreux moments d'attente du ranger, parfois comblé par l'apprentissage de cette belle danse qu'est le chacha. Merci Quentin d'avoir diminué ta consommation de déo dans le bureau et de m'avoir

initié aux tracks techno (la meilleure track restant Silicon Love bien entendu). Je suis très fière d'avoir été témoin de tes débuts de superstar international de la techno sous le pseudonyme « Queen of Tin ». L'ambiance du bureau est vraisemblablement ce qui va le plus me manquer à présent, vous allez cruellement me manquer tous les deux. Marwane je ne t'oublie pas, merci pour ta bonne humeur communicative qui m'a aidé à tenir le coup à la fin de ma thèse, merci de m'avoir fait rire pour essuyer mes larmes ! Notre relation de cobureau fut courte mais intense, je te souhaite le meilleur pour la suite de ta thèse et au-delà !

Mes remerciements s'adressent également à toutes les personnes qui ont agrémenté mon quotidien sur le campus : le personnel du restaurant universitaire de Monod ainsi que Loïc et Romain de l'Idex qui m'ont permis d'analyser autre chose que le signal de la climatisation du spectro ! Merci pour votre bonne humeur et vos encouragements tout au long de ces années !

Toutes celles et ceux qui me connaissent bien savent que mes années à l'ENS ont été ponctuées de soirées étudiantes, de cours en amphi et d'indénombrables cours de danse. Je tiens à remercier du fond du cœur ma professeure de danse depuis maintenant 8 ans, Adriana. Merci Adrie de m'avoir transmis avec autant de passion cette belle discipline qu'est la danse. Je n'oublierai jamais mes premiers cours de rock, salsa, danse de salon, lindy que j'ai toujours autant de plaisir à suivre. Il était tellement agréable de pouvoir laisser de côté ma thèse pendant quelques heures, les jours où j'avais cours de danse le soir avaient une toute autre saveur. Merci pour ta rigueur, ta bonne humeur et ton humilité. Et merci de m'avoir fait confiance pour l'organisation du gala de cette année. La danse a ensoleillé mes années lyonnaises et je ne te remercierai jamais assez pour ça !

Je remercie ma famille, mes parents, ma sœur et Martin pour leur soutien indéfectible pendant ces quatre années de thèse, leurs conseils avisés et leur amour inconditionnel. La famille compte maintenant quatre docteurs ! Merci Marion de m'avoir permis d'être tante pour la première fois de l'adorable petite Agathe, j'ai hâte de lui donner des bonbons après les repas et de lui apprendre ses premiers pas de danse !

Robin, comment, avec des mots, te remercier d'être mon pilier et mon danseur depuis maintenant plus de 7 ans. Merci de m'avoir fait visiter ta belle région qu'est le Lot, de m'avoir emmenée partout avec toi, à Meyrac, Oléron, Norvège et j'en oublie beaucoup. Merci d'avoir supporté mes retards, mes sautes d'humeur, mes erreurs de jugement, mon étourderie. Rien n'aurait été pareil sans toi. Je me demande parfois comment aurait été mon quotidien si tu étais parti à Nancy après ta prépa, il aurait été bien terne. Merci surtout pour ta gentillesse et ta tendresse qui me touche beaucoup, même si je ne le montre pas toujours. Tu occupes et occuperas toujours une place particulière dans mon cœur.

Pierre-Jean, les mots me manquent pour exprimer à quel point tu as été un soutien sans faille pendant les moments les plus difficiles de ma thèse. Merci pour ta patience, ton indulgence et ta gentillesse au quotidien. Merci aussi pour tes bons petits plats qui ont nourri mon corps et mon esprit ! Merci pour tes petites attentions et pour tout le bonheur que tu m'apportes chaque jour.

Enfin je tiens à remercier l'ensemble des professeurs qui m'ont formée depuis le secondaire et qui m'ont donné le goût des sciences. Merci à mon professeur de SVT de seconde qui m'a bien conseillée en m'indiquant le parcours Géologie de l'ENS de Lyon qu'il avait lui-même suivi. Merci Emmanuelle Lousson de m'avoir permis de suivre toutes les UEs qui me plaisaient dans le parcours, merci pour ton accueil chaleureux à mon entrée à l'ENS.

Table des matières

Chapter 1

Introduction

Introduction: Silicon isotopes as tracers in the early Solar System

« Tout parle dans l'univers ; il n'est rien qui n'ait son langage »

Jean de la Fontaine

The actual solar system is a stable gravitational system. Physical properties of planetary objects such as angular momentum and revolution period are well-characterized by classical mechanic equations. However large number of impact craters at the surface of the Moon and the presence of the inner asteroid belt rather suggest a more chaotic environment in the past. At the beginning of their life, planetesimals may have experienced large scale impacts that could reach giant impacts, such as the one at the origin of the Earth-Moon system (Canup, 2012). Planetary objects underwent very complex processes such as metal-silicate differentiation, core formation and accretion. In this introductive chapter, we will explain the application of Si isotopes as tracers of these early processes.

1. The Silicon isotope system

Matter is made up of atoms (diameter size ≈ 10^{-10} m) which consists of a nucleus surrounded by an electron cloud consisting of electrons. The atomic nucleus contains positively charged particles (protons) and neutral particles (neutrons), the particles that make up the nucleus being called nucleons. Electrons occupy most of the volume of the atom and carry negative charges, then ensuring the electroneutrality of atoms. The mass of an atom is taken as the mass of its nucleus given that the mass of a nucleon is 1.67×10^{-27}kg (neutron being slightly heavier than proton) and a mass of an electron is 9.11×10^{-31}Kg. Isotopes represent atoms sharing the same atomic number Z (number of protons) and a different mass number A (number of protons plus neutrons). Thus, they have identical physical and chemical behaviour since they share identical electronic configuration. However, they differ slightly by their mass and this tiny mass difference will drive isotope fractionation (see next section).

Silicon has three stable isotopes ^{28}Si, ^{29}Si and ^{30}Si with respective abundance of 92.2%, 4.69% and 3.09% (Laeter *et al.*, 2003). The natural abundance of silicon was established by primary nucleosynthesis occurring at the centre of stars that experienced fusion of light elements generating atoms until they reach a maximum mass corresponding to ^{56}Fe. Physical and chemical processes have then altered the relative abundance of silicon isotopes among terrestrial and extra-terrestrial materials. These processes could have occurred very early in Solar System history in the protoplanetary disk, during

planetary formation, or could be related to igneous or surface processes. Advances in gas source mass spectrometry allowed Si isotope measurements to be precise enough to be of interest in geochemistry. The Si isotope data on terrestrial minerals and rocks as well as a "Stony meteorite, Melrose, New Mexico" were firstly reported by (Reynolds and Verhoogen, 1953). Their Si isotope dataset showed a large range of variation, with $\delta^{30}Si$ values varying from -2.1 ‰ to 1.0 ‰ relative to an olivine sample ($\delta^{30}Si_{NBS}$=-0.29‰), with an estimated uncertainty between 0.2 to 0.4 ‰. Si analyses of rocks were then obtained by (Allenby, 1954) and (Epstein and Taylor, 1970) on Apollo mission samples. Nevertheless, the limited analytical precision of Si isotope measurements could not allow these authors to fully interpret the origin of the observed variations in $^{30}Si/^{28}Si$ ratios. (Clayton and Mayeda, 1978) then performed Si isotope measurements in Allende inclusions and in an olivine from a pallasite meteorite. They found that most of Allende inclusions displayed mass-dependant Si isotope fractionation with an enrichment of ^{30}Si that could result from evaporation processes in the solar nebula. They also reported excess of ^{29}Si in two inclusions CI and EK 1-4-1 thought to be of nucleosynthetic origin. The Secondary Ion Mass Spectrometry (SIMS) technique was used in the 1980's for *in situ* analysis of presolar grains that showed strong mass-independent variations related to various nucleosynthesic sources. The improvement of analytical precision thanks to the introduction of Multicollector Inductively Coupled Plasma Mass Spectrometers (MC-ICP-MS) demonstrated Si isotope variability among inner System Solar rocky bodies (Armytage *et al.*, 2012, 2011; Chakrabarti and Jacobsen, 2010; Dauphas *et al.*, 2015; Fitoussi *et al.*, 2009; Fitoussi and Bourdon, 2012; Georg *et al.*, 2007; Pringle *et al.*, 2014, 2013; Savage and Moynier, 2013; Zambardi *et al.*, 2013; Mendybaev *et al.*, 2021; Martins *et al.*, 2021). The latest methodological improvement relied on coupling a Laser Ablation system to a MC-ICP-MS to perform *in situ* analysis. Compared to SIMS, LA-MC-ICP-MS presented the advantage of lowering interference level and sensitivity to matrix effect (Poitrasson, 2017). A summary of Si isotope data of planets, differentiated and undifferentiated meteorites is shown in Figure 1. A detailed review of the different analytical techniques for silicon isotope measurements is presented in the methodological Chapter (Chapter 2). For the purpose of this work, measurements were performed by MC-ICP-MS which present the best analytical precision, simple and rapid sample preparation and good measurement sensitivity, in particular through the use of a desolvating system. The detailed analytical settings for Si isotopes analyses are discussed in Chapter 2.

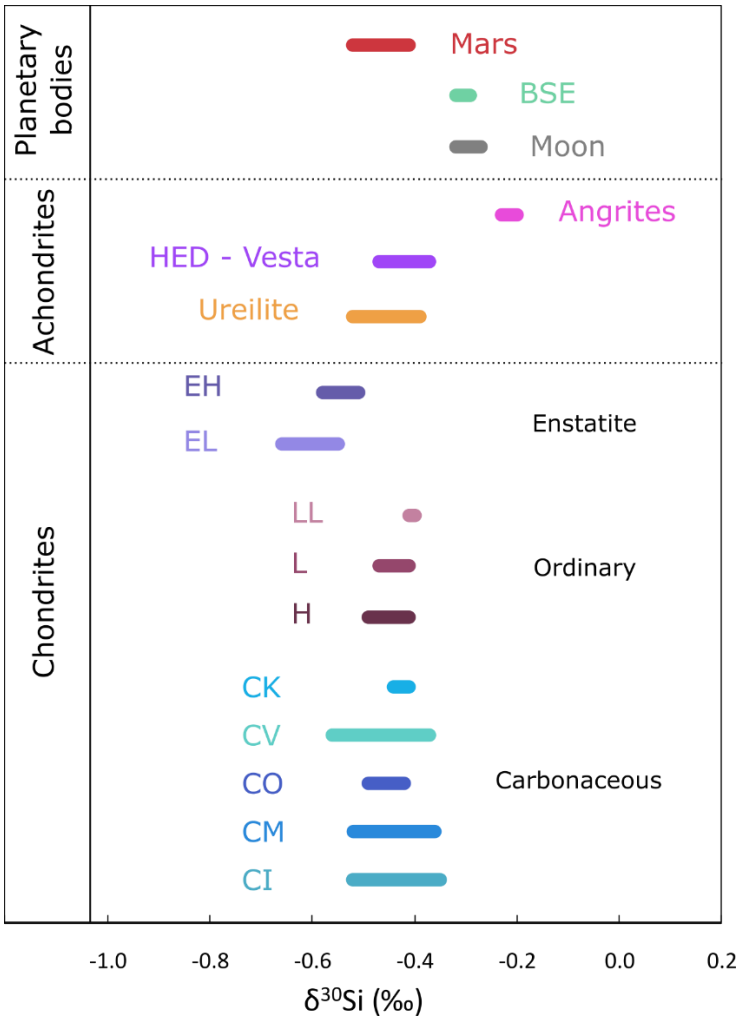

Figure 1: Isotope composition of undifferentiated meteorites (chondrites), differentiated meteorites (achondrites) and planetary bodies (see main text for references).

2. Isotope fractionation: theoretical background

The isotope composition of natural material is related to the isotope composition of its natural reservoir and to the fractionation mechanisms that can modify isotope compositions. Isotope fractionation can operate under thermodynamic or kinetic control. In the case of thermodynamic equilibrium, the amplitude of isotope fractionation is controlled by the thermodynamic constant of the isotope exchange reaction. The equilibrium isotope fractionation factor then depends on the temperature and was shown to vary as the inverse of the square of the temperature (Bigeleisen and Mayer, 1947; Urey, 1947). The pioneer work of Urey (1947) opened the application of isotope fractionation of oxygen isotopes to paleotemperature reconstructions. The established formalism of isotope fractionation was applied to gas phases as well as condensed phases. Here we summarize

briefly the key parameters controlling silicon isotope fractionation in gas and solid phases, while isotope fractionation in liquids will not be discussed here.

2.1. Isotope fractionation factor

The process of isotope exchange can be described in term of chemical reaction in which isotopes are exchanged between two coexisting species A and B. This reaction can occur either under equilibrium condition or disequilibrium conditions (implications for isotope fractionation is discussed further in the text). In the case of an isotope exchange under equilibrium conditions, the associated reaction can be expressed as:

$$A^{light}Si + B^{heavy}Si \leftrightarrow A^{heavy}Si + B^{light}Si \quad (1)$$

The isotope fractionation factor α between two compounds A and B is defined as the ratio of silicon isotope ratio in the two compounds A and B as follows:

$$\alpha_{A-B}^{Si} = \frac{R_A^{Si}}{R_B^{Si}} \quad (2)$$

This is analogous to an equilibrium constant written for the isotope exchange reaction (1). The term R_A^{Si} representing the $^{30}Si/^{28}Si$ or $^{29}Si/^{28}Si$ ratio in the compound A. The Si isotope ratios measured by mass spectrometry are reported relative to Si isotope ratios of a reference standard (usually NBS28, see Chapter 2) in the delta notation:

$$\delta_A^{30}Si = \left(\frac{R_A^{Si}}{R_{NBS}^{Si}} - 1\right) * 1000\ (‰) \quad (3)$$

The relationship between the isotope fractionation factor and the delta notation is simple if one assumes that α<<1 which is the case in most geological settings:

$$\Delta^{30}Si_{A-B} = \delta_A^{30}Si - \delta_B^{30}Si \approx 1000\ln\left(\alpha_{A-B}^{Si}\right) \approx 1000\left(\alpha_{A-B}^{Si} - 1\right) \quad (4)$$

2.2. Kinetic isotope fractionation

Isotope fractionation under kinetic control occurs in the case of chemical reactions for which the inverse reaction cannot be achieved or when products are separated from reactants. Kinetic isotope effects are usually associated to fast, incomplete or unidirectional reactions such as evaporation, dissociation reactions, diffusion and the majority of biological reactions. In this case, isotope

fractionation is driven through velocity difference between the different isotopes, lighter isotopes moving faster than heavier isotopes across the phase or between phase boundaries. For example, we consider a molecular gas composed of ^{28}SiO, ^{29}SiO and ^{30}SiO. If one considers the gas phase as ideal, the average kinetic energy (KE) of all gaseous species are the same in the kinetic theory of gases:

$$\langle KE \rangle = \frac{3}{2} kT = \frac{1}{2} m_{SiO} \langle v_{SiO}^2 \rangle \tag{5}$$

Where m_{SiO} is the mass of the SiO molecule, k the Boltzmann constant and T the temperature of the gas. This relation leads to:

$$\frac{\langle v_{SiO\ light}^2 \rangle}{\langle v_{SiO\ heavy}^2 \rangle} = \frac{m_{SiO\ heavy}}{m_{SiO\ light}} \tag{6}$$

On average, the gaseous molecules containing the light isotope will move faster than gaseous molecules containing heavy isotopes.

For kinetic reactions, such as evaporation processes when a vapor sublimates from a solid, light species in the condensed phase will have lower molecular dissociation energy (Figure 2) and will then evaporate more easily than molecules containing heavy isotopes (Schauble, 2004). In addition, molecules with light isotopes will diffuse faster than molecules with heavy isotopes, leading to preferential evaporation of light isotope bearing molecules.

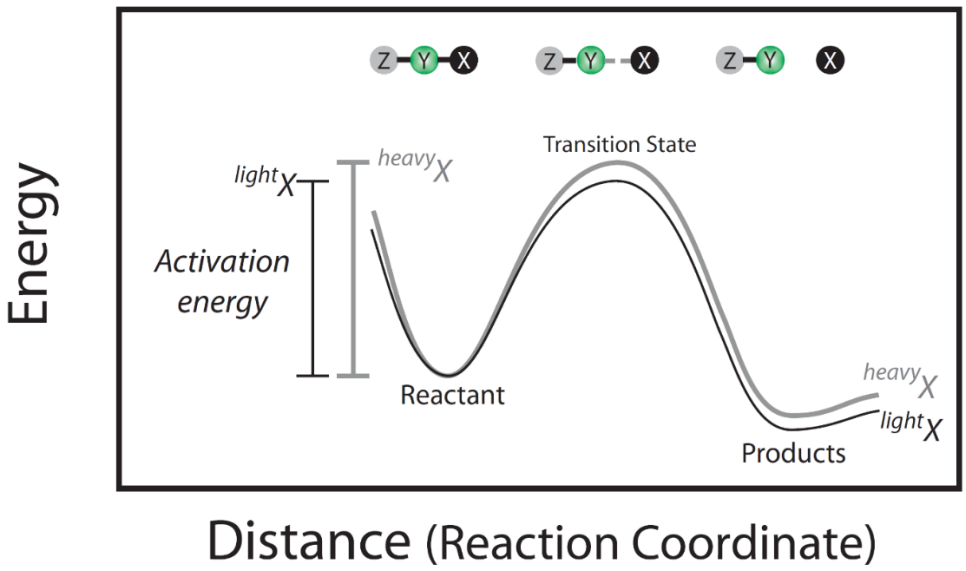

Figure 2: Example of a dissociation reaction of a molecule Z-Y-X into Z-Y and X. The potential energy barrier is easier to overcome for a molecule bearing the light isotope (black curve) compared with the molecule bearing the heavy isotope (grey curve). Since the molecule bearing the light isotope also has a larger translational energy, preferential dissociation of the molecule Z-Y-^{light}X will occur. From Schauble (2004).

2.3. Equilibrium isotope fractionation

Isotope fractionation under equilibrium conditions is a quantum-mechanical phenomenon, as a consequence of the effect of atomic mass on vibrational energy of molecules (Urey, 1947). Reporting the isotope exchange reaction between diatomic species as expressed in (1):

$$A^{light}Si + B^{heavy}Si \leftrightarrow A^{heavy}Si + B^{light}Si \tag{6}$$

The thermodynamic reaction constant of this reaction is related to the ratio of activities of the products over activities of the reactants. The equilibrium constant can be expressed using partition functions Q of the isotope species:

$$K = \frac{\left(A^{heavy}Si\right) * \left(B^{light}Si\right)}{\left(A^{light}Si\right) * \left(B^{heavy}Si\right)} = \frac{Q\left(A^{heavy}Si\right) * Q\left(B^{light}Si\right)}{Q\left(A^{light}Si\right) * Q\left(B^{heavy}Si\right)} \tag{7}$$

Partition functions describe all the possible energy states of a molecule in terms of translational, rotational, vibrational and electronic energy. For each molecule, the total partition function is the product of the translational (tr), rotational (rot) and vibrational (vib) partition functions as:

$$Q = Q_{tr} * Q_{rot} * Q_{vib} \tag{8}$$

Theoretical expressions for each term has been described in previous work and the parameters used for calculating the partition functions are the symmetry numbers of the molecules, their three principal moments of inertia, their mass, their vibrational frequencies and their temperature (Bigeleisen and Mayer, 1947; Urey, 1947; Criss, 1999; Schauble, 2004; Chacko *et al.*, 2019). The equation for minerals is similar to equations used for gas, except that the only contribution comes from the vibrational contributions, as translational and rotational motions are restricted or absent in solids (Bottinga, 1968). The vibrational component is treated as a continuous spectrum of vibrations instead of discrete vibration modes. Quantum mechanical molecular modelling based on the density functional theory (DFT) has been successful in solving these quantum mechanics equations and then characterized vibrational and structural atom properties. Partition function ratios are usually expressed in terms of reduced partition function ratios β. The isotope fractionation factor $\alpha_{A\text{-}B}$ is then expressed easily as a function of reduced partition functions:

$$\alpha_{A-B} = \frac{\beta_A}{\beta_B} \tag{9}$$

This leads to:

$$1000\ln\left(\alpha_{A-B}\right) = 1000\ln\left(\beta_A\right) - 1000\ln\left(\beta_B\right) = \Delta_{A-B} \tag{10}$$

With $\Delta_{A\text{-}B}$ refereeing to the δ difference between the two species.

3. The Early Solar System

The planets of the Solar System accreted after a molecular cloud collapsed and rapidly formed a protoplanetary disk (e.g. Chambers, 2004). The heterogeneous distribution of velocities in a molecular cloud means that upon collapse it will have an angular momentum that is responsible for the formation of a disk (Armitage, 2011). The disk consists of gas and dust with dust representing a few percent of the total mass. In the case of the Solar System, the gas is dominated by H_2, which means that it is a very reducing environment. The disk has a flared structure as illustrated in Figure 3. Protoplanetary disks that have been observed around stars usually have a lifetime of at most a few million years (Williams and Cieza, 2011) and the dissipation of the disk is due to the effect of accretion to the star but also to the effect of photoevaporation.

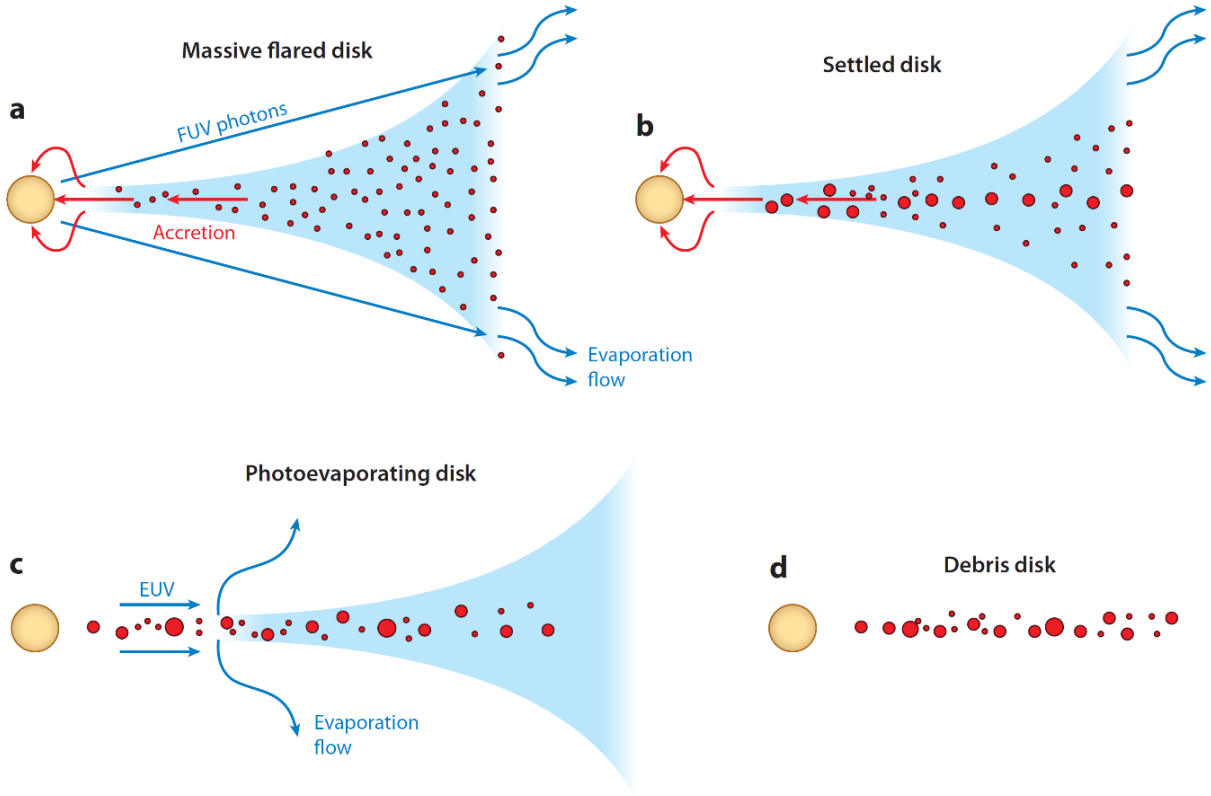

Figure 3: Typical evolution of a protoplanetary disk, with the blue area showing the repartition of gas and red points the repartition of dust (from Williams and Cieza, 2011).

Recent observations by ALMA have demonstrated the complex structure of planetary disks (ALMA Partnership *et al.*, 2015) often exhibiting one or more planetary 'gaps' that represent circular structures with lower density. These structures have been interpreted as being linked to the formation of planets.

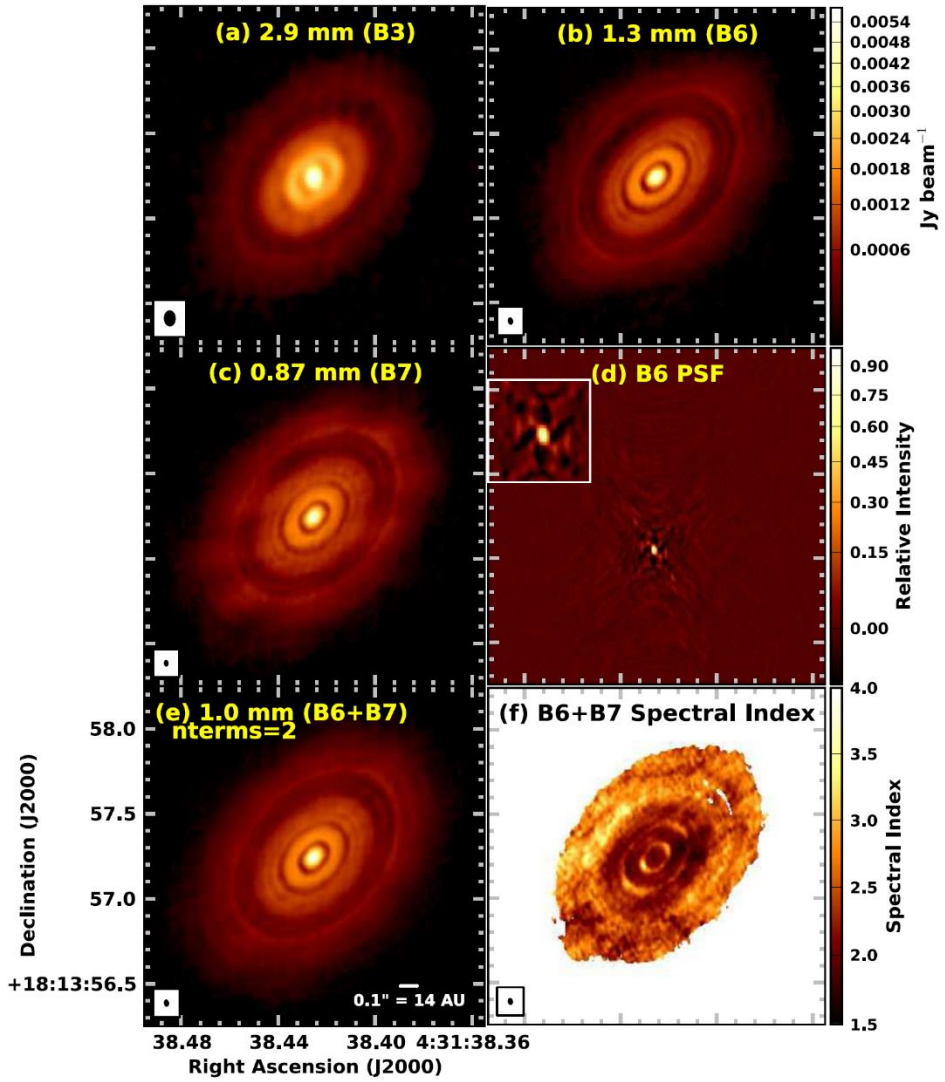

Figure 4: ALMA images of the HL Tau protoplanetary disk using various wavelengths (from ALMA Partnership et al. 2015).

The protoplanetary disks are heated due to the accretion into the Sun, thereby releasing gravitational energy that heats up the disk up to distance of a few astronomical units. The heating of the disk at temperature up to 2000K leads to the vaporisation of the pre-solar dust contained in the molecular cloud (Cassen, 1994; Ciesla, 2008). As the accretion rate of the Sun goes down, so does the temperature of the inner part of the disk, which means that dust must condensate (Ebel and Grossman,

2000; Grossman, 1972; Larimer, 1967) under conditions dictated by the cooling of the disk. However, the ongoing accretion will keep transporting dust inward towards hotter regions, this could lead to vaporization fronts as described in Cuzzi, (2004); Cuzzi *et al.* (2003).

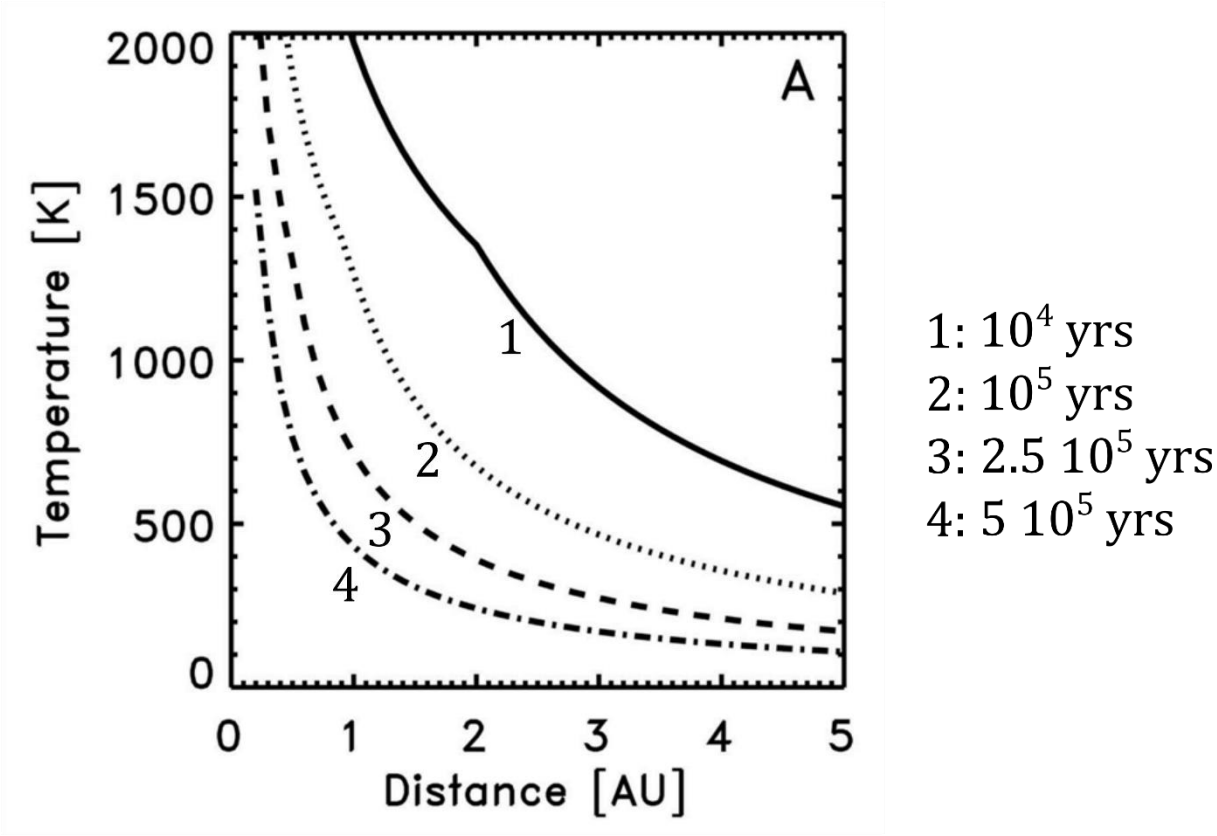

Figure 5: Temperature evolution of a nebula (after Ciesla, 2008).

The various stages of planetary accretion have been described in broad terms by Chambers (2004). The dust initially settles to the midplane and starts migrating towards the Sun. The migration of dust depends on its size (Weidenschilling, 1977) and a common problem in planetary accretion is that the coupling of dust to the gas leads to a so-called barrier for planetary accretion. For objects smaller than approximately 1 m, the dust is coupled to the gas meaning, with a limited radial drift. However if they accrete to form larger object with a meter size diameter their radial drift increases and they rapidly drift towards the Sun. In contrast for larger size object this radial velocity becomes smaller as these objects are less coupled to the Sun. This implies that planetesimals must accrete rapidly to avoid being lost to the Sun. However, the mechanism responsible for having meter size objects sticking to each other was poorly understood. The turbulence of the planetary disks (Cuzzi *et al.*, 2003) was thought to lead to 'turbulent concentration' that could favor planetesimal accretion. Several mechanisms for planetesimal accretion have been proposed but the most favored is currently the streaming instability (Johansen and Youdin, 2007). In this case, meter-sized boulders can be concentrated in high pressure regions that evolve to a gravitational collapse due to self-gravity. Another possibility is to have

planetesimal growth due to pressure bumps (Birnstiel *et al.*, 2016) where dust can get concentrated to form planetesimals.

The formation of planetesimals is following by the stage of oligarchic growth that results in the formation of embryos that have a size between that of the Moon and Mars. These embryos grow at the expense of each other thanks to the effect of gravitational focusing. In essence, the larger objects have more gravitational attraction and their effective cross section to collision and accretion are greater than their physical cross section (Armitage, 2011; Chambers, 2004). In the case of terrestrial planet, the last stage of accretion is linked to giant impacts and this stage can last over tens of millions of years as indicated by the age of the Earth.

An important process that takes place during the early stage of planet formation is that the young star will be responsible for massive irradiation at levels that are several orders of magnitude (up to 1000) than the present-day Sun (Chaussidon and Gounelle, 2006). The effect of such an irradiation has been inferred by observations of short-lived nuclides such as ^{7}Be and ^{10}Be that were discovered in Calcium Aluminium rich inclusions (Chaussidon *et al.*, 2004, 2006). The presence of these nuclides was linked to the presence of X-winds associated with solar flares. These flares consist of electrons, protons and helium particles that are accelerated at energies of MeV and greater. The fluence associated with these flares are significant, up to 2×10^{25} particles/cm2 (Shu *et al.*, 1997; Lee, 1978; Gounelle *et al.*, 2001) and besides the presence of short-lived nuclides, their impact on the chemistry of dust has been investigated experimentally (Carrez *et al.*, 2001; Shilobreeva and Kuzmin, 2004; Davoisne and Leroux, 2006; Leroux, 2009).

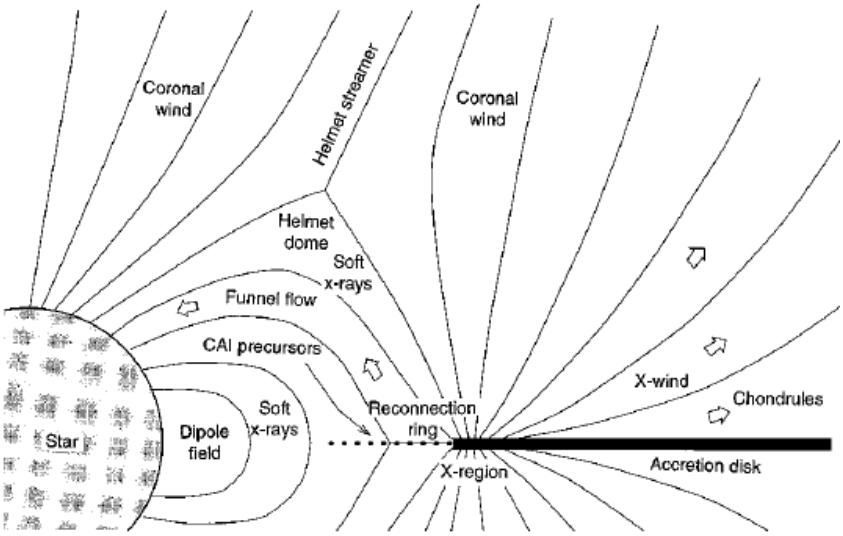

Figure 6: Schematic view of the irradiation model from X-winds produced in young stellar objects (from (Shu *et al.*, 1997)).

From a cosmochemical viewpoint, several stages of planetary accretion can lead to chemical modification of the dust initial composition. The initial dust vaporization followed by condensation could produce depletion in volatile elements relative to their initial contents, provided not all vapor is allowed to condense (e.g. Larimer 1973 ; Grossman 1972). If condensation takes place in dust rich environment this could also alter the canonical condensation sequence as described in Ebel and Grossmann (2000). Alternatively, the episodes of dust concentrations could naturally lead to concentration of refractory elements relative to volatile elements by factors that depend on the dust enrichment. The formation of chondrules which are typical features of chondritic meteorites are possibly responsible for element vaporization but the net effect is not easily quantified as recondensation are obviously also taking place (Hewins, 1991). Another high temperature process that could lead to volatile element loss are magma ocean that can form in planetesimals due to ^{26}Al heating or in larger objects due to giant impacts. In this case the gravitational energy produced by the impact can lead to complete melting of the planetary embryo.

4. Silicon isotopes as tracers of early planetary formation processes

4.1. Cosmochemical properties of silicon

Silicon is a major element in the Solar System with an abundance of 3.47×10^{-5} relative to hydrogen (Lodders, 2003). Silicon is a moderately volatile element with a 50% condensation temperature of 1310 K according to Lodders (2003) and 1314 K according to the more recent calculations of (Wood *et al.*, 2019). The chemistry of silicon is extremely versatile as it can form oxide polymeric compounds with oxygen in environments where the C/O ratio is lower than 0.90 while it will form more reduced compounds such as SiC or FeSi if C/O ratios are higher than 0.95 (Grossman *et al.*, 2008). In the Solar System (C/O= 0.57), Si is most often associated with O and the first Si-bearing compounds in the Solar System in the condensation sequence are gehlenite ($Ca_2Al_2SiO_7$), forsterite, diopside, enstatite and then anorthite (Larimer and Bartholomay 1979).

In a gas phase with a solar composition, depending on the temperature the most abundant species will be SiO or SiS (Fegley *et al.*, 2020; Grossman *et al.*, 2008; Larimer and Bartholomay, 1979), while it will be exclusively SiO in more oxidized environments corresponding to higher dust to gas ratios (Ebel and Grossman, 2000) or after a giant impact (Fegley *et al.*, 2020; Visscher and Fegley, 2013).

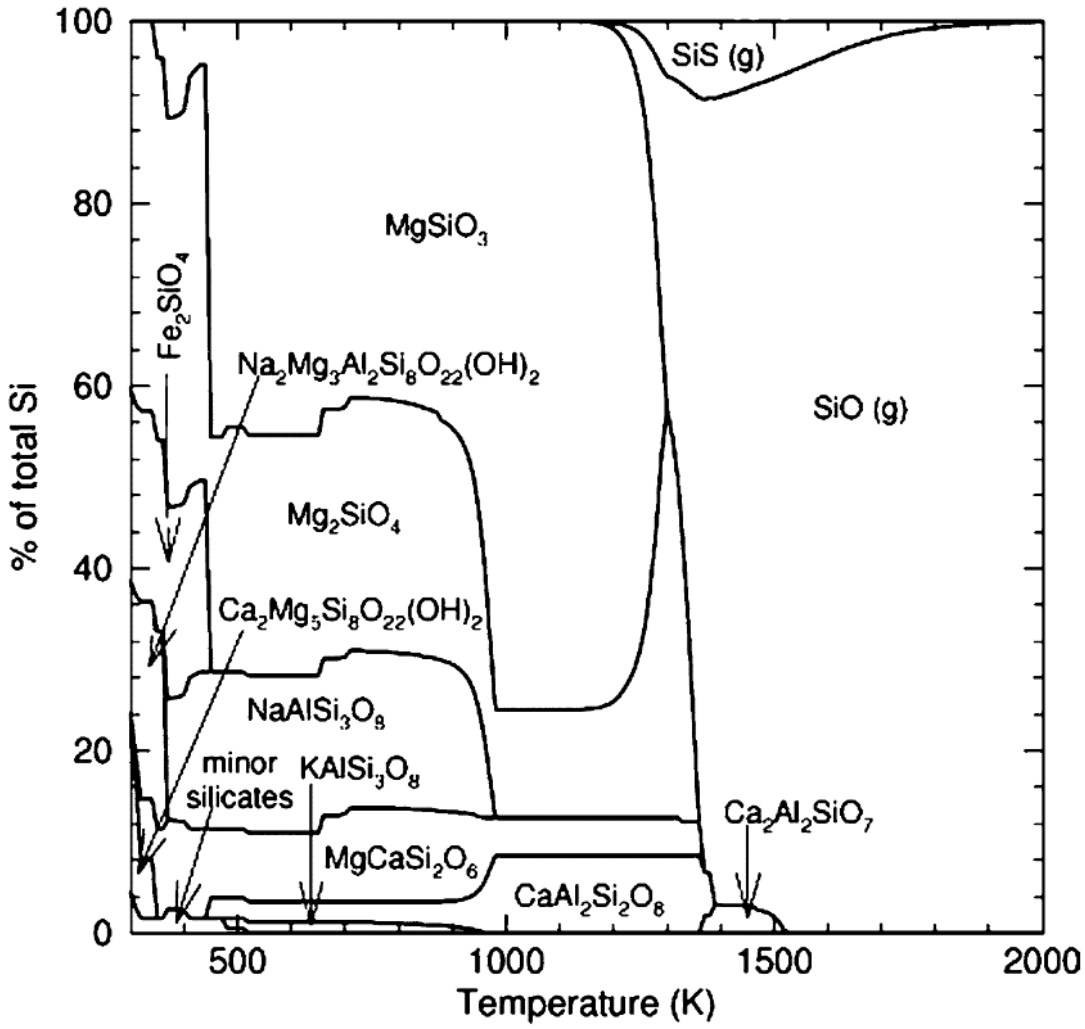

Figure 7: Diagram illustrating the condensation of Si from a solar composition gas as a function of temperature assuming a total pressure of 10^{-4} bars (from (Fegley and Schaefer, 2010). (g) indicates gaseous species.

Once planetary bodies are accreted, for oxygen fugacities typical of Earth and Mars, silicon will be mainly in the mantle part of the planet. However, a significant amount of silicon will be partition in the metal for oxygen fugacities lower than IW-2 (Kilburn and Wood, 1997; Gessmann *et al.*, 2001; Wade and Wood, 2005; Fischer *et al.*, 2015) or if metal silicate equilibration during core formation takes place at high pressure and high temperature. This means that silicon becomes more siderophile under these conditions. Thus, the amount of silicon that can dissolve in metallic iron can be an indicator of the oxygen fugacity in planetary materials (Zhang and Sears, 1996). For example in enstatite chondrites or in aubrites that formed under reduced conditions (typically IW-6), the concentrations of Si in the metal can reach a few percents (Keil, 2010; Savage and Moynier, 2013; Ziegler *et al.*, 2010).

4.2. Isotope fractionation of silicon in the early Solar System

Metal-silicate fractionation

The density of the Earth's core is lower than of pure Fe-Ni allow and this density deficit was attributed to the presence of light elements in the core (Anderson and Isaak, 2002; Birch, 1968; Boehler, 2000). Si was mentioned as a good candidate, because incorporation of Si in the core could explain the superchondritic Mg/Si ratio of the bulk silicate Earth and its heavy Si isotope composition relative to that of chondrites (Armytage *et al.*, 2011; Fitoussi *et al.*, 2009; Georg *et al.*, 2007; Zambardi *et al.*, 2013). Ziegler et al. (2010) reported an offset of 5 to 6 ‰ of the $\delta^{30}Si$ value of aubrites between Si bearing-silicates and Si bearing-metal. With the known equilibration temperature of aubrites, Ziegler et al. (2010) infered the temperature dependence of Si isotope fractionation between silicates and melt. Metal-silicate experiments were also performed to constrain directly the Si isotope fractionation during metal-silicate differentiation (Hin *et al.*, 2014; Shahar *et al.*, 2011, 2009; Moynier *et al.*, 2020). The difference between $\delta^{30}Si_{metal}$ and $\delta^{30}Si_{silicates}$ expressed as $\Delta^{30}Si_{met\text{-}sil}$ was shown to vary as the inverse of the square of the temperature. The coefficient of temperature dependence varies among the studies: $-5.5.10^{-6}$ to $-5.8.\ 10^{-6}$ (Georg *et al.*, 2007), $-7.64(\pm0.7)\times10^{-6}$ (Ziegler *et al.*, 2010),$-7.45(\pm0.41)\times10^{-6}$ (Shahar *et al.*, 2011), $-4.42(\pm0.05)\times10^{-6}$ (Hin *et al.*, 2014) and $-7.6(\pm0.7)\times10^{-6}$ (Moynier *et al.*, 2020). Using mass balance equations it is possible calculate the amount of Si incorporated into the Earth's core, for each considered core formation model, as a function of $\Delta^{30}Si_{BSE\text{-}chondrites}$. Note that these models still require an estimate of the temperature of metal silicate equilibration. The choice of the primary building blocks is also crucial, as it has a strong control on the calculated amount of Si in the core. For example, if one uses enstatite chondrites as building blocks for the Earth, it would require 28.5 % of Si in the core, and ordinary chondrites would require 12.8 %wt in the core (Fitoussi *et al.*, 2009) both values are far from the few per cent of Si constrained by recent physical studies (Badro *et al.*, 2014).

The Si isotope composition of SNC, angrites and HED meteorites were not affected by core formation processes owing to rather oxidizing conditions during mantle-core differentiation and relatively lower temperatures that prevent Si to enter into the core (Grossman *et al.*, 2008; Kilburn and Wood, 1997; Steenstra *et al.*, 2020).

Fractionation between minerals and melt

Basalts and peridotites share similar Si isotope composition, suggesting limited Si isotope fractionation due to partial melting processes (Armytage *et al.*, 2011; Fitoussi *et al.*, 2009; Zambardi *et al.*,

2013).(Savage *et al.*, 2011) reported δ^{30}Si data from a basaltic suite of the Hekla volcano which displayed a positive correlation with their SiO_2 content which confirms trend found a previous studies by Douthitt (1982). This trend was attributed to fractional crystallisation processes with removal of olivine and pyroxene that are enriched in Si light isotopes during magmatic differentiation. These results were initially supported by the positive relationship between δ^{30}Si and the degree of polymerization of Si in tetrahedron argued by an earlier study by (Grant, 1954). Ab initio calculations confirmed the role of Si-O bond length, and cationic environment of SiO_4 on Si isotope fractionation (Méheut *et al.*, 2007, 2009; Méheut and Schauble, 2014). But there is not a direct correspondence between Si isotope fractionation and degree of polymerisation, as kaolinite is less fractionated than lizardite relative to quartz despite their same polymerisation degree (Méheut *et al.*, 2009). (Huang *et al.*, 2014) computed Si isotope fractionation between high pressure mantle minerals and silicate melt during terrestrial magma ocean crystallisation. They showed that isotope fractionation occurred between two phases with different coordination number of Si or different Si-O bond lengths. This study inferred that the δ^{30}Si value 0.08 to 0.12 ‰ should be lighter in the lower mantle if it has preserved the crystallization assemblage inherited from magma ocean crystallization.

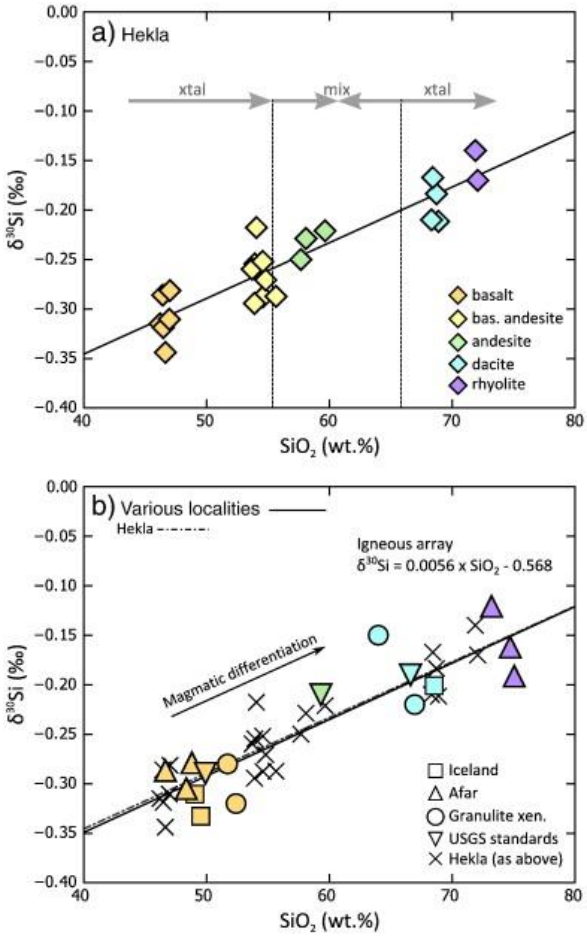

Figure 8: The Si isotope terrestrial igneous array related to magmatic differentiation, from (Savage *et al.*, 2014).

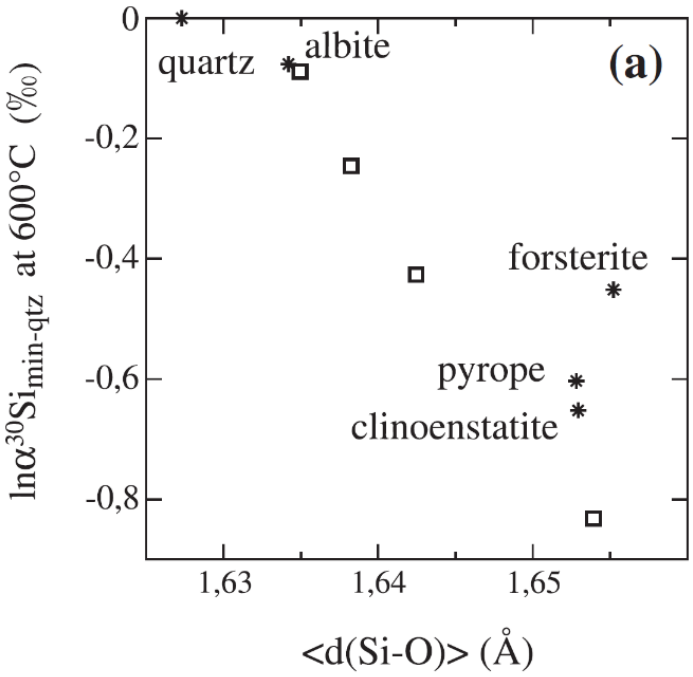

Figure 9: Si isotope fractionation factors of mineral and quartz with the average Si-O bond length. From Méheut and Schauble (2014).

5. The origin of Si isotope variations in chondrites

With the advent of inductively coupled mass spectrometry, it has been possible to measure precisely enough the Si isotope composition of chondrites (Armytage *et al.*, 2011; Fitoussi *et al.*, 2009; Georg *et al.*, 2007; Zambardi *et al.*, 2013) and these data were compiled in Savage et al. (2014). Overall, there is a clear distinction between the enstatite chondrites on the one hand and the ordinary and carbonaceous chondrites on the other hand. Fitoussi et al. (2009) have reported a correlation between δ^{30}Si and Mg/Si, with carbonaceous chondrites being characterized by slightly higher δ^{30}Si than ordinary chondrites. Several hypothesis have been proposed to explain this correlation and the difference between enstatite chondrites and the other chondrite groups.

(1) The preferred scenario of Fitoussi et al. (2009) was that the carbonaceous chondrites with high Mg/Si reflected a higher abundance of olivine and that enstatite chondrites formed by reaction of SiO rich vapor as argued in (Palme, 2000). The reaction of olivine with SiO formed enstatite, thereby

lowering the Mg/Si ratio. If one then assumes that this reaction takes place with kinetic isotope fractionation then the enstatite should be enriched in light Si isotopes as is observed.

(2) It was proposed by Dauphas et al. (2015) that fractional condensation starting from a Solar composition would initially lead to condensates with a high Mg/Si ratios (olivine) that would be enriched in heavy isotopes. Following that condensation the residual gas would be enriched in light isotopes. Mixing with condensates having the compositions of the residual gas would produce the observed correlation (Dauphas *et al.*, 2015).

(3) In contrast, Savage and Moynier (2013) interpreted the low δ^{30}Si of enstatite chondrites by the presence of a Si-bearing metallic phase characterized by a low δ^{30}Si itself. In this hypothesis there is no specific link between the low Mg/Si of enstatite chondrites (reflecting the presence of enstatite as the main silicate) and their low δ^{30}Si.

6. The difference in δ^{30}Si between the Earth and chondrites

In contrast with meteorites there is no correlation between Mg/Si ratios and δ^{30}Si in terrestrial samples including peridotites and mantle derived rocks. However, it was clear based on the earliest Si isotope data (Armytage *et al.*, 2011; Fitoussi *et al.*, 2009; Georg *et al.*, 2007; Savage *et al.*, 2010; Zambardi *et al.*, 2013) that there is a difference in silicon isotopes between the bulk Silicate Earth (δ^{30}Si=-0.29 ‰) and chondrites. Several hypotheses can be proposed to explain these important observations.

(1) One can first assume that the composition of the bulk silicate Earth (BSE) is equal to that of the bulk Earth (BE). In this case the Earth would belong to the δ^{30}Si versus Mg/Si trend defined in Fitoussi et al. (2009) and Dauphas et al. (2015). In this case the high δ^{30}Si is inherited from nebular processes and the high Mg/Si would result from a greater abundance of an olivine component compared with carbonaceous and ordinary chondrites.

(2) The higher δ^{30}Si value in the bulk silicate Earth is related to the incorporation of Si in the Earth under reducing conditions or at high pressure. As the metal phase is enriched in light silicon isotopes, the bulk silicate Earth becomes enriched in heavy isotopes (Georg *et al.*, 2007; Fitoussi *et al.*, 2009; Zambardi *et al.*, 2013; Hin *et al.*, 2014). This hypothesis is discussed in greater detail below.

(3) Highly energetic impacts during the formation of the Earth produce vaporization of silicon. This process was advocated by (Pringle *et al.*, 2014) to explain the elevated δ^{30}Si values in angrites a class

of achondrite meteorites. These authors further argued that the same process could explain part of the offset in $\delta^{30}Si$ between the Earth and chondrites.

(4) Another possibility is that Si was lost during magma ocean stages. The loss of silicon in the form of SiO would lead to an enrichment in heavy Si isotopes in the residual magma ocean (Hin *et al.*, 2017) with a preferential loss of SiO relative to Mg.

(5) Last, since mantle peridotites are derived from the upper mantle, one could argue that the lower mantle has a different $\delta^{30}Si$ value due to an early mantle differentiation event such as the crystallisation of a magma ocean. Such a hypothesis was proposed by (Huang *et al.*, 2014) based on ab initio calculations of Si isotope fractionation factors for high pressure mantle minerals.

In what follows we discuss in more detail each of these possibilities.

7. Si isotope fractionation due to core formation

It has long been known (e.g. Jagoutz *et al.*, 1979) that the Mg/Si ratio of terrestrial rocks, in particular in fertile peridotites is higher than that of chondrites. If one plots Mg/Si as a function of Al/SI ratios in terrestrial rocks and chondrites, there is a negative trend for terrestrial peridotites while chondrites form a positive trend, which has been called the 'cosmochemical trend' (Figure 11). One interpretation of the higher Mg/Si ratio in the bulk Silicate Earth was that some Si has been incorporated in the terrestrial core (Palme *et al.*, 2014).

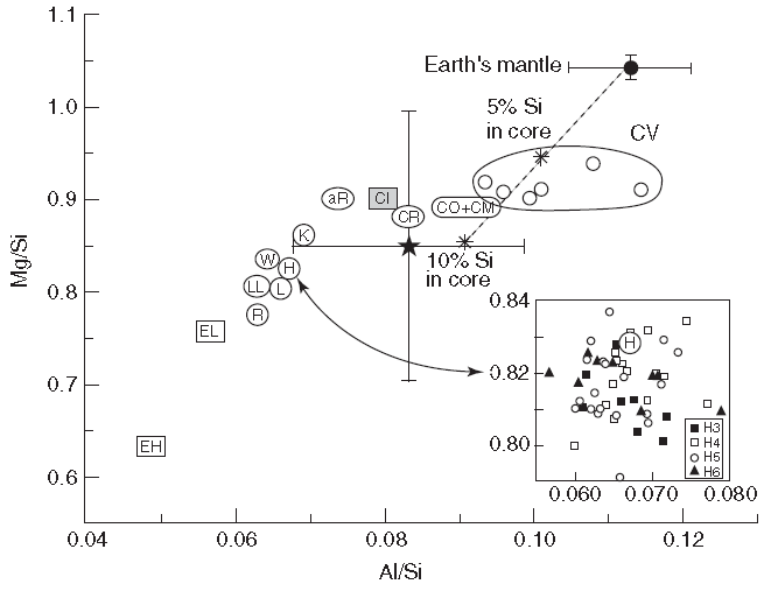

Figure 10: Mg/Si versus Al/Si in chondrites and the Earth's mantle. From (Palme and O'Neill, 2007)

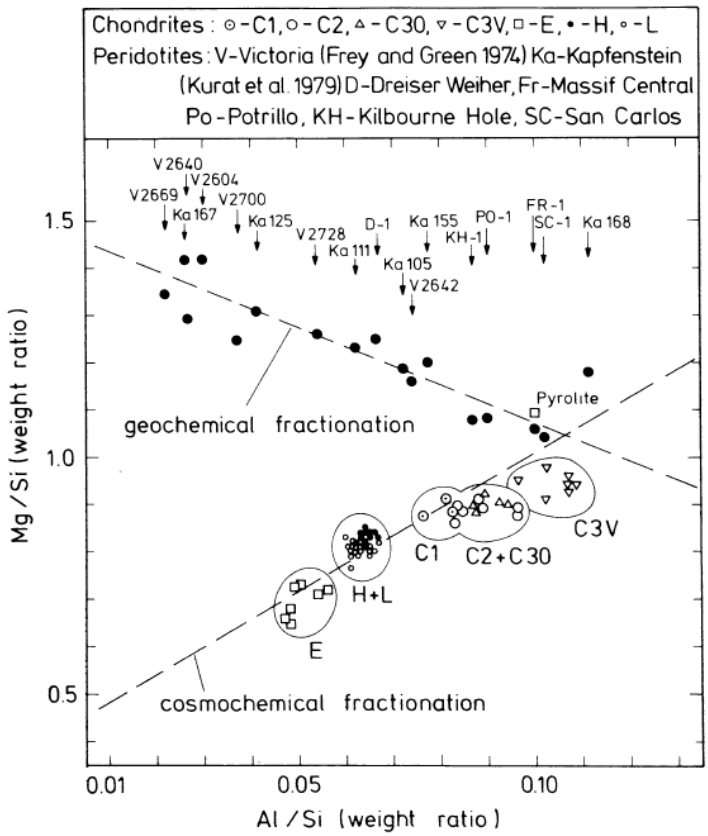

Figure 11: Mg/Si versus Al/Si in chondrites and the Earth's mantle. From Jagoutz *et al.* (1979).

Bulk composition of the Earth

One may assume that the bulk chemical composition of the Earth is chondritic as the abundances of refractory lithophile elements of the Earth are similar to those of chondrites (Allègre *et al.*, 1995; McDonough and Sun, 1995). If one selects carbonaceous chondrites, then the amount of silicon that must enter the core is roughly 7wt%, while it should be 12.8wt% et 28.5wt% if one assumes that the Earth is made of ordinary or enstatite chondrites, respectively. One should not however, that mineral physics and geophysical constraints would argue for a much lower Si content in the Earth's core (e.g. Badro *et al.*, 2007).

Model for the formation of the Earth's core based on siderophile elements

As the process of core formation is extremely complex (Stevenson, 1990; Deguen *et al.*, 2014; Brian Tonks and Jay Melosh, 1992; Deguen *et al.*, 2011; Landeau *et al.*, 2021), geochemists have generally made assumptions to make this problem tractable.

Most models assume for example that there is complete chemical (and isotopic) equilibrium between the metal and silicate (e.g. Corgne *et al.*, 2008; Fischer *et al.*, 2015; Rubie *et al.*, 2011; Wade and Wood, 2005). As the formation of the core is probably dependent on the rate of terrestrial accretion which must have lasted a few tens of millions of years, it is often assumed that the nature of accreted material could have changed over time. This is the model of heterogeneous accretion where the oxygen fugacity of accreted material increases over time, starting from reducing material (Fitoussi *et al.*, 2009; Rubie *et al.*, 2011, 2015; Schönbächler *et al.*, 2010; Wade and Wood, 2005) and ending with more oxidizing material akin to carbonaceous chondrites. The more reducing stages plays a particular important role for Si as Si is more siderophile at low oxygen fugacities (Fischer *et al.*, 2015; Gessmann *et al.*, 2001; Kilburn and Wood, 1997; Wade and Wood, 2005). Another possibility to make Si more siderophile is to have core formation taking place at very high pressures and temperatures (e.g. Fischer *et al.*, 2015; Siebert *et al.*, 2011) that favor the siderophile character of Si.

Various models used to interpret Si isotopes in the Earth are summarized in Table 1.

Table 1: Summary of the different models proposed by Fitoussi et al. (2009) for interpreting the Si isotope record of the Earth

Reference	(Wänke *et al.*, 1981)		(Rubie *et al.*, 2003)	(Wade and Wood, 2005)	
Accretion stage	Stage 1	Stage 2		Stage 1	Stage 2
P-T Conditions	Low P=2.5GPa T=2023K		High P=30GPa High T=3000K	P=18GPa T=2473K	P=40GPa T=3000K
Oxygen fugacity	Highly reducing conditions IW-6	Very oxidizing conditions	IW-2	IW-4	increasing
Metal-silicate partition coefficient	from Georg et al. (2007) at 1bar Ab initio calculation		from (Schauble *et al.*, 2007) Ab initio calculation	from Georg et al. (2007) at 1bar Ab initio calculation	from Schauble et al. (2007) Ab initio calculation
% Si in the core	8 wt%	Oxidized material, no Si enters the core	8% must be incorporated in the core to match the Mg/Si ratio of the BSE	10 wt% from Gessmann et al. (2001) Metal-silicate experiments and models	
$\Delta 30Si_{BSE-CC}$	> 0.23 ‰		≈ 0.08‰	≈ 0.08‰	

8. A nebular process for explaining the high $\delta^{30}Si$ of the Earth

Based on the existence of high $\delta^{30}Si$ found in angrites (Pringle et al. 2014 ; Dauphas et al. 2015), it was argued by Dauphas et al. (2015) that the Si isotope composition of the Earth was due to an early effect of olivine condensation. Indeed the Mg/Si molar ratio of olivine is equal to 2, therefore a high proportion of olivine relative to enstatite in a planetary body should result in a higher Mg/Si. Dauphas et al. (2015) developed a model based on equilibrium isotope fractionation from a gas with a solar composition and in this case, forsterite should be enriched in heavy isotope relative to SiO which is the main Si phase in the vapor phase. (Larimer and Anders, 1970; Yoneda and Grossman, 1995) showed that in the conditions of the Solar nebula (P 10^{-3} atm et T 1370K), forsterite should condense with Mg/Si = 2 and this should lower the Mg/Si ratio of the residual nebular gas. Most of the magnesium is then in the condensed phase while only half of the Si is condensed. The olivine rich condensate should be characterized by a high $\delta^{30}Si$ value (Huang *et al.*, 2014). The composition of the Earth and of chondrites in this case would be explained by mixing with Si depleted nebular gas that would be characterized by lower $\delta^{30}Si$ values. (See Figure 12).

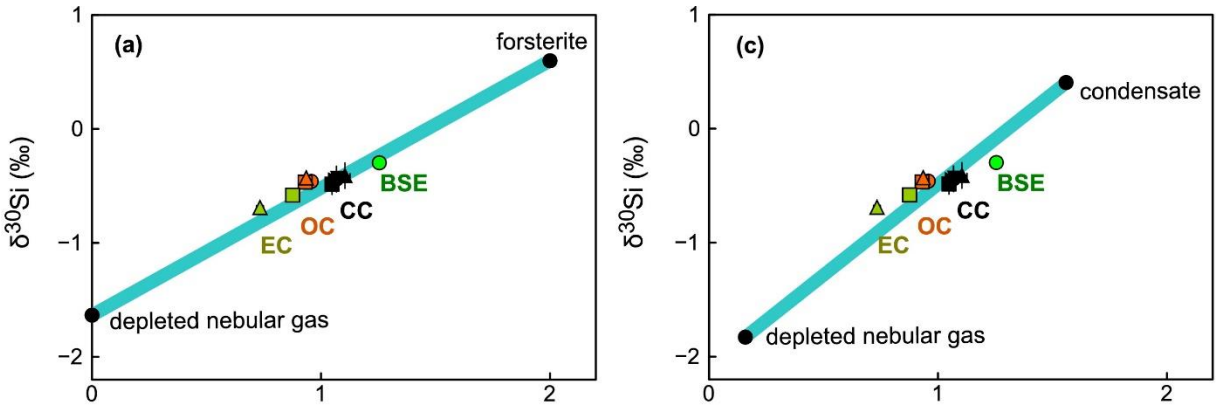

Figure 12: Model of Dauphas et al. (2015) to explain the variations in $\delta^{30}Si$ in the Solar System. The composition of the BSE is explained by a mixture of forsterite with 'Si depleted nebular gas' having low $\delta^{30}Si$.

9. Loss of silicon during a magma ocean stage

The last stages of terrestrial planet accretion was dominated by multiple giant impact such as the Moon forming impact (Chambers, 2004; Tucker and Mukhopadhyay, 2014). These impacts generated a large amount of gravitational energy that was sufficient entirely melt the Earth (Rubie *et al.*, 2007) and thus

generated a large scale magma ocean that could have resulted in the loss of elements partitioned in the vapor phase (Hin *et al.*, 2017). The basis for the model of Hin et al. (2017) is that Mg isotope show a resolvable difference betwen the Earth and chondrites, with chondrites being characterized by a $^{25}Mg/^{24}Mg$ 0.02‰ lower than the $^{25}Mg/^{24}Mg$ ratio of the Earth. Since Mg isotopes do not fractionate significantly during magmatic processes this difference is ascribed to a planetary scale difference. In contrast with Si, Mg is a lithophile element and should not partition into the Earth's core and it would become siderophile only at temperatures where the Mg isotope fractionation would be prohibitively small (O'Rourke and Stevenson, 2016). Hin et al. (2017) rejected a nebular process as argued in Dauphas et al. (2015) as such a model would predict that enstatite chondrites should be characterized by the lowest $^{25}Mg/^{24}Mg$ ratio, which is not observed.

This type of model implies that one can no longer use the difference in $\delta^{30}Si$ between the BSE and chondrites to determine the Si in the Earth's core.

The production of a magma ocean also generates a dense Si, Na and O rich atmosphere that will be characterized by a relatively high pressure compared with the solar nebula. Thus, the conditions of SiO vaporization will be very different from those of chondrule formation (Kadlag *et al.*, 2019, 2021) or early condensation (Larimer, 1967). The existence of a vapor will limit the degree of Si isotope fractionation (Davis and Richter, 2003; Dauphas *et al.*, 2015; Bourdon and Fitoussi, 2020). However, for the vapor to escape, the size of the planetary object should not be too large as a large body implies a high escape velocity. Thus Hin et al. (2017) proposed that this process should take place in bodies with 10% of the mass of the Earth (embryos). Starting from an enstatite chondrite composition, this would imply that 47% of the mass would be lost by vaporization, which would correspond to 14%, 65% and 99.9% of the initial amounts of Mg, Si, Na and K, respectively. Furthermore it was argued in Hin et al. (2017) that there should be isotope and chemical equilibrium at the interface between the vapor and the magma ocean, which limits the magnitude of Si isotope fractionation. (Young *et al.*, 2019) and (Tang and Young, 2020) have even developed a model that showed that the isotope fractionation in the residual magma should be very limited.

10.The consequences of terrestrial magma ocean crystallization on Si isotopes

If some intra-mantle process over the Earth's history could produce a difference in Si isotopes between the lower and the upper mantle, then the difference between the BSE and chondrites could perhaps have an explanation. The concept of a lower mantle different from the upper mantle has been

suggested in the literature (e.g. Javoy *et al.*, 2010) and such a hypothesis has been revived by Huang et al. (2014) who examined the potential role of magma ocean crystallization. These authors calculated the Si isotope fractionation factor between olivine and various lower mantle minerals and found that the change in Si isotope coordination caused variations in the isotope fractionation factors. At high pressure, the coordination of Si with surrounding oxygens becomes higher, which inevitably corresponds to longer Si-O bond lengths. For example, in olivine, clinopyroxene, enstatite the typical Si-O bond lengths is approximately 1.64 Å, while it is 1.80 in perovskite where Si is octahedrally coordinated with O. Accordingly, as predicted by Schauble et al. (2004), heavy Si isotopes are enriched in olivine relative to perovskite (Huang et al. 2014).

Huang et al. (2014) have examined whether these differences in isotope fractionation factors could result in difference in δ^{30}Si between the upper and the lower mantle, after crystallization of a magma ocean. If one assumes that the lower mantle and the upper mantle do not get remixed by convection, one can calculate the effect of high pressure crystallization on δ^{30}Si by making some hypothesis on the Si isotope fractionation in silicate melts. Huang et al. (2014) found that the lower mantle could have a δ^{30}Si value ranging between -0.37 to -0.41 ‰ while the δ^{30}Si of the upper mantle is -0.29 ‰. Thus, the bulk composition of the mantle is actually significantly lower, which means that the amount of Si that must be incorporated into the core in order to explain the difference in δ^{30}Si between the BSE and chondrites can be revalued downwards.

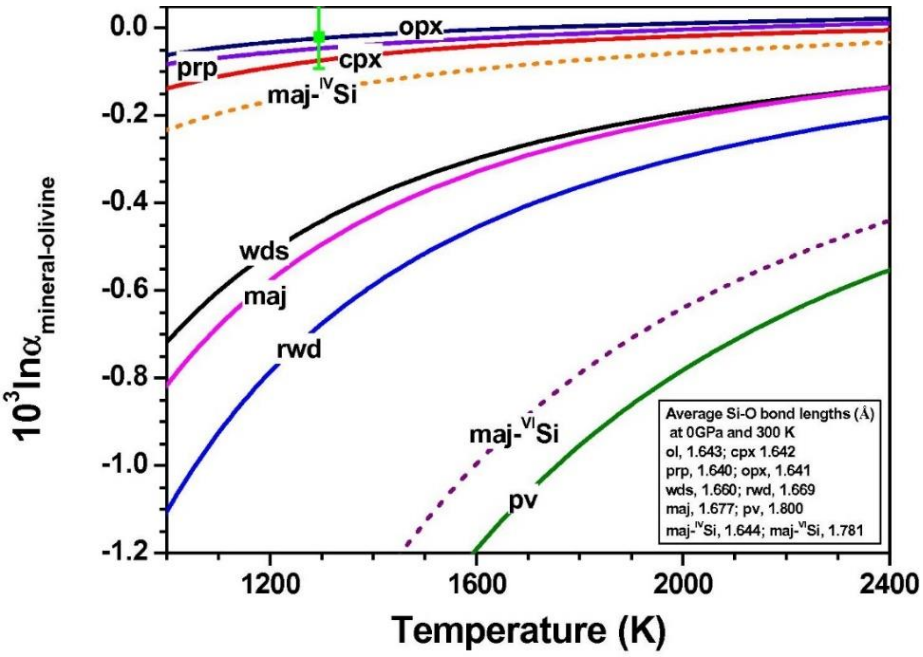

Figure 13: Si isotope fractionation factors between olivine and various mantle minerals calculated by ab initio methods (Huang et al. 2014). Perovskite (green curve) is the most fractionated mantle mineral.

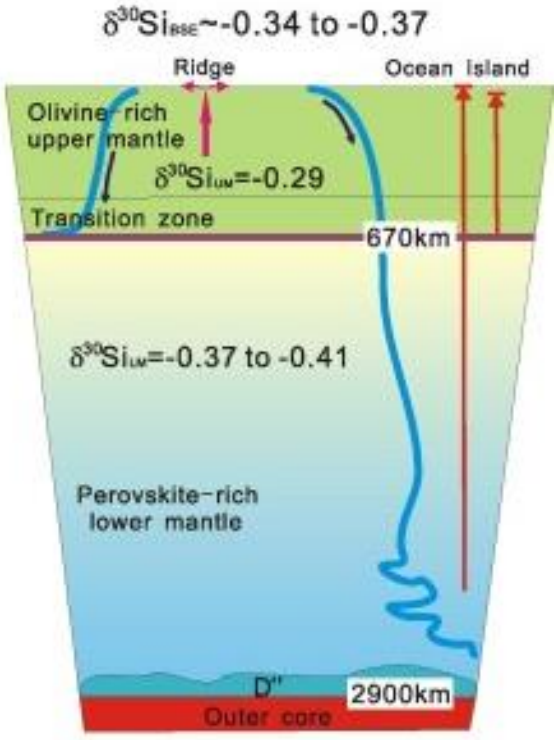

Figure 14: The effect of magma ocean crystallization on the Si isotope composition of the upper and lower mantle in the Earth (from Huang et al., 2014).

11.Research topics addressed in this doctoral thesis

Based on this short review of the applications of silicon isotopes in cosmochemistry, it is obvious that there are still some open questions regarding the interpretation of silicon isotopes in meteorites and planetary materials. In what follows, we describe briefly the topics that were addressed in this thesis, in light of previous work. Since an important aspect of published data is the presence of disagreements and controversies about Si isotope measurements, a great deal of time was spent on developing an accurate and precise analytical method for measuring silicon isotopes in planetary materials, the method is described in the second chapter. This chapter was written in french but many elements illustrated as figures should be understandable to the non-french reader and the analytical methods given in the following chapters summarize the most important features of this chapter.

It has been known for some time that the smaller size of Mars compared with the Earth suggests that it cooled more rapidly than the Earth. In addition, the presence of anomalies in ^{142}Nd and ^{182}W in SNC meteorites indicates that the martian mantle was differentiated at a very early stage and that this differentiation was still detectable in rocks formed at a much later stage. Thus, in light of the work of Huang et al. (2014), it could be tempting to investigate whether the martian mantle could reveal some

ancient heterogeneities similarly to the Hf-W and Sm-Nd systems that could reflect the crystallization of the magma ocean or the effect of vaporization during a magma ocean stage.

Similarly, the observations of high δ^{30}Si in angrites indicated some affinities with the terrestrial mantle. Furthermore, there appeared to be discrepancy between the data sets of Pringle et al. (2014) and Dauphas et al. (2015). The Si isotope data of Pringle et al. (2014) showed a comparatively large range that could reflect Si isotope mantle heterogeneity, in spite of the fact that it has been argued that the angrite parent body has experienced a magma ocean stage. This means that there could be uncertainties about the mean δ^{30}Si of the angrite parent body. In contrast, the four angrite data points of Dauphas et al. (2015) suggest a much narrower range indicating that the δ^{30}Si signature of angrites was possibly acquired at an early stage. Our work has extended the angrite data base using a precise analytical technique with the goal of better understanding this unique δ^{30}Si signature in planetary materials.

Last, we attempted a more exploratory project by measuring the Si isotope compositions of olivine that have previously irradiated with high energy helium (200 keV and 6 MeV) particles to find out whether this process could produce Si isotope fractionation in addition to the elemental fractionation already described in the literature (e.g. Shilobreeva and Kuzmin, 2004).

References

Allègre, C.J., Poirier, J.-P., Humler, E., Hofmann, A.W. (1995) The chemical composition of the Earth. *Earth and Planetary Science Letters* 134, 515–526.

Allenby, R.J. (1954) Determination of the isotopic ratios of silicon in rocks. *Geochimica et Cosmochimica Acta* 5, 40–48.

ALMA Partnership *et al.* (2015) The 2014 ALMA Long Baseline Campaign: First Results from High Angular Resolution Observations toward the HL Tau Region. *The Astrophysical Journal* 808, L3.

Anderson, O.L., Isaak, D.G. (2002) Another look at the core density deficit of Earth's outer core. *Physics of the Earth and Planetary Interiors* 131, 19–27.

Armitage, P.J. (2011) Dynamics of Protoplanetary Disks. *Annual Review of Astronomy and Astrophysics* 49, 195–236.

Armytage, R.M.G., Georg, R.B., Savage, P.S., Williams, H.M., Halliday, A.N. (2011) Silicon isotopes in meteorites and planetary core formation. *Geochimica et Cosmochimica Acta* 75, 3662–3676.

Armytage, R.M.G., Georg, R.B., Williams, H.M., Halliday, A.N. (2012) Silicon isotopes in lunar rocks: Implications for the Moon's formation and the early history of the Earth. *Geochimica et Cosmochimica Acta* 77, 504–514.

Badro, J., Cote, A.S., Brodholt, J.P. (2014) A seismologically consistent compositional model of Earth's core. *Proceedings of the National Academy of Sciences* 111, 7542–7545.

Badro, J., Fiquet, G., Guyot, F., Gregoryanz, E., Occelli, F., Antonangeli, D., d'Astuto, M. (2007) Effect of light elements on the sound velocities in solid iron: Implications for the composition of Earth's core. *Earth and Planetary Science Letters* 254, 233–238.

Bigeleisen, J., Mayer, M.G. (1947) Calculation of Equilibrium Constants for Isotopic Exchange Reactions. *The Journal of Chemical Physics* 15, 261–267.

Birch, F. (1968) On the possibility of large changes in the Earth's volume. *Physics of the Earth and Planetary Interiors* 1, 141–147.

Birnstiel, T., Fang, M., Johansen, A. (2016) Dust Evolution and the Formation of Planetesimals. *Space Science Reviews* 205, 41–75.

Boehler, R. (2000) High-pressure experiments and the phase diagram of lower mantle and core materials. *Reviews of Geophysics* 38, 221–245.

Bottinga, Y. (1968) Calculation of fractionation factors for carbon and oxygen isotopic exchange in the system calcite-carbon dioxide-water. *The Journal of Physical Chemistry* 72, 800–808.

Bourdon, B., Fitoussi, C. (2020) Isotope Fractionation during Condensation and Evaporation during Planet Formation Processes. *ACS Earth and Space Chemistry*. American Chemical Society 4, 1408–1423.

Brian Tonks, W., Jay Melosh, H. (1992) Core formation by giant impacts. *Icarus* 100, 326–346.

Canup, R.M. (2012) Forming a Moon with an Earth-like Composition via a Giant Impact. *Science*. American Association for the Advancement of Science 338, 1052–1055.

Carrez, P., Leroux, H., Cordier, P., Guyot, F. (2001) Electron-irradiation-induced phase transformation and fractional volatilization in (Mg, Fe) $_2$ SiO $_4$ olivine thin films. *Philosophical Magazine A* 81, 2823–2840.

Cassen, P. (1994) Utilitarian Models of the Solar Nebula. *Icarus* 112, 405–429.

Chacko, T., Cole, D., Horita, J. (2019) Equilibrium oxygen, hydrogen and carbon isotope fractionation factors applicable to geologic systems. *Stable Isotope Geochemistry*, 1–81.

Chakrabarti, R., Jacobsen, S.B. (2010) Silicon isotopes in the inner Solar System: Implications for core formation, solar nebular processes and partial melting. *Geochimica et Cosmochimica Acta* 74, 6921–6933.

Chambers, J.E. (2004) Planetary accretion in the inner Solar System. *Earth and Planetary Science Letters* 223, 241–252.

Chaussidon, M., Gounelle, M. (2006) Irradiation Processes in the Early Solar System. *Meteorites and the Early Solar System II*.

Chaussidon, M., Robert, F., McKeegan, K.D. (2004) Li and B Isotopic Variations in Allende Type B1 CAI 3529-41: Traces of Incorporation of Short-lived 7Be and 10Be. Lunar and Planetary Science Conference 2004 1568.

Chaussidon, M., Robert, F., McKeegan, K.D. (2006) Li and B isotopic variations in an Allende CAI: Evidence for the in situ decay of short-lived 10Be and for the possible presence of the short-lived nuclide 7Be in the early solar system. *Geochimica et Cosmochimica Acta* 70, 224–245.

Ciesla, F.J. (2008) Radial transport in the solar nebula: Implications for moderately volatile element depletions in chondritic meteorites. *Meteoritics & Planetary Science* 43, 639–655.

Clayton, R.N., Mayeda, T.K. (1978) Isotopic fractionation of silicon in Allende Inclusions. *Proc. Lunar PLanet Sci. Conf. 9th* 1267–1278.

Corgne, A., Keshav, S., Wood, B.J., McDonough, W.F., Fei, Y. (2008) Metal–silicate partitioning and constraints on core composition and oxygen fugacity during Earth accretion. *Geochimica et Cosmochimica Acta* 72, 574–589.

Criss, R.E. (1999) Isotopic Exchange and Equilibrium Fractionation. *Isotopic Exchange and Equilibrium Fractionation*. Oxford University Press.

Cuzzi, J.N., Davis, S.S., Dobrovolskis, A.R. (2003) Blowing in the wind. II. Creation and redistribution of refractory inclusions in a turbulent protoplanetary nebula. *Icarus* 166, 385–402.

Cuzzi, J.N. (2004) Blowing in the wind: III. Accretion of dust rims by chondrule-sized particles in a turbulent protoplanetary nebula. *Icarus* 168, 484–497.

Dauphas, N., Poitrasson, F., Burkhardt, C., Kobayashi, H., Kurosawa, K. (2015) Planetary and meteoritic Mg/Si and δ30Si variations inherited from solar nebula chemistry. *Earth and Planetary Science Letters* 427, 236–248.

Davis, A.M., Richter, F.M. (2003) Condensation and Evaporation of Solar System Materials. *Treatise on Geochemistry* 1, 711.

Davoisne, C., Leroux, H. (2006) Structural and compositional modifications of fayalite Fe_2SiO_4 under electron irradiation. *Nuclear Instruments and Methods in Physics Research Section B: Beam Interactions with Materials and Atoms* 243, 371–376.

Deguen, R., Olson, P., Cardin, P. (2011) Experiments on turbulent metal-silicate mixing in a magma ocean. *Earth and Planetary Science Letters* 310, 303–313.

Deguen, R., Landeau, M., Olson, P. (2014) Turbulent metal–silicate mixing, fragmentation, and equilibration in magma oceans. *Earth and Planetary Science Letters* 391, 274–287.

Douthitt, C.B. (1982) The geochemistry of the stable isotopes of silicon. *Geochimica et Cosmochimica Acta* 46, 1449–1458.

Ebel, D.S., Grossman, L. (2000) Condensation in dust-enriched systems. *Geochimica et Cosmochimica Acta* 64, 339–366.

Epstein, S., Taylor, H. (1970) The concentration and isotopic composition of hydrogen, carbon and silicon in Apollo 11 lunar rocks and minerals. *Geochimica et Cosmochimica Acta Supplement, Volume 1. Proceedings of the Apollo 11 Lunar Science Conference held 5-8 January, 1970 in Houston, TX. Volume 2: Chemical and Isotope Analyses. Edited by A. A. Levinson. New York: Pergammon Press, 1970., p.1085*.

Fegley, B., Lodders, K., Jacobson, N.S. (2020) Volatile element chemistry during accretion of the earth. *Geochemistry* 80, 125594.

Fegley, B., Schaefer, L. (2010) Cosmochemistry. In: Goswami, A., Reddy, B.E. (eds) *Principles and Perspectives in Cosmochemistry*. Springer, Berlin, Heidelberg, 347–377.

Fischer, R.A., Nakajima, Y., Campbell, A.J., Frost, D.J., Harries, D., Langenhorst, F., Miyajima, N., Pollok, K., Rubie, D.C. (2015) High pressure metal–silicate partitioning of Ni, Co, V, Cr, Si, and O. *Geochimica et Cosmochimica Acta* 167, 177–194.

Fitoussi, C., Bourdon, B., Kleine, T., Oberli, F., Reynolds, B.C. (2009) Si isotope systematics of meteorites and terrestrial peridotites: implications for Mg/Si fractionation in the solar nebula and for Si in the Earth's core. *Earth and Planetary Science Letters* 287, 77–85.

Fitoussi, C., Bourdon, B. (2012) Silicon Isotope Evidence Against an Enstatite Chondrite Earth. *Science* 335, 1477–1480.

Georg, R.B., Halliday, A.N., Schauble, E.A., Reynolds, B.C. (2007) Silicon in the Earth's core. *Nature* 447, 1102–1106.

Gessmann, C.K., Wood, B.J., Rubie, D.C., Kilburn, M.R. (2001) Solubility of silicon in liquid metal at high pressure: implications for the composition of the Earth's core. *Earth and Planetary Science Letters* 184, 367–376.

Gounelle, M., Shu, F.H., Shang, H., Glassgold, A.E., Rehm, K.E., Lee, T. (2001) Extinct Radioactivities and Protosolar Cosmic Rays: Self-Shielding and Light Elements. American Astronomical Society 548, 1051–1070.

Grant, F.S. (1954) The geological significance of variations in the abundances of the isotopes of silicon in rocks. *Geochimica et Cosmochimica Acta* 5, 225–242.

Grossman, L. (1972) Condensation in the primitive solar nebula. *Geochimica et Cosmochimica Acta* 36, 597–619.

Grossman, L., Beckett, J.R., Fedkin, A.V., Simon, S.B., Ciesla, F.J. (2008) Redox Conditions in the Solar Nebula: Observational, Experimental, and Theoretical Constraints. *Reviews in Mineralogy and Geochemistry* 68, 93–140.

Hewins, R.H. (1991) Retention of sodium during chondrule melting. *Geochimica et Cosmochimica Acta* 55, 935–942.

Hin, R.C., Fitoussi, C., Schmidt, M.W., Bourdon, B. (2014) Experimental determination of the Si isotope fractionation factor between liquid metal and liquid silicate. *Earth and Planetary Science Letters* 387, 55–66.

Hin, R.C. *et al.* (2017) Magnesium isotope evidence that accretional vapour loss shapes planetary compositions. *Nature* 549, 511–515.

Huang, F., Wu, Z., Huang, S., Wu, F. (2014) First-principles calculations of equilibrium silicon isotope fractionation among mantle minerals. *Geochimica et Cosmochimica Acta* 140, 509–520.

Jagoutz, E., Palme, H., Baddenhausen, H., Blum, K., Cendales, M., Dreibus, G., Spettel, B., Lorenz, V., Wänke, H. (1979) The abundances of major, minor and trace elements in the earth's mantle as derived from primitive ultramafic nodules. *Lunar and Planetary Science Conference Proceedings* 2, 2031–2050.

Javoy, M. *et al.* (2010) The chemical composition of the Earth: Enstatite chondrite models. *Earth and Planetary Science Letters* 293, 259–268.

Johansen, A., Youdin, A. (2007) Protoplanetary Disk Turbulence Driven by the Streaming Instability: Nonlinear Saturation and Particle Concentration. American Astronomical Society 662, 627–641.

Kadlag, Y., Tatzel, M., Frick, D.A., Becker, H. (2019) The origin of unequilibrated EH chondrites – Constraints from in situ analysis of Si isotopes, major and trace elements in silicates and metal. *Geochimica et Cosmochimica Acta* 267, 300–321.

Kadlag, Y., Tatzel, M., Frick, D.A., Becker, H., Kühne, P. (2021) In situ Si isotope and chemical constraints on formation and processing of chondrules in the Allende meteorite. *Geochimica et Cosmochimica Acta* 304, 234–257.

Keil, K. (2010) Enstatite achondrite meteorites (aubrites) and the histories of their asteroidal parent bodies. *Geochemistry* 70, 295–317.

Kilburn, M.R., Wood, B.J. (1997) Metal–silicate partitioning and the incompatibility of S and Si during core formation. *Earth and Planetary Science Letters* 152, 139–148.

Laeter, J.R. de, Böhlke, J.K., Bièvre, P.D., Hidaka, H., Peiser, H.S., Rosman, K.J.R., Taylor, P.D.P. (2003) Atomic weights of the elements. Review 2000 (IUPAC Technical Report). *Pure and Applied Chemistry*. De Gruyter 75, 683–800.

Landeau, M., Deguen, R., Phillips, D., Neufeld, J.A., Lherm, V., Dalziel, S.B. (2021) Metal-silicate mixing by large Earth-forming impacts. *Earth and Planetary Science Letters* 564, 116888.

Larimer, J.W. (1967) Chemical fractionations in meteorites—I. Condensation of the elements. *Geochimica et Cosmochimica Acta* 31, 1215–1238.

Larimer, J.W., Anders, E. (1970) Chemical fractionations in meteorites—III. Major element fractionations in chondrites. *Geochimica et Cosmochimica Acta* 34, 367–387.

Larimer, J.W., Bartholomay, M. (1979) The role of carbon and oxygen in cosmic gases: some applications to the chemistry and mineralogy of enstatite chondrites. *Geochimica et Cosmochimica Acta* 43, 1455–1466.

Lee, T. (1978) A local proton irradiation model for isotopic anomalies in the solar system. *The Astrophysical Journal* 224, 217.

Leroux, H. (2009) Dust modification under photon, electron and ion irradiation. *EAS Publications Series*. EDP Sciences 35, 153–169.

Lodders, K. (2003) Solar System Abundances and Condensation Temperatures of the Elements. *The Astrophysical Journal*. IOP Publishing 591, 1220.

Martins, R., Chaussidon, M., Deng, Z., Pignatale, F., Moynier, F. (2021) A condensation origin for the mass-dependent silicon isotopic variations in Allende components: implications for complementarity. *Earth and Planetary Science Letters* 554, 116678.

McDonough, W.F., Sun, S. (1995) The composition of the Earth. *Chemical Geology* 120, 223–253.

Méheut, M., Lazzeri, M., Balan, E., Mauri, F. (2007) Equilibrium isotopic fractionation in the kaolinite, quartz, water system: Prediction from first-principles density-functional theory. *Geochimica et Cosmochimica Acta* 71, 3170–3181.

Méheut, M., Lazzeri, M., Balan, E., Mauri, F. (2009) Structural control over equilibrium silicon and oxygen isotopic fractionation: A first-principles density-functional theory study. *Chemical Geology* 258, 28–37.

Méheut, M., Schauble, E.A. (2014) Silicon isotope fractionation in silicate minerals: Insights from first-principles models of phyllosilicates, albite and pyrope. *Geochimica et Cosmochimica Acta* 134, 137–154.

Mendybaev, R.A., Kamibayashi, M., Teng, F.-Z., Savage, P.S., Georg, R.B., Richter, F.M., Tachibana, S. (2021) Experiments quantifying elemental and isotopic fractionations during evaporation of CAI-like melts in low-pressure hydrogen and in vacuum: Constraints on thermal processing of CAIs in the protoplanetary disk. *Geochimica et Cosmochimica Acta* 292, 557–576.

Moynier, F., Deng, Z., Lanteri, A., Martins, R., Chaussidon, M., Savage, P., Siebert, J. (2020) Metal-silicate silicon isotopic fractionation and the composition of the bulk Earth. *Earth and Planetary Science Letters* 549, 116468.

O'Rourke, J.G., Stevenson, D.J. (2016) Powering Earth's dynamo with magnesium precipitation from the core. *Nature* 529, 387–389.

Palme, H. (2000) Are there Chemical Gradients in the Inner Solar System? In: Benz, W., Kallenbach, R., Lugmair, G.W. *From Dust to Terrestrial Planets*. Springer Netherlands, Dordrecht, 237–262.

Palme, H., O'Neill, H.St.C. (2007) 2.01 - Cosmochemical Estimates of Mantle Composition. In: Holland, H.D., Turekian, K.K. *Treatise on Geochemistry*. Pergamon, Oxford, 1–38.

Palme, H., Lodders, K., Jones, A. (2014) Solar System Abundances of the Elements. *Planets, Asteriods, Comets and The Solar System, Volume 2 of Treatise on Geochemistry (Second Edition). Edited by Andrew M. Davis. Elsevier, 2014., p.15-36* 2.

Poitrasson, F. (2017) Silicon Isotope Geochemistry. *Reviews in Mineralogy and Geochemistry* 82, 289–344.

Pringle, E.A., Savage, P.S., Badro, J., Barrat, J.-A., Moynier, F. (2013) Redox state during core formation on asteroid 4-Vesta. *Earth and Planetary Science Letters* 373, 75–82.

Pringle, E.A., Moynier, F., Savage, P.S., Badro, J., Barrat, J.-A. (2014) Silicon isotopes in angrites and volatile loss in planetesimals. *Proceedings of the National Academy of Sciences* 111, 17029–17032.

Reynolds, J.H., Verhoogen, J. (1953) Natural variations in the isotopic constitution of silicon. *Geochimica et Cosmochimica Acta* 3, 224–234.

Rubie, D.C., Melosh, H.J., Reid, J.E., Liebske, C., Righter, K. (2003) Mechanisms of metal–silicate equilibration in the terrestrial magma ocean. *Earth and Planetary Science Letters* 205, 239–255.

Rubie, D.C., Nimmo, F., Melosh, H.J. (2007) 9.03 Formation of the Earth's Core. *Earth Evolution Sciences* 9, 43–79.

Rubie, D.C., Frost, D.J., Mann, U., Asahara, Y., Nimmo, F., Tsuno, K., Kegler, P., Holzheid, A., Palme, H. (2011) Heterogeneous accretion, composition and core–mantle differentiation of the Earth. *Earth and Planetary Science Letters* 301, 31–42.

Rubie, D.C., Jacobson, S.A., Morbidelli, A., O'Brien, D.P., Young, E.D., de Vries, J., Nimmo, F., Palme, H., Frost, D.J. (2015) Accretion and differentiation of the terrestrial planets with implications for the compositions of early-formed Solar System bodies and accretion of water. *Icarus* 248, 89–108.

Savage, P.S., Georg, R.B., Armytage, R.M.G., Williams, H.M., Halliday, A.N. (2010) Silicon isotope homogeneity in the mantle. *Earth and Planetary Science Letters* 295, 139–146.

Savage, P.S., Georg, R.B., Williams, H.M., Burton, K.W., Halliday, A.N. (2011) Silicon isotope fractionation during magmatic differentiation. *Geochimica et Cosmochimica Acta* 75, 6124–6139.

Savage, P.S., Moynier, F. (2013) Silicon isotopic variation in enstatite meteorites: Clues to their origin and Earth-forming material. *Earth and Planetary Science Letters* 361, 487–496.

Savage, P.S., Armytage, R.M.G., Georg, R.B., Halliday, A.N. (2014) High temperature silicon isotope geochemistry. *Lithos* 190–191, 500–519.

Schauble, E.A. (2004) Applying Stable Isotope Fractionation Theory to New Systems. *Reviews in Mineralogy and Geochemistry* 55, 65–111.

Schauble, E.A., Georg, R.B., Halliday, A.N. (2007) Silicate-metal fractionation of silicon isotopes at high pressure and temperature. AGU Fall Meeting Abstracts 2007 2007, V42A-07.

Schönbächler, M., Carlson, R.W., Horan, M.F., Mock, T.D., Hauri, E.H. (2010) Heterogeneous Accretion and the Moderately Volatile Element Budget of Earth. *Science* 328, 884–887.

Shahar, A., Ziegler, K., Young, E.D., Ricolleau, A., Schauble, E.A., Fei, Y. (2009) Experimentally determined Si isotope fractionation between silicate and Fe metal and implications for Earth's core formation. *Earth and Planetary Science Letters* 288, 228–234.

Shahar, A., Hillgren, V.J., Young, E.D., Fei, Y., Macris, C.A., Deng, L. (2011) High-temperature Si isotope fractionation between iron metal and silicate. *Geochimica et Cosmochimica Acta* 75, 7688–7697.

Shilobreeva, S.N., Kuzmin, L.E. (2004) Simulation of the Ion Modification Processes in the Silicate Dust of Protoplanetary Disks. *Solar System Research* 38, 59–65.

Shu, F.H., Shang, H., Glassgold, A.E., Lee, T. (1997) X-rays and Fluctuating X-Winds from Protostars. *Science*. American Association for the Advancement of Science 277, 1475–1479.

Siebert, J., Corgne, A., Ryerson, F.J. (2011) Systematics of metal–silicate partitioning for many siderophile elements applied to Earth's core formation. *Geochimica et Cosmochimica Acta* 75, 1451–1489.

Steenstra, E.S., Seegers, A.X., Putter, R., Berndt, J., Klemme, S., Matveev, S., Bullock, E.S., van Westrenen, W. (2020) Metal-silicate partitioning systematics of siderophile elements at reducing conditions: A new experimental database. *Icarus* 335, 113391.

Stevenson, D.J. (1990) Fluid dynamics of core formation. In: Newsom, H.E., Jones, J.H. (eds) Oxford University Press, New York, 231–249.

Tang, H., Young, E.D. (2020) Evaporation from the Lunar Magma Ocean Was Not the Mechanism for Fractionation of the Moon's Moderately Volatile Elements. *The Planetary Science Journal* 1, 49.

Tucker, J.M., Mukhopadhyay, S. (2014) Evidence for multiple magma ocean outgassing and atmospheric loss episodes from mantle noble gases. *Earth and Planetary Science Letters* 393, 254–265.

Urey, H.C. (1947) The thermodynamic properties of isotopic substances. *Journal of the Chemical Society (Resumed)* 562.

Visscher, C., Fegley, B. (2013) Chemistry of impact-generated silicate melt-vapor debris. American Astronomical Society 767, L12.

Wade, J., Wood, B.J. (2005) Core formation and the oxidation state of the Earth. *Earth and Planetary Science Letters* 236, 78–95.

Wänke, H., Gold, T., Hutchinson, R., Massey, H.S.W., Runcorn, S.K., Guest, J.E., Hunt, G.E., Woolfson, M.M. (1981) Constitution of terrestrial planets. *Philosophical Transactions of the Royal Society of London. Series A, Mathematical and Physical Sciences*. Royal Society 303, 287–302.

Weidenschilling, S.J. (1977) Aerodynamics of solid bodies in the solar nebula. *Monthly Notices of the Royal Astronomical Society* 180, 57–70.

Williams, J.P., Cieza, L.A. (2011) Protoplanetary Disks and Their Evolution. *Annual Review of Astronomy and Astrophysics* 49, 67–117.

Wood, B.J., Smythe, D.J., Harrison, T. (2019) The condensation temperatures of the elements: A reappraisal. *American Mineralogist*. Mineralogical Society of America 104.

Yoneda, S., Grossman, L. (1995) Condensation of CaO-MgO-Al_2O_3-SiO_2 liquids from cosmic gases. *Geochimica et Cosmochimica Acta* 59, 3413–3444.

Young, E.D., Shahar, A., Nimmo, F., Schlichting, H.E., Schauble, E.A., Tang, H., Labidi, J. (2019) Near-equilibrium isotope fractionation during planetesimal evaporation. *Icarus* 323, 1–15.

Zambardi, T., Poitrasson, F., Corgne, A., Méheut, M., Quitté, G., Anand, M. (2013) Silicon isotope variations in the inner solar system: Implications for planetary formation, differentiation and composition. *Geochimica et Cosmochimica Acta* 121, 67–83.

Zhang, Y., Sears, D.W.G. (1996) The thermometry of enstatite chondrites: A brief review and update. *Meteoritics & Planetary Science* 31, 647–655.

Ziegler, K., Young, E.D., Schauble, E.A., Wasson, J.T. (2010) Metal–silicate silicon isotope fractionation in enstatite meteorites and constraints on Earth's core formation. *Earth and Planetary Science Letters* 295, 487–496.

Chapter 2

Analytical procedure for Silicon isotope measurements by MC-ICP-MS

Ce chapitre est divisé en trois parties. La première établit un état de l'art sur l'ensemble des techniques de mesure utilisées pour les analyses isotopiques du silicium. La deuxième partie s'intéresse à la préparation et la mesure isotopique des échantillons de roches et de météorites, en s'attardant sur le principe de la mesure par spectrométrie de masse à multi-collection. Enfin les spécificités liées à l'analyse du Si sont explicitées dans la troisième partie de ce chapitre, en détaillant le protocole analytique utilisé par la suite pour l'ensemble des mesures isotopiques présentées dans ce manuscrit.

1. Techniques d'analyse des isotopes du silicium

La mesure des variations isotopiques en silicium dans des échantillons naturels s'appuie sur quatre techniques analytiques qui sont, par ordre chronologique d'apparition dans la littérature : la spectrométrie de masse à source gazeuse (IRMS pour isotope ratio mass spectrometry), la spectrométrie de masse des ions secondaires (SIMS pour secondary ion mass spectrometry), la spectrométrie de masse à plasma à couplage inductif en multi-collection (MC-ICP-MS pour multi collector-inductively coupled plasma-mass spectrometry) et l'ablation laser couplée à un MC-ICP-MS (LA-MC-ICP-MS avec LA pour laser ablation).

1.1. Analyses GC-IRMS

La spectrométrie de masse à source gazeuse a été la première méthode utilisée pour établir la composition isotopique en silicium d'échantillons naturels. Le principe est d'obtenir le silicium sous la forme de tétrafluorure de silicium (SiF_4) qui sert à produire des ions SiF_3^+ détectés par la suite par l'IRMS. Le choix de l'espèce SiF_4 comme analyte réside dans sa stabilité aux conditions de pression et de température ambiante ainsi qu'au fait que le fluor ne possède qu'un isotope et de ce fait une correction isotopique sur SiF_4 n'est pas nécessaire. La première procédure analytique a été proposée par Reynolds and Verhoogen (1953). Elle repose sur plusieurs étapes successives de précipitations qui amènent à l'obtention de l'espèce $BaSiF_6$. Ce précipité de fluosilicate de baryum se présente sous la forme d'un solide blanc qui se décompose par chauffage en BaF_2 et en SiF_4 gazeux. D'autres procédures analytiques ont été proposées pour générer l'espèce SiF_4 et reposent sur la réaction de SiO_2 avec l'acide fluorhydrique (HF) (Allenby, 1954), le difluor (F_2) (De La Rocha *et al.*, 1996) ou encore BrF_5 (Ding *et al.*, 2004). Les différentes procédures analytiques sont résumées en détail par Ding (2004). Une procédure plus récente propose de générer SiF_4 par décomposition de l'espèce Cs_2SiF_6 qui est selon les auteurs plus facile à obtenir à partir de silicium solide ou dissous (Brzezinski *et al.*, 2006). Le système de préparation des échantillons est un système complexe constitué d'un ensemble de vannes et de tubes

en verre et en cuivre ou en téflon pour les parties accueillant les gaz fluorés (l'exemple du dispositif utilisé par Allenby en 1954 est présenté ci-après). Une attention toute particulière doit être apportée au contrôle de la quantité d'eau présente dans les différentes parties du dispositif étant donné que SiF_4 réagit avec l'eau pour former l'acide fluorhydrique gazeux et SiO_2 solide (Momot, 1964).

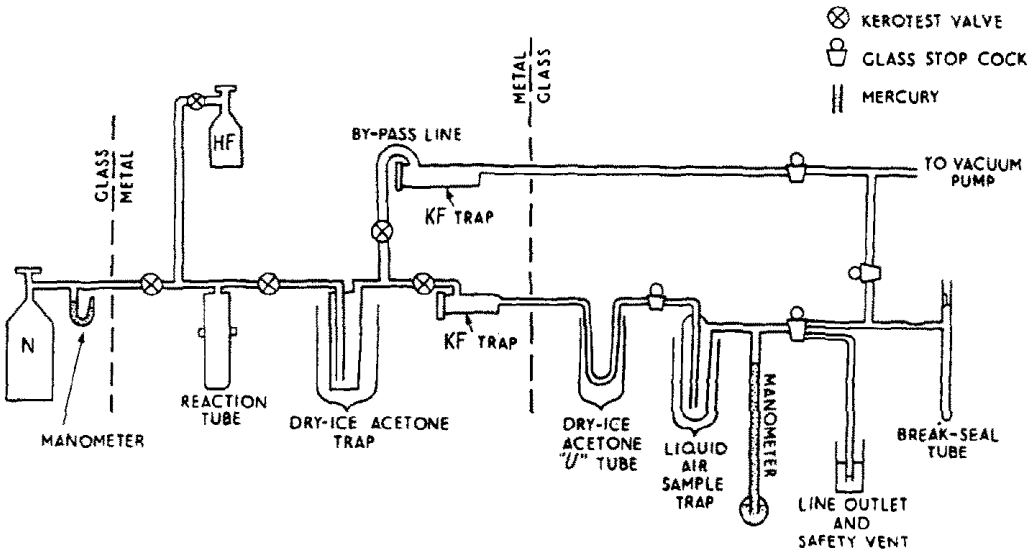

1.2. Analyses SIMS

La spectrométrie de masse des ions secondaires a pris sa place dans les années 80 pour permettre la mesure *in situ* de grains présolaires présents dans certains types de météorites primitives (pour plus de détails, consulter la review de Poitrasson (2017)). L'analyse SIMS de ces carbures de silicium (SiC) a mis en évidence de fortes anomalies en $\delta^{30}Si$ générées par la nucléosynthèse stellaire (Stone *et al.*, 1991; Zinner *et al.*, 1987). Le point fort de cette technique de mesure réside dans sa résolution spatiale permettant l'analyse d'inclusions dans la météorite Allende (Huneke *et al.*, 1983), de silcrètes (roches sédimentaires) (Basile-Doelsch *et al.*, 2005), l'analyse de formations ferrifères rubanées (BIFs pour banded iron formations) (Heck *et al.*, 2011) et plus récemment l'analyse de minéraux (Villeneuve *et al.*, 2019).

1.3. Analyses par MC-ICP-MS

La spectrométrie de masse à source plasma a donné un nouveau souffle aux mesures isotopiques en silicium par le développement d'une grande variété de procédures pour la préparation et l'analyse des échantillons. Les premières mesures sur des échantillons d'éponges et de diatomées se sont révélées très prometteuses avec une reproductibilité sur 10 analyses de NBS28 de ±0.18‰ sur $\delta^{29}Si$ (2SD) et une précision de ±0.2‰ sur $\delta^{29}Si$ (2SD) (De La Rocha, 2002). L'amélioration de la reproductibilité et de

la précision des mesures isotopiques est obtenue par l'utilisation d'un désolvateur en amont du système d'introduction ou par une meilleure estimation du biais en masse instrumental via un dopage au magnésium en plus du traditionnel encadrement standard-échantillon ou « sample-standard bracketing » (Cardinal *et al.*, 2003). Les auteurs obtiennent sur le standard Big Batch une meilleure reproductibilité de ±0.08‰ sur δ^{29}Si (2SD) contre ±0.18‰ en GC-IRMS et une précision analytique moindre, de ±0.09‰ sur δ^{29}Si (2SD) contre ±0.05‰ en GC-IRMS. Ces premières analyses par MC-ICP-MS sont limitées par la faible résolution en masse des spectromètres de masse utilisés qui empêchent la mesure directe de $^{30}Si^{+}$ à cause de l'interférence avec $^{14}N^{16}O^{+}$. Cette limitation est par la suite écartée grâce à l'utilisation de MC-ICP-MS de haute résolution (Georg, 2006; van den Boorn *et al.*, 2006). Une nouvelle procédure basée sur une technique de fusion alcaline suivie d'une purification sur colonne chromatographique a considérablement simplifié la procédure analytique en supprimant l'utilisation d'HF qui produit des espèces volatiles de silicium et rendent les mesures instables. Georg et al. (2006) a également montré que l'utilisation de HF engendrait une baisse de 30 à 40% de la sensibilité instrumentale accompagnée d'une précision dégradée d'un facteur deux sur les rapports isotopiques mesurés. Cette procédure sans HF a par la suite été largement reprise et adaptée dans le cadre de l'étude des processus de haute température dont l'amplitude de fractionnement est moindre comparée aux processus dits de basse température, ceci implique des variations de δ^{30}Si de l'ordre de plusieurs ‰ contre δ^{30}Si n'excédant pas 0.5 ‰ pour les processus dits de haute température (Armytage *et al.*, 2011; Chakrabarti and Jacobsen, 2010; Dauphas *et al.*, 2015; Fitoussi *et al.*, 2009; Fitoussi and Bourdon, 2012; Georg *et al.*, 2007; Pringle *et al.*, 2013, 2014; Savage *et al.*, 2011; Zambardi *et al.*, 2013).

1.4. Analyses par LA-MC-ICP-MS

L'ablation laser couplée à un MC-ICP-MS est une technique de mesure isotopique *in situ* qui présente des avantages par rapport à la méthode SIMS telle qu'une diminution des interférences et une plus faible sensibilité aux effets de matrice (Poitrasson, 2017). Une grande variété de protocoles a été développée pour appliquer notamment cette technique à des échantillons précieux de météorites et de BIFs (pour *Banded Iron Formations*) (Chmeleff *et al.*, 2008; Kadlag *et al.*, 2019, 2021; Shahar *et al.*, 2011; Shahar and Young, 2007; Steinhoefel *et al.*, 2010). Par rapport aux générations précédentes de laser, la nouvelle génération de laser femtoseconde limite les biais instrumentaux reliés à la géométrie de la cible impactée par le laser, à la distribution de la taille des particules injectées ensuite sous forme d'aérosol dans le plasma et à des biais apparentés à des effets de matrice (Horn and von Blanckenburg,

2007), permettant notamment la mesure du standard NBS28 facilitant la calibration nécessaire aux mesures *in situ*.

1.5. Comparaison des méthodes analytiques

Une comparaison des différentes techniques de mesure décrites plus haut est présentée dans le Tableau 1 et regroupe trois méthodes IRMS annotées 1-2-3 (Brzezinski *et al.*, 2006; De La Rocha *et al.*, 1996; Douthitt, 1982) ; deux méthodes SIMS annotées 4-5 (Basile-Doelsch *et al.*, 2005; Heck *et al.*, 2011) ; quatre méthodes MC-ICP-MS annotées 6-7-8-9 (Cardinal *et al.*, 2003; De La Rocha, 2002; Hin *et al.*, 2014; van den Boorn *et al.*, 2006) et cinq méthodes LA-MC-ICP-MS annotées 10-11-12-13-14 (Chmeleff *et al.*, 2008; Kadlag *et al.*, 2019, 2021; Shahar *et al.*, 2011; Shahar and Young, 2007). Les différentes méthodes se comparent par la quantité d'échantillon nécessaire pour la mesure, la sensibilité de l'appareil, le niveau de blanc ainsi que la précision et la justesse des mesures.

Masse d'échantillon

La masse d'échantillon nécessaire aux mesures isotopiques étant assez similaire entre les différentes techniques, elle ne représente pas un facteur discriminant. Les mesures SIMS et LA-MC-ICP-MS permettent des mesures ciblées au contraire des mesures par MC-ICP-MS qui proposent généralement des mesures « bulk », c'est-à-dire globales de l'échantillon.

Blanc et sensibilité

A part pour les mesures par IRMS et SIMS où les valeurs de blanc sont peu documentées, les valeurs de blanc sont assez similaires entre les mesures par MC-ICP-MS et par ablation laser, avec un signal variant de 10 à 100 mV sur ^{28}Si. La sensibilité du spectromètre de masse a été considérablement améliorée par ajout d'un désolvateur avec une sensibilité passant de 0.6 V/ppm (flux de nébuliseur 600 µL/min) à 6 V/ppm sur le ^{28}Si (flux de nébuliseur de 90 µL/min), réduisant significativement la masse de silicium nécessaire pour la mesure isotopique (Cardinal *et al.*, 2003).

Précision et justesse

Les méthodes IRMS les plus récentes (par exemple Brzezinski et al., 2006) mesurent δ^{30}Si avec une précision d'environ 0.1 ‰ comparable aux méthodes par MC-ICP-MS. Cependant la valeur à 1.38 ‰ de la diatomite est bien trop élevée par rapport aux données obtenues par MC-ICP-MS (1.23 ± 0.15, 2SD, cf §3.3), soulignant un problème de justesse des mesures, peut-être lié à la perte de silicium gazeux au cours de la procédure de fluorination. La précision des mesures par MC-ICP-MS reste la meilleure avec une précision moyenne sur δ^{30}Si de ± 0.15 pour la diatomite et ± 0.11 pour BHVO-2, un échantillon de basalte, contre une précision de 0.4 ou 0.2 (2SE) pour les méthodes par ablation laser (cf Tableau 1). La justesse des mesures par MC-ICP-MS est assurée par la mesure de deux standards diatomite et BHVO-2 par une dizaine de laboratoires (cf §3.3).

Au cours de cette thèse, nous nous sommes notamment intéressés à des échantillons de météorites martiennes et à des angrites (météorites différenciées) dont le fractionnement attendu est de l'ordre de ≈ 0.1 ‰ par rapport à la valeur terrestre (Armytage *et al.*, 2011; Dauphas *et al.*, 2015; Pringle *et al.*, 2013, 2014; Zambardi *et al.*, 2013), d'où la nécessité de choisir la méthode la plus précise possible. Les méthodes MC-ICP-MS, en plus de présenter la meilleure précision analytique, ont l'avantage de proposer une préparation d'échantillon simple et rapide en plus d'une bonne sensibilité de mesure, notamment grâce à l'utilisation d'un désolvateur. La mise en place détaillée de la procédure analytique est présentée dans la suite.

2. Préparation des échantillons

2.1. Fusion alcaline

La fusion alcaline est un procédé utilisé pour mettre en solution des composés insolubles avec les acides traditionnels (comme l'acide chlorhydrique et l'acide nitrique). La première étape consiste à diviser finement l'échantillon sous forme de poudre à laquelle est ajoutée un fondant alcalin (métaborate de lithium, carbonate alcalin, hydroxyde et peroxyde alcalin, pyrosulfate/disulfate de potassium, fluorides alcalins) qui va abaisser la température de fusion de l'élément d'intérêt. Le mélange est introduit dans un creuset dont la nature chimique dépend du fondant utilisé (platine, nickel, graphite, zirconium, or ou argent) puis chauffé à haute température. L'ensemble des procédures de fusion est détaillée dans (Potts, 1992). Il convient de choisir la bonne procédure de fusion selon l'élément chimique à analyser. La procédure de fusion alcaline appliquée à l'analyse

Tableau 1 : Compilation des quatre méthodes d'analyse isotopique du silicium.

Technique	Préparation de l'échantillon par	Type d'échantillon	Instrument	Isotopes mesurés	Correction du biais en masse[a]	Quantité d'échantillon	Sensibilité sur ^{28}Si	Blanc sur ^{28}Si	Reproductibilité sur $\delta^{30}Si$ (‰)	Précision analytique sur $\delta^{30}Si$ (‰)	Justesse (‰)
IRMS (1-2-3)	Fusion alcaline avec Na_2CO_3 suivie par une fluorination	organismes siliceux, roches	Nier-type MS	^{28}Si - ^{29}Si - ^{30}Si	SSB avec RQS				0.3	0.6	Roches terrestres
	Fluorination par technique laser	particules de silice biogénique et lithogénique	VG Prism MS	^{28}Si - ^{29}Si - ^{30}Si	SSB avec RQS	15 -100 µmol de Si purifié		négligeable[b]	0.1		
	Dissolution HF	particules de silice biogénique et lithogénique	Kiel III "Carbonate" Device et MAT 252 gas source	^{28}Si - ^{29}Si - ^{30}Si	SSB avec NBS28	entre 1.2 et 1.5 mg (3-4 µmol de Si)		non détectable	0.14	0.08	$\delta^{30}Si$(Big Batch) = -10.39 ± 0.14 (2SD,n=23) $\delta^{30}Si$(diatomite) = 1.38 ± 0.16 (2SD,n=23)
SIMS (4-5)		sédiments et rivières	Cameca 1270	^{28}Si - ^{30}Si	SSB avec NBS28	faisceau de 50 µm de diamètre			0.7	0.75	$\delta^{30}Si$(RQS) = 0.26 ± 0.62 (2SD,n=11)
		Banded Iron Formations	Cameca IMS-1280 Ion Microprobe	^{28}Si - ^{30}Si	SSB avec NBS28	carré de 25 mm de diamètre			0.3	0.2	$\delta^{30}Si$(UWQ-1) = -0.03 ± 0.29 (2SD)
MC-ICP-MS (6-7-8-9)	Dissolution HCl : HF	éponges, diatomés	Nu Instrument - mode statique	^{28}Si - ^{29}Si	SSB avec NBS28	10 ppm Si sous la forme SiF_6	0.45 V/ppm	35 à 100 mV	0.18	0.2	
	Dissolution HCl : HF	éponges	Nu Instrument - mode dynamique - désolvateur	^{28}Si - ^{29}Si	SSB avec NBS28 et correction avec Mg	100-1000 ppm Si en solution	6 V/ppm	30 à 65 mV	0.16	0.18	
	Fusion alcaline	standards	Neptune	^{28}Si - ^{29}Si - ^{30}Si		1-2 mg (2-5 ppm)	6 V/ppm	20-65 mV		0.18-0.31	$\delta^{30}Si$(Big Batch) = -10.52 ± 0.41 (2SD)
	Fusion alcaline	métal et silicates	Nu Plasma 1700 - désolvateur DSN	^{28}Si - ^{29}Si - ^{30}Si	SSB avec NBS28	1 mg	6 V de signal	15 mV		<0.2	$\delta^{30}Si$(diatomite) = 1.22 ± 0.32 (2SD)
LA-MCICPMS (10-11-12-13-14)		Leoville CAI 144A	Ablation laser UV	^{28}Si - ^{29}Si - ^{30}Si	SSB avec San Carlos Olivine	100 µm diamètre et 20-30 µm de profondeur				0.04	Verre synthétique
		standards, éponge, verre	100 fs Ti-Sapphire regenerative amplifier system modifié couplé à un Neptune	^{28}Si - ^{29}Si - ^{30}Si	SSB avec NBS28	35 µmm de diamètre et 2-40 µm de profondeur	10 V de signal pour 50 ng d'échantillon	10 mV	0.24	0.22	$\delta^{30}Si$(IRMM-017) = -0.65 ± 0.14 (2SD)
		métal et silicates	193 nm excimer laser UV (Photon Machines, Analyte 193)	^{28}Si - ^{29}Si - ^{30}Si	SSB avec San Carlos Olivine	86 µm pour les silicates et 172 µm pour le métal / entre 30 et 50 µm de profondeur	230 mV[c]	92 mV	0.1 - 0.2	0.4	
		chondrites type EH	LASS[d] + Neptune (Neptune Plus Jet Interface)	^{28}Si - ^{29}Si - ^{30}Si	SSB avec NBS28	100-150 µm de diamètre			< 0.23 (2SE) sur NBS28	≈0.2 (2SE)	$\delta^{30}Si$(IRMM-17) = -1.2 ± 0.14 (2SD,n=12) $\delta^{30}Si$(BHVO-2G) = -0.29 ± 0.08 (2SD,n=10) $\delta^{30}Si$(NIST SRM610) = -0.09 ± 0.11 (2SD,n=22) $\delta^{30}Si$(GOR132G) = -0.42 ± 0.11 (2SD,n=2)
		chondrules	LASS[d] + Neptune Plus	^{28}Si - ^{29}Si - ^{30}Si	SSB avec NBS28	carré de 100µm de côté			< 0.23 (2SE) sur NBS28	≈0.15 (2SE)	

[a] SSB pour Standard Sample Bracketing

[b] signal correspondant à 0.0015% de la masse de l'échantillon et donc considéré comme négligeable

[c] intensité sur 29Si

[d] LASS pour Laser Ablation Split Stream

isotopique de silicium dans des échantillons de roches a été décrite entre autres par Douthitt (1982) et adaptée par Georg et al. (2006) et elle permet ainsi d'éliminer l'utilisation de l'acide fluorhydrique (HF). En effet cet acide, inodore et incolore, est particulièrement dangereux pour l'expérimentateur et nécessite beaucoup de précautions au cours de sa manipulation en plus de diminuer d'un facteur 2 la reproductibilité de la mesure.

Quelques mg d'échantillon sont introduits dans un creuset en argent auquel est ajoutée une pastille de ≈ 200 mg de soude (NaOH). Le creuset est placé dans un four à 730°C pendant 7min. Il est ensuite laissé quelques minutes à température ambiante pour permettre la cristallisation du « gâteau de fusion » avant d'être introduit dans un Savillex de 30 mL contenant ≈ 25 mL de d'eau déminéralisée MilliQ. L'ensemble des réactions chimiques qui ont lieu pendant cette étape peuvent se résumer comme suit, en considérant la formule chimique générale de l'olivine avec X représentant les espèces Fe et Mg en proportion x et (1-x) respectivement :

$X_2SiO_4 + 4NaOH \rightarrow Na_4SiO_4 + 2X(OH)_2$ cristaux collés à la paroi du creuset

$Na_4SiO_4 + 4H^+ \rightarrow 4Na^+ + Si(OH)_4$ silicate de sodium très soluble dans l'eau

$2X(OH)_2 + 4H^+ \rightarrow 2X^{2+} + 2H_2O$ hydroxyde métallique soluble dans l'acide

Au cours de la fusion alcaline, le sodium prend la place des cations présents dans la structure silicatée et permet ainsi de former des silicates de sodium qui sont très solubles dans l'eau. La solution aqueuse résultant de la fusion est ensuite transférée dans un récipient dont le volume dépend de la concentration finale en silicium souhaitée. Le bécher contenant le creuset est rincé plusieurs fois avec de l'eau MilliQ en prenant soin de bien de noter le volume final de la solution. La solution est ensuite acidifiée par une solution de HCl 6N. Il faut noter que les deux acides HCl et HNO_3 peuvent être utilisés pour l'ajustement du pH, le choix de l'un ou l'autre n'induisant pas de biais isotopique ni d'augmentation significative du signal de l'interférence $^{14}N^{16}O^+$ dans le cadre d'une matrice HNO_3. Le volume d'acide à ajouter est calculé à partir de la masse de soude introduite au début de la fusion. Pour s'assurer que l'acide silicique (H_4SiO_4) soit l'espèce dominante du silicium en solution, le pH de la solution doit être compris entre 2 et 8 et plus précisément entre 2 et 3 pour éviter la polymérisation du silicium en solution (Iler, 1979). De plus, un pH final autour de 2 assure la solubilité des autres cations en solution, notamment le fer pour les échantillons de roche. Pour assurer la validité de la mesure, les précipités métalliques doivent être complètement dissous et ne plus être visibles dans la solution finale avant chargement sur la colonne chromatographique (Fitoussi *et al.*, 2009).

2.2. Séparation sur colonne chromatographique

Avant analyse par spectrométrie de masse, chaque échantillon (ainsi que le standard de quartz) est purifié par chromatographie échangeuse d'ions. Les résines échangeuses d'ions sont composées d'un squelette macromoléculaire plus ou moins réticulé (correspondant à un milieu plus ou moins poreux) sur lequel sont fixés des groupements fonctionnels ionisés. Selon la nature chimique et la charge du groupement fonctionnel, la résine fixera les cations ou les anions. La résine utilisée pour purifier les solutions contenant le silicium est une résine cationique (ou échangeuse de cations) Biorad AG® 50W-X8 200-400 mesh qui va piéger les cations présents en solution et laisser les anions et les espèces neutres la traverser. Sa structure chimique comprend un polymère R (polystyrène réticulé par du divinylbenzène) fonctionnalisé par des groupements sulfoniques SO_3^- (Walton, 1965). Les groupements fonctionnels sont associés à des ions H^+ par interaction électrostatique et assurent ainsi la neutralité électronique globale de la résine. Au cours de la séparation chromatographique, les cations présents en solution vont venir se fixer aux groupements sulfoniques et libérer en solution des ions H^+ qui vont avoir pour effet d'abaisser le pH de la solution interstitielle à environ 2. L'échange des ions H^+ avec des groupements de charge similaire (M^+) est régi par la réaction suivante :

$$R - SO_3^- / H^+ + M^+ \rightarrow R - SO_3^- / M^+ + H^+$$

Préalablement à son utilisation, la résine subit une procédure de lavage qui fait appel à trois types d'acide : l'acide chlorhydrique (HCl), l'acide nitrique (HNO_3) pour éliminer toute trace de pollution organique et l'acide fluorhydrique (HF) pour retirer les traces éventuelles de silicium. La procédure utilisée est détaillée Tableau 2, l'acide utilisé étant en permanence recyclé pour les étapes suivantes.

Tableau 2 : Procédure de lavage préalable de la résine cationique utilisée pour les analyses isotopiques en silicium (haut) et de la résine préfiltre (bas).

{ HCl 6N + MilliQ }	5 fois
{ HNO_3 5N + MilliQ }	5 fois
{ HF 1N + MilliQ }	1 fois
{ HCl 6N + MilliQ }	5 fois
{ HCl 6N (renouvelé) + MilliQ }	4 fois
{ HCl 6N (renouvelé) + MilliQ }	1 fois
{ HNO_3 3N + MilliQ }	10 fois

En combinaison avec la résine cationique, une fine épaisseur de résine 'Préfiltre' (de la société Triskem) est ajoutée au-dessus du fritté de la colonne. La résine préfiltre est constituée d'un polymère d'ester acrylique inerte chimiquement. Cette résine est connue pour retenir les traces de matières organiques présentes dans les solutions aqueuses. La résine suit une procédure de lavage en amont de l'analyse détaillée (Tableau 2).

En solution aqueuse, le silicium se présente sous la forme d'acide silicique H_4SiO_4 en équilibre avec sa base conjuguée $H_3SiO_4^-$ (pKa = 9.5 à 25°C). Lorsque le pH est compris entre 2 et 3, le silicium est majoritairement sous sa forme neutre H_4SiO_4 et va ainsi passer à travers la colonne sans être retenu par la résine, ainsi que toutes les autres espèces neutres et chargées négativement présentes dans la solution de chargement (notamment la matière organique). Cette procédure de purification d'apparence très simple par rapport à d'autres éléments aboutit à beaucoup de disparités dans les mesures isotopiques entre les laboratoires. On peut citer par exemple la présence de matière organique ou encore de soufre dans un échantillon comme pouvant générer d'importants effets de matrice et aboutir à une mauvaise justesse de la mesure isotopique (illustré dans van den Boorn et al. 2009).

Après avoir introduit environ 200 µL de résine préfiltre au-dessus du fritté de la colonne, un volume de 1mL de résine cationique est ajouté lentement pour éviter au maximum la remobilisation et le mélange des deux résines. La purification de l'échantillon suit la procédure décrite dans le Tableau 3. Au cours de l'étape de séparation, les ions Na^+ largement présents en solution suite à la fusion alcaline ainsi que les métaux comme le fer vont être retenus par la résine (illustré Figure 1). Au cours de cette étape, la quasi intégralité du Si est collectée en fin de colonne avec un rendement proche de 100%. Les échantillons sont ensuite dilués avec de l'eau MilliQ pour atteindre une concentration finale comprise entre 0.4 et 0.5 ppm de Si.

3. Analyse par spectrométrie de masse

3.1. Principe de la mesure et description de l'appareil

La spectrométrie de masse est une méthode d'analyse qui permet de déterminer les abondances isotopiques relatives d'un mélange isotopique en séparant les différentes isotopes selon leur rapport masse sur charge (m/q). Les compositions isotopiques en silicium des échantillons sont mesurées grâce

à un MC-ICP-MS (multi collector inductively coupled plasma mass spectrometer) de type Neptune Plus de la société Thermo Fisher.

Tableau 3 : Protocole de séparation sur colonne des échantillons et des standards préalablement à l'analyse isotopique au MC-ICP-MS.

Etape de séparation	Solution	Volume
Pré-lavage de la résine	3 N HCl	Un réservoir de colonne
Pré-lavage de la résine	6 N HCl	Un réservoir de colonne
Pré-lavage de la résine	15 N HNO3	200 µl
Pré-lavage de la résine	6 N HCl	Un réservoir de colonne
Pré-lavage de la résine	3 N HCl	Un réservoir de colonne
Pré-lavage de la résine	Milli-Q	Un réservoir de colonne
Chargement de l'échantillon	Solution acidifiée	≈ 0.5 ml
Elution	Milli-Q	2 mL
Dilution à la concentration de travail	Milli-Q	≈ 3 ml

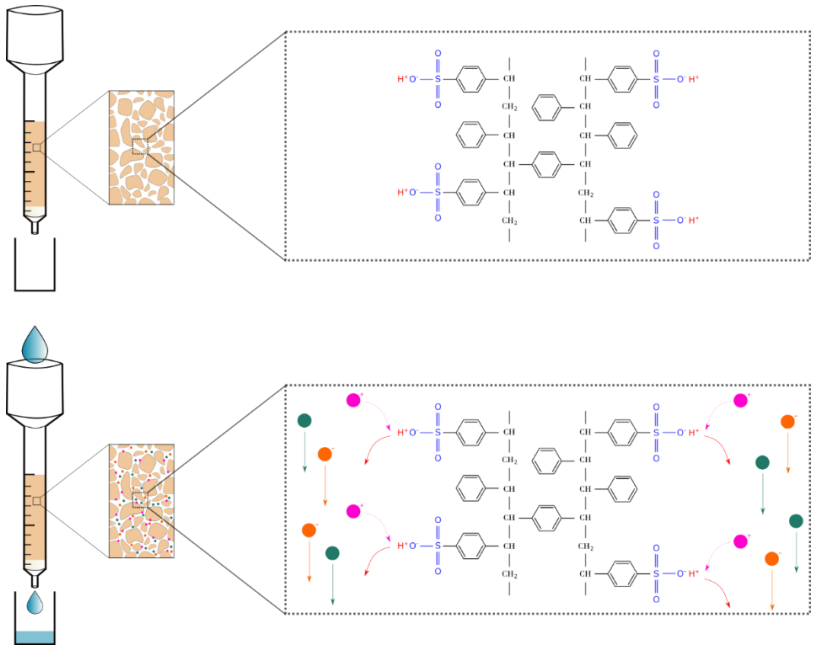

Figure 1 : Principe de la séparation sur une résine cationique avec en haut la résine « au repos » et en bas la résine « au travail ». L'analyte représenté en bleu est introduit dans la colonne : les espèces cationiques (représentées en rose) vont venir se lier aux groupements fonctionnels en s'échangeant avec des H^+ tandis que les anions (représentés en orange) et les espèces neutres (représentés en vert) vont traverser la colonne.

L'appareil utilisé est représenté schématiquement Figure 2, il est doté de cinq parties ayant chacune une fonction bien distincte :

1. Le système d'introduction : génère l'échantillon sous forme d'aérosol
2. Le plasma : a pour fonction de rompre les liaisons chimiques entre atomes et d'ioniser les atomes
3. Le secteur électrostatique est utilisé pour la focalisation du faisceau d'ions produit dans le plasma
4. Le secteur magnétique : sépare les ions selon leur rapport m/q
5. Le système de détection : se compose de cages de Faraday qui vont collecter les ions et fournir les abondances isotopiques

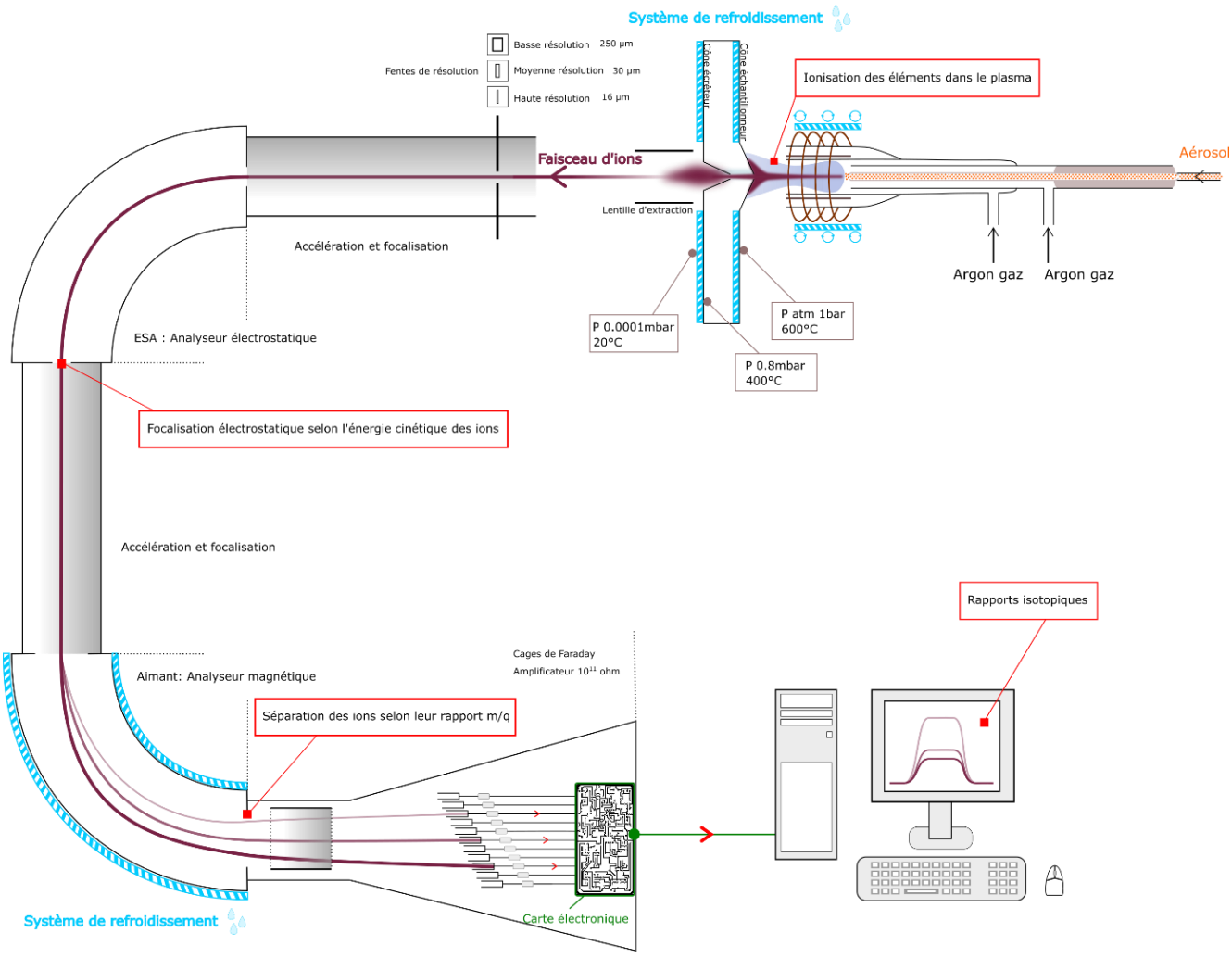

Figure 2 : Représentation schématique du Neptune Plus MC-ICP-MS. Plus le trait est léger plus la masse de l'ion est faible. Le lecteur est référé au texte pour plus de détails sur le fonctionnement des différentes parties de l'appareil.

Le système d'introduction

La solution à analyser est aspirée par un nébuliseur (la valeur du flux d'aspiration dépend de l'élément, environ 70 µL/min pour Si) et transportée sous la forme d'un aérosol (gouttelettes de liquide en suspension dans un gaz, ici un gaz d'Ar inerte prévenant ainsi toute interaction entre le gaz et l'échantillon). L'aérosol est introduit dans le plasma sous la forme d'un aérosol humide via une chambre de nébulisation (mode dit « plasma humide ») ou d'un aérosol sec via un désolvateur (mode dit « plasma sec »). La première option consiste à introduire la solution dans une chambre de nébulisation cyclonique. Les gouttelettes les plus grosses vont venir tapisser les parois de la chambre et sont éliminées du dispositif par gravité, ainsi seules les gouttelettes les plus fines (diamètre < 10µm) vont pouvoir entrer dans le plasma, rendant ainsi l'ionisation plus efficace. La deuxième option repose sur l'utilisation d'un désolvateur. Les molécules d'eau vont être éliminées par absorption au travers d'une membrane poreuse en fluoropolymère grâce à un flux d'Ar (Figure 3). La température du système de désolvatation est d'environ 100°C, ce qui permet la vaporisation du solvant aqueux. Ce procédé permet d'augmenter sensiblement l'efficacité d'ionisation dans le plasma en plus de réduire la formation d'interférences par formation d'oxydes et d'hydrures. Néanmoins l'utilisation d'un désolvateur peut générer des interférences par libération aléatoire de certaines espèces piégées par la membrane. Les deux systèmes d'introduction éliminent la majorité de l'échantillon avec un rendement total de 0.03% pour le « plasma humide » et 0.14% pour le « plasma sec » (cf Annexe 1) constituant un inconvénient majeur des mesures par ICP-MS.

L'interface et le plasma

L'interface fait la transition entre le système d'introduction qui est à pression atmosphérique et le reste de l'instrument qui est à 10^{-9} mbar. Entre les deux cônes, une première pompe à vide maintient la pression autour de 1 mbar et évacue le flux de gaz en surplus (cf Figure 2). Un deuxième jeu de pompes installées après l'interface permet de maintenir un vide poussé à 10^{-9} mbar dans le reste de l'appareil. Le système d'introduction de l'aérosol dans le plasma d'argon se compose d'un injecteur (en quartz, en alumine ou en saphir) introduit dans une torche en quartz. Le choix d'un injecteur en alumine ou en saphir plutôt qu'en quartz est particulièrement important dans le cadre de l'analyse du silicium car il permet de minimiser le niveau de Si instrumental. Le plasma d'argon est un milieu comportant de l'argon ionisé et des électrons qui reste globalement électriquement neutre. L'application d'une décharge électrique en amont de la torche va ioniser de proche en proche les atomes d'Ar et ainsi générer le plasma en aval de la torche. Le plasma se maintient via l'application d'un champ magnétique généré par une bobine en cuivre qui entoure l'aval de la torche. En changeant

la polarité du courant qui traverse la bobine, les ions sont forcés d'emprunter une direction puis une direction contraire à une fréquence radio, entraînant l'augmentation de la température du plasma par friction entre 10000K et 7000K. De telles températures nécessitent un refroidissement continu de l'interface via un flux d'argon et une circulation d'eau froide (maintenue à 20°C).

Au moment de l'introduction de l'aérosol dans le plasma, l'eau s'évapore et toutes les molécules sont atomisées. Le taux d'ionisation (comprendre le nombre d'ions formés par rapport au nombre total d'atomes) est régi par l'équation de Saha et dépend de la température du plasma et du potentiel d'ionisation de l'élément d'intérêt (Houk, 1986). L'ion peut porter une charge positive (mono-ionisation) ou plusieurs charges positives (poly-ionisation, notamment pour les alcalino-terreux). Le plasma génère efficacement des ions monochargés et plus rarement des ions polychargés (cf Tableau 4). Le silicium n'est pas ionisé totalement dans le plasma d'argon avec un taux d'ionisation de 85 %. Malgré son faible rendement d'ionisation, l'ion Ar^+ est l'ion majoritaire dans le plasma, suivi par les ions issus des molécules présentes dans l'air tels que O^+, H^+ et N^+. Une des caractéristiques de l'ionisation par plasma est de produire des ions ayant une dispersion en énergie non négligeable, ce qui nécessite l'utilisation d'une double focalisation (voir plus bas) pour garantir une bonne résolution en masse de l'instrument.

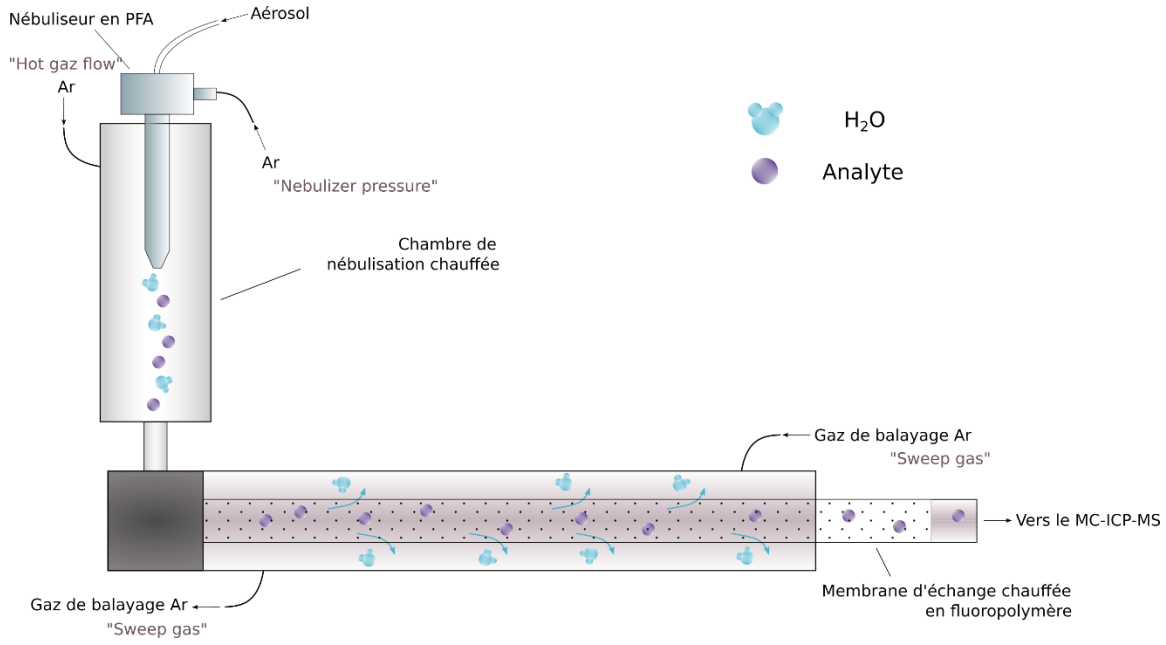

Figure 3 : Représentation schématique du DSN-100 utilisé pour les mesures isotopiques. L'utilisation d'un désolvateur permet l'élimination du solvant qui est absorbé par la membrane poreuse sous l'action d'un flux d'argon et vaporisé. Contrairement à l'Aridus II, la chambre de nébulisation n'est pas oblique mais verticale, limitant ainsi les effets mémoires (cf texte pour plus de détails). Figure modifiée d'après (Amet, 2021).

Tableau 4 : Rendement d'ionisation des atomes : M^+ représente un ion monochargé, T la température du plasma et n_e la densité électronique du plasma, d'après Houk (1986).

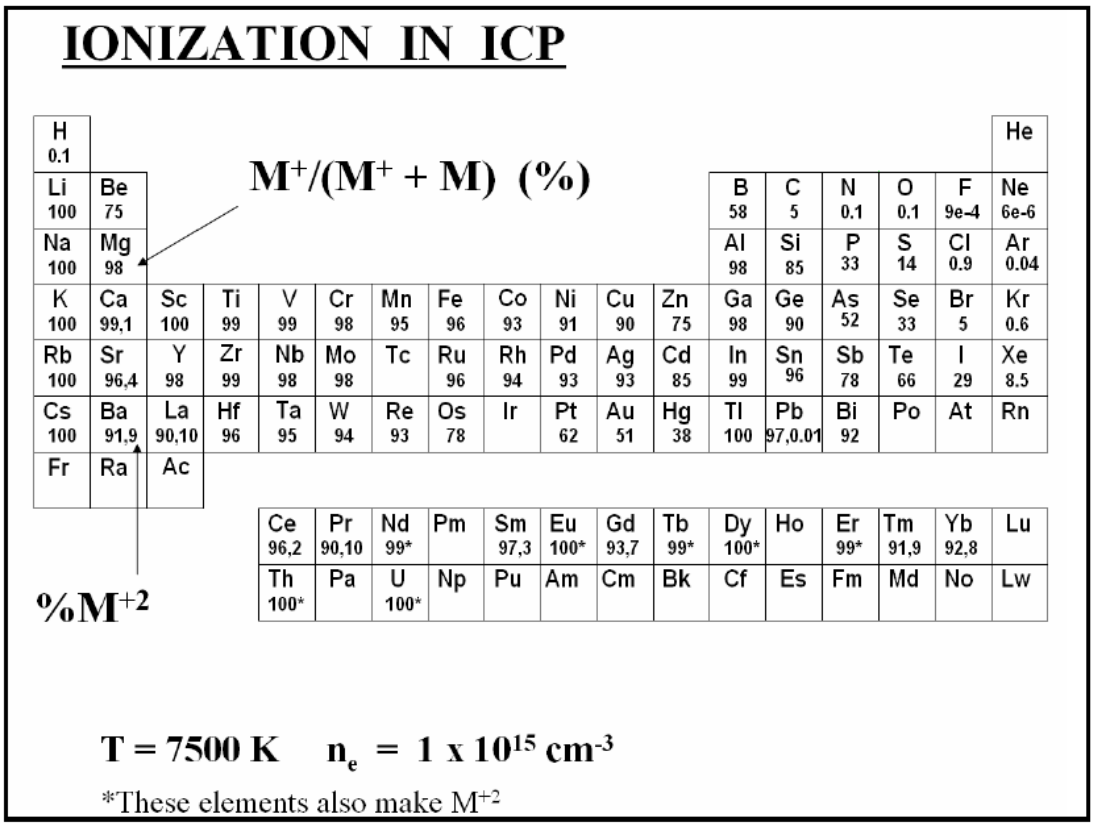

H 0.1																	He
Li 100	Be 75											B 58	C 5	N 0.1	O 0.1	F 9e-4	Ne 6e-6
Na 100	Mg 98											Al 98	Si 85	P 33	S 14	Cl 0.9	Ar 0.04
K 100	Ca 99,1	Sc 100	Ti 99	V 99	Cr 98	Mn 95	Fe 96	Co 93	Ni 91	Cu 90	Zn 75	Ga 98	Ge 90	As 52	Se 33	Br 5	Kr 0.6
Rb 100	Sr 96,4	Y 98	Zr 99	Nb 98	Mo 98	Tc	Ru 96	Rh 94	Pd 93	Ag 93	Cd 85	In 99	Sn 96	Sb 78	Te 66	I 29	Xe 8.5
Cs 100	Ba 91,9	La 90,10	Hf 96	Ta 95	W 94	Re 93	Os 78	Ir	Pt 62	Au 51	Hg 38	Tl 100	Pb 97,0.01	Bi 92	Po	At	Rn
Fr	Ra	Ac															

Ce 96,2	Pr 90,10	Nd 99*	Pm	Sm 97,3	Eu 100*	Gd 93,7	Tb 99*	Dy 100*	Ho	Er 99*	Tm 91,9	Yb 92,8	Lu
Th 100*	Pa	U 100*	Np	Pu	Am	Cm	Bk	Cf	Es	Fm	Md	No	Lw

Deux cônes montés en parallèle permettent d'échantillonner les ions formés au cœur du plasma d'argon. La géométrie de ce premier cône, appelé cône échantillonneur (ou « sampler cone ») ainsi que celle du deuxième cône, appelé cône écrêteur (ou « skimmer cone ») permet de minimiser les turbulences générées par le flux de matière incident ainsi que le flux d'air généré par les pompes assurant le vide de l'appareil. Les deux cônes fonctionnent généralement par paires. La première paire qualifiée de standard est la première historiquement à avoir été utilisée pour les analyses isotopiques. La deuxième a été développée il y a une dizaine d'années suite à un besoin croissant en sensibilité, notamment pour les analyses isotopiques des éléments traces et ultra-traces. Cette deuxième paire qualifiée de « jet » augmente sensiblement le signal mais augmente en même temps la formation d'espèces polyatomiques et de surcroît les interférences.

Le secteur électrostatique

Le faisceau d'ions est focalisé en un faisceau cylindrique à l'aide d'une première lentille en graphite appelée lentille d'extraction. Portée à une différence de potentiel de -2000V, elle guide les ions vers une autre série de lentilles qui débouche sur l'ESA (pour Electrostatic Analyzer). Cet analyseur

électrostatique a pour rôle de trier les ions selon leur énergie cinétique à l'aide d'une différence de potentiel appliquée sur deux plaques incurvées de géométrie cylindrique (Figure 4). Le champ électrique est radial (sa direction est perpendiculaire aux plaques) et la vitesse tangente au champ électrique. Soit en appelant E l'intensité du champ électrique, q la charge portée par l'ion, m sa masse, v sa vitesse, E_c son énergie cinétique et r le rayon de courbure de sa trajectoire, on aura :

Composante radiale de la force électrostatique : $F_e = qE$

Expression de l'accélération dans un mouvement circulaire : $a = v^2/R$

Energie cinétique de l'ion : $E_c = \frac{1}{2}mv^2$

En appliquant la deuxième loi de Newton à l'ion dans le référentiel terrestre galiléen on obtient que l'accélération de l'ion multipliée par sa masse est égale à la composante radiale de la force électrostatique, soit :

$$qE = \frac{mv^2}{r}$$

En faisant intervenir l'énergie cinétique de l'ion :

$$r = \frac{2E_c}{qE}$$

En maintenant l'intensité du champ électrique constante, la trajectoire de l'ion est directement dépendante de son énergie cinétique. L'ESA permet ainsi de réaliser une première focalisation des ions en fonction de leur énergie initiale présentant une dispersion non négligeable. Sans cette première focalisation, deux ions $^{28}Si^+$ ne présentant pas strictement la même énergie cinétique seront dispersés par le secteur magnétique, diminuant ainsi la résolution de l'appareil (le faisceau correspondant à la masse 28 sera plus large). Ce secteur électrostatique (couplé au secteur magnétique) permet de réaliser une double focalisation des ions en fonction de leur dispersion spatiale et de leur énergie initiale propre à l'ionisation par plasma.

Le secteur magnétique

Le faisceau d'ions est ensuite guidé vers l'analyseur en masse via une série de lentilles électrostatiques. Selon le type d'ICP-MS, l'analyseur en masse prend la forme d'un quadripole, d'un aimant ou d'un analyseur à temps de vol. En ICP-MS à multicollection (MC-ICP-MS), le système de discrimination en masse se compose d'un aimant qui courbe les trajectoires des ions via l'application d'un champ magnétique (Figure 5). En effet l'expression du rayon de courbure de la trajectoire de l'ion découle de l'égalité entre la force magnétique (induite par le champ magnétique) et la force centripète (qui a

tendance à attirer l'ion vers le centre de sa trajectoire). Soit en appelant B le champ magnétique de l'aimant, v la vitesse de l'ion, et r le rayon de courbure de la trajectoire de l'ion, on aura :

Composante radiale de la force magnétique : $F_m = qvB$

Expression de l'accélération dans un mouvement circulaire : $a = v^2/r$

Energie cinétique de l'ion : $E_c = \frac{1}{2}mv^2$

On peut en déduire le rayon de la trajectoire dans un champ magnétique homogène dont la direction est orthogonale au plan de la trajectoire des ions en écrivant que l'accélération des ions multipliée par la masse des ions ($m\,v^2/r$) dans un mouvement circulaire est égal à la composante radiale de la force s'exerçant sur l'ion :

$$r = \frac{m}{q}\,\frac{v}{B}$$

La vitesse de l'ion étant reliée à son énergie cinétique, on peut écrire :

$$r = \frac{\sqrt{2mE_c}}{qB}$$

La valeur de B étant fixée par l'expérimentateur et E_c étant constant après la traversée des ions dans l'ESA, deux ions de m/q différent seront séparés après passage dans le secteur magnétique, les ions les plus lourds étant les moins déviés.

Le système de détection

Après passage dans l'aimant, les ions sont détectés individuellement et de manière synchrone par des cages de Faraday : c'est le principe de la multi-collection (MC). L'avantage de la multicollection est que les fluctuations du signal sont détectées par l'ensemble des signaux collectés et vont donc se compenser quand on calcule un rapport d'abondance isotopique. Chaque impact d'ion dans la cage de Faraday génère un courant électrique. Ce courant électrique passe au travers d'un amplificateur couplé à une résistance de 10^{11} ohms, ce qui produit un potentiel qui est donné en volt (V) par l'instrument suivant la loi d'Ohm, U=RI où R est la résistance associée à l'amplificateur et I le courant d'ions. Le potentiel mesuré au niveau des amplificateurs est directement proportionnel aux abondances des isotopes et ceci permet ensuite de calculer des rapports isotopiques. Les amplificateurs génèrent un bruit de fond électronique qui est corrigé pour chaque mesure d'échantillons et de standards par mesure de la ligne de base (ou « baseline »).

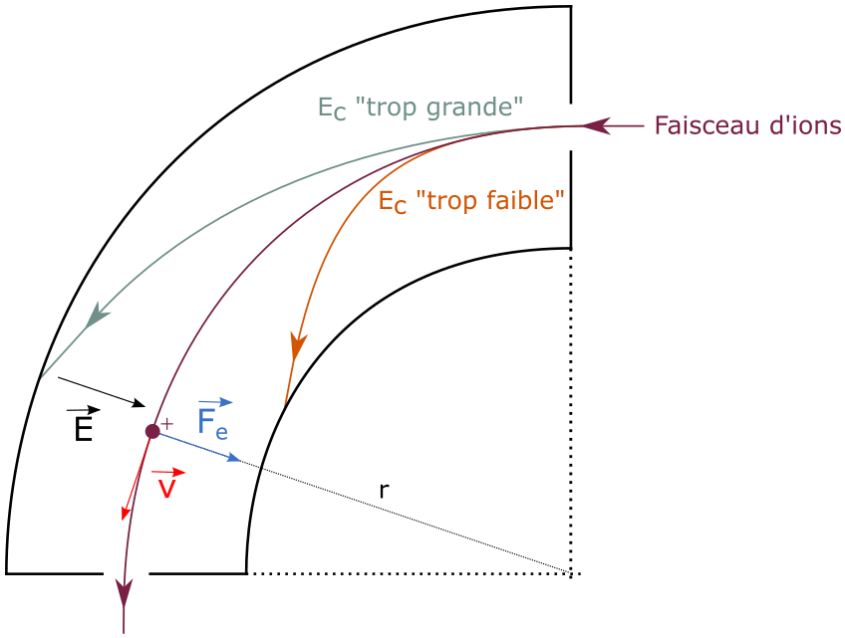

Figure 4 : Représentation schématique de l'analyseur élcrostatique (ESA). Chaque ion suit une trajectoire courbe caractérisée par un rayon de courbure r et est soumis à la force électrostatique F_e. Seuls les ions avec la « bonne énergie cinétique » peuvent traverser l'ESA et continuer vers l'analyseur magnétique.

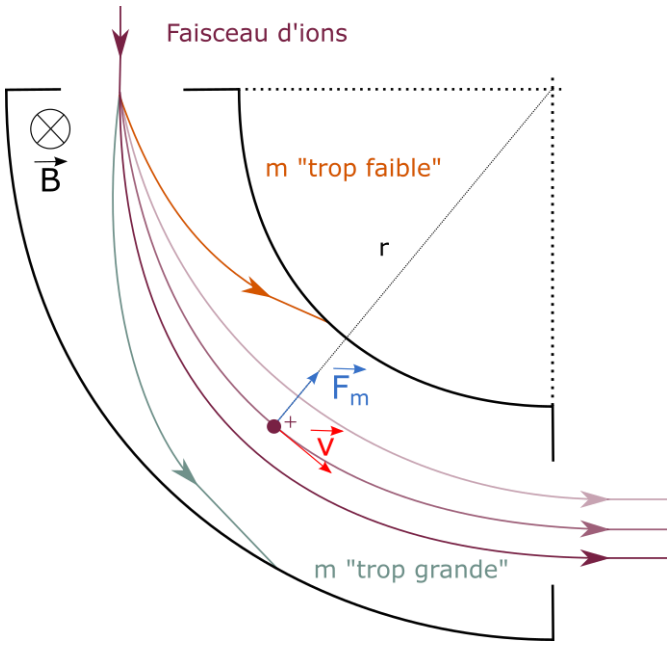

Figure 5 : Représentation schématique de l'analyseur magnétique (aimant). Chaque ion suit une trajectoire courbe caractérisée par un rayon de courbure r qui dépend du rapport m/q de chaque ion. Dans le champ magnétique B généré par l'aimant, chaque ion subit la force magnétique F_m.

3.2. Interférences et résolution en masse

L'une des principales limites aux mesures isotopiques par ICP-MS repose sur la formation d'interférences au sein du plasma d'argon, c'est-à-dire d'une espèce présentant le même rapport m/q que l'isotope d'intérêt. L'espèce interférente isobare peut correspondre à l'isotope d'un autre élément (interférence monoatomique) ou correspondre à un édifice polyatomique composé la plupart du temps de combinaisons entre l'argon et les atomes présents dans l'air (oxygène, azote, carbone, hydrogène).

Par construction le signal de l'espèce interférente sera collecté conjointement au signal de l'isotope qui nous intéresse (Figure 6). Il s'avère que les deux espèces n'ont pas strictement la même masse qui diffère très légèrement. L'exemple le plus fréquent est celui de l'isotope 56 du fer qui présente une interférence isobare polyatomique avec $^{40}Ar^{16}O$. La masse de ^{56}Fe est de 55.9349393 uma et la masse de l'édifice $^{40}Ar^{16}O$ est de 39.9623837 + 15.99491463 = 55.95729833 uma, ce qui donne une différence de masse de 0.02235903 uma entre les deux espèces. La capacité d'un spectromètre de masse à détecter cette différence de masse infime entre deux espèces est quantifiée par ce qu'on appelle la résolution en masse. Le Tableau 5 résume l'ensemble des interférences isobares (monoatomiques et polyatomiques) pour les isotopes du silicium et la résolution nécessaire pour que leur pic soit au moins partiellement résolu (d'après Engström et al. 2006). On peut noter les interférences polyatomiques de type hydrure (combinaison entre un isotope de masse inférieure à l'isotope d'intérêt et un atome d'hydrogène).

Tableau 5 : Compilation des interférences en ICP-MS sur les isotopes du Si.

Isotope	Hydrures	R[1]	Oxydes	R[1]	Combinaison avec N	R[1]	Double charge	R[1]
^{28}Si			$^{12}C^{16}O^+$	1560	$^{14}N_2^+$	960	$^{56}Fe^{2+}$	2960
^{29}Si	$^{28}SiH^+$	3510	$^{12}C^{16}OH^+$	1100	$^{14}N^{15}N^+$	1090	$^{58}Fe^{2+}$	2940
			$^{12}C^{17}O^+$	1280	$^{14}N_2H^+$	770	$^{58}Ni^{2+}$	3280
			$^{13}C^{16}O^+$	1330				
^{30}Si	$^{29}SiH^+$	2840	$^{14}N^{16}O^+$	1240	$^{14}N^{15}NH^+$	810	$^{60}Ni^{2+}$	3580
			$^{13}C^{17}O^+$	1044	$^{14}N^{14}ND^+$	650		

[1] Résolution nécessaire pour distinguer l'isotope de son interférence.

La résolution nécessaire à la distinction des pics de deux espèces de masse proche dépend de la masse de l'isotope considéré m et de la différence de masse entre l'interférence et l'isotope ΔM selon :

$$R_{résolution} = \frac{m}{\Delta M} = \frac{m}{m_{interférence} - m}$$

Par exemple pour séparer ^{30}Si de son interférence principale $^{14}N^{16}O^{+}$, la résolution nécessaire est de 29.9737707/(29.9737707-(12+14.0030740052)) soit environ 1240. Ce qui signifie que le spectromètre utilisé doit avoir une résolution en masse au moins égale à 1240 pour pouvoir distinguer les deux pics. Le pouvoir de résolution en masse du spectromètre de masse peut se calculer de la manière suivante, en se basant sur la définition donnée par Weyer and Schwieters (2003) :

$$R_{power}(5, 95\%) = \frac{m}{\Delta m^{*}} = \frac{m}{m_{5\%} - m_{95\%}}$$

Avec m la masse de l'isotope considéré ; $\mathrm{m}_{5\%}$ la masse à 5% de la hauteur du pic ; $\mathrm{m}_{95\%}$ la masse à 95% de la hauteur du pic (Figure 6). Ainsi plus la pente du pic sera abrupte et plus il sera facile de distinguer (résoudre) les pics. Le Neptune Plus utilisé pour ce travail de thèse a une résolution $R_{power}(5, 95\%)$ calculée de ≈ 7000 en haute résolution et permet ainsi de résoudre partiellement les interférences sur les isotopes du Si (Figure 7). Pour prévenir au maximum la perturbation de la mesure par des interférences qui se situent pour la plupart à une masse légèrement plus importante que la masse de l'isotope considéré (soit à droite du pic de l'isotope), les mesures isotopiques sont effectuées en fixant la masse de la cage centrale au centre du demi plateau gauche (voir Figure 6).

3.3. Correction du biais en masse instrumental

Le biais en masse instrumental correspond à la dérive de la mesure des rapports isotopique au cours du temps. Cette dérive suit une loi exponentielle explicitée par (Russell *et al.*, 1978). Pour corriger de cet effet, la mesure isotopique d'un échantillon est encadrée par la mesure de deux standards. Une interpolation linéaire entre les rapports isotopiques de ces deux standards permet de découpler la composante instrumentale du fractionnement naturel mesuré au cours de la mesure isotopique de l'échantillon. Cette méthode porte ainsi le nom d' « encadrement de l'échantillon par un standard » ou « standard-sample bracketing ». Une autre méthode consistant à doper l'échantillon en Mg a été proposée pour corriger du fractionnement en masse instrumental du Si (Zambardi and Poitrasson, 2011) et repose sur l'hypothèse forte d'égalité du biais en masse pour ces deux éléments proches qui doit être vérifiée à chaque session de mesure (Maréchal *et al.*, 1999).

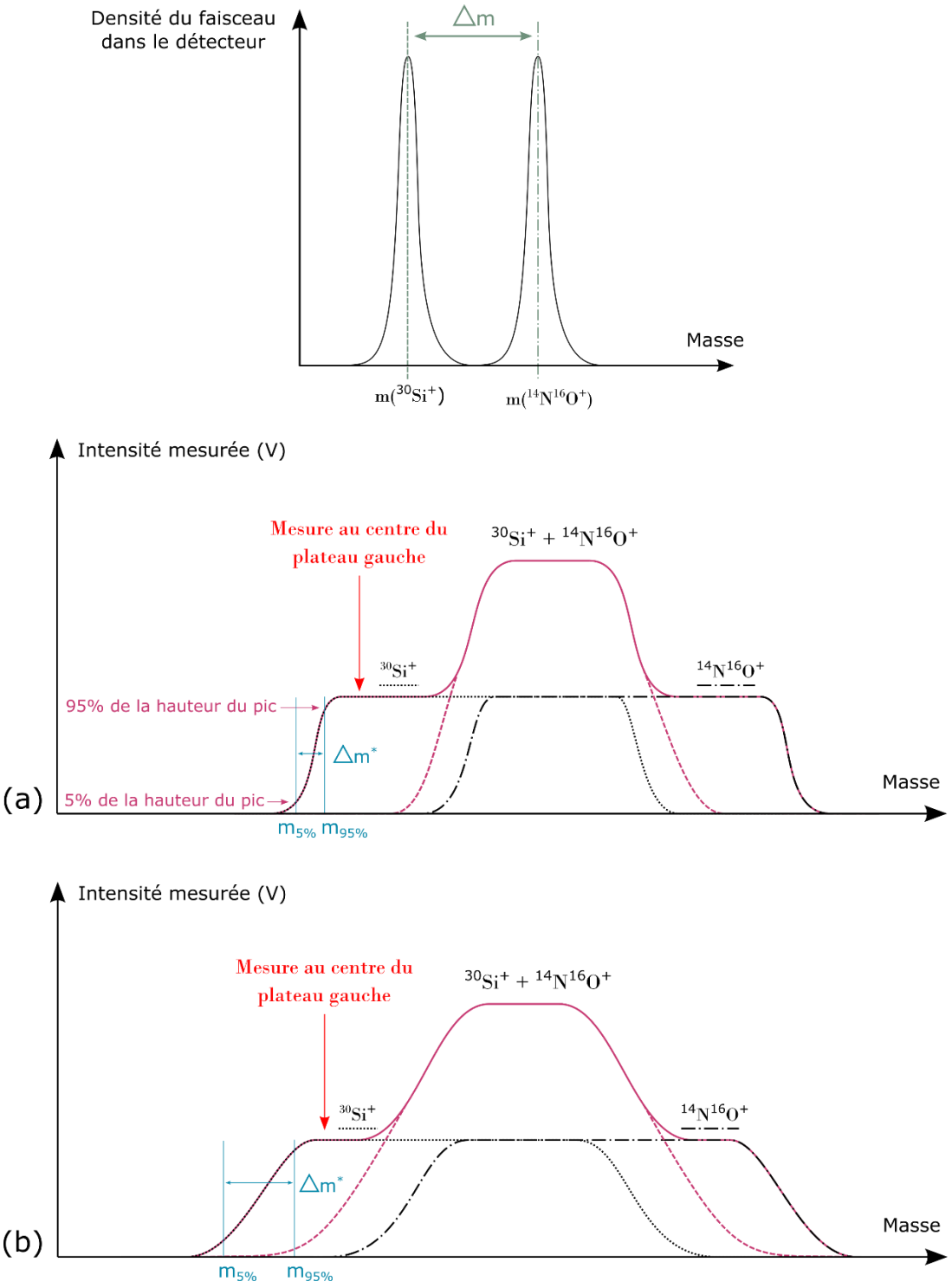

Figure 6 : Résolution en masse et pouvoir de résolution en spectrométrie de masse, exemple de ^{30}Si avec son interférence principale $^{14}N^{16}O^+$. Les pics des deux espèces sont partiellement résolus et se chevauchent en haute et basse résolution (respectivement la figure 3a-3b). La mesure de ^{30}Si est possible sur un plateau à gauche du pic principal correspondant à la somme du signal de ^{30}Si avec son interférence $^{14}N^{16}O^+$. En basse résolution (figure 3b) la mesure sur le plateau est plus hasardeuse étant donné que le pic de l'interférence est beaucoup plus étendu en masse qu'en haute résolution (figure 3a).

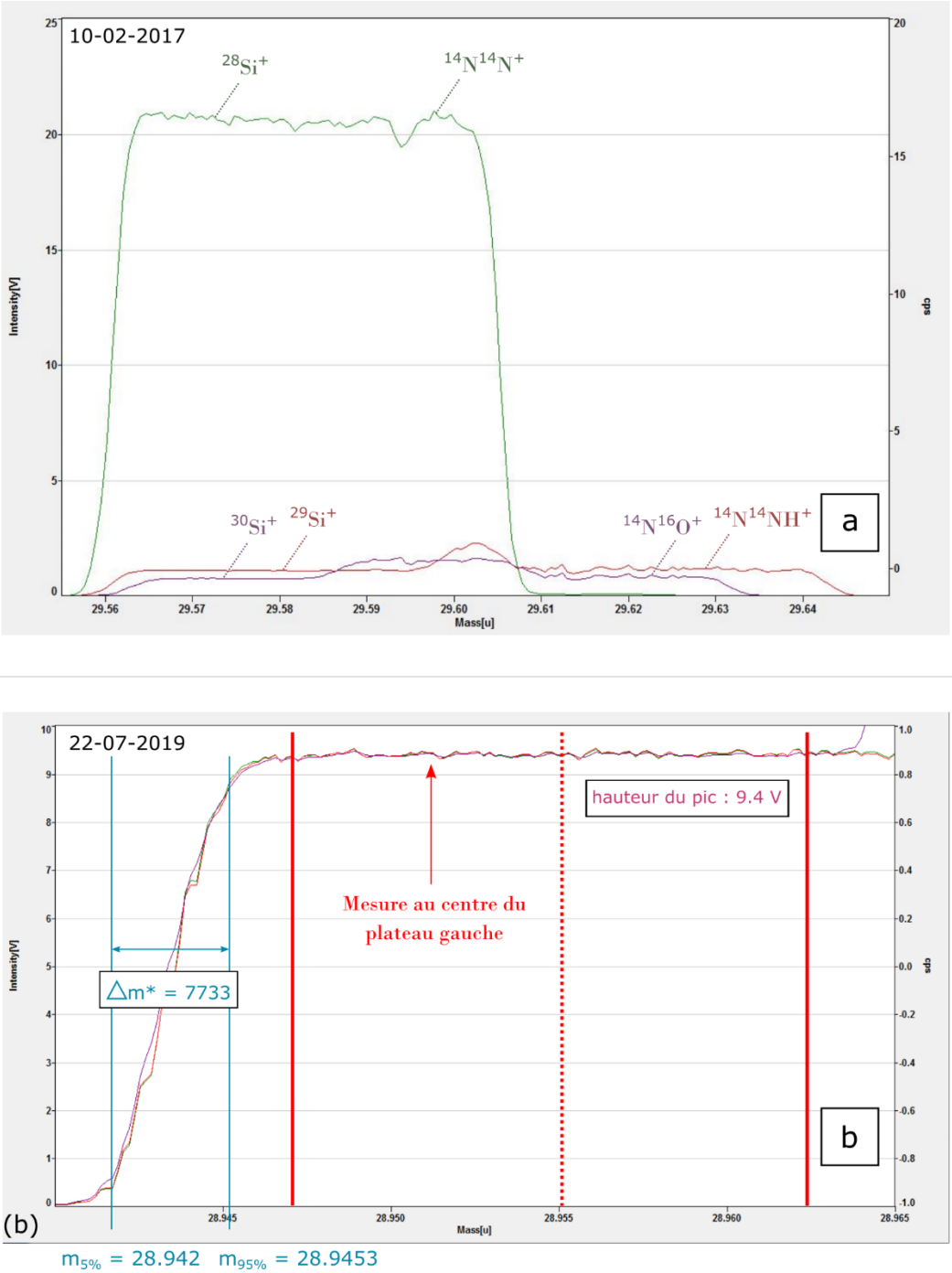

Figure 7 : Spectre de masse obtenu avec le Neptune Plus MC-ICP-MS utilisé au cours de cette thèse. La courbe verte, rouge et violette correspond respectivement à l'intensité (en V) générée à la masse 28, 29 et 30 dans la cage L3, la cage centrale et la cage H3. La figure (a) donne le spectre élargi avec le plateau de chaque isotope du silicium où la mesure est possible et le plateau de leur interférence principale ; la figure (b) illustre le calcul de la résolution R_{power}(5%, 95%) avec un changement d'échelle pour la coïncidence des pics, ainsi que la masse de la cage centrale à fixer, au centre gauche du demi-plateau.

3.4. Justesse, précision et répétabilité

Une mesure juste est une mesure en accord avec des données déjà existantes dont la justesse est elle-même prouvée. La justesse d'une mesure se vérifie par la mesure d'un standard secondaire comme le standard « diatomite » qui représente une diatomite naturelle préparée à l'université de Santa Barbara en Californie, disponible sur demande jusqu'en 2025 (Poitrasson, 2017) ; et le standard BHVO, un échantillon de basalte hawaïen fourni par l' « US Geological Survey ». Ces deux échantillons ont été caractérisés par de nombreuses études indépendamment (Figure 8) et permettent d'établir une moyenne de la composition isotopique de ces deux standards à $\delta^{30}Si$=1.23±0.15‰ (2SD) pour la diatomite et $\delta^{30}Si$=-0.29±0.11‰ (2SD) pour BHVO-2 (Abraham *et al.*, 2008; Armytage *et al.*, 2011, 2012; Chakrabarti and Jacobsen, 2010; Dauphas *et al.*, 2015; Fitoussi *et al.*, 2009; Fitoussi and Bourdon, 2012; Pringle *et al.*, 2013, 2014; Reynolds *et al.*, 2007; Savage *et al.*, 2011; Savage and Moynier, 2013; Zambardi *et al.*, 2013; Zambardi and Poitrasson, 2011; Ziegler *et al.*, 2010). L'obtention de la valeur juste de ces deux standards secondaires à travers le protocole analytique développé dans le cadre de cette thèse valide la méthode d'analyse utilisée (voir Figure 8). L'avantage de ces deux standards est qu'ils sont homogènes et que leur valeur ne varie pas significativement entre les laboratoires contrairement à ce qui a été montré pour d'autres standards tels que BHVO-1, ou encore IRMM 18 (fourni par le European Institute for Reference Material and Measurements).

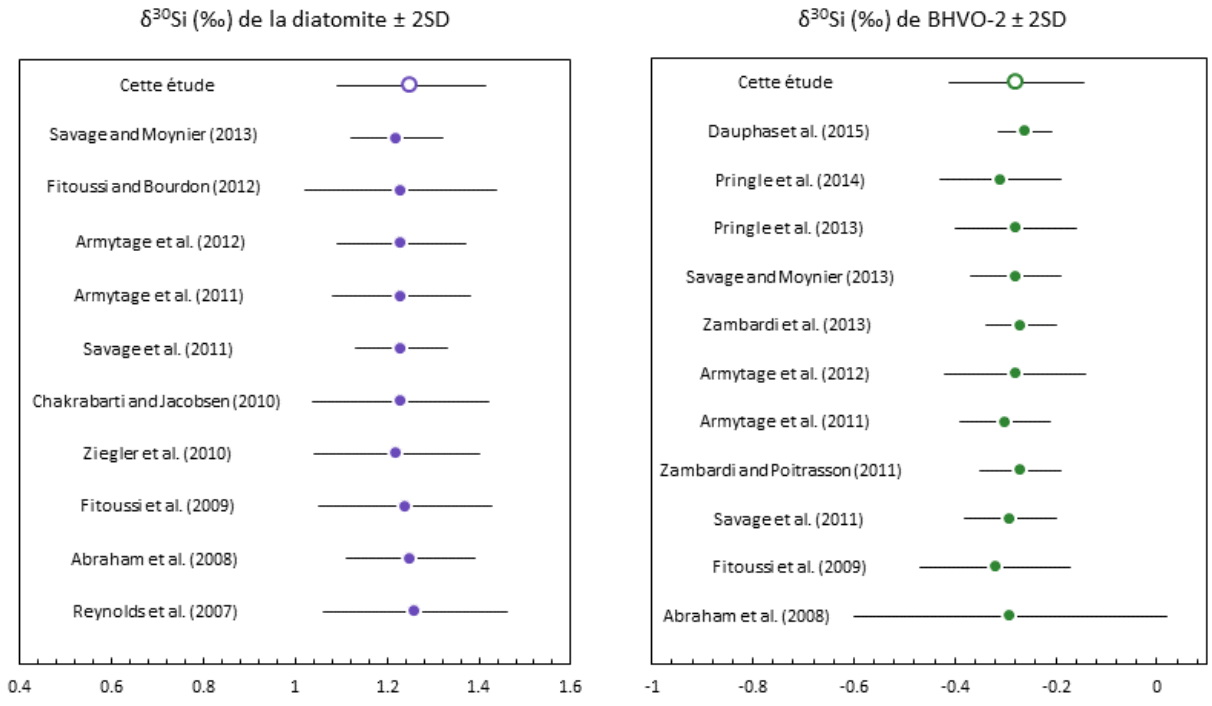

Source des données pour la diatomite	**$\delta^{30}Si$ (‰)**	**2SD**	**$\delta^{29}Si$ (‰)**	**2SD**	**N**
Reynolds et al. (2007)[1]	1.26	0.2	0.64	0.14	82
Abraham et al. (2008)[2]	1.25	0.14	0.64	0.1	24
Fitoussi et al. (2009)	1.24	0.19	0.64	0.09	89
Ziegler et al. (2010)[3]	1.22	0.18	0.63	0.008	1
Chakrabarti and Jacobsen (2010)	1.23	0.19	0.61	0.13	41
Savage et al. (2011)	1.23	0.1	0.64	0.08	177
Armytage et al. (2011)	1.23	0.15	0.63	0.1	400
Armytage et al. (2012)	1.23	0.14	0.63	0.09	250
Fitoussi and Bourdon (2012)	1.23	0.21	0.64	0.10	110
Savage and Moynier (2013)	1.22	0.1	0.63	0.06	43
Cette étude	1.25	0.16	0.64	0.09	429
Moyenne (cf légende)	1.23	0.15	0.63	0.09	11
Source des données pour BHVO-2	**$\delta^{30}Si$ (‰)**	**2SD**	**$\delta^{29}Si$ (‰)**	**2SD**	**N**
Abraham et al. (2008)[2]	-0.29	0.31	-0.17	0.11	8
Fitoussi et al. (2009)	-0.32	0.15	-0.16	0.15	14
Savage et al. (2011)	-0.29	0.09	-0.15	0.08	188
Zambardi and Poitrasson (2011)	-0.27	0.08	-0.14	0.05	360
Armytage et al. (2011)	-0.30	0.09	-0.18	0.07	11
Armytage et al. (2012)	-0.28	0.14	-0.15	0.08	210
Zambardi et al. (2013)	-0.27	0.07	-0.14	0.04	54
Savage and Moynier (2013)	-0.28	0.09	-0.15	0.06	44
Pringle et al. (2013)	-0.28	0.12	-0.15	0.09	26
Pringle et al. (2014)	-0.31	0.12	-0.16	0.08	57
Dauphas et al. (2015)[4]	-0.262	0.053	-0.132	0.037	9
Cette étude	-0.28	0.13	-0.15	0.07	131
Moyenne (cf légende)	-0.29	0.11	-0.15	0.08	12

[1] Etude comparative des données de diatomite obtenues par différents laboratoires

[2] Compilation des données de BHVO-2 de la littérature

[3] Erreur en ± 2SE

[4] Erreur sur un intervalle de confiance de 95% autour de la moyenne obtenue sur 9 mesures

Figure 8 : Compilation des données de la littérature pour la mesure des standards diatomite et BHVO-2 et comparaison avec les mesures effectuées dans le cadre du développement analytique présenté dans cette thèse. Les données utilisées sont présentés dans le tableau ci-contre, la moyenne et l'erreur associée sont calculées à partir de toutes les données exceptées celles dont l'erreur n'est pas exprimée en ± 2SD et celles issues de compilation de données (Abraham *et al.*, 2008; Dauphas *et al.*, 2015; Reynolds *et al.*, 2007; Ziegler *et al.*, 2010).

La précision se quantifie par la mesure répétée sur le spectromètre de masse d'un même échantillon. La précision d'une mesure dépend de l'échantillon considéré ainsi que du type et des paramètres du spectromètre de masse.

La reproductibilité correspond à la capacité d'un expérimentateur à reproduire ses données isotopiques en répétant strictement la même démarche analytique. En réalité, le concept de reproductibilité s'apparente à celui de répétabilité.

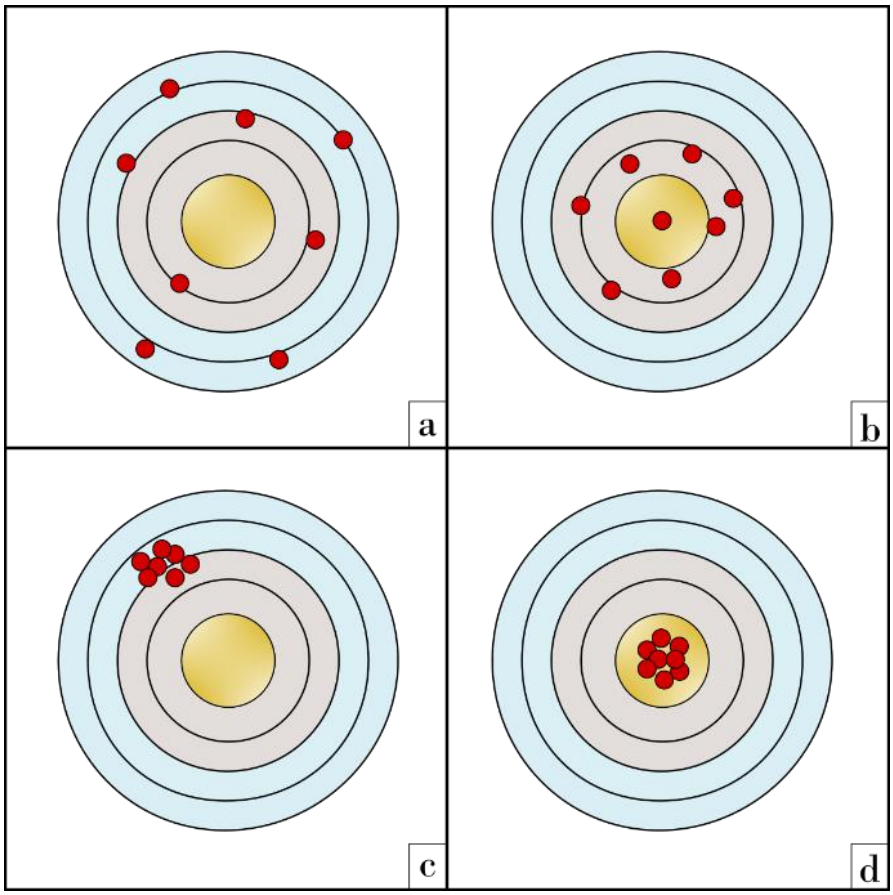

Figure 9 : Illustration des notions de justesse et de précision dans le cas de huit mesures isotopiques successives, matérialisées par des ronds rouges. La gamme de valeurs attendues pour la mesure est matérialisée par le cercle central de la cible, analogue à une cible de tir à l'arc. Dans le cas (a) les mesures sont dispersées mais difficiles à interpréter ; dans le cas (b) les mesures sont plus justes car elles arrivent proche du centre de la cible mais elles sont peu précises car dispersées ; dans le cas (c) les mesures sont précises mais pas justes car systématiquement écartées de la valeur attendue ; dans le cas (d) les mesures sont dans la gamme attendue et précises autour de cette valeur. Le travail de l'expérimentateur est de réussir à se rapprocher au maximum de la situation (d) et de repérer les cas de figure trompeurs correspondant au cas de figure (c).

4. Mise en place de la méthode pour l'analyse isotopique de Si

Dans les paragraphes suivants les différentes étapes du développement analytique spécifiques à notre méthode d'analyse sont passées en revue.

4.1. Optimisation de la valeur du blanc

Une des particularités du Si est qu'il peut facilement s'adsorber sur des parois, ce qui fait qu'il est difficile à nettoyer dans les systèmes d'introduction de par un important effet de mémoire. Le silicium est de ce point de vue un élément analogue au bore (Louvat *et al.*, 2014). Son omniprésence dans le spectromètre de masse (par exemple au sein d'éléments en quartz comme la torche) a pour effet d'augmenter significativement les valeurs du blanc et par conséquent de réduire le rapport signal sur bruit (noté S/N pour « Signal over Noise ratio »). Plus ce rapport sera élevé et moins les fluctuations aléatoires du signal du blanc affecteront le signal isotopique, générant de surcroît une mesure plus précise et reproductible. Le signal en silicium des échantillons et du blanc instrumental doit aussi être le plus stable possible pour assurer la qualité de la mesure une fois qu'on aura soustrait la valeur du blanc. La première partie du développement analytique a ainsi été consacrée à l'optimisation du rapport S/N conjointement à l'obtention d'un signal stable, en travaillant sur les paramètres du spectromètre de masse. La solution type « échantillon » se présente sous la forme d'une solution mono-élémentaire de silicium à 2 ppm et à 0.2 ppm préparée dans HCl 0.02 M. La solution de référence pour la mesure du blanc est une solution de HCl 0.02 M. Le rapport S/N est le rapport de l'intensité de ^{28}Si dans la solution type « échantillon » par rapport à l'intensité de ^{28}Si dans la solution de blanc. Les paramètres suivants ont été optimisés :

- Le flux des différents gaz (sweep gaz, sample, gaz, auxiliary gaz, cool gaz) ;
- La géométrie du plasma (RF power) ;
- La position de la torche (Z-position, indicateur de proximité de la torche avec les cônes) ;
- La combinaison des 4 différents cônes (2 cônes « standard » et 2 cônes « jet ») ;
- L'utilisation de la « Guard Electrode » entourant l'extrémité de la torche ;

Le choix des paramètres optimaux est un mélange subtil entre une bonne sensibilité c'est-à-dire un signal suffisamment élevé pour la mesure des échantillons naturels), une bonne stabilité du signal et un rapport S/N élevé. La variation du rapport S/N en fonction de la valeur des paramètres exposés plus haut est présenté Figure 10. La variation du rapport S/N en fonction de la position de la torche atteint un optimum pour Z = – 2.5 mm pour le DSN et Z = – 4 mm pour l'Aridus. La valeur du « RF power »

influence peu le rapport S/N qui est néanmoins plus élevé lorsque le flux de gaz auxiliaire est plus élevé. Le rapport S/N semble d'autant plus important que la valeur du flux de gaz auxiliaire est élevée. Finalement les paramètres finaux utilisés pour les mesures sont résumés dans le Tableau 6. La détermination des paramètres optimaux pour l'Apex Ω et pour la chambre de nébulisation ont été obtenus en partant des optimums pour l'Aridus II. Un mélange entre les deux familles de cônes est utilisé, soit un cône échantillonneur du type « standard » et un cône écrêteur de type « jet ». Cette combinaison a été sélectionnée en fonction de l'amplitude du signal, sa stabilité et de l'intensité des interférences. L'utilisation d'une chambre de nébulisation optimise le rapport S/N au détriment de la sensibilité qui est bien meilleure avec l'utilisation d'un désolvateur. Le DSN est le désolvateur avec la meilleure sensibilité par ppm.

Tableau 6 : Paramètres utilisés pour la mesure des rapports isotopiques en fonction du système d'introduction et comparaison de leurs caractéristiques principales.

Paramètres	DSN	Aridus	Apex Ω	Chambre de nébulisation
RF power	1200	1100	1100	1200
Position Z de la torche (mm)	-2.5	-4.5	-4.5	-5
Aux gaz (L/min)	1.25	1.15	1.1	1
Rapports S/N optimisé	350	400	/	90
Flux du nébuliseur (µL/min)	76	76	76	76
Intensité moyenne de ^{28}Si de NBS28 en MR (V)	Entre 15 et 30	15	10	5.5
Intensité moyenne de ^{28}Si dans le blanc en MR (V)	Entre 0.2 et 0.4	0.16	0.12	0.045
Rapport S/N	75	94	83	122
Sensibilité V/ppm	De 30 à 60	33	22	12

4.2. Choix du système d'introduction

Une grande variété de configurations est utilisée pour les analyses isotopiques du Si dans la littérature. Un résumé des techniques récentes utilisées est présenté dans le Tableau 8. Les différents systèmes d'introduction ont tous été testés dans le cadre de cette thèse et une synthèse des principaux résultats est présenté Figure 11. Aucune mesure acceptable des deux standards secondaires n'a pu être obtenue dans la configuration de plasma humide (chambre cyclonique). La sensibilité en plasma humide est nettement plus faible qu'en configuration de plasma sec, avec une sensibilité allant de 7 à 13 V/ppm avec la chambre de nébulisation contre une sensibilité allant de 22 à 49 V/ppm en utilisant un désolvateur (cf Tableau 6). La bonne sensibilité obtenue en utilisant un désolvateur est un argument

en faveur de l'adoption d'une telle configuration pour les mesures isotopiques. Trois systèmes de désolvatation ont été testés : le DSN-100 produit par Nu Instruments, l'Aridus II produit par Cetac et l'Apex Ω produit par la société ESI.

Le DSN

Le DSN présente une chambre de nébulisation verticale chauffée par un flux de gaz. Cette configuration n'est pas favorable à la persistance des effets mémoires et s'avère particulièrement intéressante pour l'analyse du Si. En cas de saturation de la membrane, la procédure de lavage faisant intervenir les acides chlorhydrique, nitrique ainsi que fluorhydrique est simple à mettre en place et s'avère efficace. Le DSN fournit des mesures justes et précises (cf Figure 11).

L'Aridus II

L'Aridus II présente une chambre de nébulisation oblique rendant les effets mémoires plus fréquents contrairement au DSN avec sa configuration verticale. Il comprend également une entrée de gaz d'azote à la sortie de la membrane. Cet ajout d'azote permet certes de stabiliser le plasma mais introduit également une quantité d'azote importante favorisant les interférences isobares qui font intervenir cet élément, notamment sur les masses 28 ($^{14}N_2$) et 29 ($^{14}N^{15}N$). Une méthode sans utilisation de N_2 via des modifications mineures au niveau du désolvateur a récemment été proposée (Kamber and Schoenberg, 2020; Rosca *et al.*, 2019; Suhr *et al.*, 2018). Malheureusement les tests effectués sur notre propre matériel n'ont pas été probants en adoptant cette configuration avec un $\delta^{30}Si$ mesuré de 1.35 ± 0.6 ‰ (2SD, n=5) pour la diatomite par rapport à la valeur de la littérature à 1.23 ± 0.15 ‰ (2SD), mettant en évidence une mauvaise justesse et précision des mesures isotopiques avec cette configuration (cf Figure 11).

L'Apex Ω

L'Apex Ω est un désolvateur récent qui a produit des résultats très prometteurs. La Figure 11 met en évidence la très bonne stabilité et la précision des rapports isotopiques. Cependant la saturation de la membrane en quelques semaines et l'impossibilité de la nettoyer aussi efficacement que celle du DSN a entraîné un arrêt net des mesures avec ce dispositif.

Ainsi, les mesures isotopiques présentées dans ce travail ont été produites avec le DSN et l'Apex si spécifié (pour le détail des paramètres, se référer à la partie méthode du Chapitre 4 de ce manuscrit).

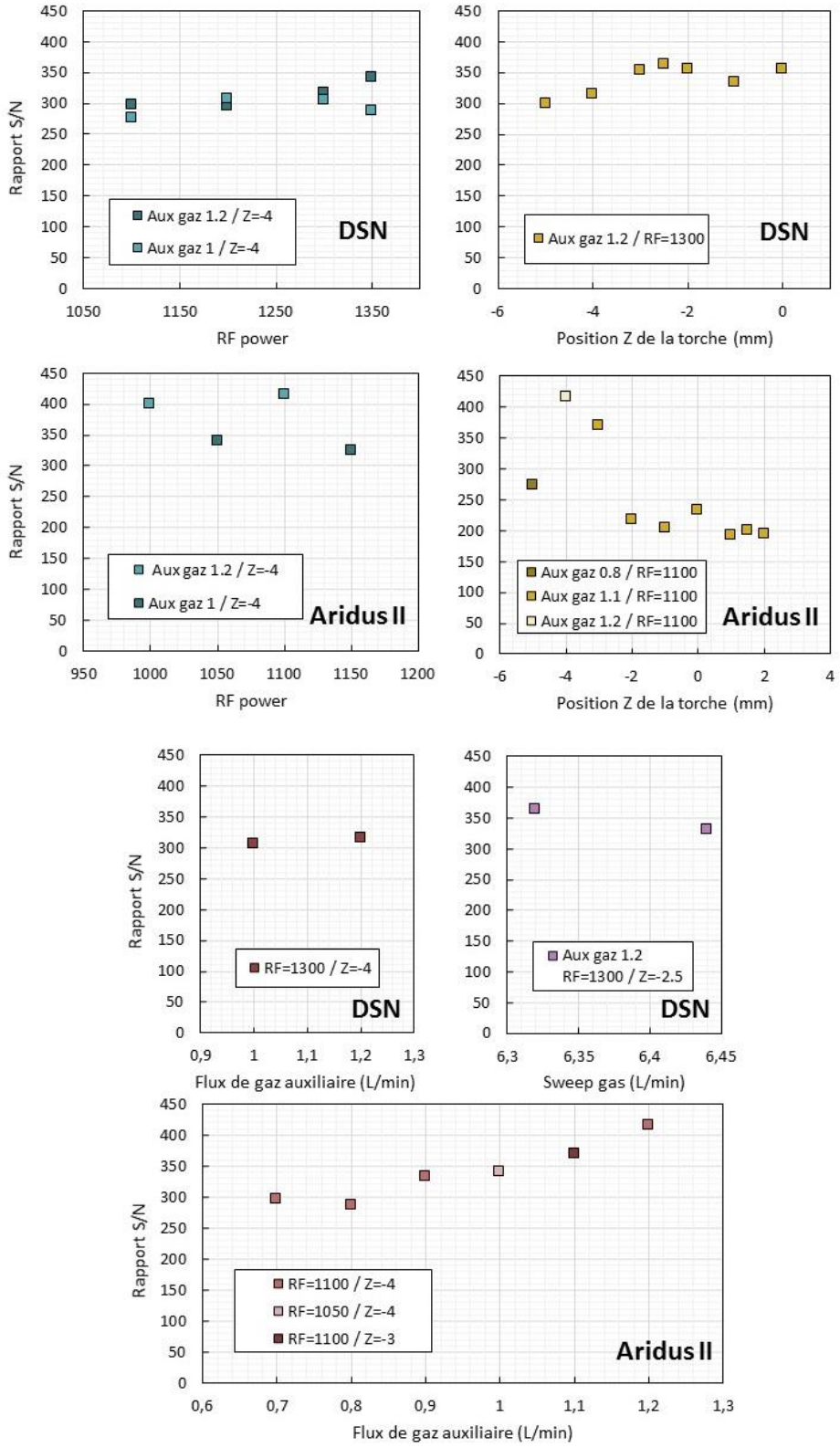

Figure 10 : Valeur du rapport signal sur bruit (S/N) en fonction de la valeur du RF power, de la position en Z de la torche et de différents flux de gaz avec le DSN et l'Aridus II.

4.3. Optimisation du protocole analytique de préparation

Le protocole de préparation des échantillons a été optimisé de manière à atteindre la justesse et la précision sur les mesures de $\delta^{29}Si$ et $\delta^{30}Si$ des standards. Ainsi plusieurs paramètres ont été testés : la taille du réservoir des colonnes (1mL et 2mL qui décalait de manière systématique la valeur des $\delta^{29}Si$ et $\delta^{30}Si$) ; l'ajout d'une fine couche de résine préfiltre déposée au-dessus du fritté de la colonne (améliore la précision des mesures) ; le type de résine cationique (50W X8 200-400 mesh et 50W X12 200-400 mesh qui correspond à une résine plus réticulée) ; le protocole de lavage préalable de la résine cationique (10 fois HCl 6 N et MilliQ contre la procédure plus longue adoptée qui est exposée Tableau 2).

4.4. Choix du milieu : HCl ou HNO_3?

L'étape d'acidification des échantillons après la fusion peut être réalisée avec de l'acide chlorhydrique ou de l'acide nitrique (cf Tableau 8). Certaines études préfèrent l'acide chlorhydrique à cause de la possibilité d'augmentation du signal des interférences par l'utilisation de HNO_3 via l'introduction d'atomes d'azote et d'oxygène supplémentaires dans le plasma. Cependant le choix de l'acide chlorhydrique peut entraîner une baisse de la sensibilité, relié au fort potentiel d'ionisation du chlore (De La Rocha, 2002; Savage and Moynier, 2013). Cet effet n'a pas été observé au cours de la phase de développement analytique avec une sensibilité analogue sur le standard NBS en milieu HNO_3 et HCl, avec une sensibilité respectivement de 28 V/ppm et 32 V/ppm sur deux séquences séparées de quelques jours. Les deux standards secondaires de diatomite et BHVO-2 ont ainsi été mesurés en milieu HCl et HNO_3 par souci de comparaison de la qualité des mesures. La Figure 11 illustre la meilleure reproductibilité des mesures en milieu HCl (cercles roses) par rapport aux mesures en HNO_3 (cercles bleus), ces différences sont attribuées à l'existence d'interférences plus importantes en milieu nitrique. Ainsi les échantillons ont été acidifiés pour atteindre un pH entre 2 et 3 avec une solution de HCl 6 N.

4.5. Vérification de la dépendance en masse

L'ensemble des données en $\delta^{29}Si$ et $\delta^{30}Si$ pour les deux standards secondaires Diatomite et BHVO-2 mesurées avec le DSN (Figure 12) et l'Apex Ω (Figure 13) sont dépendantes de la masse et dessinent une droite de fractionnement qui coïncide avec les droites de fractionnement théoriques décrivant les fractionnements dépendants de la masse pour les isotopes du silicium (cf Chapitre 1). Chaque donnée isotopique correspond à la moyenne d'environ 10 mesures du même échantillon au cours d'une

séquence durant en moyenne 24h. La dépendance en masse constitue un critère suffisant de rejet de certaines mesures isotopiques. Un éloignement significatif de quelques mesures à la droite de fractionnement en masse peut être observé, notamment pour certaines mesures de BHVO-2 obtenues avec le DSN. Elles sont associées à la mesure conjointe d'une interférence ou le relargage aléatoire de silicium en amont du plasma. La non dépendance en masse quasi-systématique des mesures en milieu HNO_3 a été un critère supplémentaire dans le choix du milieu HCl pour les mesures isotopiques.

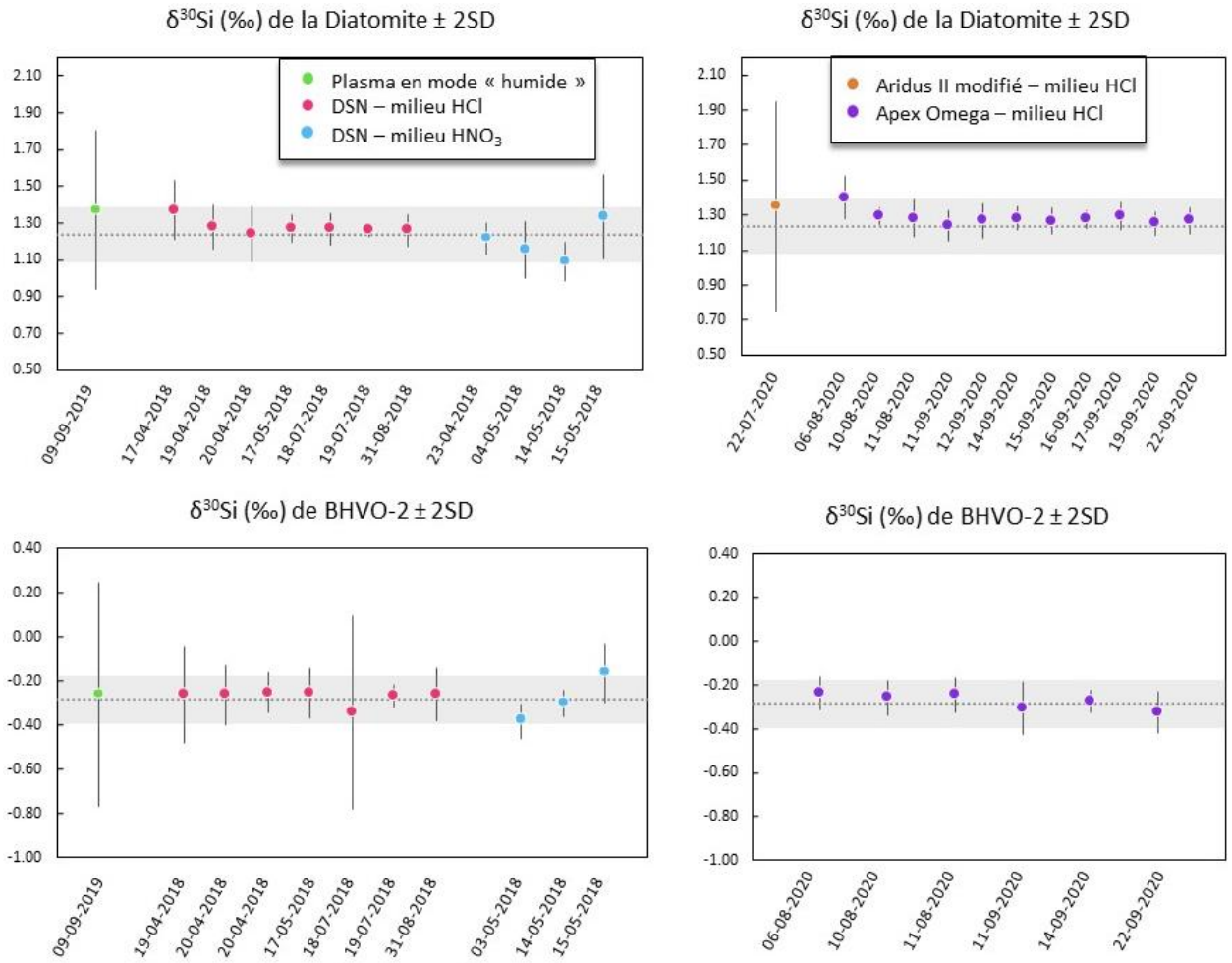

Figure 11: Synthèse des principales données pour la diatomite et BHVO-2 obtenues en suivant strictement le même protocole analytique mais avec différents systèmes d'introduction : une chambre de nébulisation ; l'Aridus II modifié (cf texte) ; l'Apex Ω ; le DSN. Les deux standards en milieu HCl et HNO_3 ont également été mesurés avec le DSN pour comparer la qualité des mesures. La droite en pointillé correspond à la moyenne des mesures tirées de la littérature et la partie grisée à l'erreur associée (cf §3.4).

Tableau 7 : Valeurs des $\delta^{29}Si$ et $\delta^{30}Si$ de la diatomite et de BHVO-2 obtenus lors des différents tests représentées Figure 11 (cf texte pour plus de détails sur les différentes configurations testées).

Diatomite								
Système d'introduction	**Matrice**	**Date**	**$\delta^{29}Si$**	**2SD**	**$\delta^{30}Si$**	**2SD**	**Pente**	**N**
Chambre de nébulisation	HCl	09-09-2019	0.64	0.29	1.29	0.68	0.49	12
DSN	HCl	17-04-2018	0.72	0.07	1.37	0.16	0.52	8
		19-04-2018	0.64	0.05	1.28	0.12	0.50	8
		20-04-2018	0.64	0.09	1.24	0.15	0.52	8
		17-05-2018	0.66	0.03	1.27	0.08	0.52	6
		18-07-2018	0.64	0.01	1.27	0.08	0.51	6
		19-07-2018	0.63	0.02	1.26	0.03	0.50	3
		31-08-2018	0.65	0.09	1.26	0.09	0.52	6
	HNO_3	23-04-2018	0.63	0.06	1.22	0.09	0.51	9
		04-05-2018	0.59	0.11	1.15	0.15	0.51	4
		14-05-2018	0.55	0.04	1.09	0.11	0.50	7
		15-05-2018	0.67	0.15	1.33	0.23	0.50	6
Aridus II	HCl	22-07-2020	0.71	0.33	1.35	0.60	0.52	5
Apex Ω	HCl	06-08-2020	0.75	0.15	1.40	0.12	0.54	4
		10-08-2020	0.68	0.04	1.29	0.05	0.53	13
		11-08-2020	0.66	0.02	1.28	0.11	0.52	4
		11-09-2020	0.64	0.05	1.24	0.09	0.51	14
		12-09-2020	0.66	0.07	1.27	0.10	0.52	13
		14-09-2020	0.66	0.04	1.28	0.07	0.51	13
		15-09-2020	0.66	0.04	1.27	0.07	0.52	14
		16-09-2020	0.66	0.06	1.28	0.05	0.52	14
		17-09-2020	0.65	0.05	1.29	0.08	0.50	14
		19-09-2020	0.65	0.07	1.25	0.07	0.52	14
		22-09-2020	0.66	0.06	1.27	0.08	0.52	13

BHVO-2								
Système d'introduction	**Matrice**	**Date**	**$\delta^{29}Si$**	**2SD**	**$\delta^{30}Si$**	**2SD**	**Pente**	**N**
Chambre de nébulisation	HCl	09-09-2019	-0.12	0.24	-0.26	0.50	0.47	10
DSN	HCl	19-04-2018	-0.12	0.11	-0.26	0.22	0.44	6
		20-04-2018	-0.13	0.13	-0.26	0.13	0.48	5
		20-04-2018	-0.15	0.12	-0.25	0.09	0.58	5
		17-05-2018	-0.14	0.09	-0.26	0.11	0.54	6
		18-07-2018	-0.15	0.04	-0.34	0.44	0.43	6
		19-07-2018	-0.12	0.03	-0.27	0.05	0.45	4
		31-08-2018	-0.15	0.14	-0.26	0.12	0.57	6
	HNO_3	03-05-2018	-0.20	0.06	-0.38	0.08	0.52	6
		14-05-2018	-0.18	0.08	-0.30	0.06	0.61	6

		15-05-2018	-0.10	0.06	-0.16	0.13	0.59	6
Apex Ω	HCl	06-08-2020	-0.13	0.04	-0.24	0.07	0.54	4
		10-08-2020	-0.12	0.04	-0.26	0.08	0.46	12
		11-08-2020	-0.12	0.04	-0.25	0.08	0.49	4
		11-09-2020	-0.15	0.07	-0.31	0.12	0.49	12
		14-09-2020	-0.14	0.04	-0.27	0.05	0.49	12
		22-09-2020	-0.15	0.05	-0.33	0.10	0.46	12

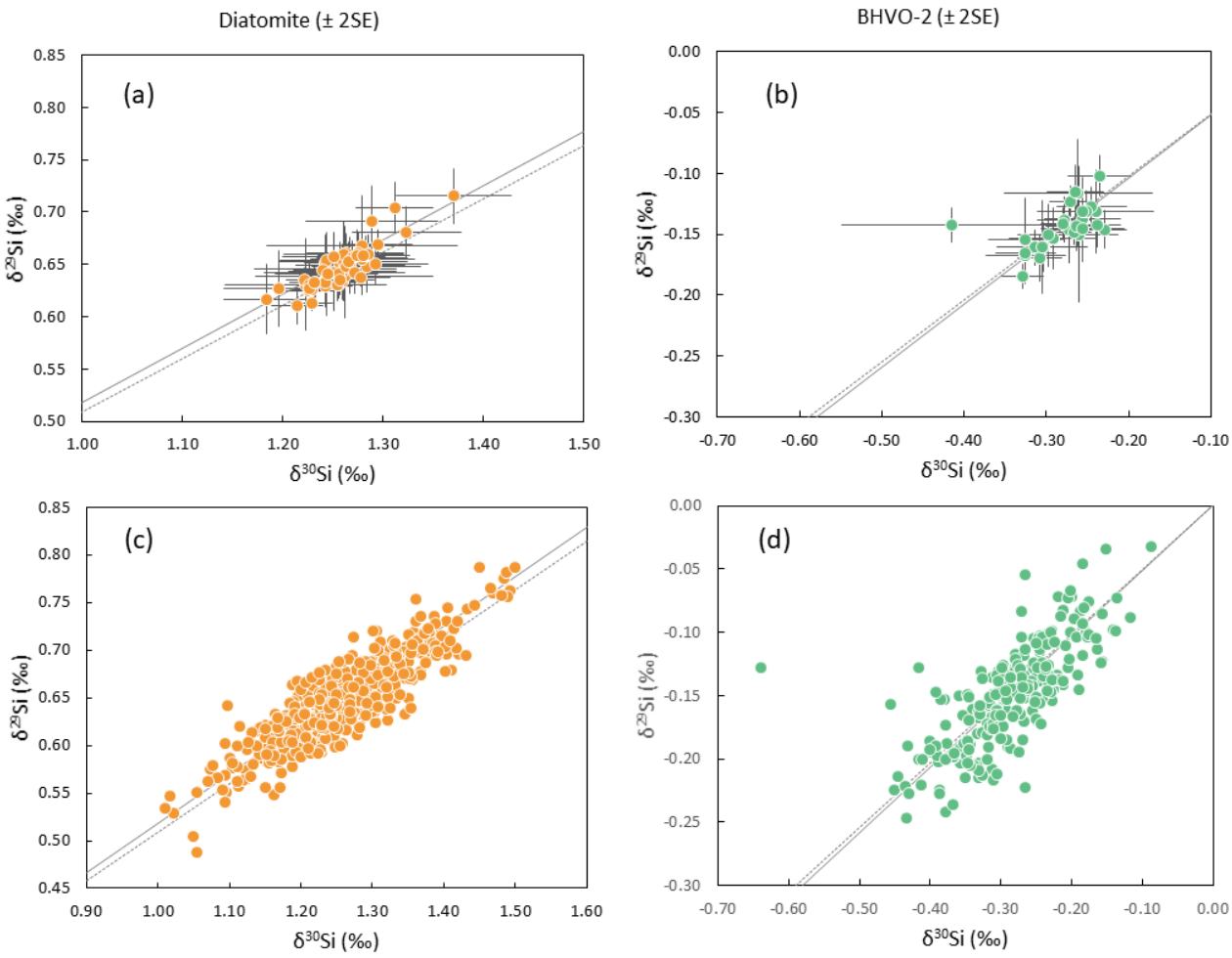

Figure 12 : Compilation de l'ensemble des mesures isotopiques effectuées avec le DSN sur les deux standards Diatomite et BHVO-2 au cours de ce travail de thèse. Les données présentées en (a) et (b) correspondent à la moyenne des mesures effectuées au cours d'une séquence de mesure de 24h avec leur erreur associée en 2SE (avec en moyenne 10 mesures par séquence), le détail de chaque point de mesure est indiqué respectivement en (c) pour la diatomite et en (d) pour BHVO-2. Un total de 668 mesures de diatomite et de 309 mesures de BHVO-2 sont ainsi représentées. Les pentes théoriques de fractionnement cinétique et thermodynamique dépendants de la masse sont représentées respectivement en trait pointillé et en trait plein (pentes respectives 0.5092 et 0.5178).

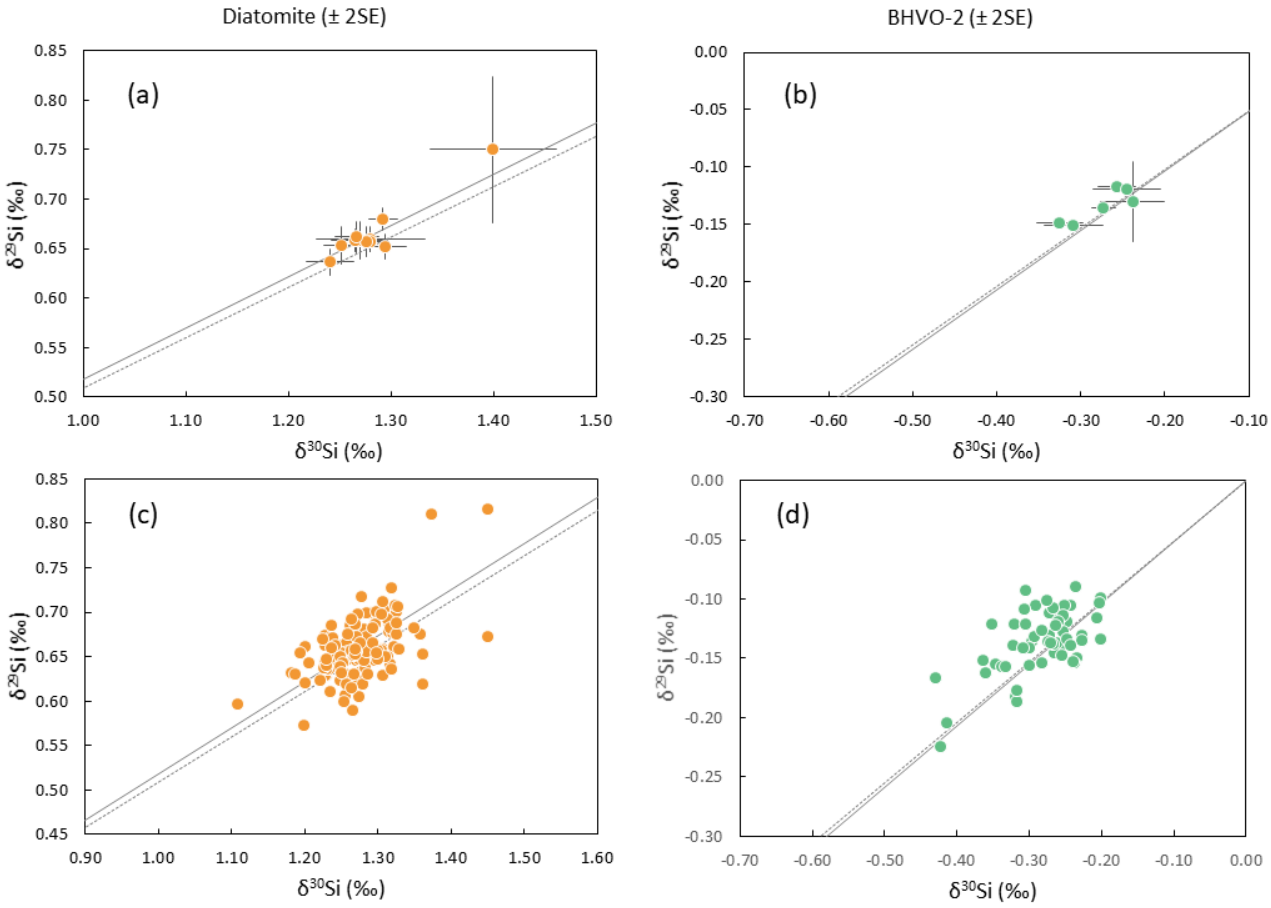

Figure 13 : Compilation de l'ensemble des mesures isotopiques effectuées avec l'Apex Ω sur les deux standards Diatomite et BHVO-2 au cours de ce travail de thèse. Un total de 130 mesures de diatomite et de 44 mesures de BHVO-2 est représentés (cf Figure 12 pour le détail des figurés).

Tableau 8 : Compilation des méthodes les plus récentes pour l'analyse isotopique du Si.

Nom	Fitoussi et al.	Chakrabarti and Jacobsen	Ziegler et al.	Savage et al.	Armytage et al.	Zambardi and Poitrasson	Armytage et al.	Fitoussi and Bourdon	Savage and Moynier	Pringle et al.	Pringle et al.	Dauphas
Date	2009	2010	2010	2011	2011	2011	2012	2012	2013	2013	2014	2015
Type de résine (H^+) 200-400 mesh	BioRad AG50-X8	BioRad AG50-X12	Dowex 50W-X12	Dowex 50W-X12	Dowex 50W-X12h	BioRad AG50-X12	Dowex 50W-X12	BioRad AG50-X8	BioRad AG50-X12	BioRad AG50-X12	BioRad AG50-X12	BioRad AG50-X12
Méthode de préparation des échantillons	Fusion alcaline	Fusion alcaline (bombe téflon)	Dissolution HF	Fusion alcaline	Fusion alcaline	Fusion alcaline	Fusion alcaline	Fusion alcaline	Fusion alcaline	Fusion alcaline	Fusion alcaline	Fusion alcaline
Milieu	HCl	HNO3	HNO3 + HF	HNO3	HCl et HNO3	HCl	HCl	HCl	HNO3	HNO3	HNO3	HCl
Instrument (MC-ICP-MS)	NuPlasma1700 ETH Zurich	GV IsoProbe-P	Laser ablation - Neptune	NuPlasma	NuPlasma	Neptune	NuPlamsa	NuPlasma1700	Neptune Plus	Neptune Plus	Neptune Plus	Thermo Electron Neptune
Résolution	HR - pouvoir de résolution 2000	HR - pouvoir de résolution 5000	MR - pouvoir de résolution 12000	MR - pouvoir de résolution 3300	MR - pouvoir de résolution 4000	HR - pouvoir de résolution 7000	MR - pouvoir de résolution 4000	HR - pouvoir de résolution 2000	MR - pouvoir de résolution 7500	MR	MR	MR
Système d'introduction	DSN	chambre de nébulisation (APEXIR, de Elemental Scientific Inc.)	Cetac Aridus I	Cetac Aridus II	Cetac Aridus II	Chambre de nébulisation	Cetac Aridus II	DSN	Chambre de nébulisation	Chambre de nébulisation	Chambre de nébulisation	Chambre de nébulisation
Correction du biais en masse instrumental	SSB relatif à NBS28	SSB relatif à NBS28	SSB relatif à NBS28	SSB relatif à NBS28	SSB relatif à NBS28	Mg standard interne et SSB relatif à NBS28	SSB relatif à NBS28	SSB relatif à NBS28	SSB relatif à NBS28	SSB relatif à NBS28	SSB relatif à NBS28	Mg standard interne et SSB relatif à NBS28
Rapport S/N	> 300	400			350	1167	350		700			
Type d'échantillon	terrestre - cosmochimique	terrestre - cosmochimique	terrestre - cosmochimique	terrestre	terrestre - cosmochimique	cosmochimique	cosmochimique	cosmochimique	cosmochimique	cosmochimique	cosmochimique	cosmochimique

5. Conclusion

Un nombre important de tests a été mené afin de déterminer les paramètres les plus favorables à la génération de données isotopiques du Si de qualité, à savoir des données isotopiques justes, précises et présentant une bonne répétabilité. Ainsi, chaque paramètre du Neptune Plus et chaque paramètre analytique a été minutieusement examiné pour aboutir aux conditions optimales de mesure. Les analyses isotopiques présentées dans ce manuscrit sont produites à partir d'échantillons préparées par fusion alcaline puis acidifiés avec HCl 6N pour atteindre un pH de solution compris entre 2 et 3. Les échantillons sont ensuite chargés sur une colonne chromatographique contenant 1 mL de résine cationique de type X8 200-400 mesh. Les analyses par spectrométrie de masse sont effectuées avec un DSN couplé à un Neptune Plus MC-ICP-MS avec des paramètres optimisés pour minimiser le rapport signal sur bruit, soit une position Z de la torche à -2.5 mm, un RF power à 1200 et un flux de gaz auxiliaire à 1.2 L/min. Les autres paramètres sont optimisés chaque jour pour atteindre une meilleure sensibilité. Le couplage des différents types de cônes réduit les interférences tout en donnant une sensibilité optimale. La sensibilité varie de 15 V à 30 V en moyenne résolution pour un échantillon équivalent à une sensibilité de 30 à 60 V/ppm. Les résultats obtenus sur les deux standards secondaires mesurés au cours de ce développement analytique, diatomite et BHVO-2, sont en accord avec les précédentes mesures isotopiques et aboutissent respectivement à une valeur de $\delta^{30}Si_{diatomite}$ = 1.26 ± 0.15 ; 0.005 (2SD ; 2SE, n=798) et $\delta^{29}Si_{diatomite}$ = 0.65 ± 0.08 ; 0.003 (2SD ; 2SE) ; $\delta^{30}Si_{BHVO\text{-}2}$ = -0.28 ± 0.14 ; 0.007 (2SD ; 2SE, n=365) et $\delta^{39}Si_{BHVO\text{-}2}$ = -0.14 ± 0.08 ; 0.004 (2SD ; 2SE). Les valeurs isotopiques sur les standards sont en accord avec les valeurs référencées, validant ainsi le protocole analytique. La configuration inédite utilisée pour les mesures isotopiques, c'est-à-dire un DSN couplé avec un Neptune Plus, et le soin tout particulier accordé au choix des paramètres de mesures a abouti à l'obtention de données isotopiques de qualité qui ont notamment permis de trancher sur les valeurs isotopiques en silicium débattues de Mars et des angrites.

Dans le chapitre suivant, le protocole décrit ci-contre est appliqué à la mesure de météorites marsiennes ainsi qu'à des angrites (météorites différentiées) et à des échantillons synthétiques d'olivines irradiées. L'ensemble des résultats est discuté dans les chapitres suivants.

Références

Abraham, K., Opfergelt, S., Fripiat, F., Cavagna, A.-J., de Jong, J.T.M., Foley, S.F., André, L., Cardinal, D. (2008) δ^{30} Si and δ^{29}Si Determinations on USGS BHVO-1 and BHVO-2 Reference Materials with a New Configuration on a Nu Plasma Multi-Collector ICP-MS. *Geostandards and Geoanalytical Research* 32, 193–202.

Allenby, R.J. (1954) Determination of the isotopic ratios of silicon in rocks. *Geochimica et Cosmochimica Acta* 5, 40–48.

Amet, Q. (2021) Les isotopes du zinc et de l'étain en géochimie et cosmochimie. These de doctorat, Lyon.

Armytage, R.M.G., Georg, R.B., Savage, P.S., Williams, H.M., Halliday, A.N. (2011) Silicon isotopes in meteorites and planetary core formation. *Geochimica et Cosmochimica Acta* 75, 3662–3676.

Armytage, R.M.G., Georg, R.B., Williams, H.M., Halliday, A.N. (2012) Silicon isotopes in lunar rocks: Implications for the Moon's formation and the early history of the Earth. *Geochimica et Cosmochimica Acta* 77, 504–514.

Basile-Doelsch, I., Meunier, J.D., Parron, C. (2005) Another continental pool in the terrestrial silicon cycle. *Nature* 433, 399–402.

Brzezinski, M.A., Jones, J.L., Beucher, C.P., Demarest, M.S., Berg, H.L. (2006) Automated Determination of Silicon Isotope Natural Abundance by the Acid Decomposition of Cesium Hexafluosilicate. *Analytical Chemistry* 78, 6109–6114.

Cardinal, D., Alleman, L.Y., de Jong, J., Ziegler, K., André, L. (2003) Isotopic composition of silicon measured by multicollector plasma source mass spectrometry in dry plasma mode. *Journal of Analytical Atomic Spectrometry* 18, 213–218.

Chakrabarti, R., Jacobsen, S.B. (2010) Silicon isotopes in the inner Solar System: Implications for core formation, solar nebular processes and partial melting. *Geochimica et Cosmochimica Acta* 74, 6921–6933.

Chmeleff, J., Horn, I., Steinhoefel, G., von Blanckenburg, F. (2008) In situ determination of precise stable Si isotope ratios by UV-femtosecond laser ablation high-resolution multi-collector ICP-MS. *Chemical Geology* 249, 155–166.

Dauphas, N., Poitrasson, F., Burkhardt, C., Kobayashi, H., Kurosawa, K. (2015) Planetary and meteoritic Mg/Si and δ30Si variations inherited from solar nebula chemistry. *Earth and Planetary Science Letters* 427, 236–248.

De La Rocha, C.L., Brzezinski, M.A., DeNiro, M.J. (1996) Purification, Recovery, and Laser-Driven Fluorination of Silicon from Dissolved and Particulate Silica for the Measurement of Natural Stable Isotope Abundances. *Analytical Chemistry* 68, 3746–3750.

De La Rocha, C.L. (2002) Measurement of silicon stable isotope natural abundances via multicollector inductively coupled plasma mass spectrometry (MC-ICP-MS): Silicon stable isotope natural abundances. *Geochemistry, Geophysics, Geosystems* 3, 1–8.

Ding, T. (2004) Chapter 25 - Analytical Methods for Silicon Isotope Determinations. In: de Groot, P.A. (ed.) *Handbook of Stable Isotope Analytical Techniques*. Elsevier, Amsterdam, 523–537.

Ding, T., Wan, D., Wang, C., Zhang, F. (2004) Silicon isotope compositions of dissolved silicon and suspended matter in the Yangtze River, China. *Geochimica et Cosmochimica Acta* 68, 205–216.

Douthitt, C.B. (1982) The geochemistry of the stable isotopes of silicon. *Geochimica et Cosmochimica Acta* 46, 1449–1458.

Engström, E., Rodushkin, I., Baxter, D.C., Öhlander, B. (2006) Chromatographic Purification for the Determination of Dissolved Silicon Isotopic Compositions in Natural Waters by High-Resolution Multicollector Inductively Coupled Plasma Mass Spectrometry. *Analytical Chemistry* 78, 250–257.

Fitoussi, C., Bourdon, B., Kleine, T., Oberli, F., Reynolds, B.C. (2009) Si isotope systematics of meteorites and terrestrial peridotites: implications for Mg/Si fractionation in the solar nebula and for Si in the Earth's core. *Earth and Planetary Science Letters* 287, 77–85.

Fitoussi, C., Bourdon, B. (2012) Silicon Isotope Evidence Against an Enstatite Chondrite Earth. *Science* 335, 1477–1480.

Georg, R.B., Reynolds, B.C., Frank, M., Halliday, A.N. (2006) New sample preparation techniques for the determination of Si isotopic compositions using MC-ICPMS. *Chemical Geology* 235, 95–104.

Georg, R.B. (2006) Geochemistry of stable silicon isotopes measured by high-resolution multi-collector inductively-coupled-plasma mass-spectrometry (HR-MC-ICP-MS). ETH Zurich, 144 S.

Georg, R.B., Halliday, A.N., Schauble, E.A., Reynolds, B.C. (2007) Silicon in the Earth's core. *Nature* 447, 1102–1106.

Heck, P.R., Huberty, J.M., Kita, N.T., Ushikubo, T., Kozdon, R., Valley, J.W. (2011) SIMS analyses of silicon and oxygen isotope ratios for quartz from Archean and Paleoproterozoic banded iron formations. *Geochimica et Cosmochimica Acta* 75, 5879–5891.

Hin, R.C., Fitoussi, C., Schmidt, M.W., Bourdon, B. (2014) Experimental determination of the Si isotope fractionation factor between liquid metal and liquid silicate. *Earth and Planetary Science Letters* 387, 55–66.

Horn, I., von Blanckenburg, F. (2007) Investigation on elemental and isotopic fractionation during 196 nm femtosecond laser ablation multiple collector inductively coupled plasma mass spectrometry. *Spectrochimica Acta Part B: Atomic Spectroscopy* 62, 410–422.

Houk, R.S. (1986) Mass spectrometry of inductively coupled plasmas. *Analytical Chemistry*. American Chemical Society 58, 97A-105A.

Huneke, J.C., Armstrong, J.T., Wasserburg, G.J. (1983) FUN with PANURGE: High mass resolution ion microprobe measurements of Mg in Allende inclusions. *Geochimica et Cosmochimica Acta* 47, 1635–1650.

Iler, K. (1979) The Chemistry of Silica. *Solubility, Polymerization, Colloid and Surface Properties and Biochemistry of Silica*. John Wiley and Sons Inc.

Kadlag, Y., Tatzel, M., Frick, D.A., Becker, H. (2019) The origin of unequilibrated EH chondrites – Constraints from in situ analysis of Si isotopes, major and trace elements in silicates and metal. *Geochimica et Cosmochimica Acta* 267, 300–321.

Kadlag, Y., Tatzel, M., Frick, D.A., Becker, H., Kühne, P. (2021) In situ Si isotope and chemical constraints on formation and processing of chondrules in the Allende meteorite. *Geochimica et Cosmochimica Acta* 304, 234–257.

Kamber, B.S., Schoenberg, R. (2020) Evaporative loss of moderately volatile metals from the superheated 1849 Ma Sudbury impact melt sheet inferred from stable Zn isotopes. *Earth and Planetary Science Letters* 544, 116356.

Louvat, P., Moureau, J., Paris, G., Bouchez, J., Noireaux, J., Gaillardet, J. (2014) A fully automated direct injection nebulizer (d-DIHEN) for MC-ICP-MS isotope analysis: application to boron isotope ratio measurements. *J. Anal. At. Spectrom.* 29, 1698–1707.

Maréchal, C.N., Télouk, P., Albarède, F. (1999) Precise analysis of copper and zinc isotopic compositions by plasma-source mass spectrometry. *Chemical Geology* 156, 251–273.

Momot, J. (1964) Le rôle du fluor dans le chimisme volcanique. *Bulletin mensuel de la Société linnéenne de Lyon* 33, 330–334.

Poitrasson, F. (2017) Silicon Isotope Geochemistry. *Reviews in Mineralogy and Geochemistry* 82, 289–344.

Potts, P.J. (1992) Classical and rapid methods of analysis. In: Potts, P.J. (ed.) *A Handbook of Silicate Rock Analysis*. Springer US, Boston, MA, 47–76.

Pringle, E.A., Moynier, F., Savage, P.S., Badro, J., Barrat, J.-A. (2014) Silicon isotopes in angrites and volatile loss in planetesimals. *Proceedings of the National Academy of Sciences* 111, 17029–17032.

Pringle, E.A., Savage, P.S., Badro, J., Barrat, J.-A., Moynier, F. (2013) Redox state during core formation on asteroid 4-Vesta. *Earth and Planetary Science Letters* 373, 75–82.

Reynolds, B.C. *et al.* (2007) An inter-laboratory comparison of Si isotope reference materials. *J. Anal. At. Spectrom.* 22, 561–568.

Reynolds, J.H., Verhoogen, J. (1953) Natural variations in the isotopic constitution of silicon. *Geochimica et Cosmochimica Acta* 3, 224–234.

Rosca, C., Schoenberg, R., Tomlinson, E.L., Kamber, B.S. (2019) Combined zinc-lead isotope and trace-metal assessment of recent atmospheric pollution sources recorded in Irish peatlands. *Science of The Total Environment* 658, 234–249.

Russell, W.A., Papanastassiou, D.A., Tombrello, T.A. (1978) Ca isotope fractionation on the Earth and other solar system materials. *Geochimica et Cosmochimica Acta* 42, 1075–1090.

Savage, P.S., Georg, R.B., Williams, H.M., Burton, K.W., Halliday, A.N. (2011) Silicon isotope fractionation during magmatic differentiation. *Geochimica et Cosmochimica Acta* 75, 6124–6139.

Savage, P.S., Moynier, F. (2013) Silicon isotopic variation in enstatite meteorites: Clues to their origin and Earth-forming material. *Earth and Planetary Science Letters* 361, 487–496.

Shahar, A., Young, E.D. (2007) Silicon Isotope Ratio Analysis of a CAI by Laser Ablation MC-ICPMS and Implications for the Astrophysics of CAI Formation. Lunar and Planetary Science Conference 2007 1445.

Shahar, A., Hillgren, V.J., Young, E.D., Fei, Y., Macris, C.A., Deng, L. (2011) High-temperature Si isotope fractionation between iron metal and silicate. *Geochimica et Cosmochimica Acta* 75, 7688–7697.

Steinhoefel, G., von Blanckenburg, F., Horn, I., Konhauser, K.O., Beukes, N.J., Gutzmer, J. (2010) Deciphering formation processes of banded iron formations from the Transvaal and the Hamersley successions by combined Si and Fe isotope analysis using UV femtosecond laser ablation. *Geochimica et Cosmochimica Acta* 74, 2677–2696.

Stone, J., Hutcheon, I.D., Epstein, S., Wasserburg, G.J. (1991) Correlated Si isotope anomalies and large ^{13}C enrichments in a family of exotic SiC grains. *Earth and Planetary Science Letters* 107, 570–581.

Suhr, N., Schoenberg, R., Chew, D., Rosca, C., Widdowson, M., Kamber, B.S. (2018) Elemental and isotopic behaviour of Zn in Deccan basalt weathering profiles: Chemical weathering from bedrock to laterite and links to Zn deficiency in tropical soils. *Science of The Total Environment* 619–620, 1451–1463.

van den Boorn, S.H.J.M., Vroon, P.Z., van Belle, C.C., van der Wagt, B., Schwieters, J., van Bergen, M.J. (2006) Determination of silicon isotope ratios in silicate materials by high-resolution MC-ICP-MS using a sodium hydroxide sample digestion method. *Journal of Analytical Atomic Spectrometry* 21, 734.

van den Boorn, S.H.J.M., Vroon, P.Z., van Bergen, M.J. (2009) Sulfur-induced offsets in MC-ICP-MS silicon-isotope measurements. *Journal of Analytical Atomic Spectrometry* 24, 1111.

Villeneuve, J., Chaussidon, M., Marrocchi, Y., Deng, Z., Watson, E.B. (2019) High-precision *in situ* silicon isotopic analyses by multi-collector secondary ion mass spectrometry in olivine and low-calcium pyroxene. *Rapid Communications in Mass Spectrometry* 33, 1589–1597.

Walton, H.F. (1965) Ion exchange in analytical chemistry. *Journal of Chemical Education*. American Chemical Society 42, 111.

Weyer, S., Schwieters, J.B. (2003) High precision Fe isotope measurements with high mass resolution MC-ICPMS. *International Journal of Mass Spectrometry* 226, 355–368.

Zambardi, T., Poitrasson, F. (2011) Precise Determination of Silicon Isotopes in Silicate Rock Reference Materials by MC-ICP-MS. *Geostandards and Geoanalytical Research* 35, 89–99.

Zambardi, T., Poitrasson, F., Corgne, A., Méheut, M., Quitté, G., Anand, M. (2013) Silicon isotope variations in the inner solar system: Implications for planetary formation, differentiation and composition. *Geochimica et Cosmochimica Acta* 121, 67–83.

Ziegler, K., Young, E.D., Schauble, E.A., Wasson, J.T. (2010) Metal–silicate silicon isotope fractionation in enstatite meteorites and constraints on Earth's core formation. *Earth and Planetary Science Letters* 295, 487–496.

Zinner, E., Ming, T., Anders, E. (1987) Large isotopic anomalies of Si, C, N and noble gases in interstellar silicon carbide from the Murray meteorite. *Nature* 330, 730–732.

Annexe 1 : Rendement des systèmes d'introduction

La majeure partie du silicium introduit est perdue au cours de son passage dans le système d'introduction et dans le spectromètre de masse. Le rendement de l'analyse est défini comme la proportion d'atomes de silicium effectivement collectés par les détecteurs par seconde. Les détecteurs ne collectant que les ions $^{28}Si^{+}$, $^{29}Si^{+}$ et $^{30}Si^{+}$, le calcul du rendement peut se faire sur chacun des trois isotopes. En appelant N le nombre d'atomes ou d'ions correspondant à l'isotope 28 majoritaire (92.23%), on obtient :

$$R = N_{détectés}/N_{introduits}$$

Le nombre d'atomes ^{28}Si introduits dans le système dépend de la concentration en silicium de l'échantillon $C(Si)_{échantillon}$, du flux d'aspiration du nébuliseur f_{neb}, de la masse molaire du silicium M_{Si}, du nombre d'Avogadro N_A et de l'abondance de l'isotope 28 selon :

$$N_{introduits} = ab^{28}Si \times N(Si)_{introduits}$$

Avec

$$N(Si)_{introduits} = C(Si)_{échantillon} \times f_{neb} \times N_A/M_{Si}$$

Avec une concentration de 0.47 ppm pour NBS et un flux de nébuliseur de 76 µL/min (soit 1.27 g/s) dans chacune des configurations, c'est-à-dire en configuration « dry plasma » et « wet plasma », le nombre d'atomes introduit par seconde dans le système est de 1.17 10^{13} atomes de ^{28}Si/s.

Le nombre d'atomes effectivement détecté par seconde N par une cage de Faraday est fonction de l'intensité généré par l'impact d'un ion I exprimée en Coulomb/s (ou Ampère) et de la charge de l'ion q exprimée en Coulomb :

$$N \times q = I$$

La loi d'ohm relie l'intensité du courant électrique généré par l'impact d'un ion avec la tension du signal U et la valeur de l'amplificateur R (10^{11} ohm) selon :

$$U = R \times I$$

Ainsi on obtient

$$N = \frac{U}{R \times q}$$

Pour une sensibilité de 25V sur NBS avec le DSN et 5.6V sur NBS avec une chambre de nébulisation on obtient respectivement 1.6 10^9 atomes de ^{28}Si/s et 3.5 10^8 atomes de ^{28}Si/s qui sont effectivement détectés.

Finalement, le rendement de l'analyse est de 0.14% en utilisant un désolvateur et 0.03% en utilisant une chambre de nébulisation, ce qui est cohérent avec l'écart observé en sensitivité entre les deux systèmes d'introduction.

Chapter 3

Early differentiation processes on Mars inferred from silicon isotopes

Early differentiation processes on Mars inferred from silicon isotopes

Keywords: Mars, magma ocean, silicon isotope, isotope fractionation

Abstract:

Accretion of planets involved partial or global melting events such as magma oceans or magma ponds. Mars experienced large-scale differentiation very early in its history, as shown by their ^{146}Sm-^{142}Nd and ^{182}Hf-^{182}W record. The broad range in ε^{142}Nd and ε^{142}W variations of SNC meteorites highlights the presence of mantle sources that must have formed after the crystallization of a global magma ocean. In this study, we have investigated whether the events that generated these mantle reservoirs could have also generated different silicon isotope signatures, as Si isotopes are known to fractionate between high pressure mantle minerals. Thus, the goal of this study was to define any relationship between magma ocean crystallisation and possible variations in the Si isotope record of SNC meteorites. High resolution silicon isotope measurements were performed on twelve meteorites from the Shergottite, Nakhlite and Chassignite group on a Neptune Plus MC-ICP-MS in dry plasma mode. The δ^{30}Si values are in good agreement with previous studies but display a narrower range of variations with a mean value at -0.46 ‰ ± 0.07 (2SD). A magma ocean crystallisation model shows that SNCs could represent different mantle source reservoirs generated by magma ocean crystallisation. In particular, there is a correlation between calculated ^{147}Sm/^{144}Nd for the SNC depleted mantle sources with δ^{30}Si values that is consistent with

magma ocean crystallization of high pressure mantle phases. In contrast, the crustal samples (enriched Shergottites) displayed a very homogenous composition in Sm/Nd ratios despite significant variability in $\delta^{30}Si$. This observation could be related to either fluid-rock interactions or change in coordination of Si during crustal differentiation. Altogether, silicon isotope compositions of SNC provide new constraints about magma ocean crystallization processes in Mars.

1. Introduction

The analysis of the isotope composition of major elements such as Fe, Mg and Si in rocky planets has been the focus of various studies aiming at better understanding accretion and differentiation processes leading to the chemical diversity among planetary bodies (e.g. Dauphas *et al.*, 2015; Fitoussi *et al.*, 2009; Hin *et al.*, 2017; Magna *et al.*, 2017; Sossi *et al.*, 2016). The Earth, Moon, Mars and smaller objects of the inner solar system likely experienced a partially or totally molten state following their accretion (Elkins-Tanton, 2012; Reese and Solomatov, 2006; Schaefer and Elkins-Tanton, 2018; Solomatov, 2000, 2007). The sources of energy to produce such a magma ocean rely on accretion processes, core formation and radioactive decay of short-lived radioisotope such as ^{26}Al (half-life of 0.717 Myr) (Elkins-Tanton, 2012). The large amount of energy released from impacts during accretion and differentiation was sufficient to melt entirely a Mars-size mantle (Elkins-Tanton, 2005; Nimmo and Kleine, 2007; Plesa *et al.*, 2014). The complete separation of metal and silicates during core formation of the Earth and Mars should yield complete mantle melting, thereby allowing metallic liquid percolation through the entire mantle (Terasaki et al. 2005).

The SNC meteorites (Shergottite, Nahklite and Chassignite group) are basaltic to ultramafic rocks ejected from the surface of Mars (McSween, 1994; Treiman *et al.*, 2000). The shergottites show a large range of variations in short-lived radioactive systems, such as $^{146}Sm \rightarrow {}^{142}Nd$ (half-life of 103 Myr) and

$^{182}Hf \rightarrow {}^{182}W$ (half-life of 9 Myr) indicating heterogeneous mantle sources that were formed at an early stage of martian mantle evolution(Caro *et al.*, 2008; Debaille *et al.*, 2007; Foley *et al.*, 2005; Harper *et al.*, 1995; Kruijer *et al.*, 2017) . Mantle differentiation must have occurred very early in Mars history and the time scale of differentiation was estimated from at least 20 Myr after the formation of the Solar System (Bouvier *et al.*, 2018; Kruijer *et al.*, 2020) to ≈ 100 Myr in the case of a protracted magma ocean (Borg *et al.*, 2016; Caro *et al.*, 2008; Debaille *et al.*, 2007; Kruijer *et al.*, 2017). Various models of martian magmatism were proposed to reconcile the geochemical characteristics of the SNC but highlight a more complex magmatic history (Blichert-Toft *et al.*, 1999; Jones, 2003; McCubbin *et al.*, 2013; Papike *et al.*, 2009).

The preservation of ^{142}Nd and ^{182}W anomalies in SNC evidenced for inefficient mantle convection following magma ocean crystallization and is corroborated by dynamical models of mantle evolution (e.g. Breuer and Spohn, 2003). Therefore, silicon isotope signatures of SNC could potentially reflect the composition of their various mantle sources, as magmatic melting and differentiation does not fractionate silicon isotopes, provided the SiO_2 contents are below 55 wt% (Fitoussi *et al.*, 2009; Savage *et al.*, 2014). It has been suggested that evaporation processes from the surface of the magma ocean could have fractionated silicon isotopes in the case of the Earth (Hin et al. 2017). Thus, one could argue that similar processes could have operated since Mars also experienced a magma ocean stage. Nevertheless, a recent study by Tang and Young (2020) indicates that no significant Si mass-dependent fractionation is likely to take place while a planet sized body had a magma ocean. Incidentally, we found no correlation between $\delta^{30}Si$ and any indicator of volatile element loss (e.g. moderately volatile to refractory element ratios). It was also shown by Dauphas et al. (2015) that impact-induced Si volatilization was also not likely to have induced silicon isotope fractionation on Moon and Mars sized planetesimals.

Previous studies of Si isotopes in SNC meteorites have shown a large range in $\delta^{30}Si$ values and this could be indicative of analytical biases between laboratories (Armytage *et al.*, 2011; Pringle *et al.*,

2013; Zambardi *et al.*, 2013), although it is difficult to conclude as these studies had few samples in common.

In this study we revisited this issue by analyzing in a larger collection of martian meteorites using a Neptune Plus MC-ICP-MS operating in dry plasma mode. These new isotope measurements define a precise dataset of silicon isotope signature of the different martian mantle sources and this data set is used to investigate whether magma ocean signatures could still be present in the martian mantle.

2. Samples and analytical method

2.1. Sample description

Samples analysed in this study include 10 martian meteorites which belong to the shergottite group (LAR06319, LAR12011, RBT04262, NWA856, NWA480, EET790010-A and B, Zagami and NWA), 1 meteorite from the nakhlite group (MIL03346) and 1 from the chassignite group (NWA2737) (see Supplementary Materials). The three different groups share similar oxygen isotope composition Clayton and Mayeda, 1983) and redox state (Stolper *et al.*, 1979). The relatively young crystallization age of the shergottites, between 170 and 341 Ma (see compilation by McSween and McLennan, 2014) compared with other extraterrestrial materials meant that the formation of SNC were associated with relatively recent igneous processes that could be related to Mars mantle-crust evolution (Bogard and Johnson, 1983).The similarity between the noble gas content of trapped gas from EET79001 and the noble gas data of martian atmosphere acquired from the Viking spacecraft represented strong arguments for associating the SNC parent body with Mars (Treiman *et al.*, 2000). The SNC consist of mafic and ultramafic cumulate rocks with various magmatic history (McSween, 1994). The shergottite group is the most geochemically diverse group and was divided in four subgroups related to their mineralogy: basaltic, olivine-phyric, olivine-orthopyroxene-phyric and lherzolitic (Symes *et al.*, 2008). The classification of shergottite meteorites was summurized in Goodrich (2002). The basaltic

shergottites have basaltic textures with major mineral phases consisting of clinopyroxenes (pigeonite and augite) and plagioclase (in the form of glass or maskelynite produced by shocks). Lherzolitic shergottites present a poikilitic texture consisting mainly of olivine with clinopyroxene and orthopyroxene. The olivine-phyric group present olivine porphyritic texture, low augite content and chromite in addition to other minor mineral phases. Nakhlite MIL03346 consisting mainly of clinopyroxene was classified as a clinopyroxenite and Chassignite NWA2737 is composed essentially of olivine was classified as a dunite. The nakhlite and chassignite group share similar crystallization ages, ejection ages and trace element compositions that suggested a co-magmatic petrogenesis (Jones, 1989; McCubbin *et al.*, 2013). The 12 analysed samples were not exposed to significant terrestrial or martian weathering and presented shock features as melt pockets (see Supplementary Materials).

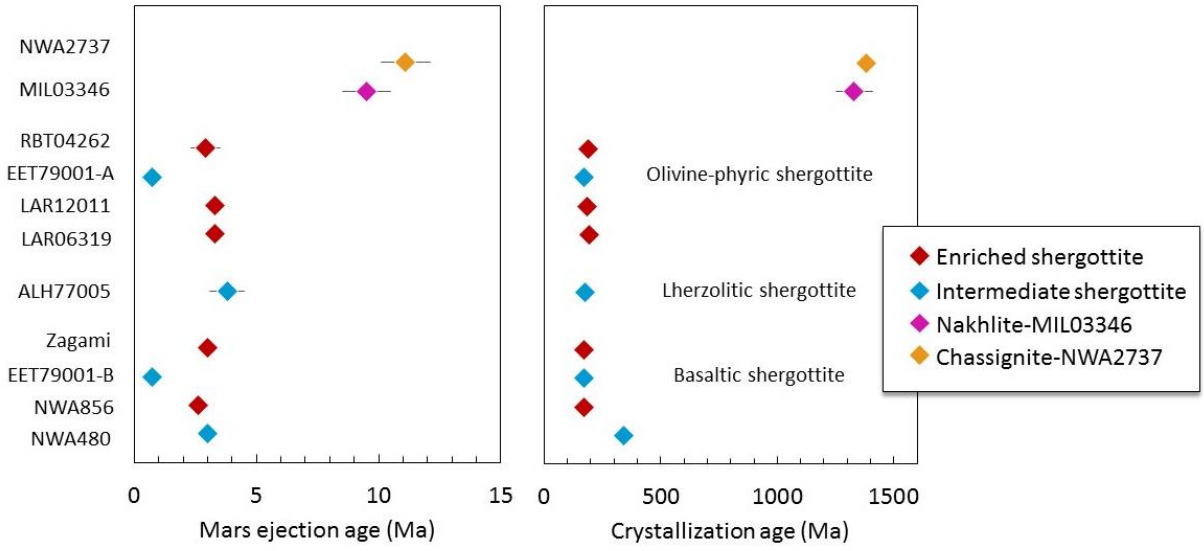

Figure 1: The crystallization age and mars ejection age of the 12 samples analysed in this study, “enriched” is for enriched and “interm” is for intermediate shergottite. Data are from the review of (McSween and McLennan, 2014) and (Bellucci et al., 2015) for the crystallization age of LAR12011 (see Supplementary Materials).

2.2. Sample preparation

The samples were first cleaned in an ultrasonic bath with distilled water followed by distilled ethanol. Samples were then powdered in an agate mortar that was pre-cleaned with 0.5 M HNO_3. Primary standard reference material SRM 8546 (consisting of ultra-pure silica powder), secondary standards Diatomite and BHVO-2 and martian samples were dissolved using an alkaline fusion method adapted from the procedure described in (Georg *et al.*, 2006). Between 1 and 4 mg of powdered sample was melted at 730 °C in a silver crucible with a ≈ 200 mg NaOH pellet for 7 minutes 30 seconds. After letting the fusion cake cool down, the crucible was transferred to a 30 mL Savillex vial filled with Milli-Q Element water. An ultrasonic tip was introduced in the vial for 4 minutes and the solution was left to equilibrate at 120° on a hotplate overnight. The solutions were then transferred to Teflon bottles and the vials were rinsed with Milli-Q until silicon concentration was diluted to 6 ppm. A solution of 6 M HCl was then added to reach a pH between 2 and 3 which is a necessary condition for reliable silicon isotope analysis (Fitoussi et al. 2009).

2.3. Column chromatography

A solution corresponding to approximately 3 µg of silicon was loaded on a BioRad column filled with 1 mL of cation exchange resin BioRad 50W-X8, 200-400 mesh in H^+ form. The separation procedure was adapted from the initial procedure described by (Georg *et al.*, 2006) and the new separation protocol is summarized in Table 1. The cations stick to the resin whereas the silicic acid (H_4SiO_4 and $H_3SiO_4^-$ in acidic water solution) go through the column and thus the Si fraction is collected with a yield close to 100%.

Table 1: Column chromatography procedure for silicon separation.

Separation Stage	Solution	Volume
Pre-cleaning resin	3 N HCl	Column reservoir
Pre-cleaning resin	6 N HCl	Column reservoir
Pre-cleaning resin	15 N HNO_3	200 µl
Pre-cleaning resin	6 N HCl	Column reservoir
Pre-cleaning resin	3 N HCl	Column reservoir
Pre-cleaning resin	Milli-Q	4 column reservoirs
Sample load	Acidified sample solution to pH 2-3	≈ 0.5 ml
Elution	Milli-Q	2 ml
Dilution to running concentration	Milli-Q	Between 2 ml and 5 ml

2.4. Mass spectrometry

Silicon isotopic measurements were performed on a Neptune Plus MC-ICP-MS in dry plasma mode with a DSN-100 desolvating nebulizer introduction system. The aerosol was introduced in the plasma by a silicon torch equipped with a sapphire injector to minimize Si instrumental blank. The mass-spectrometer was run in medium resolution mode with a resolving power of ≈ 7500 which allows to resolve silicon isotope ion beams from polyatomic interferences on the high mass side of the peak plateau (e.g. $^{12}C^{16}O^{+}$ and $^{14}N_2$ on $^{28}Si^{+}$; $^{12}C^{17}O^{+}$, $^{14}N^{15}N^{+}$, $^{12}C^{17}O^{+}$ on $^{29}Si^{+}$; $^{12}C^{18}O^{+}$, $^{14}N^{16}O^{+}$ on $^{30}Si^{+}$). All instrumental parameters were optimized to reach maximum sensitivity, signal stability and signal to noise ratio and the running conditions are given in Table 2. The initial instrumental blank level of about 2 V on mass 28 was lowered to 0.15 V by optimizing the mass spectrometer running parameters. The instrumental mass fractionation was corrected by the sample-standard bracketing method. Silicon isotope compositions are expressed in per mil variation relative to the NBS-28 standard using the following equation with exponent x corresponding to either 29 or 30:

$$\delta^x Si = \left[\frac{\left(\frac{\delta^x Si}{\delta^{28} Si}\right)_{sample}}{\left(\frac{\delta^x Si}{\delta^{28} Si}\right)_{NBS-28}} - 1 \right] \times 1000 \qquad (1)$$

The electronic background level produced by Faraday cup amplifiers was measured over 60s and subtracted prior to each sample measurement. Each sample was measured in one block of 36 cycles with an integration time of 8.389 seconds. An on-peak-zero (OPZ) correction was carried out by measuring the intensities of the three silicon masses in the cleanest 0.002 M HCl wash over 75 seconds before and after each analysis.

The Diatomite was used as a secondary standard at the beginning and within each measurement sequence to ensure the accuracy and mass dependence of the measurements. The well-characterized terrestrial Hawaiian basalt BHVO-2 was also used to assess the reproducibility of our measurements. The $\delta^{30}Si$ for these standards are 1.25 ± 0.16 ‰ (± 2SD, N=429) for the diatomite and -0.28 ± 0.07 ‰ (± 2SD, N=131) for BHVO-2, which is in good agreement with literature data as summarized in Table 5.

Table 2: Instrumental settings for silicon isotope analysis on the Neptune Plus MC-ICP-MS.

Parameter	Neptune Plus
Rf power	1200
Sampler cone	Standard "H"-type, Nickel
Skimmer cone	Jet "X"-type, Nickel
Coolant gas (Ar) flow	16 l/min
Auxiliary gas (Ar) flow	1.23 l/min
Z torch position	2.5 mm
Nebulizer uptake rate	≈ 70 µl/min
Cup configuration	H3: ^{30}Si; C: ^{29}Si; L3: ^{28}Si
Si runing concentration	0.5 ppm
Sensitivity on ^{28}Si beam	≈ 15 V
Instrumental blank	≈ 150 mV
Desolvating device	DSN-100
DSN nebulizer pressure	30 PSI
DSN hot gaz flow	0.2 l/min
DSN membrane gas (Ar) flow	≈ 4 - 5 l/min

3. Results

The silicon isotope compositions for 12 martian meteorites, 1 lunar sample 70017 and the two secondary standards Diatomite and BHVO-2 are reported in Table 3. All measured Si isotope data were

mass dependent and this was used as a validity check. The three-isotope plot, $\delta^{29}Si$ versus $\delta^{30}Si$ yielded a slope of 0.5055 which is consistent with the slopes of equilibrium (0.5178) and kinetic (0.5092) fractionation (Figure 2).

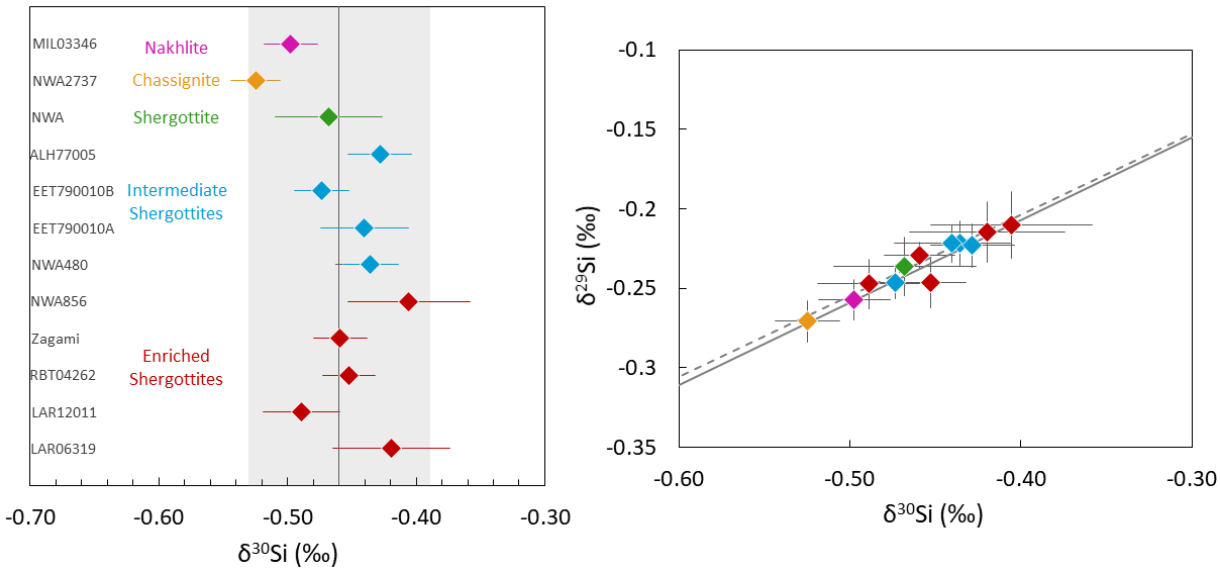

Figure 2: (a) Si isotope composition of the 12 martian meteorites measured in this study. The error bars correspond to the 2SE for each sample. The shaded area corresponds to the 2SD of all samples and shows the limited dispersion of our data. (b) Mass dependence of the Si isotope data in a three-isotope plot (same colours as in (a)). The grey line represents equilibrium fractionation (slope 0.5178) and the dashed line kinetic fractionation (slope 0.5092).

The lunar $\delta^{30}Si$ value of -0.33 ± 0.01 ‰ (2SE, N=12) coincides with recent $\delta^{30}Si$ reported in the literature (Armytage *et al.*, 2012; Fitoussi and Bourdon, 2012; Georg *et al.*, 2007; Zambardi *et al.*, 2013). The $\delta^{30}Si$ values of martian meteorites analysed in this study range from -0.41 to -0.52 ‰ leading to a mean SNC equal to -0.46 ± 0.07 ‰ (2SD, N = 12) in agreement with previous studies (Table 4). Nevertheless, the spread in $\delta^{30}Si$ values of SNC is more limited than in previous studies. The $\delta^{30}Si$ of Nakhlite MIL03346 was previously measured by Zambardi et al. (2013) with a mean of -0.49 ± 0.06 ‰ (2E) close to the value of -0.50 ± 0.02 ‰ (2E) obtained in this study. The enriched shergottite Zagami was also measured by Zambardi et al. (2013) with a $\delta^{30}Si$ value of -0.49 ± 0.05 ‰ (2E) and by (Armytage *et al.*, 2011) with a higher $\delta^{30}Si$ value equal to -0.39 ± 0.04 ‰ (2E). The $\delta^{30}Si$ for Zagami obtained in this study

(-0.46±0.02) is closer to the value given by Zambardi et al. (2013) (-0.49 ± 0.05 ‰ (2E)). The δ^{30}Si value of the Nakhlite MIL03346 (-0.50±0.02) and Chassignite NWA2737 (-0.52±0.02) analysed in this study indicate a slight enrichment in light isotopes compared with the mean of -0.45 ± 0.02 ‰ (2E) of shergottites.

4. Discussion

4.1. Role of core formation on the Si isotope composition of SNC meteorites

Silicon partitioning experiments between metal and silicate have shown that the metal fraction should be enriched in light isotopes, while an enrichment of heavy isotopes was found for the silicate phase (Hin *et al.*, 2014; Javoy *et al.*, 2012; Shahar *et al.*, 2009, 2011). The silicon isotope composition of martian mantle rocks could thus have been shifted due to core formation processes. Temperature, pressure and oxygen fugacity (fO_2) conditions under which martian core formed have been established based on the abundances of siderophile elements in SNC (Righter and Drake, 1996; Righter and Chabot, 2011; Rai and van Westrenen, 2013; Yang *et al.*, 2015). According to these studies, the conditions of Mars core formation were rather oxidizing conditions with a calculated ΔIW (fO_2 relative to the iron-wüstite buffer) of -1.25 at a temperature of ≈ 2400 K. These redox conditions and the moderate temperature of core segregation prevented silicon from entering into the metallic phase in substantial amounts (Gessmann *et al.*, 2001; Kilburn and Wood, 1997; Steenstra *et al.*, 2020). Silicon isotope compositions of SNC were thus not affected by core formation processes.

4.2. Si isotope fractionation during magmatic differentiation

The behaviour of silicon isotopes during magmatic differentiation was reviewed by Savage et al. (2014) who showed a positive slope between silica content and δ^{30}Si for a suite of terrestrial rocks as already suggested by an older study of (Douthitt (1982). As magmatic differentiation occurs, magma becomes more enriched in silica and in heavy isotopes.

Table 3: Silicon isotope data for martian meteorites

	Nature	$\delta^{29}Si$	2SE	$\delta^{30}Si$	2SE	N[1]	SiO_2 (wt%)[2]
Standards							
Diatomite (±2SD)		0.64	0.09	1.25	0.16	429	100
BHVO-2	Hawaïan basalt	-0.16	0.01	-0.29	0.02	43	49.9
Moon							
70017	Ilmenite basalt	-0.16	0.01	-0.33	0.01	12	38.5
Martian Meteorites							
Depleted[3]							
DaG-476	Ol-phyric Shergottite	-0.20	0.03	-0.43	0.03	5	45.4
SaU-005	Ol-phyric Shergottite	-0.21	0.02	-0.45	0.02	5	46.3
Intermediate							
NWA480	Basaltic Shergottite	-0.22	0.01	-0.44	0.02	12	50.3
EET790010A	Basaltic Shergottite	-0.22	0.01	-0.44	0.03	10	51.7
EET790010B	Basaltic Shergottite	-0.25	0.01	-0.47	0.02	12	49.9
ALH77005	Lherzolitic Shergottite	-0.22	0.01	-0.43	0.02	12	41.3
Enriched							
LAR06319	Ol-phyric Shergottite	-0.21	0.02	-0.42	0.05	8	46.7
LAR12011	Ol-phyric Shergottite	-0.25	0.02	-0.49	0.03	12	46.7
RBT04262	Ol-phyric Shergottite	-0.25	0.02	-0.45	0.02	12	47.6
Zagami	Basaltic Shergottite	-0.23	0.01	-0.46	0.02	12	51.2
NWA856	Basaltic shergottite	-0.21	0.02	-0.41	0.05	8	48.9
NWA		-0.24	0.02	-0.47	0.04	18	
NWA2737	Chassignite	-0.27	0.01	-0.52	0.02	17	37
MIL03346	Naklite, cpxnite	-0.26	0.01	-0.50	0.02	26	49.5
Mars average (±2SD)		-0.24	0.04	-0.46	0.07	N=12	

[1] N is the number of measurements of each sample.

[2] Silicon concentration are obtained from the Lunar Sample Compendium for 70017 and the Martian Meteorite Compendium for the SNC and from the United States Geological Survey for BHVO-2.

[3] Silicon isotope data of depleted shergottites are from Zambardi et al. (2013).

Table 4: Comparison of recent Si isotope data for martian meteorites.

Martian mean from	$\delta^{29}Si$	2SD	$\delta^{30}Si$	2SD	Number of samples
This study	-0.24	0.04	-0.46	0.07	N = 12
Pringle et al. (2013)	-0.24	0.04	-0.48	0.07	N = 6
Zambardi et al. (2013)	-0.22	0.08	-0.49	0.09	N = 9
Armytage et al. (2011)	-0.25	0.08	-0.48	0.13	N = 5

Table 5: Silicon isotope composition of Diatomite and BHVO-2 standards from literature and from this study.

	$\delta^{30}Si$	2SD	$\delta^{29}Si$	2SD	N
Diatomite					
Reynolds et al. (2007)	1.26	0.2	0.64	0.14	82
Abraham et al. (2008)	1.25	0.14	0.64	0.1	24
Fitoussi et al. (2009)	1.24	0.19	0.64	0.09	89
Ziegler et al. (2010) [1]	1.22	0.18	0.63	0.008	1
Chakrabarti and Jacobsen (2010)	1.23	0.19	0.61	0.13	41
Savage et al. (2011)	1.23	0.1	0.64	0.08	177
Armytage et al. (2011)	1.23	0.15	0.63	0.1	400
Armytage et al. (2012)	1.23	0.14	0.63	0.09	250
Fitoussi and Bourdon (2012)	1.23	0.21	0.64	0.10	110
Savage and Moynier (2013)	1.22	0.1	0.63	0.06	43
This study	1.25	0.16	0.64	0.09	429
BHVO-2					
Abraham et al. (2008)	-0.29	0.31	-0.17	0.11	8
Fitoussi et al. (2009)	-0.32	0.15	-0.16	0.15	14
Savage et al. (2011)	-0.29	0.09	-0.15	0.08	188
Zambardi and Poitrasson (2011)	-0.27	0.08	-0.14	0.05	360
Armytage et al. (2011)	-0.30	0.09	-0.18	0.07	11
Armytage et al. (2012)	-0.28	0.14	-0.15	0.08	210
Zambardi et al. (2013)	-0.27	0.07	-0.14	0.04	54
Savage and Moynier (2013)	-0.28	0.09	-0.15	0.06	44
Pringle et al. (2013)	-0.28	0.12	-0.15	0.09	26
Pringle et al. (2014)	-0.31	0.12	-0.16	0.08	57
Dauphas et al. (2015) [2]	-0.262	0.053	-0.132	0.037	9
This study	-0.28	0.13	-0.15	0.07	131

[1] Error given as 2SE

[2] Errors given as 95% intervals of the means of 9 analysis

When considering the effect of partial melting, there was no offset between mantle peridotites and the most mafic compositions (i.e. basalts) and mantle peridotites, suggesting that the $\delta^{30}Si$ of basalts were representative of their mantle sources (Armytage *et al.*, 2011; Fitoussi *et al.*, 2009; Zambardi *et al.*, 2013). The variations of the isotope composition of martian meteorites with their silica content do not show a strong correlation (R^2=0.14) (Figure 3). Hence the isotope differences among the samples described either small or even imperceptible variations related to magmatic differentiation or partial melting. Unlike the terrestrial mantle which appears to be homogeneous with respect to Si isotopes, the Martian mantle did not experience global mixing, as suggested by the large range in Nd and Hf isotope systematics, such that the Si isotope variations among the SNC could be inherited from different mantle sources generated by the crystallization of the magma ocean.

4.3. Silicon behaviour during magma ocean crystallisation

The crystallization of a magma ocean in Mars has left W and Nd isotope signatures that clearly indicate that mantle convection did not rehomogenize the martian mantle in its subsequent history. Given that Si isotope have been shown to fractionation between various high pressure minerals and melts (Huang *et al.*, 2014; Méheut and Schauble, 2014; Qin *et al.*, 2016), it is reasonable to investigate whether such signatures can be detected in SNC meteorites.

The mass-dependent inter-mineral silicon isotope fractionation between minerals has been shown to depend on melt polymerization, Si-O bond lengths and Si coordination number in minerals and melts (Huang *et al.*, 2014; Méheut and Schauble, 2014; Qin *et al.*, 2016). Using ab initio methods to calculate the Si isotope fractionation factors between mineral phases crystallizing from a terrestrial magma ocean, Huang et al. (2014) showed that the lower mantle should be lighter than the upper mantle with $\Delta^{30}Si_{\text{upper mantle – lower mantle}}$ = 0.08 ‰ to 0.12 ‰. However, in the case of the Earth's mantle, its more vigorous convection may have erased these early signatures, which is perhaps not the case in Mars. Following an approach similar to Huang et al. (2014), we will investigate the possible effect of magma ocean crystallization on the Si isotope composition of SNC meteorites.

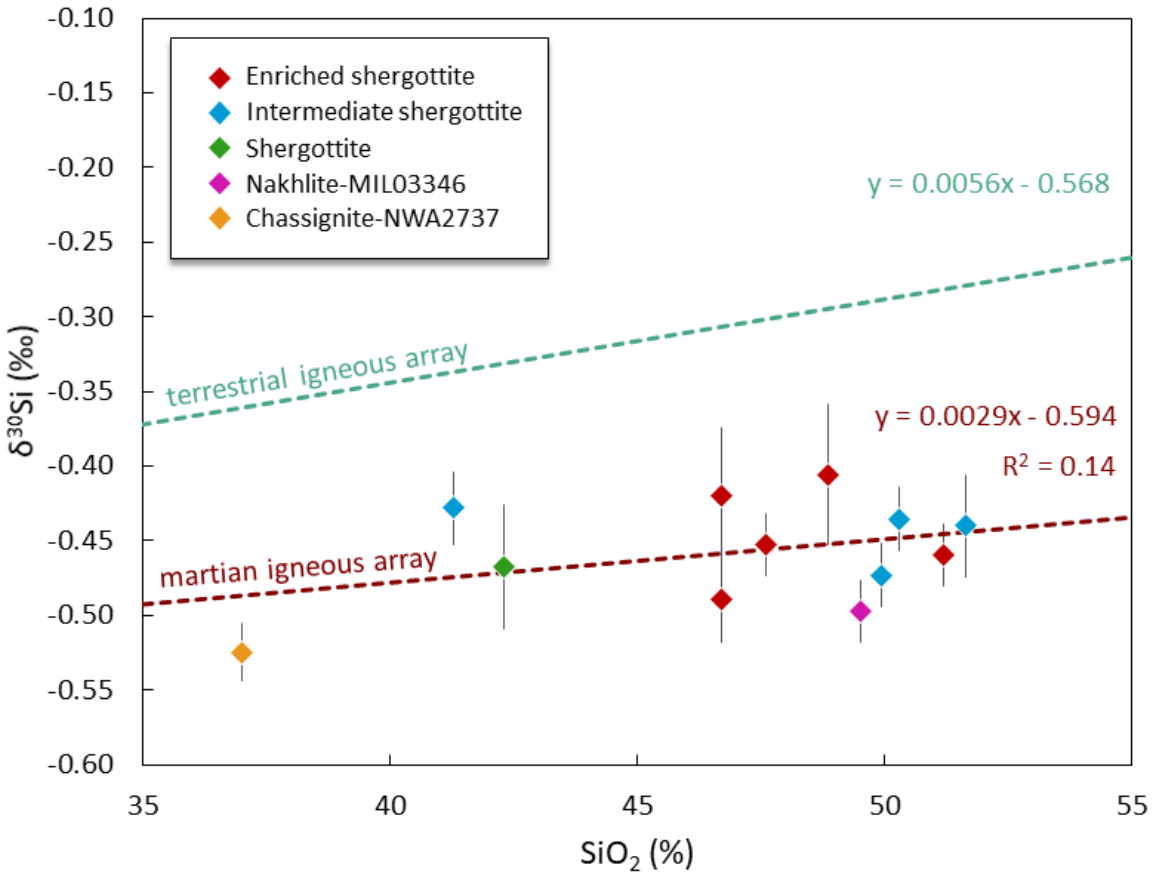

Figure 3: Variation of the Si isotope composition of SNC as a function of silica content. The dotted green line corresponds to the "terrestrial igneous array" defined in *(Savage* et al.*, 2011)*.

4.3.1. Crystallization sequence

Models of magma ocean crystallisation were developed based on the crystallisation sequence described in the studies of Draper et al. (2005) and Elkins-Tanton et al. (2005). Both models involve the crystallization of a ~ 2000 km deep magma ocean and imply mineral phases such as olivine and its high-pressure equivalent (γ-olivine or ringwoodite), pyroxenes (px), garnet and ilmenite (Table 6). A thin layer of perovskite with garnet and magnesiowüstite might be present at the very bottom of the martian mantle (Bertka and Fei, 1997) and its implication on silicon isotopes will also be discussed.

At each crystallization stage, the mineral assemblage is assumed to be in chemical equilibrium with the surrounding melt before being isolated from the residual melt and the melt is assumed to be chemically homogeneous due to vigorous convection of the molten mantle (Elkins-Tanton *et al.*, 2003; Solomatov, 2000). The Si isotope composition of the residual melt R_{melt} was calculated using a mass-balance equation at each crystallisation stage according to:

$$R_0 = F_{melt} \times R_{melt} + \sum_i F_i \times R_i \quad (2)$$

R_0 and R_i are respectively the isotope ratio $^{30}Si/^{28}Si$ of the bulk magma ocean (minerals+melt) and of the mineral i; F_i corresponds to the mass fraction of silicon in mineral i while F_{melt} is the mass fraction of Si in the melt. This mass balance equation can be rewritten with the delta notation to calculate the $\delta^{30}Si$ of the melt and each mineral phase as follows:

$$\delta^{30}Si_{melt} = \delta^{30}Si_0 + \sum_i F_i \times \Delta^{30}Si_{mineral\ i-melt} \quad (3)$$

where

$$\Delta^{30}Si_{mineral\ i-melt} = \delta^{30}Si_{mineral\ i} - \delta^{30}Si_{melt} \quad (4)$$

The initial composition of the magma ocean $\delta^{30}Si_0$ was supposed to be equal to the mean isotope composition of the SNC, i.e. -0.46 ± 0.07 ‰. For the second step of crystallization, $\delta^{30}Si_0$ corresponded to the isotope composition of the residual melt. The $\delta^{30}Si$ of each mineral was calculated from the definition of $\Delta^{30}Si_{mineral\ i-melt}$. The isotope composition of the cumulates were calculated with the following equation:

$$\delta^{30}Si_{cumulate} = \sum_i F_i \times \delta^{30}Si_{mineral\ i} \Big/ \sum_i F_i \quad (5)$$

Table 6: Models of martian magma ocean crystallisation, "pv" is for perovskite (high pressure olivine) and "mw" is for magnesiowüstite (iron and magnesium oxide).

Crystallisation sequence from	Percent solid (%)	Mineral phases
Model 1 ***Elkins-Tanton et al. (2005)***	100 27 22	olivine + px (60:40) garnet ringwoodite + majorite (54:46)
Model 2 ***Draper et al. (2005)***	98 90 65 35 10	cpx + ilmenite (90:10) opx + cpx (60:40) olivine + opx (50:50) olivine + majorite (95:5) majoritic garnet

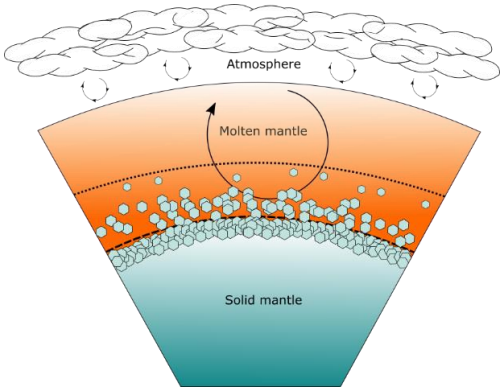

Crystallisation sequence from	Percent solid (%)	Mineral phases
Model 1 + pv	100 27 22 3	olivine + px (60:40) garnet ringwoodite + majorite (54:46) pv + majorite + mw (64:20:16)
Model 2 + pv	98 90 65 35 10 3	cpx + ilmenite (90:10) opx + cpx (60:40) olivine + opx (50:50) olivine + majorite (95:5) majoritic garnet pv + majorite + mw (64:20:16)

The mass fraction of Si in each mineral phase F_i ($m^{Si}_{\min i}$ / m^{Si}_{bulk}) was calculated according to the following equation:

$$F_i = \frac{D_{\min i} \times X_i}{\sum_j \quad D_{\min j} \times X_j + X_{melt}} \qquad (6)$$

The mass fraction of each phase X_j is calculated at each crystallization stage (Table 6). The partition coefficient of silicon between mineral and melt $D_{min\ j}$ was obtained from the literature and are summarized in Table 11 (Borg and Draper, 2003a; Corgne *et al.*, 2005).

4.3.2. Isotope fractionation factor between mineral and melt

Huang et al. (2014) calculated silicon isotope fractionation factors for the following mantle minerals that should be present in the martian mantle: olivine, orthopyroxene, clinopyroxene, majorite and Mg-perovskite using density functional theory. For determining the isotope fractionation between a mineral and a melt, we assumed as in Huang et al. (2014) that a silicate melt contained Si in various coordinations (IV, V and VI) and that the isotope composition between a Si in coordination IV was identical to that of a silicon inside a mineral with a similar coordination. The isotope fractionation coefficient between a mineral i and the surrounding melt was thus calculated according to the following equation:

$$\Delta^{30}Si_{\min i-melt} = f_{IVSi}\Delta^{30}Si_{\min i-IVSi\ melt} + f_{VSi}\Delta^{30}Si_{\min i-VSi\ melt} + f_{VISi}\Delta^{30}Si_{\min i-VISi\ melt} \quad (7)$$

f_{IV}, f_V and f_{VI} are respectively the fractions of Si in the melt with a coordination number (CN) of 4, 5 and 6. The f-values depend on the temperature and pressure conditions and were derived for a peridotitic melt in a recent study by Solomatova and Caracas (2019) at 2000 K, which is close to the average temperature of the martian magma ocean (Plesa *et al.*, 2014). $\Delta^{30}Si_{\min i-IVSi\ melt}$ is the isotope fractionation factor between the mineral and fourfold coordinated Si in the melt, the expressions being similar for a CN of 5 and 6 for Si in the melt. The calculation involves reduced partition function ratio of Si isotopes which cannot be directly obtained by ab initio calculations for a silicate melt. Thus, we assumed as in Huang et al. (2014) that the Si isotope fractionation factor between a mineral and a fourfold coordinated Si in the melt is similar to the fractionation factor between a mineral and a mineral with the same CN in the melt, and so for the CN of 5 and 6. This can be expressed by the following equations (with perov for perovskite):

$$\Delta^{30}Si_{perov-IVSi\ melt} = \Delta^{30}Si_{Si_{perov}-olivine} \quad (8)$$

$$\Delta^{30}Si_{perov-VSi\ melt} = 0.5 \times \Delta^{30}Si_{perov-IVSi\ melt} \quad (9)$$

$$\Delta^{30}Si_{\min i-VISi\ melt} = \Delta^{30}Si_{\min i-perov} \quad (10)$$

The Si isotope fractionation factor between two mineral phases depending on temperature and pressure are calculated via the reduced partition function ratio β, for example for the IV- coordinated Si:

$$\Delta^{30}Si_{\min i-\,IVSi\,melt} = \Delta^{30}Si_{\min i-\,olivine} = 1000(ln\beta_{\min i} - ln\beta_{olivine}) \quad (11)$$

The Si isotope fractionation coefficients were calculated at 0 GPa, 10 GPa and 20 GPa. The temperatures were constrained using the crystallization sequences described in Table 6 and the temperature profile of the magma ocean (Elkins-Tanton *et al.*, 2003; Plesa *et al.*, 2014).

4.3.3. Silicon isotope composition of mantle reservoirs

The results of the two crystallisation models are shown in Figure 4 that shows the Si isotope composition of each mineral phase and of the cumulates, as well as the δ^{30}Si of the residual melt calculated at each crystallisation stage. The two models lead to the formation of widely heterogeneous mantle reservoirs with respect to their silicon isotope compositions. The "high pressure" mineral phases, i.e. majorite and ringwoodite, were enriched in light silicon isotopes compare with the melt, in agreement with isotope fractionation studies of high pressure mineral phases (Huang *et al.*, 2014). Light isotope reservoirs were thus generated at the bottom of the magma ocean with a δ^{30}Si for the cumulates reaching either -0.59 or -0.58 ‰ for model 1 and model 2, respectively (Table 7). Pyroxenes and olivine were isotopically less fractionated compared to the high pressure phases, leading to isotope composition for the last-stage cumulates closer to the initial magma ocean value (-0.46,±0.07). The addition of a perovskite layer of approximately 360 km at the very bottom of the magma ocean representing 3 wt% of solid (Bertka and Fei, 1997) produced cumulates with a very light δ^{30}Si value of -0.82 ‰ (Table 7). The average δ^{30}Si of our samples ranged between -0.41 to -0.52 ‰ which means that their composition overlaps with that of the calculated δ^{30}Si of cumulates, except for perovskite-bearing cumulates. To better constrain the correspondance between SNC compositions with specific

mantle reservoirs, we used our magma ocean crystallisation model to calculate the trace element signature in the crystallized magma ocean.

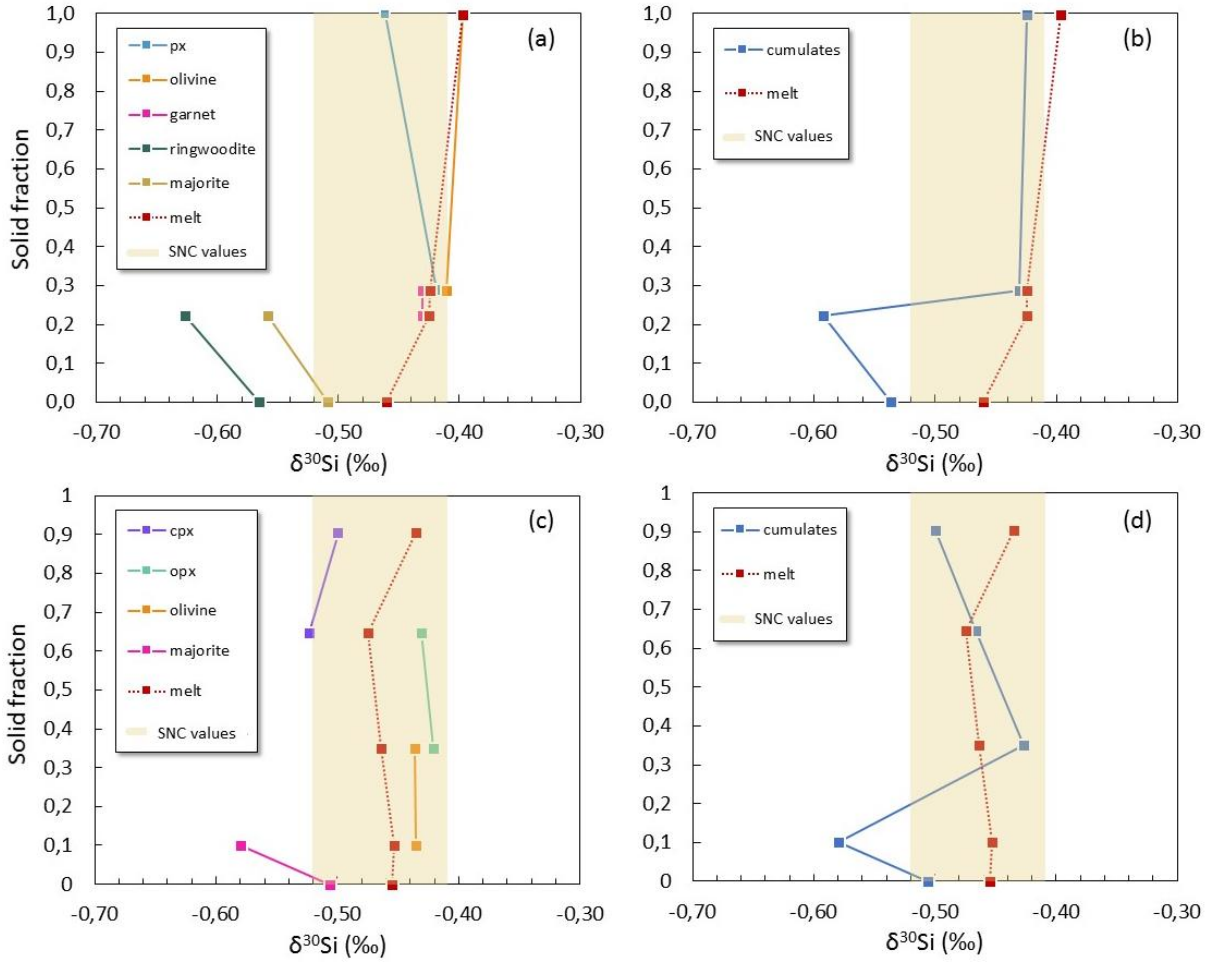

Figure 4 : Silicon isotope composition of martian mantle after magma ocean crystallisation. (a) Individual minerals using Model 1 based on the crystallisation sequence of Elkins-Tanton (2005) and (b) δ^{30}Si of cumulates. (c) Individual minerals using Model 2 based on the crystallisation sequence of Draper et al. (2005) and (d) δ^{30}Si of cumulates. The vertical axis corresponds to the crystallized fraction. The shaded area represents the range of δ^{30}Si variation of the SNC.

4.4. Incompatible element behavior during magma ocean crystallisation

Elemental ratios of incompatible trace elements can be useful tracers of magma ocean crystallization, as the high pressure phase typical of magma ocean crystallization may impart signature that differ from those of typical mantle-crust evolution (Kato et al. 1988; Caro et al. 2005; Rizo et al. 2011; Jackson

et al. 2014). In order to assess the effect of magma ocean crystallization on Mars, the partitioning of selected trace elements at each magma ocean crystallization stage was calculated using the same formalism as described in section 4.3. The composition of each mineral phase with the resulting cumulate and of the residual melt was calculated following the crystallisation sequences described in Table 6 using crystal-melt partition coefficients determined in previous studies (Borg and Draper, 2003b; Corgne *et al.*, 2005, 2012; Corgne and Wood, 2004; Dunn and Sen, 1994; Mallmann and O'Neill, 2009).

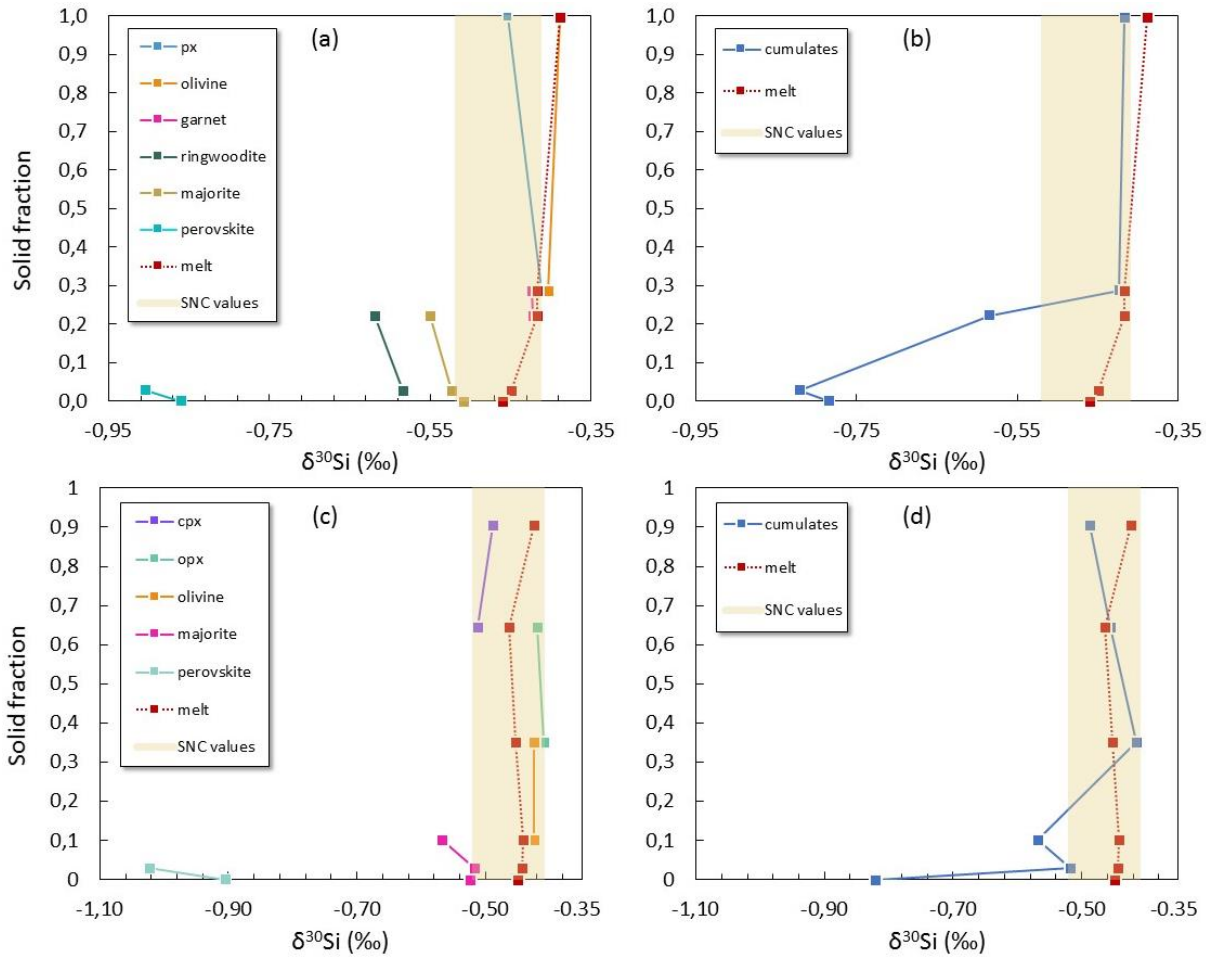

Figure 5: Silicon isotope composition of martian mantle based on our crystallisation model with a perovskite layer added at the beginning of the crystallisation sequences of Elkins-Tanton (2005) (a and b) and Draper et al. (2005) (c and d). (a) and (c) δ^{30}Si values calculated for each mineral phase; (b) and (d) δ^{30}Si values for the corresponding cumulates. The shaded area represents the range of δ^{30}Si variation of the SNC.

Table 7 : Isotope composition of the martian mantle calculated from the models developed in this study, each crystallisation stage is numbered according to the corresponding crystallisation sequence (see text for details).

	Model 1		Model 1 + pv	
	δ^{30}Si cumulate (‰)	δ^{30}Si melt (‰)	δ^{30}Si cumulate (‰)	δ^{30}Si melt (‰)
Stage 4			-0.42	-0.39
Stage 3	-0.42	-0.40	-0.42	-0.42
Stage 2	-0.43	-0.42	-0.58	-0.42
Stage 1	-0.59	-0.42	-0.82	-0.45

	Model 2		Model 2 + pv	
	δ^{30}Si cumulate (‰)	δ^{30}Si melt (‰)	δ^{30}Si cumulate (‰)	δ^{30}Si melt (‰)
Stage 6			-0.49	-0.42
Stage 5	-0.50	-0.44	-0.46	-0.46
Stage 4	-0.47	-0.47	-0.42	-0.45
Stage 3	-0.43	-0.46	-0.57	-0.44
Stage 2	-0.58	-0.45	-0.52	-0.44
Stage 1	-0.51	-0.46	-0.82	-0.45

For example, the concentration of Nd in a mineral i $C_{min\,i}^{Nd}$ was calculated as:

$$C_{min\,i}^{Nd} = D_{min\,i}^{Nb} \times C_0^{Nd} / \left(\sum_i X_i \times C_{min\,i}^{Nd} + X_{melt} \right) \quad (12)$$

with

$$C_{melt}^{Nd} = C_{min\,i}^{Nd} / D_{min\,i}^{Nd} \quad (13)$$

and X_i representing the mass fraction of each phase; $D_{min\,i}^{Nd}$ the partition coefficient of Nd between a mineral i and the melt; C_0^{Nd} the initial concentration of Nd of the magma ocean (Taylor, 2013) for the

first crystallisation stage and of the residual melt for the following crystallisation stages. By analogy with the calculation of the isotope compositions of the cumulates, the distribution of REE in the cumulates was calculated as follows:

$$C_{cumulates}^{Nd} = \sum_i X_i \times C_{min\,i}^{Nd} \; / \sum_i X_i \qquad (14)$$

The shergottites were classified in three subgroups depending on their incompatible element contents relative to the bulk silicate mars (BSM): enriched, intermediate and depleted (Borg and Draper, 2003b; Symes *et al.*, 2008). The trace element signature of SNC meteorites was interpreted either as linked to mantle-crust differentiation (Jones, 1989) or to the existence of distinct mantle reservoirs (Blichert-Toft *et al.*, 1999; Day *et al.*, 2018; Symes *et al.*, 2008). The nakhlite and chassignite were supposed to share the same mantle source which is distinct from the shergottite mantle sources (McCubbin *et al.*, 2013; Udry and Day, 2018). In what follows, we will examine the behaviour of the Sm/Nd ratio through magma ocean crystallisation to trace SNC mantle sources.

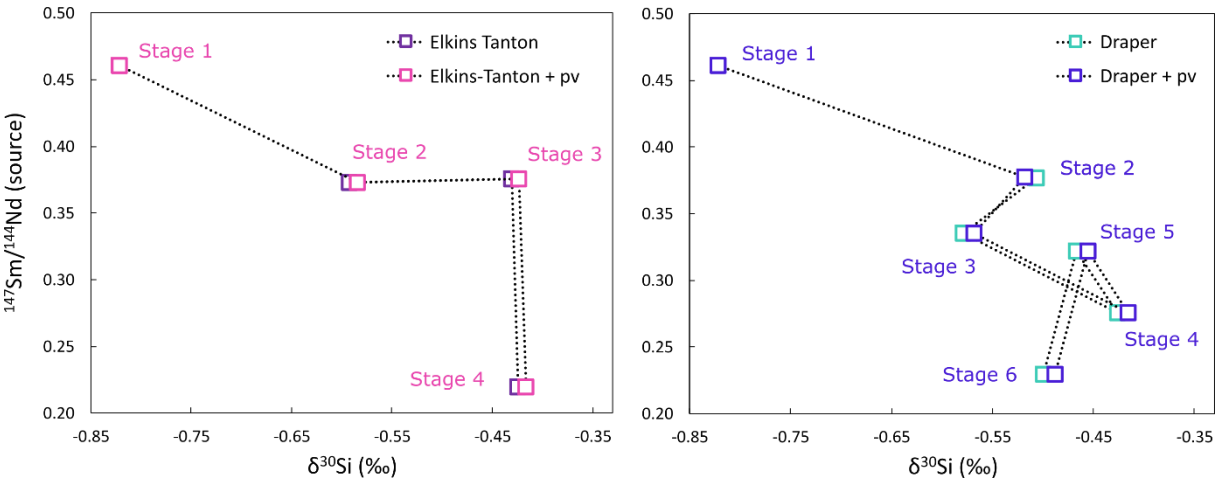

Figure 6: Silicon isotope composition and Sm/Nd ratio calculated from the different developed models. Details of the crystallisation stages are given in Table 6.

As Sm is more compatible than Nd, it is expected that the effect of magma ocean crystallization will be to decrease the Sm/Nd ratio. This is in good agreement with the trend observed for the Sm/Nd ratio of cumulates during magma ocean crystallisation of the four different models (Figure 6). In order to

examine the effect of magma ocean crystallization on the Sm/Nd ratio, one needs to take into account the role of more recent magmatic processes such as partial melting or magma differentiation. Thus, rather than using the Sm/Nd measured in the SNC meteorites, we calculated the integrated Sm/Nd ratio of its mantle source. First , the present day $^{143}Nd/^{144}Nd$ isotope ratio, together with the measured $^{147}Sm/^{144}Nd$ (Borg *et al.*, 2016; Borg and Draper, 2003b; Caro *et al.*, 2008; Nyquist and Reese, 2009; Kruijer *et al.*, 2017) and crystallisation age of the sample (see Supplementary Materials) are used to calculate the $^{143}Nd/^{144}Nd$ isotope composition at the time of eruption (formation):

$$\frac{^{143}Nd}{^{143}Nd}_{present} = \frac{^{143}Nd}{^{144}Nd}_{T_{erupt}} + \frac{^{147}Sm}{^{144}Nd}\left(e^{\lambda T_{erupt}} - 1\right) \quad (15)$$

Hence:

$$\frac{^{143}Nd}{^{144}Nd}_{T_{erupt}} = \frac{^{143}Nd}{^{143}Nd}_{present} - \frac{^{147}Sm}{^{144}Nd}\left(e^{\lambda T_{erupt}} - 1\right) \quad (16)$$

We now assume that this sample evolved from a chondritic Nd isotope composition starting from the beginning of the Solar System at 4568 Ma (Bouvier and Wadhwa, 2010) until the time of eruption (T_{erupt}):

$$\frac{^{143}Nd}{^{144}Nd}_{T_{erupt}} = \frac{^{143}Nd}{^{144}Nd}_{T0} + \frac{^{147}Sm}{^{144}Nd}_{source}\left(e^{\lambda T_0} - e^{\lambda T_{erupt}}\right)$$

From these equations, it is possible to derive the Sm/Nd ratio of the source of SNC meteorite sample:

$$\frac{^{147}Sm}{^{144}Nd}_{source} = \frac{\frac{^{143}Nd}{^{144}Nd}_{T_{erupt}} - \frac{^{143}Nd}{^{144}Nd}_{T_0}}{e^{\lambda T_0} - e^{\lambda T_{erupt}}}$$

The calculated $^{147}Sm/^{144}Nd$ ratio of the SNC sources are given in Table 8 and these ratios are plotted as a function of $\delta^{30}Si$ in Figure 7. The Sm/Nd ratio of the sources of intermediate shergottites, nakhlite sample MIL03346 and chassignite sample NWA2737 show a negative correlation with their $\delta^{30}Si$, which is in agreement with the negative trend observed between the different mantle sources (see Figure 6).

Thus, the measured $\delta^{30}Si$ variations in these mantle-derived samples can be attributed to magma ocean crystallisation rather than magmatic differentiation, which is consistent with the lack of a correlation between the $\delta^{30}Si$ and the SiO_2 concentrations.

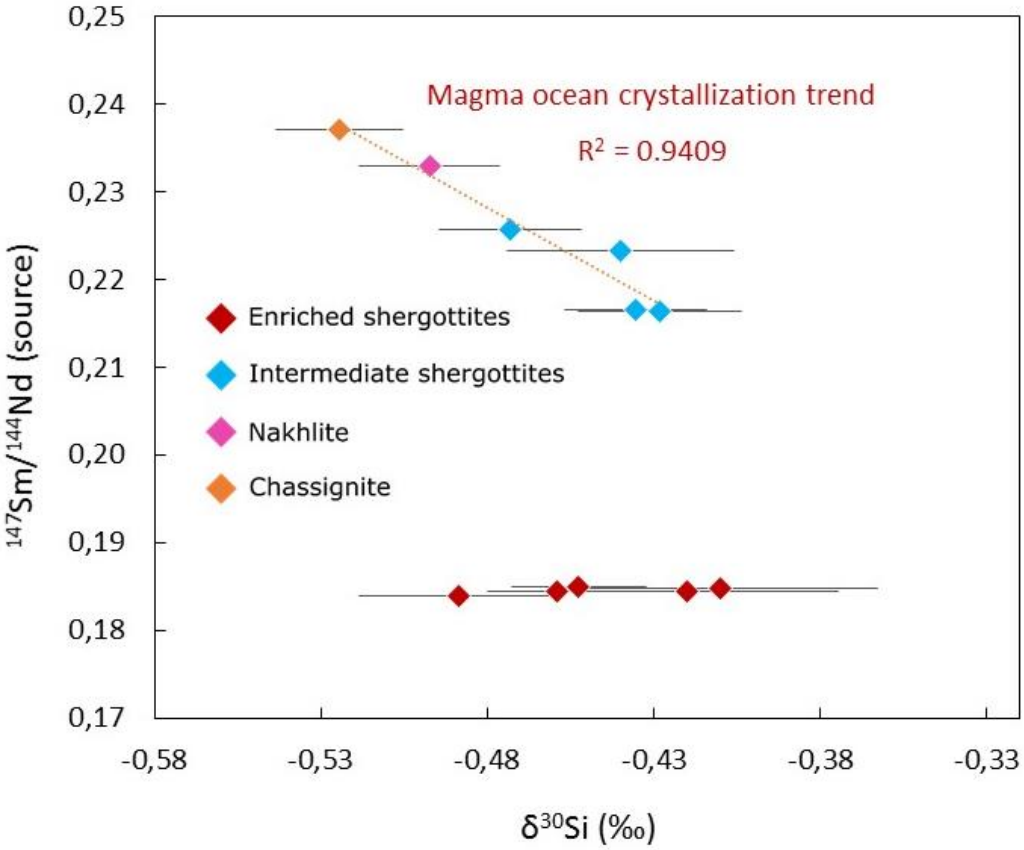

Figure 7: Variation of silicon isotope compositions of SNC with the Sm/Nd of their mantle sources. The dotted line corresponds to a linear correlation between the intermediate shergottites, the nakhlite sample MIL03346 and the chassignite sample NWA2737 (R^2=0.94).

In contrast, the enriched shergottites display a constant Sm/Nd source value while $\delta^{30}Si$ values are variable. The constant Sm/Nd ratio of the enriched shergottites indicates that the variability of their $\delta^{30}Si$ must be ascribed to a process unrelated to magma ocean crystallization. As enriched shergottites represent crustal reservoirs, their long-term Si isotope evolution could have been affected by a different set of processes compared with mantle reservoirs. For example, one could speculate that fluid-rock interactions could have modified Si isotopes during recent events with affecting the long

term Sm/Nd systematics. Enriched shergottites are known to be more oxidized than depleted shergottites and this property may indirectly affect Si isotope evolution. It has been shown that silicate polymerization is modified by the redox state of magmas (e.g. Mysen *et al.*, 1984) with oxidized magma being more depolymerized. There is a weak correlation between V/Sc ratios, an indicator of redox state (Lee *et al.*, 2005; Mallmann and O'Neill, 2009) and δ^{30}Si values (Figure 8), which could lend some credence to this hypothesis. It has been documented that enriched shergottites are characterized by greater fO_2 (Herd, 2003). Thus; one could imagine that the corresponding modification of melt structure directly affecting the bond length of Si-O in the melt could directly impact the δ^{30}Si of magmas. The observed δ^{30}Si variations are small, which means that such an effect was perhaps not detected in previous studies.

Table 8: Calculated $^{147}Sm/^{144}Nd$ present-day ratios of the sources, sh-shergottite, ol phyr-olivine-phyric, lh-lherzolitic and interm for intermediate.

Sample name	Type	$^{147}Sm/^{144}Nd$ (source)
LAR06319	enriched-ol phyr sh	0.1845
LAR12011	enriched-ol phyr sh	0.1840
RBT04262	enriched-ol phyr sh	0.1849
Zagami	enriched-sh	0.1844
NWA856	enriched-sh	0.1849
ALH77005	interm-lh sh	0.2164
NWA480	interm-sh	0.2166
EET790010A	interm-sh	0.2234
EET790010B	interm-sh	0.2258
MIL03346	nakhlite	0.2330
NWA2737	chassignite	0.2371

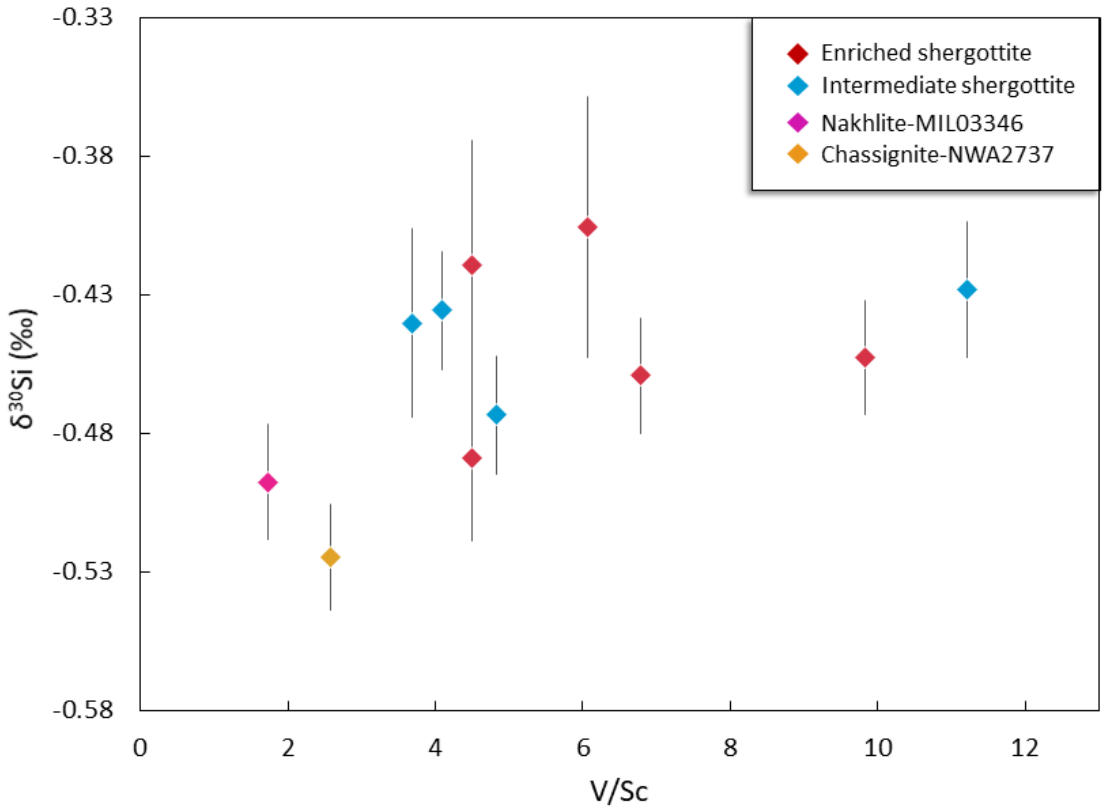

Figure 8 : Variation of δ^{30}Si of SNC as a function of their V/Sc ratio. The smooth trend suggests a relationship between Si silicon composition and oxidation state of SNC (see main text for details).

Overall, our results suggest that mante derived shergottites do carry a δ^{30}Si signature that may reflect the early crystallization of a magma ocean, as it correlates with the Sm/Nd of their mantle source. Unfortunately, there is not enough ^{182}W data for our samples to further document such an inference. In contrast, the enriched shergottites may have been affected by a different set of processes that could be related to the more oxidized nature of these samples or to fluid-rock interactions if the source of these samples was indeed in the martian crust.

5. Conclusions

The Si isotope composition of SNC meteorites shows a small but resolvable variation with δ^{30}Si values ranging between -0.41 and -0.52 ‰. These Si isotope variations do not correlate with indicators of magma differentiation and thus considered to play little role in the observed variations. Similarly the

δ^{30}Si values show no correlation with indicators of volatile element loss that could be observed if there had been volatile SiO loss during an early magma ocean vaporization.

Thus, we have explored whether the crystallization of a magma ocean could explain the small δ^{30}Si variations. First, the crystallization in the presence of perovskite at the bottom of the Martian mantle should have produced much large δ^{30}Si than what is observed. Our observations are thus consistent with the recent finding of a large core for Mars, precluding the stability of perovskite near the core mantle boundary. As all the SNC rocks have a rather complex history there are no simple correlation with major element variations. However, we did find a correlation with our $^{147}Sm/^{144}Nd$ estimates of the SNC mantle sources with δ^{30}Si for the most depleted samples, while the enriched rocks showed no trend. This correlation is attributed to changes in Si coordination in high pressure minerals formed during magma ocean crystallization, relative to the mean coordination of the silicate melt in equilibrium with these minerals. The crustal-derived samples displayed a large range of δ^{30}Si values despite a constant Sm/Nd ratio. This singular behaviour was attributed either to Si isotope fractionation related to change in coordination in the derived enriched melts or to fluid-rock interactions.

More data on the most depleted shergottites and on a common data set including Hf/W data would be useful to fully assess our inferences regarding the role of a magma ocean on the Si isotope signature of martian rocks.

References

Armytage, R.M.G., Georg, R.B., Savage, P.S., Williams, H.M., Halliday, A.N. (2011) Silicon isotopes in meteorites and planetary core formation. *Geochimica et Cosmochimica Acta* 75, 3662–3676.

Armytage, R.M.G., Georg, R.B., Williams, H.M., Halliday, A.N. (2012) Silicon isotopes in lunar rocks: Implications for the Moon's formation and the early history of the Earth. *Geochimica et Cosmochimica Acta* 77, 504–514.

Bellucci, J.J., Nemchin, A.A., Whitehouse, M.J., Snape, J.F., Bland, P., Benedix, G.K. (2015) The Pb isotopic evolution of the Martian mantle constrained by initial Pb in Martian meteorites. *Journal of Geophysical Research* 17.

Bertka, C.M., Fei, Y. (1997) Mineralogy of the Martian interior up to core-mantle boundary pressures. *Journal of Geophysical Research: Solid Earth* 102, 5251–5264.

Blichert-Toft, J., Gleason, J.D., Télouk, P., Albarède, F. (1999) The Lu–Hf isotope geochemistry of shergottites and the evolution of the Martian mantle–crust system. *Earth and Planetary Science Letters* 173, 25–39.

Bogard, D.D., Johnson, P. (1983) Martian Gases in an Antarctic Meteorite? Science 221, 651–654.

Borg, L.E., Brennecka, G.A., Symes, S.J.K. (2016) Accretion timescale and impact history of Mars deduced from the isotopic systematics of martian meteorites. *Geochimica et Cosmochimica Acta* 175, 150–167.

Borg, L.E., Draper, D.S. (2003b) A petrogenetic model for the origin and compositional variation of the martian basaltic meteorites. *Meteoritics & Planetary Science* 38, 1713–1731.

Bouvier, A., Wadhwa, M. (2010) The age of the Solar System redefined by the oldest Pb–Pb age of a meteoritic inclusion. *Nature Geoscience* 3, 637–641.

Bouvier, L.C. *et al.* (2018) Evidence for extremely rapid magma ocean crystallization and crust formation on Mars. *Nature* 558, 586–589.

Breuer, D., Spohn, T. (2003) Early plate tectonics versus single-plate tectonics on Mars: Evidence from magnetic field history and crust evolution. *Journal of Geophysical Research* 108, 5072.

Caro, G., Bourdon, B., Halliday, A.N., Quitté, G. (2008) Super-chondritic Sm/Nd ratios in Mars, the Earth and the Moon. *Nature* 452, 336–339.

Clayton, R.N., Mayeda, T.K. (1983) Oxygen isotopes in eucrites, shergottites, nakhlites, and chassignites. *Earth and Planetary Science Letters* 62, 1–6.

Corgne, A., Armstrong, L.S., Keshav, S., Fei, Y., McDonough, W.F., Minarik, W.G., Moreno, K. (2012) Trace element partitioning between majoritic garnet and silicate melt at 10–17GPa: Implications for deep mantle processes. *Lithos* 148, 128–141.

Corgne, A., Liebske, C., Wood, B.J., Rubie, D.C., Frost, D.J. (2005) Silicate perovskite-melt partitioning of trace elements and geochemical signature of a deep perovskitic reservoir. *Geochimica et Cosmochimica Acta* 69, 485–496.

Corgne, A., Wood, B.J. (2004) Trace element partitioning between majoritic garnet and silicate melt at 25GPa. *Physics of the Earth and Planetary Interiors* 143–144, 407–419.

Dauphas, N., Poitrasson, F., Burkhardt, C., Kobayashi, H., Kurosawa, K. (2015) Planetary and meteoritic Mg/Si and δ30Si variations inherited from solar nebula chemistry. *Earth and Planetary Science Letters* 427, 236–248.

Day, J.M.D., Moynier, F. (2014) Evaporative fractionation of volatile stable isotopes and their bearing on the origin of the Moon. *Philosophical Transactions of the Royal Society A: Mathematical, Physical and Engineering Sciences* 372, 20130259.

Day, J.M.D., Tait, K.T., Udry, A., Moynier, F., Liu, Y., Neal, C.R. (2018) Martian magmatism from plume metasomatized mantle. *Nature Communications* 9, 4799.

Debaille, V., Brandon, A.D., Yin, Q.Z., Jacobsen, B. (2007) Coupled ^{142}Nd–^{143}Nd evidence for a protracted magma ocean in Mars. *Nature* 450, 525–528.

Douthitt, C.B. (1982) The geochemistry of the stable isotopes of silicon. *Geochimica et Cosmochimica Acta* 46, 1449–1458.

Draper, D.S., Borg, L.E., Agee, C.B. (2005) Crystallization of a Martian Magma Ocean and the Formation of Shergottite Source Regions: A Less Fe-rich Mars? 36th Annual Lunar and Planetary Science Conference, abstract no.1429.

Dunn, T., Sen, C. (1994) Mineral/matrix partition coefficients for orthopyroxene, plagioclase, and olivine in basaltic to andesitic systems: A combined analytical and experimental study. *Geochimica et Cosmochimica Acta* 58, 717–733.

Elkins-Tanton, L.T. (2005) Possible formation of ancient crust on Mars through magma ocean processes. *Journal of Geophysical Research* 110, E12S01.

Elkins-Tanton, L.T. (2012) Magma Oceans in the Inner Solar System. *Annual Review of Earth and Planetary Sciences* 40, 113–139.

Elkins-Tanton, L.T., Parmentier, E.M., Hess, P.C. (2003) Magma ocean fractional crystallization and cumulate overturn in terrestrial planets: Implications for Mars. *Meteoritics & Planetary Science* 38, 1753–1771.

Fitoussi, C., Bourdon, B. (2012) Silicon isotope evidence against an enstatite chondrite Earth. *Science* 335, 1477–1480.

Fitoussi, C., Bourdon, B., Kleine, T., Oberli, F., Reynolds, B.C. (2009) Si isotope systematics of meteorites and terrestrial peridotites: implications for Mg/Si fractionation in the solar nebula and for Si in the Earth's core. *Earth and Planetary Science Letters* 287, 77–85.

Foley, C.N., Wadhwa, M., Borg, L.E., Janney, P.E., Hines, R., Grove, T.L. (2005) The early differentiation history of Mars from 182W-142Nd isotope systematics in the SNC meteorites. *Geochimica et Cosmochimica Acta* 69, 4557–4571.

Georg, R.B., Halliday, A.N., Schauble, E.A., Reynolds, B.C. (2007) Silicon in the Earth's core. *Nature* 447, 1102–1106.

Georg, R.B., Reynolds, B.C., Frank, M., Halliday, A.N. (2006) New sample preparation techniques for the determination of Si isotopic compositions using MC-ICPMS. *Chemical Geology* 235, 95–104.

Gessmann, C.K., Wood, B.J., Rubie, D.C., Kilburn, M.R. (2001) Solubility of silicon in liquid metal at high pressure: implications for the composition of the Earth's core. *Earth and Planetary Science Letters* 184, 367–376.

Goodrich, C.A. (2002) Olivine-phyric martian basalts: A new type of shergottite. *Meteoritics & Planetary Science* 37, B31–B34.

Harper, C.L.H., Nyquist, L.E., Bansal, B., Wiesmann, H., Shih, C.-Y. (1995) Rapid Accretion and Early Differentiation of Mars Indicated by $^{142}Nd/^{144}Nd$ in SNC Meteorites. 267, 5.

Herd, C.D.K. (2003) The oxygen fugacity of olivine-phyric martian basalts and the components within the mantle and crust of Mars. *Meteoritics & Planetary Science* 38, 1793–1805.

Hin, R.C. *et al.* (2017) Magnesium isotope evidence that accretional vapour loss shapes planetary compositions. *Nature* 549, 511–515.

Hin, R.C., Fitoussi, C., Schmidt, M.W., Bourdon, B. (2014) Experimental determination of the Si isotope fractionation factor between liquid metal and liquid silicate. *Earth and Planetary Science Letters* 387, 55–66.

Huang, F., Wu, Z., Huang, S., Wu, F. (2014) First-principles calculations of equilibrium silicon isotope fractionation among mantle minerals. *Geochimica et Cosmochimica Acta* 140, 509–520.

Javoy, M., Balan, E., Méheut, M., Blanchard, M., Lazzeri, M. (2012) First-principles investigation of equilibrium isotopic fractionation of O- and Si-isotopes between refractory solids and gases in the solar nebula. *Earth and Planetary Science Letters* 319–320, 118–127.

Jones, J.H. (1989) Isotopic relationships among the shergottites, the nakhlites and Chassigny. *Lunar and Planetary Science Conference Proceedings* 19, 465–474.

Jones, J.H. (2003) Constraints on the structure of the martian interior determined from the chemical and isotopic systematics of SNC meteorites. *Meteoritics & Planetary Science* 38, 1807–1814.

Kato, C., Moynier, F., Valdes, M.C., Dhaliwal, J.K., Day, J.M.D. (2015) Extensive volatile loss during formation and differentiation of the Moon. *Nature Communications* 6, 7617.

Kilburn, M.R., Wood, B.J. (1997) Metal–silicate partitioning and the incompatibility of S and Si during core formation. *Earth and Planetary Science Letters* 152, 139–148.

Kruijer, T.S., Borg, L.E., Wimpenny, J., Sio, C.K. (2020) Onset of magma ocean solidification on Mars inferred from Mn-Cr chronometry. *Earth and Planetary Science Letters* 542, 116315.

Kruijer, T.S., Kleine, T., Borg, L.E., Brennecka, G.A., Irving, A.J., Bischoff, A., Agee, C.B. (2017) The early differentiation of Mars inferred from Hf–W chronometry. *Earth and Planetary Science Letters* 474, 345–354.

Lee, C.-T.A., Leeman, W.P., Canil, D., Li, Z.X.A. (2005) Similar V/Sc systematics in MORBs and arc basalts: Implications for the oxygen fugacities of their mantle source regions. *Geochimica et Cosmochimica Acta Supplement* 69, A639.

Magna, T., Hu, Y., Teng, F.-Z., Mezger, K. (2017) Magnesium isotope systematics in Martian meteorites. *Earth and Planetary Science Letters* 474, 419–426.

Mallmann, G., O'Neill, H.St.C. (2009) The Crystal/Melt Partitioning of V during Mantle Melting as a Function of Oxygen Fugacity Compared with some other Elements (Al, P, Ca, Sc, Ti, Cr, Fe, Ga, Y, Zr and Nb). *Journal of Petrology* 50, 1765–1794.

McCubbin, F.M., Elardo, S.M., Shearer, C.K., Smirnov, A., Hauri, E.H., Draper, D.S. (2013) A petrogenetic model for the comagmatic origin of chassignites and nakhlites: Inferences from chlorine-rich minerals, petrology, and geochemistry. *Meteoritics & Planetary Science* 48, 819–853.

McSween, H.Y. (1994) What we have learned about Mars from SNC meteorites. *Meteoritics* 29, 757–779.

McSween, H.Y., McLennan, S.M. (2014) 2.10 - Mars. In: Holland, H.D., Turekian, K.K. (eds) *Treatise on Geochemistry (Second Edition)*. Elsevier, Oxford, 251–300.

Méheut, M., Schauble, E.A. (2014) Silicon isotope fractionation in silicate minerals: Insights from first-principles models of phyllosilicates, albite and pyrope. *Geochimica et Cosmochimica Acta* 134, 137–154.

Mysen, O.B., Virgo, D., Seifert, F.A. (1984) Redox equilibria of iron in alkaline earth silicate melts: relationships between melt structure, oxygen fugacity, temperature and properties of iron-bearing silicate liquids. 69, 834–847.

Nimmo, F., Kleine, T. (2007) How rapidly did Mars accrete? Uncertainties in the Hf–W timing of core formation. *Icarus* 191, 497–504.

Nyquist, L.E., Reese, Y. (2009) Rb-Sr and Sm-Nd studies of olivine-phyric shergottites RBT 04262 AND LAR 06319: isotopic evidence for relationship to enriched basaltic shergottites. 40th Lunar and Planetary Science Conference, (Lunar and Planetary Science XL), 2.

Papike, J.J., Karner, J.M., Shearer, C.K., Burger, P.V. (2009) Silicate mineralogy of martian meteorites. *Geochimica et Cosmochimica Acta* 73, 7443–7485.

Plesa, A.-C., Tosi, N., Breuer, D. (2014) Can a fractionally crystallized magma ocean explain the thermo-chemical evolution of Mars? *Earth and Planetary Science Letters* 403, 225–235.

Pringle, E.A., Savage, P.S., Badro, J., Barrat, J.-A., Moynier, F. (2013) Redox state during core formation on asteroid 4-Vesta. *Earth and Planetary Science Letters* 373, 75–82.

Qin, T., Wu, F., Wu, Z., Huang, F. (2016) First-principles calculations of equilibrium fractionation of O and Si isotopes in quartz, albite, anorthite, and zircon. *Contributions to Mineralogy and Petrology* 171, 91.

Rai, N., van Westrenen, W. (2013) Metal-Silicate Partitioning of Siderophile Elements: Application to Core-mantle differentiation in Mars. *Journal of Geophysical Research: Planets* 118, 1195–1203.

Reese, C., Solomatov, V. (2006) Fluid dynamics of local martian magma oceans. *Icarus* 184, 102–120.

Righter, K., Chabot, N.L. (2011) Moderately and slightly siderophile element constraints on the depth and extent of melting in early Mars: Siderophile elements and core formation on Mars. *Meteoritics & Planetary Science* 46, 157–176.

Righter, K., Drake, M.J. (1996) Core Formation in Earth's Moon, Mars, and Vesta. *Icarus* 124, 513–529.

Savage, P.S., Armytage, R.M.G., Georg, R.B., Halliday, A.N. (2014) High temperature silicon isotope geochemistry. *Lithos* 190–191, 500–519.

Savage, P.S., Georg, R.B., Williams, H.M., Burton, K.W., Halliday, A.N. (2011) Silicon isotope fractionation during magmatic differentiation. *Geochimica et Cosmochimica Acta* 75, 6124–6139.

Schaefer, L., Elkins-Tanton, L.T. (2018) Magma oceans as a critical stage in the tectonic development of rocky planets. *Philosophical Transactions of the Royal Society A: Mathematical, Physical and Engineering Sciences* 376, 20180109.

Shahar, A., Hillgren, V.J., Young, E.D., Fei, Y., Macris, C.A., Deng, L. (2011) High-temperature Si isotope fractionation between iron metal and silicate. *Geochimica et Cosmochimica Acta* 75, 7688–7697.

Shahar, A., Ziegler, K., Young, E.D., Ricolleau, A., Schauble, E.A., Fei, Y. (2009) Experimentally determined Si isotope fractionation between silicate and Fe metal and implications for Earth's core formation. *Earth and Planetary Science Letters* 288, 228–234.

Solomatov, V.S. (2000) *Fluid Dynamics of a Terrestrial Magma Ocean*. *Origin of the Earth and Moon*, 323–338.

Solomatov, V.S. (2007) Magma Oceans and Primordial Mantle Differentiation. *Treatise on Geophysics*, 91–119.

Solomatova, N.V., Caracas, R. (2019) Pressure-Induced Coordination Changes in a Pyrolitic Silicate Melt from Ab Initio Molecular Dynamics Simulations. *Journal of Geophysical Research: Solid Earth* 124, 11232–11250.

Sossi, P.A., Nebel, O., Anand, M., Poitrasson, F. (2016) On the iron isotope composition of Mars and volatile depletion in the terrestrial planets. *Earth and Planetary Science Letters* 449, 360–371.

Steenstra, E.S., Seegers, A.X., Putter, R., Berndt, J., Klemme, S., Matveev, S., Bullock, E.S., van Westrenen, W. (2020) Metal-silicate partitioning systematics of siderophile elements at reducing conditions: A new experimental database. *Icarus* 335, 113391.

Stolper, E., McSween, H.Y., Hays, J.F. (1979) A petrogenetic model of the relationships among achondritic meteorites. *Geochimica et Cosmochimica Acta* 43, 589–602.

Symes, S.J.K., Borg, L.E., Shearer, C.K., Irving, A.J. (2008) The age of the martian meteorite Northwest Africa 1195 and the differentiation history of the shergottites. *Geochimica et Cosmochimica Acta* 72, 1696–1710.

Tang, H., Young, E.D. (2020) Evaporation from the Lunar Magma Ocean Was Not the Mechanism for Fractionation of the Moon's Moderately Volatile Elements. *The Planetary Science Journal* 1, 49.

Taylor, G.J. (2013) The bulk composition of Mars. *Geochemistry* 73, 401–420.

Terasaki, H., Rubie, D.C., Mann, U., Frost, D., Langenhorst, F. (2005) The Effects of Oxygen, Sulphur and Silicon on the Dihedral Angles Between Fe-rich Liquid Metal and Olivine, Ringwoodite and Silicate Perovskite: Implications for Planetary Core Formation. 36th Annual Lunar and Planetary Science Conference 2005 1129.

Treiman, A.H., Gleason, J.D., Bogard, D.D. (2000) The SNC meteorites are from Mars. *Planetary and Space Science* 48, 1213–1230.

Udry, A., Day, J.M.D. (2018) 1.34 billion-year-old magmatism on Mars evaluated from the co-genetic nakhlite and chassignite meteorites. *Geochimica et Cosmochimica Acta* 238, 292–315.

Yang, S., Humayun, M., Righter, K., Jefferson, G., Fields, D., Irving, A.J. (2015) Siderophile and chalcophile element abundances in shergottites: Implications for Martian core formation. *Meteoritics & Planetary Science* 50, 691–714.

Zambardi, T., Poitrasson, F., Corgne, A., Méheut, M., Quitté, G., Anand, M. (2013) Silicon isotope variations in the inner solar system: Implications for planetary formation, differentiation and composition. *Geochimica et Cosmochimica Acta* 121, 67–83.

Supplementary materials

Table 9: Sample description.

Name	Petrologic type	Incompatible element level	Location	Year of discovery	Mass (g)	Cristallization age (Ma)[a]	± (Ma)	Mars ejection age (Ma)[a]	± (Ma)
Shergottites									
NWA480	Basaltic (coarse grained)	intermediate	Morocco, Africa	2000	28	341	18	3	0.3
NWA856	Basaltic (fine grained)	enriched	Morocco, Africa	2001	320	170	19	2.6	0.2
EET79001-B	Basaltic	intermediate	Elephant Moraine, Antartica	1980	7942	173	3	0.73	0.15
Zagami	Basaltic	enriched	Zagami, Nigeria, Africa	1962	18000	169	7	3	0.3
ALH77005	Lherzolitic (cumulate gabbroic rock)	intermediate	Allan Hills, Antartica	1977	482.5	177	6	3.8	0.7
LAR06319	Olivine-phyric (very fine grained)	enriched	Larkman Nunatak, Antartica	2007	78.572	193	20	3.3	
LAR12011	Olivine-phyric	enriched	Larkman Nunatak, Antartica	2012	701.17	185[b]	11	3.3	
EET79001-A	Olivine-phyric	intermediate	Elephant Moraine, Antartica	1980	7942	173	3	0.73	0.15
RBT04262	Olivine-phyric	enriched	Roberts Massif, Antartica	2004	283.4	189	14	2.9	0.6
Nakhlite									
MIL03346	Clinopyroxenite		Miller Range, Antartica	2003	715	1330	80	9.5	1
Chassignite									
NWA2737	Dunite		Moroccan Sahara	2000	611	1380		11.1	1

Table 10: Petrology, alteration and shock features of the samples.

Name	Petrologic type	Major mineral phases[c]	Minor mineral phases (<5%)[c]	Alteration[c]	Shock[c]
Shergottites					
NWA480	Basaltic (coarse grained)	Pyx as phenocrysts (72%) Plagioclase (25%)	Phosphate Opaques	Rather fresh with only a few spots of weathering product on the surface	Melt pockets indicating that it has been shock melted
NWA856	Basaltic (fine grained)	Pyx (68%) Plagioclase (23%)		Well preserved (Cs, Ba, Sr, U not elevated)	Highly fracturated at all scales-Shock melt pockets
EET79001-B	Basaltic	Pigeonite (31.8-54.4%) Augite (11.6-24.5%) Maskelynite (22-29.6%)	Whitlockite Opaque Mesostasis		Impact melts
Zagami	Basaltic	Pyx (69.7-80.4) Maskelynite (10.3-24.7%)	Mesostasis Oxides Sulfides Phosphate		Minor shock-melted glass
ALH77005	Lherzolitic (cumulate gabbroic rock)	Olivine (44-60%) Pyx (13-43%) Maskelynite (8-12%)	Phosphate Chromite Ilmenite Pyrrhotite		More heavily shocked than other SNC
LAR06319	Olivine-phyric (very fine grained)	Olivine (24.4%) Pigeonite (27.7%) Augite (22.2%) Plagioclase (17.8%)	Opx Phosphate Oxides Sulfides		Shock melt veins
LAR12011	Olivine-phyric	Paired to LAR06319	Paired to LAR06319	Paired to LAR06319	Paired to LAR06319

Table 10 (continued)

Name	Petrologic type	Major mineral phases[c]	Minor mineral phases (<5%)[c]	Alteration[c]	Shock[c]
EET79001-A	Olivine-phyric	Pigeonite (42-62.8%) Augite (3.2-8.5%) Maskelynite (15.9-18.3%) Opx (3.4-7.2%) Olivine (7.2-10.3%)	Whitlockite Opaque Mesostasis		Impact melts
RBT04262	Olivine-phyric	Olivine (30-42.1%) Pigeonite (21.5-43%) Augite (10-12.4%) Plagioclase (13-20.2)	Chromite Ilmenite Phosphate	No visible alteration (except for terrestrial noble gaz)	Intensive shock metamorphism-Rare shock melt-Thin melt vein
Nakhlite MIL03346	Clinopyroxenite	Pyx (67.7-79.8%) Intercumulus matrix (15.7-31.5%)	Olivine	Highly altered	
Chassignite NWA2737	Dunite	Olivine (85.1-89.6%) Augite (3.1-5%)	Pigeonite Chromite Sanadine Glass Phosphate Carbonate	Not highly altered by weathering (low U, Sr, Ba)	Highly shocked

[a] Data from the review of McSween and McLennan (2014)

[b] Data from Bellucci et al. (2015)

[c] Mineral data and description of the samples are from the Martian Meteorite Compendium

Table 11: Partition coefficient of SiO_2 between mineral and melt D_{min_melt}.

Dolivine_melt[1]	0.88
Dopx_melt[1]	1.4
Dcpx_melt[1]	0.99
Dmajorite_melt[1]	1.07
Dmajoritic garnet_melt[1]	1.09
Dperovskite_melt[2]	1.21

[1] From Borg *et al.* (2003)

[2] From Corgne *et al.* (2005)

Chapter 4

Silicon isotope composition of angrites inherited from early condensation in the protoplanetary disk

Silicon isotope composition of angrites inherited from early condensation in the protoplanetary disk

Keywords: angrite, silicon isotope, condensation, isotope fractionation

Abstract:

Angrites represent a unique group of achondrites characterized by their enrichment in refractory elements, together with an extreme depletion in moderately volatile elements such as K or Rb. Their low SiO_2 contents also suggest a distinct major element chemistry. We have measured the Si isotope composition of six angrites and confirm the earlier work of Dauphas et al. (2015), showing very homogeneous Si isotope compositions. This observation favors an early process as most scenarios that would take place on the parent body should result in heterogeneous δ^{30}Si values. Our modelling of condensation in a dust rich environment shows that the angrite parent body (APB) could represent early condensates characterized by high Al/Si and Mg/Si ratios, accreted in a dust rich environment that produced a higher oxygen fugacity typical of angrites. Our Si isotope data is also consistent with angrites being early condensates in this dust rich environment, where the higher δ^{30}Si values compared with chondrites are explained by olivine condensation. The amount of metallic iron forming the core and the FeO content in the mantle are consistent with those inferred for angrites. We estimated the bulk composition of the mantle of the angrite parent body using thermodynamic calculations and showed that partial melts of this mantle overlap with the compositions of angrites, without excluding the possibility of magmatic differentiation. Thus, the Si isotope of angrites combined with thermodynamic modelling provides new clues about the origin of this meteorite groups, possibly suggesting a significant contribution to the building blocks of terrestrial planets.

1. Introduction

Angrites form a geochemically specific group of achondrite meteorites from an as yet unidentified parent body. These meteorites are silica undersaturated rocks (SiO_2 contents generally below 40 wt%), that are highly depleted in volatile elements such as Na, K and enriched in refractory elements such as Ca, Al and Ti (Keil, 2012; Riches *et al.*, 2012). As igneous rocks, they are thought to be derived from melting of a differentiated parent body, with an asteroid-size of at most 700 ± 100 km diameter (Scott and Bottke, 2011; Suzuki *et al.*, 2014). The very specific mineralogy of angrites coupled with their high depletion in alkali elements is difficult to accommodate with the melting of a purely chondritic precursor (Jurewicz *et al.*, 1993; Longhi, 1999; Jurewicz *et al.*, 2004; Kurat *et al.*, 2004 and references therein). A component of calcium aluminium rich inclusions was proposed to generate the alkali-depleted and silica undersaturated melt but was difficult to reconcile with the absence of specific ^{48}Ca or ^{50}Ti anomalies that are typical of CAIs (Lugmair and Galer, 1992). Melting experiments performed under oxidizing conditions (oxygen fugacity at IW+1 and IW+2) of CV (Allende) and CM (Murchison) chondrites succeeded in reproducing major element abundances of some angrites using a devolatilized Allende sample (Jurewicz *et al.*, 1993, 2004). Thus, the angrite parent body (APB) should have differentiated under oxidizing conditions, which was suggested by previous studies (McKay *et al.*, 1994; Steenstra *et al.*, 2017). Angrites are the most oxidized planetary materials in the Solar System, as the oxygen fugacity of most of the primitive meteorite material ranges from 1 to 6 log unit below the Iron-Wüstite buffer (IW) (see review by Righter *et al.*, 2016). The high oxygen fugacity (f_{O_2}) of angrites could be the result of aqueous alteration, as shown for carbonaceous chondrites (Brearley, 2006). However, aqueous alteration is not relevant to explain the oxidation state of angrites owing to the lack of hydrous alteration minerals in angrites (see Keil, 2012). No consensus explanation on the unusual petrogenesis of these samples has been reached yet.

Silicon isotope data in angrites have previously been reported in the literature as an attempt to better constrain the evolution of the APB (Dauphas *et al.*, 2015; Pringle *et al.*, 2014). Pringle et al. (2014) reported a significant range of $\delta^{30}Si$ between -0.23 to -0.42‰ and attributed the high $\delta^{30}Si$ values in

angrites to impact induced volatilization. In contrast, Dauphas et al. (2015) measured Si isotope compositions enriched in heavy isotopes with a mean δ^{30}Si of -0.22‰, which they attributed to nebular processes. The relationship between the Mg/Si ratio and silicon isotope compositions of chondrites was used to infer atomic bulk Mg/Si of planetary bodies, leading to a Mg/Si ratio of 1.31 ± 0.09 for the APB. This Mg/Si of the APB based on Si isotopes was significantly higher than the Mg/Si ratio inferred by Longhi (1999). Thus, previous studies show conflicting Si isotope data in detail and the corresponding interpretations differ.

The first step of this study was to reexamine the Si isotope compositions of angrites using a high precision silicon isotope analytical method with a Neptune Plus MC-ICP-MS. Our goal was to better constrain the origin of the angrite meteorite group and examine whether its chemical affinities with the Earth (e.g. Fitoussi *et al.*, 2016) could provide further insights into the formation of the Earth.

2. Samples and method

2.1. Sample description

There are currently only sixteen known angrite samples and they represent ≈ 1 % of recorded differentiated meteorite finds over the past twenty years(Burbine *et al.*, 2002). The six angrites analysed in this study include three plutonic (slowly-cooled) angrites NWA4590, NWA 10463 and NWA4801; three volcanic (rapidly-cooled or quenched) angrites D'Orbigny; NWA12320 (diabase), and Sahara99555. The common origin of angrites was supported by their specific petrology and their common Δ^{17}O isotope characteristics, distinct from the mass fractionation line of the Earth, Mars and Vesta (Greenwood *et al.*, 2005). Volcanic and plutonic angrites present very young crystallization ages of respectively ≈ 4 Ma and ≈ 10 Ma after CAI, based on the Hf-W chronometer (Kleine *et al.*, 2012). The mineralogy of angrites consists mainly of anorthite, Al-Ti-bearing diopside, olivine and minor phases (Mittlefehldt et *al.* 2002, Keil 2012). The particularity of D'Orbigny is the presence of cm-diameter vesicles that could be related to the presence of volatile species in the source magma (Mittlefehldt *et*

al., 2002). Sahara 99555 contains also mm-sized vesicles, that account for 1.38 vol. %. Angrites are characterized by their depletion in alkali elements and enrichment in refractory elements such as Ca, and Ti comparing to chondrites. Angrites did not suffer significant post-crystallisation processes as impact-related shocks or intense terrestrial weathering (Keil, 2012) and thus represent good candidates for studying asteroidal igneous processes.

2.2. Analytical procedure

The bulk samples were first cleaned in an ultrasonic bath filled with deionized MQe water and were then cleaned using distilled ethanol prior to sample processing. The samples were crushed into fine powder in an agate mortar that was pre-cleaned with 0.5 M HNO_3. A mass of 5 to 6 mg of each sample and of 1 to 4 mg of bracketing standard NBS28 and secondary standards, Diatomite and BHVO-2, were dissolved using an alkaline fusion technique adapted from (Georg *et al.*, 2006). Sample powder was mixed with a ≈ 200 mg NaOH pellet and heated at 730 °C in a furnace over 7 min 30 seconds. The mixture was then left a few minutes at room temperature to allow the fusion cake to crystallize inside the crucible before being introduced into a 30 mL Savillex containing ≈ 25 mL of MQe water. The solutions were transferred carefully into Teflon bottles and rinsed several times with MQe water to ensure the entire recovery of the sample during this procedure. MQe water was added until the silicon concentration reached approximately 6 ppm. Sample solutions were then acidified with 6N HCl to a pH of 2-3 following the procedure described in (Fitoussi *et al.*, 2009). A mass of 3 µg of silicon was loaded on a BioRad column filled with 1 mL of resin BioRad (H^+) 50W-X8, 200-400 mesh. Cleaning and loading procedure are described in Table 1. Silicon in aqueous solutions (either as H_4SiO_4 or $H_3SiO_4^-$) pass through the column, whereas the cations stick to the column, leading to a Si yield close to 100 %

Table 1: Column chromatography procedure for silicon separation

Separation Stage	Solution	Volume
Pre-cleaning resin	3 N HCl	1 column reservoir
Pre-cleaning resin	6 N HCl	1 column reservoir
Pre-cleaning resin	15 N HNO_3	200 µl
Pre-cleaning resin	6 N HCl	1 column reservoir
Pre-cleaning resin	3 N HCl	1 column reservoir
Pre-cleaning resin	Milli-Q H_2O	4 column reservoirs
Sample load	Acidified sample solution to pH 2-3	0.2 to 0.5 ml
Elution	Milli-Q H_2O	2 ml
Dilution to running concentration	Milli-Q H_2O	2 ml to 5 ml to reach ≈ 0.5 ppm

Table 2: Instrumental settings for Si isotope analysis on the Neptune Plus MC-ICP-MS.

Parameter	Neptune Plus
Rf power	1200
Sampler cone	Standard "H"-type, Nickel
Skimmer cone	Jet "X"-type, Nickel
Coolant gas (Ar) flow	16 l/min
Auxiliary gas (Ar) flow	1.23 l/min
Z torch position	2.5 mm
Nebulizer uptake rate	76 µl/min
Cup configuration	H3: ^{30}Si; C: ^{29}Si; L3: ^{28}Si
Si runing concentration	0.5 ppm
Sensitivity on ^{28}Si beam	≈ 15 V
Instrumental blank	≈ 300 mV
Desolvating device	DSN-100
DSN nebulizer pressure	30 PSI
DSN hot gas flow	0.2 l/min
DSN membrane gas (Ar) flow	≈ 4 - 5 l/min

2.3. Mass spectrometry

High precision isotope analysis were performed on a Neptune Plus MC-ICP-MS equipped with a Standard-H sample cone, a Jet-X skimmer cone and a sapphire injector to enhance sensitivity and minimize instrumental blank. The mass spectrometer was operating in a dry plasma mode with a DSN-100 desolvating system which notably minimized memory effects and isobaric interferences. Measurements were done at a medium resolution mode with a resolving power of ≈ 7500 which allows to partially resolve silicon peaks from their major interferences (e.g. $^{14}N_2$ on ^{28}Si, $^{14}N^{15}N$ on ^{29}Si and $^{14}N^{16}O$ on ^{30}Si). The sensitivity obtained with sample solution reached 35 V/ppm with a PFA nebulizer flow rate of 76 µL/min. The blank sensitivity of ≈ 250 mV led to a sample over noise ratio of approximately 65. The parameters of the mass spectrometer and the introduction system are summarized in Table 2. Each isotope measurement represented one block of 36 cycles with an integration time of 8.389 s and an uptake time of 3 s. The electronic background produced by the amplifiers of the Faraday collectors was measured by the signal of the deflected ion beam from the electrostatic analyser over 60 s. The instrumental blank was subtracted by measuring an on-peak-zero (OPZ) representing the average intensities of the three silicon masses in the cleanest 0.002 M HCl wash over 75 s, prior and after each analysis. Between two measurements, the system was cleaned with 0.002 N HCl for a few minutes to recover the blank signal level. The instrumental mass bias was corrected by the sample-standard bracketing technique. The isotope ratios are expressed relative to the standard NBS-28 in the delta notation $\delta^{29}Si$ and $\delta^{30}Si$ (‰) as follows (with exponent x = 29 or 30):

$$\delta^x Si = \left[\frac{\left(\frac{\delta^x Si}{\delta^{28} Si}\right)_{sample}}{\left(\frac{\delta^x Si}{\delta^{28} Si}\right)_{NBS-28}} - 1 \right] \times 1000$$

At the beginning of each measurement session, the secondary standard Diatomite and the hawaïan basalt BHVO-2 were measured as a quality check for accuracy, precision, reproducibility and mass dependence of the Si isotope measurement. The isotope measurements of the two secondary

standards relative to NBS-28 were mass-dependent with $\delta^{30}Si$ = 1.27 ± 0.10 ‰ (2SD,n=65), $\delta^{29}Si$ = 0.65 ± 0.07 ‰ (2SD,n=65) for the Diatomite and $\delta^{30}Si$ = -0.31 ± 0.12 ‰ (2SD,n=24),$\delta^{29}Si$ = -0.16 ± 0.06 ‰ (2SD,n=24) for BHVO-2 (Table 3), in good agreement with previously reported data (Armytage *et al.*, 2011, 2012; Dauphas *et al.*, 2015; Fitoussi *et al.*, 2009; Fitoussi and Bourdon, 2012; Pringle *et al.*, 2013, 2014; Savage *et al.*, 2011; Savage and Moynier, 2013; Zambardi *et al.*, 2013; Zambardi and Poitrasson, 2011).

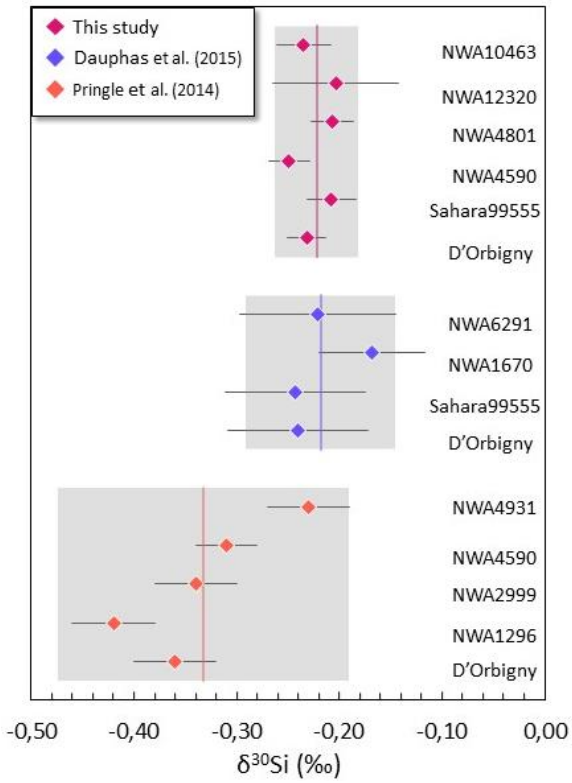

Figure 1: Isotope composition of the 6 angrites analysed in this study compared with data from the literature (see main text for details). Errors bars refer to internal precision (2SE or 95% confidence intervals of the mean for data from (Dauphas et al., 2015) and shaded areas refer to external precision (reproducibility, 2SD).

3. Results

The silicon isotope data are reported Table 3. The $\delta^{30}Si$ of angrites ranges between -0.20 to -0.25 ‰ with an average $\delta^{30}Si$ value of -0.22 ± 0.02 ‰ (2SD, N=6) (Figure 1) coincides within error with the

previous reported value of -0.22 ± 0.07 ‰ (2SD, N=4) reported in Dauphas et al. (2015). The data of Pringle et al. (2014) gave a lower average δ^{30}Si of -0.33 ± 0.14 ‰ (2SD, N=4). Pringle et al. (2014) reported strong isotope variations among the angrites related to their petrologic type that are not observed in this study, similarly to the study of (Dauphas *et al.*, 2015). The discrepancy of the data between the groups may be attributed to the different analytical procedures and instrumental mass bias correction summarized in Table 5. The δ^{30}Si of D'Orbigny and Sahara 99555, respectively of -0.23 ± 0.02 ‰ (2SE) and -0.21 ± 0.02 ‰ (2SE), are in good agreement with the previous values of -0.24 ± 0.07 ‰ (95% c.i.) reported by Dauphas et al. (2015) for the two samples (Table 4). Overall, our new data suggests a narrower range of δ^{30}Si values in angrites than previously reported.

Table 3 : Silicon isotope data of the two secondary standards and the six analysed angrites.

Name	**Petrologic type**	**δ^{30}Si (‰)**	**2SE**	**δ^{29}Si (‰)**	**2SE**	**N[1]**	**SiO_2 (wt%)**
Standards							
Diatomite		1.27	0.01	0.65	0.01	65	100
BHVO-2	Basalt	-0.31	0.02	-0.16	0.01	24	49.9[2]
Angrites							
D'Orbigny	Volcanic	-0.23	0.02	-0.10	0.01	26	36.9[3]
Sahara99555	Volcanic	-0.21	0.02	-0.11	0.02	12	38.6[3]
NWA12320	Volcanic	-0.20	0.06	-0.11	0.02	7	41.8
NWA4590	Plutonic	-0.25	0.02	-0.12	0.02	8	38.3[4]
NWA4801	Plutonic	-0.21	0.02	-0.10	0.02	10	40.9[4]
NWA10463	Plutonic	-0.23	0.03	-0.12	0.02	8	41.8
Average Angrites (±2SD)		-0.22	0.02	-0.11	0.01	6	

[1] number of measurements for each sample
[2] from the United States Geological Survey
[3] from (Keil, 2012)
[3] from (Riches *et al.*, 2012)

Table 4 : Isotope data of angrites from the literature (Dauphas et al., 2015; Pringle et al., 2014).

Reference	Name	Petrologic type	$\delta^{30}Si$ (‰)	95% c.i.[1]	$\delta^{29}Si$ (‰)	95% c.i.[1]	N
Dauphas et al. (2015)	D'Orbigny	Quenched	-0.24	0.07	-0.12	0.06	6
	Sahara99555	Quenched	-0.24	0.07	-0.10	0.05	3
	NWA1670	Plutonic	-0.17	0.05	-0.08	0.02	6
	NWA6291	Plutonic	-0.22	0.08	-0.11	0.06	6
	Average Angrites (±2SD)		-0.22	0.07	-0.10	0.03	4

[1] Errors are given as 95% confidence intervals of the means of N analysis

Reference	Name	Petrologic type	$\delta^{30}Si$ (‰)	2SE	$\delta^{29}Si$ (‰)	2SE	N
Pringle et al. (2014)	D'Orbigny	Quenched	-0.36	0.04	-0.16	0.02	12
	NWA1296	Quenched	-0.42	0.04	-0.19	0.03	10
	NWA2999	Plutonic	-0.34	0.04	-0.17	0.02	10
	NWA4590	Plutonic	-0.31	0.03	-0.13	0.01	10
	NWA4931	Plutonic	-0.23	0.04	-0.10	0.02	10
	Average Angrites (±2SD)		-0.33	0.14	-0.15	0.07	5

Table 5 : Comparison of the different analytical methods used for the silicon isotope analysis of angrites.

From	Instrument	Plasma mode	Introduction System	Mass bias correction	Sample Matrix
This study	Neptune Plus MC-ICP-MS	dry plasma	DSN-100 desolvating system	Standard-Sample Bracketing relative to NBS28	HCl
Dauphas et al. (2015)	Neptune MC-ICP-MS	wet plasma	Spray Chamber	Mg-Doping approach from (Zambardi and Poitrasson, 2011)	HCl
Pringle et al. (2014)	Neptune Plus MC-ICP-MS	wet plasma	Spray Chamber	Standard-Sample Bracketing relative to NBS28	HNO_3

4. Discussion

4.1. Understanding the Si isotope record of angrites

Previous studies of Si isotopes in angrites have discussed various scenarios for explaining their distinct isotope record. The preferred scenario of Pringle et al. (2014) was that the elevated δ^{30}Si of angrites was due to evaporation following impacts. Dauphas et al. (2015) dismissed this scenario arguing that the angrite parent body was too small to experience enough volatilization upon impact as the fraction that gets volatilized is directly linked to the escape velocity of the body. Our Si isotope data that shows homogeneous Si isotope does not favor such a scenario as impact would not have affected the whole mantle of the angrite parent body. Similarly, one can rule out the effect of magma differentiation as all the SiO_2 of angrites are low and high δ^{30}Si are found in rocks characterized by high SiO_2 (e.g. Savage *et al.*, 2014). Dauphas et al. (2015) had also ruled out a role for core formation since little Si would be dissolved in the angrite core as the oxygen fugacity during core formation was too high (Righter *et al.*, 2008; Shirai *et al.*, 2009). This conclusion has been reemphasized in a recent study by (Steenstra *et al.*, 2017) based on a large set of siderophile elements. These authors have concluded that the core of the APB formed at IW-1.45 (and with P=0.1GPa), which confirms, under these conditions, the absence of Si in the metal.

Thus, the very homogeneous Si isotope record of angrites definitely suggests an early planetary process that would have produced an enrichment in heavy Si isotopes. Recent work on Mg isotopes by (Hin *et al.*, 2017) has suggested that evaporation at the surface of a magma ocean followed by an atmospheric escape could result in an enrichment in heavy Mg and Si isotopes in planetesimals precursors to the Earth. In the next section, this hypothesis is reexamined in light of this work.

4.2. Evaporation of Si from a magma ocean

The volatility of silicon is sufficiently large that in a fully molten mantle a significant fraction of Si would be partitioned in the atmosphere as SiO. If the Si-bearing species is then lost to space, then this could ultimately affect the Si isotope composition of the residual magma ocean. Young et al. (2019) have

studied the conditions under which it is possible to produce Mg or Si isotope fractionation with such a process. The relatively high pressure above the magma ocean due to vaporization of the most volatile species means that the Si isotope fractionation between the vapor and the magma will be rather limited. A more efficient process of isotope fractionation can take place only if atmospheric escape is through Jean's escape (Young *et al.*, 2019). Conversely, if atmospheric escape is by hydrodynamic escape then the isotope fractionation becomes negligible. Thus, one must first identify whether the temperature conditions at the surface of the APB magma ocean will allow significant Si isotope fractionation. This can be done by calculating the value of λ, the hydrodynamic escape parameter defined as (Young *et al.*, 2019):

$$\lambda = \frac{GMm_{vapor}}{rk_bT(r)}$$

Where G is the gravitational constant, M the mass of the planetesimal, T the temperature at distance r, m_{vapor} the mean mass of the vapor and k_b the Boltzmann constant. As shown in Young et al. (2019) following the earlier work of Volkov et al. (2011), if the radius of the angrite parent does not exceeded 700 km, then the expected mass of the APB will not be greater than $5x10^{21}$ kg assuming a mean density of 3500 kg/m^3. The temperature necessary to fully melt the APB mantle is approximately 1800 K (see Section 4.3). In this case, the value of λ will always be lower than 2-3, representing the minimum value to reach Jean's escape. This means that the size of the angrite parent body as well as its surface temperature will preclude any significant Si isotope fractionation resulting from magma ocean vaporization.

4.3. Angrites as first condensates in the early Solar System

The peculiar composition of angrites which are characterized by an enrichment in refractory components (Longhi 1999) while being the most depleted material in volatile elements has been a topic of discussion with some suggestions that angrites could even come from Mercury. Morbidelli et al. (2020) have modeled the chemical composition of the first condensates that would form during the

condensation sequence in a typical solar gas composition and have observed that these condensates should be characterized by a high Al/Si ratio (similar to angrites) and high Mg/Si ratios. We have re-examined this question by calculating the chemical composition of first condensates under variable of P-T-f_{O2} conditions with the goal of comparing these compositions with those of angrites. Following the study of Dauphas et al. (2015) we also calculated the Si isotope composition of these condensates using recent ab initio calculations of Si isotope fractionation factors between minerals and the SiO in the vapor phase.

For this purpose, we calculated the condensation sequence using the Factsage software (Bale *et al.*, 2016) that can calculate equilibrium conditions for multicomponent systems as a function of temperature starting from a solar composition taken from Lodders (2020) with a total pressure of 10^{-3} atm with temperatures ranging between 2000 and 1000K. In order to simplify the calculations, we used only a limited number of elements: H, He, C, N, O, S, Fe, Ni, Ca, Mg, Si, K, Al, Na, Cr and Ti. The following data bases were used: Ftstel for the metallic iron mixtures, FT-oxid for all the oxide solutions and FTSage for pure compounds. With this data base, it is possible to include solid solutions for olivine, enstatite and clinopyroxene as well as molten oxide mixtures or molten and solid iron solutions. We investigated the possibility that angrite condensation took place under more oxidizing conditions corresponding to those described in (Ebel and Grossman, 2000) with enhancement of dust by a factor of 1 (solar gas), 100 and 500 relative to the Solar composition. For each run the oxygen fugacity was determined and it matches perfectly with those reported in Ebel and Grossman (2000) (Figure 2).

The equilibrium condensation was calculated by minimizing the Gibbs energy of the mixture and at each temperature step, the composition of the vapor phase, the solids or possibly melts was calculated. The partitioning of Si in various phases was specifically examined with the goal of calculating the Si isotope composition of each phase. The results of the calculations for Si are depicted in Figure 3 showing the fraction of Si in each phase as a function of temperature, for each dust enrichment factor. The first mineral to condense from a gas of solar composition (i.e. 1xCI) is corundum

(Al_2O_3). At lower temperature, corundum reacts with the nebular gas to form hibonite and perovskite (Ebel and Grossman, 2000). The appearance of melilite at 1550 K starts condensing Si and Mg, with Mg

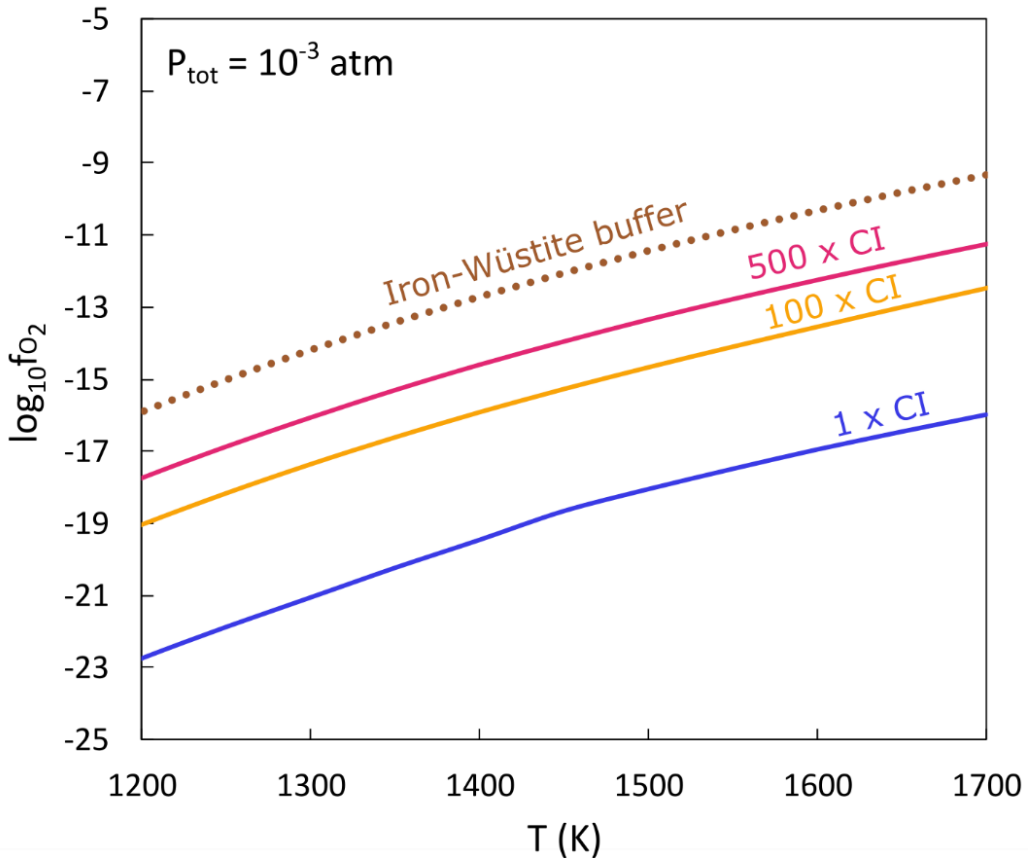

Figure 2: Oxygen fugacity determined for each condensation model. Dust enrichment factors (corresponding to more oxidized conditions) are indicated on the model curves for f_{O_2}. The curve for the iron-wüstite curve is taken from (Myers and Eugster, 1983).

continuing to condense into a Ti-rich spinel. At 1425 K, metallic Fe, olivine and clinopyroxene appear, beginning to condense significant amounts of Si. Orthopyroxene appearing at 1325 K incorporates most of the remaining gaseous Si. At the end of the condensation sequence, Si is mostly present in olivine (27%), orthopyroxene (43%) and feldspar (20%) and a small amount of Si is in clinopyroxene (10%). The condensation sequence presented in this work is in good agreement with previous calculations at the same pressure of 10^{-3} bar performed by Grossman and Larimer (1976) and Yoneda and Grossman (1995). Increasing the dust/gas ratio produces stable silicate melt that incorporates up

to 32 % and 57 % of the total amount of condensed Si in the 100 x CI and 500 x CI dust enriched model, respectively. Refractory phases such as corundum, hibonite, melilite and perovskite are dissolved completely in the liquid phase, leading the first melt condensate to be enriched in Ti, Ca and Al. The condensation of partial melts at a total pressure of 10^{-3} atm were already observed by Yoneda and Grossman (1995) and Ebel and Grossman (2000) who predicted the appearance of a liquid phase at 2300 K for a dust enrichment factor of 500, which matches perfectly with the 2350 K reported in this study.

An important outcome of these calculations is that the first condensates are enriched in olivine, which means that their Mg/Si ratios are higher than that of the bulk solar composition. Similarly, as Al is more refractory than Si, the condensates have higher Al/Si ratios than the initial solar gas. These results are very comparable with those of Morbidelli et al. (2020). The next step was to calculate the bulk APB mantle composition by making the following assumption: Mg, Ca, Al, Na, K and Ti are lithophile elements and form oxides with the typical stoichiometry: MgO, CaO, Al_2O_3, etc. It is also safe to assume that Si is also a lithophile element as the calculated molar fraction of Si in the metallic phase does not exceed a few 8×10^{-3} in the most reducing conditions. This leaves a fraction of the total oxygen and we then consider that all this remaining oxygen is used to form FeO that becomes part of the mantle, while the remaining iron forms the core with Ni. By making this apportionment of elements between mantle and core, one can calculate a mantle composition for the angrite parent body. The calculated bulk mantle compositions as a function of condensation temperatures are given in Table 6. It is obvious that the most reducing composition (solar gas) yield an FeO content that is much lower than what is observed in angrites that are characterized by relatively high FeO content (from 9.4 to 31.2 wt%, see Table 9), once one takes into account the fact that Fe is a moderately incompatible element with a partition slightly lower than 1. In contrast, the FeO contents in the mantle obtained (Table 6) when the dust to gas ratio is enhanced by a a factor of 100 at a condensation temperature of approximately 1700 K is significantly higher and more consistent with the oxidized character of the angrite parent body (Jurewicz *et al.*, 2004, 2004; Keil, 2012).

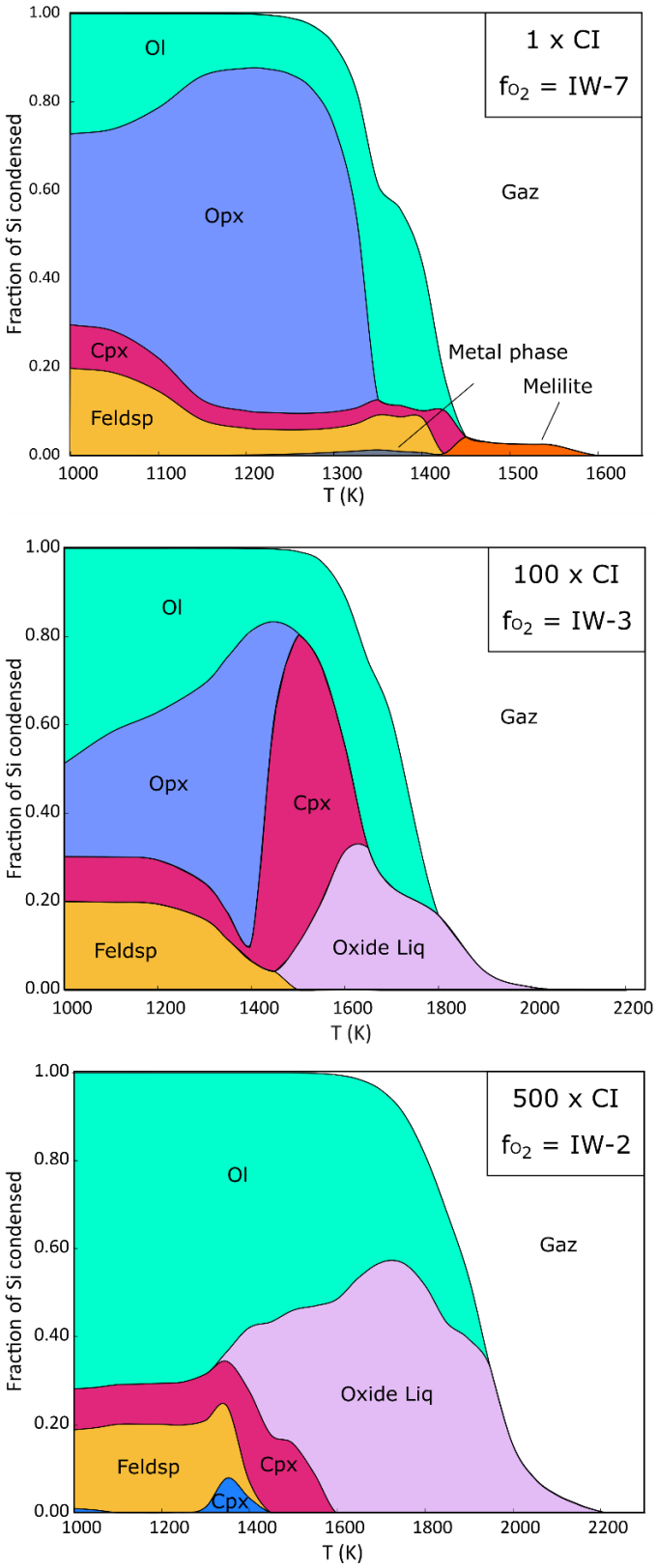

Figure 3 : Distribution of Si between the different condensed phases and the vapor at dust enrichment of 1 (solar composition), 100 and 500. List of abbreviations: Ol – olivine; Opx – orthopyroxene; Cpx – clinopyroxene; Feldsp – feldspar; Oxide Liq – oxide melt.

Table 6: Composition of the APB in function of condensation temperature for each dust enrichment model.

1 x CI	T (K)												
wt% oxide	1200	1225	1250	1275	1300	1325	1350	1375	1400	1425	1450	1475	1500
FeO	3.20	3.09	2.97	2.78	2.53	2.34	2.46	3.29	4.96	11.20	25.94	0.00	0.00
Cr_2O_3	0.87	0.87	0.86	0.85	0.84	0.83	0.84	0.72	0.62	0.67	0.00	0.00	0.00
CaO	2.82	2.83	2.84	2.88	2.96	3.17	3.69	3.99	4.98	10.13	20.31	31.59	34.77
SiO_2	52.75	52.77	52.71	52.43	51.57	49.07	42.24	41.65	40.70	34.53	15.99	17.77	17.27
Al_2O_3	3.67	3.68	3.70	3.74	3.85	4.12	4.79	5.18	6.47	13.17	26.42	41.18	45.60
MgO	36.48	36.57	36.74	37.13	38.06	40.27	45.75	44.93	41.97	29.68	10.10	7.52	0.22
Na_2O	0.03	0.02	0.01	0.004	0.002	0.002	0.001	0.0001	0.00	0.00	0.00	0.00	0.00
TiO_2	0.17	0.17	0.17	0.18	0.18	0.19	0.23	0.24	0.30	0.62	1.24	1.94	2.15

(continued)

1 x CI	T (K)				
wt% oxide	1525	1550	1600	1650	1700
FeO	0.00	0.00	0.00	0.00	0.00
Cr_2O_3	0.00	0.00	0.00	0.00	0.00
CaO	34.56	33.46	10.65	10.52	7.59
SiO_2	16.89	16.06	0.00	0.00	0.00
Al_2O_3	46.33	48.21	85.31	85.67	92.33
MgO	0.04	0.00	0.00	0.00	0.00
Na_2O	0.00	0.00	0.00	0.00	0.00
TiO_2	2.18	2.27	4.04	3.80	0.08

100 x CI	T (K)										
wt% oxide	1450	1500	1550	1600	1650	1700	1750	1800	1850	1900	1950
FeO	7.82	7.67	7.35	7.66	7.85	7.29	7.60	15.81	24.26	29.60	34.20
Cr_2O_3	0.83	0.82	0.76	0.68	0.55	0.24	0.14	0.13	0.05	0.03	0.01
CaO	2.69	2.70	2.75	2.87	3.17	3.63	4.89	11.20	17.49	20.85	21.12
SiO_2	50.21	50.19	49.90	47.99	44.19	41.88	40.43	35.52	24.84	16.67	9.55
Al_2O_3	3.49	3.51	3.57	3.73	4.12	4.73	6.36	14.56	22.83	28.01	32.42
MgO	34.75	34.91	35.46	36.86	39.91	41.99	40.29	22.10	9.46	3.56	1.23
Na_2O	0.05	0.04	0.03	0.03	0.01	0.002	0.001	0.0009	0.0003	0.0002	0.00
TiO_2	0.16	0.17	0.17	0.18	0.19	0.22	0.30	0.68	1.07	1.29	1.47

(continued)

100 x CI	T (K)				
wt% oxide	2000	2050	2100	2150	2200
FeO	39.56	42.79	44.76	46.28	47.75
Cr_2O_3	0.01	0.004	0.002	0.001	0.00
CaO	17.65	14.01	11.19	8.90	7.00
SiO_2	3.07	0.80	0.25	0.09	0.06
Al_2O_3	37.56	40.60	42.52	43.94	44.84
MgO	0.52	0.29	0.19	0.13	0.00
Na_2O	0.00	0.00	0.00	0.00	0.00
TiO_2	1.64	1.50	1.08	0.65	0.36

500 x CI	T (K)												
wt% oxide	1550	1600	1650	1700	1750	1800	1850	1900	1950	2000	2050	2100	2150
FeO	20.62	20.14	19.06	17.97	16.69	13.25	9.24	8.11	10.40	16.58	23.25	28.62	33.35
Cr_2O_3	0.71	0.70	0.70	0.68	0.64	0.54	0.39	0.27	0.21	0.09	0.05	0.03	0.02
CaO	2.30	2.33	2.37	2.44	2.57	2.86	3.37	4.21	6.57	11.56	16.50	19.70	20.30
SiO_2	43.06	43.34	43.82	44.01	43.77	43.70	43.18	42.24	40.40	34.30	25.74	17.79	10.89
Al_2O_3	2.99	3.02	3.09	3.18	3.34	3.72	4.38	5.47	8.55	15.05	21.66	26.87	31.50
MgO	29.79	30.09	30.70	31.52	32.83	35.74	39.22	39.44	33.48	21.72	11.83	5.85	2.67
Na_2O	0.38	0.24	0.11	0.05	0.02	0.01	0.004	0.002	0.002	0.001	0.0003	0.0004	0.00
TiO_2	0.14	0.14	0.15	0.15	0.16	0.18	0.21	0.26	0.40	0.70	0.97	1.14	1.27

(continued)

500 x CI	T (K)			
wt% oxide	2250	2300	2350	2400
FeO	42.23	44.57	46.29	47.53
Cr_2O_3	0.01	0.01	0.003	0.002
CaO	14.32	11.43	9.04	7.01
SiO_2	1.70	0.62	0.24	0.07
Al_2O_3	39.93	42.24	43.77	44.98
MgO	0.74	0.48	0.31	0.24
Na_2O	0.00	0.00	0.00	0.00
TiO_2	1.07	0.66	0.35	0.18

4.4. Silicon isotope fractionation between vapor and condensation

For each T, P and f_{O_2} conditions, the Si isotope composition of the condensates was calculated using the Si isotope fractionation factors between Si in the vapor phase and mineral phases. To do so, one can first write a mass balance equation for the Si isotope composition of the bulk system:

$$R_{Si}^{tot} = \sum_i X_{Si}^i R_{Si}^i$$

where X_{Si}^i and R_{Si}^i are the mass fraction of Si in phase i and the $^{30}Si/^{28}Si$ ratio of phase i, respectively. The Si isotope fractionation factor between mineral phase i and SiO(g) is α_i and thus the previous equation can be written as:

$$R_{Si}^{tot} = \sum_i X_{Si}^i \alpha_i R_{Si}^{SiO}$$

Based on these equations, one can calculate the $^{30}Si/^{28}Si$ ratio for SiO and for the mineral phases i:

$$R_{Si}^{SiO} = \frac{R_{Si}^{tot}}{\sum_i X_{Si}^i \alpha_i}$$

and:

$$R_{Si}^{i} = \frac{\alpha_i R_{Si}^{tot}}{\sum_i X_{Si}^i \alpha_i}$$

One can then determine the Si isotope composition of the condensate assemblage:

$$R_{Si}^{cond} = \frac{\sum_{i \neq SiO,SiS} X_{Si}^i R_{Si}^i}{\sum_{i \neq SiO,SiS} X_{Si}^i}$$

These equations were used for each set of T and dust enrichment factor to calculate the Si isotope composition of condensate for comparison with the Si isotope data for angrites. The Si isotope fractionation factors used for the calculation were taken from the studies of Javoy et al. (2012), Huang et al. (2014) and Qin et al. (2016) and the data used for the calculations are compiled in Table 7. We further assume that the Si isotope fractionation factor between a condensed liquid phase and the

vapour is similar to the one between quartz and vapor as the coordination of Si in a silicate melt at low pressure is identical to that of quartz (Solomatova and Caracas, 2019). The results of the calculation are shown in Figure 4, starting from a solar composition (CI chondrites) at $\delta^{30}Si$ = -0.44 ‰(Armytage *et al.*, 2011; Fitoussi *et al.*, 2009; Zambardi *et al.*, 2013). The condensates are enriched in heavy Si isotopes relative to the gas phase where the main species is SiO with minor SiS (representing up to 10% relative to SiO).

Table 7: Polynomial coefficients used for calculation of either the reduced partition function ratio β or the isotope fractionation factor.

Mineral	**Formula**	**a**	**b**	**c**
Quartz-SiO[1]		4.6409	-0.056228	0.00041
FeSi-SiO[1]		-1.7251	0.10443	-0.0026672
Quartz[2]	SiO_2	8.12067	-0.22816	0.00947
Anorthite[2]	$CaAl_2Si_2O_8$	7.97993	-0.21923	0.00875
Diopside[2]	$CaMgSi_2O_6$	7.56179	-0.20489	0.00815
Forsterite[2]	Mg_2SiO_4	7.72691	-0.20034	0.00729
Orthopyroxene[3]	$MgSiO_3$	6.985	0.647	-0.455

[1] from Javoy et al. (2012)

[2] from Qin et al. (2016)

[3] from Huang et al. (2014)

N.B.: $10^3\ln(\beta_{30/28}) = ax^3+bx^2+cx$ (with $x=10^6/T^2$, T is temperature in kelvin) or isotopic fractionation coefficient α as $10^3\ln(\alpha_{30/28}) = ax^3+bx^2+cx$ (with $x=10^6/T^2$, T is temperature in kelvin).

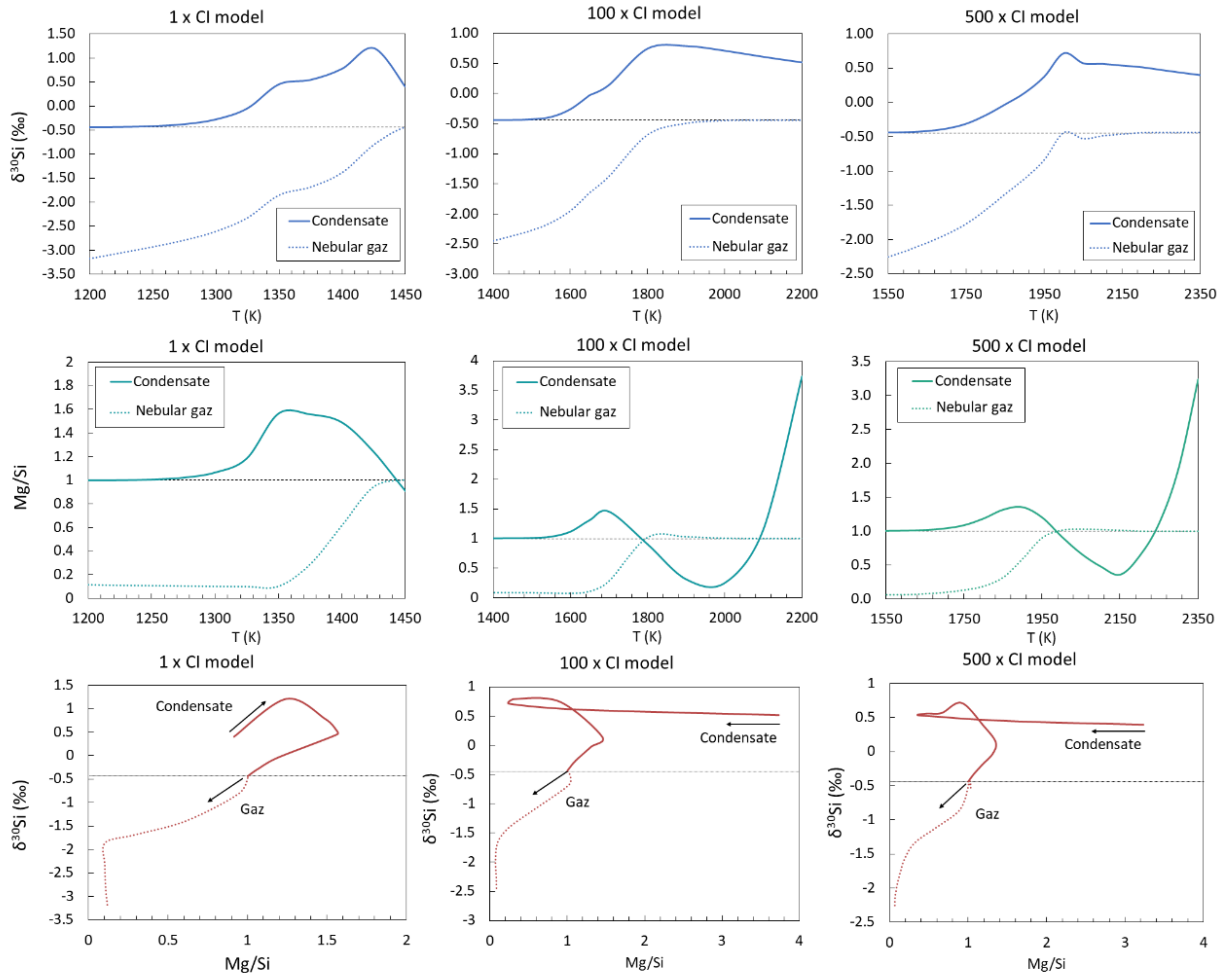

Figure 4 : Si isotope composition and Mg/Si ratio of the condensates and the vapor for the three different models. The bulk δ^{30}Si value of -0.44 ‰ corresponds to the initial solar composition, assumed to be identical to that of CI chondrites and the initial Mg/Si solar ratio is equal to 1 (see text for details).

Overall, as shown in Figure 4, it is possible to obtain a temperature that will yield a condensate characterized by the δ^{30}Si value of angrites (-0.22±0.02‰) for the three different conditions of condensation. In the case of the solar composition, the temperature that fits the δ^{30}Si value of angrites, would correspond to a very low FeO content in the mantle (~2.5 wt %). Thus, this model is probably not the most realistic for explaining the chemical composition of angrites. This is not the case for the two other models using higher dust to gas ratios, where the temperature yielding the δ^{30}Si value of angrites correspond to much higher FeO contents in the APB mantle (7-15 wt%). Thus, our model

seems consistent with the idea that the angrite parent body could represent the first condensate in the Solar System, as discussed in the model of Morbidelli et al. (2020). Our new model that also includes the Si isotope observations can attribute a direct identity to the first condensates as denominated in Morbidelli et al. (2020). These authors further argued that these condensates could have been part of the building blocks of the Earth representing up to 45% of the Earth's mass. Interestingly, Fitoussi et al. (2016) had also argued that angrites could represent a significant fraction of the Earth's mass, based on nucleosynthetic signatures of meteorites and of the Earth. The sizeable contribution of angrites was a significant factor explaining the enrichment in refractory elements. By comparison, earlier work by Dauphas et al. (2015), had calculated the isotope composition of a condensate taken from (Yoneda and Grossman, 1995) or consisting simply of olivine but it was not clear how the condensate itself directly related to the angrite bulk composition. In any case, the δ^{30}Si of the condensate (as plotted in their figure 6) was far above the value measured in angrites. Thus, angrites in their model represented a mixture between this condensate and a nebular gas endmember. Dauphas et al. (2015) also argued that the Mg/Si ratio of angrites should be high simply based on the mixing relationship between δ^{30}Si and Mg/Si. However, it has never been proven that the composition of the APB mantle should have a high Mg/Si ratio. In what follows, we examine further this question and attempt to constrain further the composition of the mantle of the angrite parent body.

4.5. Comparison of the first condensates with angrites

In order to compare the composition of the condensates with that of angrites, the composition of the bulk mantle of the angrite parent body calculated in the previous section was used to calculate the composition of mantle melts using the FACTSAGE software and compared with the major element compositions of angrites published in the literature (Table 9). The experiments of Longhi (1999), Jurewicz et al. (1993, 2004) had made some inference about the nature of the APB mantle but were not able to determine the bulk composition of the mantle. More recently, Tissot et al. (2018) have

identified the mineral phases that were saturated in the D'Orbigny angrite, i.e. olivine, cpx and anorthite or olivine-anorthite-spinel.

In our approach we have simply calculated the composition of melts in equilibrium at a pressure of 1 kbar with the APB mantle composition using the Factsage software using a simple assemblage of oxides (Table 8). The melt composition was calculated for various temperatures and their compositions were plotted in binary diagrams including also angrite major element data from the literature (see compilation in Table 9). The bulk composition of angrites is rather different compared with terrestrial rocks such as MORB or OIBs, or SNC meteorites. They have notably lower SiO_2 and higher Al_2O_3 and FeO than most terrestrial rocks. Yet the calculated melt compositions overlap fairly well with the angrite major element data (Figure 5). The high Mg/Si of our angrite mantle (weight ratio of 0.80 and 0.82 for the 100xCI model and 500xCI model respectively) is in fact consistent with the lower Mg/Si of angrites, provided one takes into account that Mg is far more compatible than Si during partial melting. Another important feature of our modeling is that the saturated mantle phases (olivine, anorthite, spinel and cpx) are consistent with those inferred in previous studies (e.g. Tissot et al. 2018; Longhi 1999). The tentative Mg/Si weight ratio of 0.9 that had been estimated by Longhi (1999) is consistent with our estimate which matches less with the high Mg/Si of 1.1 value of Dauphas et al. (2015).

One should note that the temperatures of condensation used to calculate the melt compositions are higher than those that give the perfect match for the Si isotope compositions. The source of this discrepancy could have several origins. First, there could be uncertainties in the Si isotope fractionation factors used in our calculations and in some cases the uncertainty could come from having used different data sets. Second and more importantly, we have assumed in our calculated that the Si isotope fractionation was purely due to equilibrium fractionation. However, there could also be a kinetic component and this would significantly lower the calculated δ^{30}Si of the condensed material (see for example Bourdon and Fitoussi, 2020). In other words, a kinetic isotope fractionation superimposed on the equilibrium fractionation would enrich the Si isotope composition of the

products in light isotopes (i.e. the condensates). A third possibility is that there has been mixing of various components as described in Dauphas et al. (2015) who assumed that material with a Solar composition was added to match the Si isotope composition. Last, we have only modeled a melting process but there could have been some low pressure crystallization of the angrite magmas that could have modified them and made it difficult to recover the mantle source composition. Our approach was clearly simplistic but illustrative. Overall, our modeling results do suggest that the Si isotope composition of angrites can be explained by the presence of early condensates in the angrite parent body and the calculated composition for the angrite parent body match with those of angrites, once the effect of melt is taken into account.

Table 8: Oxide composition of the initial APB silicate mantle used for the partial melting model. Oxide compositions are from condensate formed at 1800 K for the 100 x CI model and at 2000 K for the 500 x CI model.

wt% in APB mantle	100 x CI	500 x CI
SiO_2	35.52	34.30
MgO	22.10	21.72
FeO	15.81	16.58
Al_2O_3	14.56	15.05
CaO	11.20	11.56
Cr_2O_3	0.13	0.09
Na_2O	0.0009	0.001
TiO_2	0.68	0.70

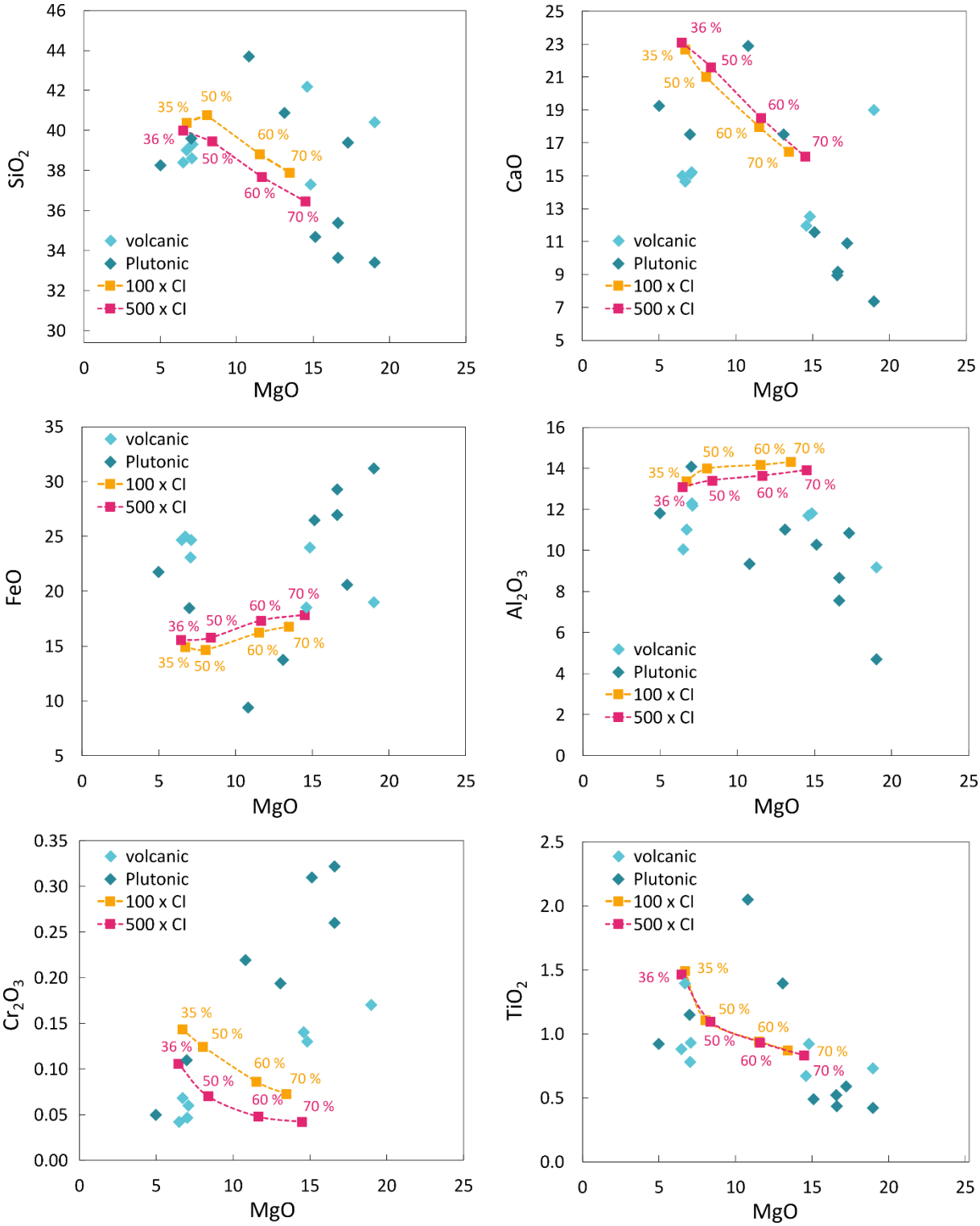

Figure 5 : Major oxide compositions of melt from two APB mantle source (Table 8). Angrite data from the literature are also shown for reference (see Table 9 for data references).

Table 9: Composition in major oxides of six volcanic angrites and nine plutonic angrites from the literature

	Sahara 99555	**D'Orbigny**	**D'Orbigny glass**	**Asuka 881371**	**NWA 1296**	**LEWIS 87051**	**NWA1670**
Reference	Mittlefehldt et al., 2002	Mittlefehldt et al., 2002	Varela et al., 2003	Yanai, 1994	Jambon et al., 2005	Jurewicz et al., 1993	Keil 2012
Petrologic type	volcanic	volcanic	volcanic	volcanic	volcanic	volcanic	volcanic
SiO_2 (wt. %)	38.60	38.40	39.30	37.30	39.00	40.40	42.18
TiO_2	0.91	0.89	0.78	0.88	0.93	0.73	0.67
Al_2O_3	12.50	12.40	12.30	10.07	12.20	9.19	11.70
FeO	23.10	24.70	24.70	24.00	25.00	19.00	18.52
MnO	0.26	0.28	0.27	0.20	0.28	19.00	0.22
MgO	7.04	6.49	7.10	14.81	6.71	19.00	14.60
CaO	15.10	15.00	15.20	12.51	14.65	19.00	11.95
Na_2O	0.02	0.02		0.03	0.03		0.01
Cr_2O_3	0.05	0.04	0.06	0.13	0.07	0.17	0.14
P_2O_5	0.15	0.16		0.17	0.17		
SO_2							
K_2O				0.02	<0.03		
Total	97.72	98.38	99.81	100.12	100.00		
Mg#	35.20	31.90	33.80	52.38	68.09		

References: Mittlefehldt and Lindstrom, 1990; Yanai, 1994; Mittlefehldt *et al.*, 2002; Jambon *et al.*, 2005; Varela *et al.*, 2003; Riches *et al.*, 2012; Keil, 2012; Irving *et al.*, 2020; Baghdadi *et al.*, 2015.

(Table 9 continued)

	Angra dosReis	**Angra dos Reis**	**NWA4590**	**NWA4590**	**NWA4801**	**NWA4931**	**LEWIS 86010**	**NWA2999**	**NWA 3164**	**NWA 5167**	**NXA 12774**
Reference	Mittlefehldt and Lindstrom, 1990	Riches et al., 2012	Riches 2012	Keil 2012	Riches et al., 2012	Riches et al., 2012	Jurewicz et al., 1993	Keil 2012	Baghdadi et al., 2015	Baghdadi et al., 2015	Irving et al., 2020
Petrologic type	plutonic	plutonic	plutonic	plutonic	plutonic	plutonic	plutonic	plutonic	plutonic	plutonic	plutonic
SiO_2 (wt. %)	43.70	43.50	38.27	37.49	40.87	33.63	39.60	33.40	35.37	34.68	39.38
TiO_2	2.05	2.01	0.92	1.46	1.40	0.44	1.15	0.42	0.52	0.49	0.59
Al_2O_3	9.35	8.94	11.82	8.50	11.04	8.69	14.10	4.71	7.58	10.30	10.86
FeO	9.40	9.81	21.75	27.16	13.74	26.96	18.50	31.20	29.29	26.52	20.63
MnO	0.10	0.12	0.27	0.31	0.16	0.22	0.20	0.24	0.21	0.21	0.23
MgO	10.80	11.42	4.98	17.84	13.10	16.62	7.00	19.00	16.60	15.12	17.25
CaO	22.90	21.93	19.25	6.80	17.52	9.18	17.50	7.37	8.95	11.55	10.90
Na_2O	0.03	0.03	0.02	0.11	0.05	0.01			0.01	0.01	0.32
Cr_2O_3	0.22	0.20	0.05		0.19	0.32	0.11		0.26	0.31	
P_2O_5	0.13	0.25	0.22		0.26	0.11					0.17
SO_2		0.12	0.31		0.05	0.03					
K_2O		0.01	0.02		0.01	0.01					
Total	99.88	98.31	97.89		98.39	96.21					
Mg#	67.20	67.49	28.99		62.96	52.32					

5. Conclusions

The Si isotope analysis of angrites in this study show a mean δ^{30}Si value of -0.22 ‰ (±0.02, 2SD, n=6) and this confirms their relatively heavy Si isotope signature comparing to other planetary materials. The Si isotope composition of angrites cannot be explained by either impact-induced volatilization or evaporation at the surface of a magma ocean.

Our modeling has shown that the Si isotope composition of angrites is consistent with their parent material having condensed at high temperature with a high dust to gas ratio (100 to 500 $\times$ CI). This could explain both the high δ^{30}Si value typical of angrites that suggests a significant fraction of olivine rather than enstatite (that forms at lower temperatures in these conditions). Our estimated composition of the mantle of the APB using high temperature condensates is consistent with the high FeO content found in angrites. Furthermore, the composition of mantle melts overlaps with the major element compositions of the angrite group. In particular, this high temperature condensation does produce the enrichment in refractory elements and the high Al/Si typical of angrites while the SiO_2 of APB melts is characteristically low.

In order to get a perfect fit with the Si isotope composition and the major element compositions of angrites, one probably needs to consider both kinetic and equilibrium isotope fractionation of Si isotope during condensation.

If the Earth has included in its building blocks, materials that were similar to angrites, then its Si isotope composition could also be high thanks to the presence of early condensates and this would also explain the enrichment in refractory lithophile elements that is a characteristic of the Earth's mantle.

(Morbidelli *et al.*, 2020)

(Qin *et al.*, 2016)

(Tissot *et al.*, 2018)

References

Armytage, R.M.G., Georg, R.B., Savage, P.S., Williams, H.M., Halliday, A.N. (2011) Silicon isotopes in meteorites and planetary core formation. *Geochimica et Cosmochimica Acta* 75, 3662–3676.

Armytage, R.M.G., Georg, R.B., Williams, H.M., Halliday, A.N. (2012) Silicon isotopes in lunar rocks: Implications for the Moon's formation and the early history of the Earth. *Geochimica et Cosmochimica Acta* 77, 504–514.

Baghdadi, B., Jambon, A., Barrat, J.-A. (2015) Metamorphic angrite Northwest Africa 3164/5167 compared to magmatic angrites. *Geochimica et Cosmochimica Acta* 168, 1–21.

Bale, C.W. *et al.* (2016) FactSage thermochemical software and databases, 2010–2016. *Calphad* 54, 35–53.

Bourdon, B., Fitoussi, C. (2020) Isotope Fractionation during Condensation and Evaporation during Planet Formation Processes. *ACS Earth and Space Chemistry*. American Chemical Society 4, 1408–1423.

Brearley, A.J. (2006) *Meteorites and the Early Solar System II*. University of Arizona Press.

Burbine, T.H., McCoy, T.J., Meibom, A., Gladman, B., Keil, K. (2002) Meteoritic parent bodies: Their number and identification. University of Arizona Press.

Dauphas, N., Poitrasson, F., Burkhardt, C., Kobayashi, H., Kurosawa, K. (2015) Planetary and meteoritic Mg/Si and δ30Si variations inherited from solar nebula chemistry. *Earth and Planetary Science Letters* 427, 236–248.

Ebel, D.S., Grossman, L. (2000) Condensation in dust-enriched systems. *Geochimica et Cosmochimica Acta* 64, 339–366.

Fitoussi, C., Bourdon, B., Kleine, T., Oberli, F., Reynolds, B.C. (2009) Si isotope systematics of meteorites and terrestrial peridotites: implications for Mg/Si fractionation in the solar nebula and for Si in the Earth's core. *Earth and Planetary Science Letters* 287, 77–85.

Fitoussi, C., Bourdon, B. (2012) Silicon Isotope Evidence Against an Enstatite Chondrite Earth. *Science* 335, 1477–1480.

Fitoussi, C., Bourdon, B., Wang, X. (2016) The building blocks of Earth and Mars: A close genetic link. *Earth and Planetary Science Letters* 434, 151–160.

Georg, R.B., Reynolds, B.C., Frank, M., Halliday, A.N. (2006) New sample preparation techniques for the determination of Si isotopic compositions using MC-ICPMS. *Chemical Geology* 235, 95–104.

Greenwood, R.C., Franchi, I.A., Jambon, A., Buchanan, P.C. (2005) Widespread magma oceans on asteroidal bodies in the early Solar System. *Nature* 435, 916–918.

Hin, R.C. *et al.* (2017) Magnesium isotope evidence that accretional vapour loss shapes planetary compositions. *Nature* 549, 511–515.

Irving, A.J., Carpenter, P.K., Tepper, J.H., Righter, M., Lapen, T.J., Busemann, H. (2020) Petrology and Chemical Composition of Olivine-Pyroxene-Phyric Quenched Angrite Northwest Africa 12774. 51st Annual Lunar and Planetary Science Conference 2020 2399.

Jambon, A., Barrat, J.A., Boudouma, O., Fonteilles, M., Badia, D., Göpel, C., Bohn, M. (2005) Mineralogy and petrology of the angrite Northwest Africa 1296. *Meteoritics & Planetary Science* 40, 361–375.

Jurewicz, A.J.G., Mittlefehldt, D.W., Jones, J.H. (1993) Experimental partial melting of the Allende (CV) and Murchison (CM) chondrites and the origin of asteroidal basalts. *Geochimica et Cosmochimica Acta* 57, 2123–2139.

Jurewicz, A.J.G., Jones, J.H., Mittlefehldt, D.W., Longhi, J., Dr, G. (2004) Devolatized-Allende partial melts as analog for primitive angrite. abstract no.1417.

Keil, K. (2012) Angrites, a small but diverse suite of ancient, silica-undersaturated volcanic-plutonic mafic meteorites, and the history of their parent asteroid. *Geochemistry* 72, 191–218.

Kleine, T., Hans, U., Irving, A.J., Bourdon, B. (2012) Chronology of the angrite parent body and implications for core formation in protoplanets. *Geochimica et Cosmochimica Acta* 84, 186–203.

Kurat, G., Varela, M.E., Brandstätter, F., Weckwerth, G., Clayton, R.N., Weber, H.W., Schultz, L., Wäsch, E., Nazarov, M.A. (2004) D'Orbigny: A non-igneous angritic achondrite? *Geochimica et Cosmochimica Acta* 68, 1901–1921.

Lodders, K. (2020) Solar Elemental Abundances. *Oxford Research Encyclopedia of Planetary Science*. Oxford University Press.

Longhi, J. (1999) Phase equilibrium constraints on angrite petrogenesis. *Geochimica et Cosmochimica Acta* 63, 573–585.

Lugmair, G.W., Galer, S.J.G. (1992) Age and isotopic relationships among the angrites Lewis Cliff 86010 and Angra dos Reis. *Geochimica et Cosmochimica Acta* 56, 1673–1694.

McKay, G., Le, L., Wagstaff, J., Crozaz, G. (1994) Experimental partitioning of rare earth elements and strontium: Constraints on petrogenesis and redox conditions during crystallization of Antarctic angrite Lewis Cliff 86010. *Geochimica et Cosmochimica Acta* 58, 2911–2919.

Mittlefehldt, D.W., Killgore, M., Lee, M.T. (2002) Petrology and geochemistry of D'Orbigny, geochemistry of Sahara 99555, and the origin of angrites. *Meteoritics & Planetary Science* 37, 345–369.

Mittlefehldt, D.W., Lindstrom, M.M. (1990) Geochemistry and genesis of the angrites. *Geochimica et Cosmochimica Acta* 54, 3209–3218.

Morbidelli, A., Libourel, G., Palme, H., Jacobson, S.A., Rubie, D.C. (2020) Subsolar Al/Si and Mg/Si ratios of non-carbonaceous chondrites reveal planetesimal formation during early condensation in the protoplanetary disk. *Earth and Planetary Science Letters* 538, 116220.

Myers, J., Eugster, H.P. (1983) The system Fe-Si-O: Oxygen buffer calibrations to 1,500K. *Contributions to Mineralogy and Petrology* 82, 75–90.

Pringle, E.A., Savage, P.S., Badro, J., Barrat, J.-A., Moynier, F. (2013) Redox state during core formation on asteroid 4-Vesta. *Earth and Planetary Science Letters* 373, 75–82.

Pringle, E.A., Moynier, F., Savage, P.S., Badro, J., Barrat, J.-A. (2014) Silicon isotopes in angrites and volatile loss in planetesimals. *Proceedings of the National Academy of Sciences* 111, 17029–17032.

Qin, T., Wu, F., Wu, Z., Huang, F. (2016) First-principles calculations of equilibrium fractionation of O and Si isotopes in quartz, albite, anorthite, and zircon. *Contributions to Mineralogy and Petrology* 171, 91.

Riches, A.J.V., Day, J.M.D., Walker, R.J., Simonetti, A., Liu, Y., Neal, C.R., Taylor, L.A. (2012) Rhenium–osmium isotope and highly-siderophile-element abundance systematics of angrite meteorites. *Earth and Planetary Science Letters* 353–354, 208–218.

Righter, K., Humayun, M., Danielson, L. (2008) Partitioning of palladium at high pressures and temperatures during core formation. *Nature Geoscience* 1, 321–323.

Righter, K., Sutton, S.R., Danielson, L., Pando, K., Newville, M. (2016) Redox variations in the inner solar system with new constraints from vanadium XANES in spinels. *American Mineralogist* 101, 1928–1942.

Savage, P.S., Georg, R.B., Williams, H.M., Burton, K.W., Halliday, A.N. (2011) Silicon isotope fractionation during magmatic differentiation. *Geochimica et Cosmochimica Acta* 75, 6124–6139.

Savage, P.S., Moynier, F. (2013) Silicon isotopic variation in enstatite meteorites: Clues to their origin and Earth-forming material. *Earth and Planetary Science Letters* 361, 487–496.

Savage, P.S., Armytage, R.M.G., Georg, R.B., Halliday, A.N. (2014) High temperature silicon isotope geochemistry. *Lithos* 190–191, 500–519.

Scott, E.R.D., Bottke, W.F. (2011) Impact histories of angrites, eucrites, and their parent bodies. *Meteoritics & Planetary Science* 46, 1878–1887.

Shirai, N., Humayun, M., Righter, K. (2009) Analysis of Moderately Siderophile Elements in Angrites: Implications for Core Formation of the Angrite Parent Body. Lunar and Planetary Science Conference 2009 2122.

Solomatova, N.V., Caracas, R. (2019) Pressure-Induced Coordination Changes in a Pyrolitic Silicate Melt From Ab Initio Molecular Dynamics Simulations. *Journal of Geophysical Research: Solid Earth* 124, 11232–11250.

Steenstra, E.S., Sitabi, A.B., Lin, Y.H., Rai, N., Knibbe, J.S., Berndt, J., Matveev, S., van Westrenen, W. (2017) The effect of melt composition on metal-silicate partitioning of siderophile elements and constraints on core formation in the angrite parent body. *Geochimica et Cosmochimica Acta* 212, 62–83.

Suzuki, H., Ozawa, K., Nagahara, H., Mikouchi, T. (2014) Estimation of the size of the angrite parent body. Japan Geoscience Union 2014.

Tissot, F.L.H., Collinet, M., Dauphas, N., Grove, T.L. (2018) Establishing the liquid phase equilibrium of angrites to constrain their petrogenesis. *49th Lunar and Planetary Science Conference, No. 2083*.

Varela, M.E., Kurat, G., Zinner, E., Métrich, N., Brandstätter, F., Ntaflos, T., Sylvester, P. (2003) Glasses in the D'Orbigny angrite. *Geochimica et Cosmochimica Acta* 67, 5027–5046.

Volkov, A.N., Johnson, R.E., Tucker, O.J., Erwin, J.T. (2011) Thermally Driven Atmospheric Escape: Transition from Hydrodynamic to Jeans Escape. *The Astrophysical Journal* 729, 16.

Yanai, K. (1994) Angrite Asuka-881371: Preliminary examination of a unique meteorite in the Japanese collection of Antarctic meteorites. *Antarctic Meteorite Research* 7, 30.

Yoneda, S., Grossman, L. (1995) Condensation of CaO-MgO-Al2O3-SiO2 liquids from cosmic gases. *Geochimica et Cosmochimica Acta* 59, 3413–3444.

Young, E.D., Shahar, A., Nimmo, F., Schlichting, H.E., Schauble, E.A., Tang, H., Labidi, J. (2019) Near-equilibrium isotope fractionation during planetesimal evaporation. *Icarus* 323, 1–15.

Zambardi, T., Poitrasson, F. (2011) Precise Determination of Silicon Isotopes in Silicate Rock Reference Materials by MC-ICP-MS. *Geostandards and Geoanalytical Research* 35, 89–99.

Zambardi, T., Poitrasson, F., Corgne, A., Méheut, M., Quitté, G., Anand, M. (2013) Silicon isotope variations in the inner solar system: Implications for planetary formation, differentiation and composition. *Geochimica et Cosmochimica Acta* 121, 67–83.

Chapter 5

Silicon isotope effects of He ion irradiation on olivine

Silicon isotope effects of He ion irradiation on olivine

Keywords: irradiation, isotope fractionation, sputtering, evaporation

Abstract

During the early history of the Solar System or in molecular clouds, dust particles are submitted to intense irradiation by protons and helium nuclei accelerated at MeV energies or greater. The isotope effects of irradiation at such energies are poorly known but major element modifications of chemical compositions suggest that there could also be isotope fractionation due to irradiation.

In this study, we have analysed the Si isotope composition of olivine layers produced by sputter deposition starting from a San Carlos olivine and the deposits were irradiated by He^{2+} for a total fluence of $1.5x10^{17}$. The olivine deposits were analysed prior to and after irradiation for Si isotopes by multi-collector ICPMS. The Si isotope composition after sputter deposition was enriched in heavy Si isotopes with a mean δ^{30}Si value of 12.6‰ relative to the NBS 28 standard whereas the irradiated olivine had lower δ^{30}Si values of 10.8 and 8.2‰ for the 200 keV and 6 MeV irradiation, respectively. In both cases, the Si isotope fractionation are strictly mass dependent. First, these results show that the process of sputter deposition induces a large enrichment in heavy Si isotopes that we attribute to a difference in sticking coefficient for the heavy Si isotopes compared with the light Si isotopes. Second, the effect of He irradiation is the reverse of what is expected from theoretical studies and numerical simulations of isotope fractionation under these conditions of irradiation. The enrichment in light Si isotopes could be due to redistribution processes and segregation that take place during the irradiation. This study suggests that Si isotopes could be powerful tracers of irradiation processes in astrophysical settings.

1. Introduction

It has long been known that young stars can produce intense X-ray flares in their early stage that come together with large fluxes of particles (Feigelson and Montmerle, 1999; Güdel, 2004). These flares correspond to enhancement factors of 10^4 to 10^5 compared with present-day activity, suggesting that they could have an effect on the elemental and isotope compositions of the fine-grained dust that would get irradiated. The energy spectrum of the stellar energetic particles around T-Tauri stars shows a predominance of protons and helium with energies between 100 keV and 100 MeV (e.g. Rab *et al.*, 2017; Rodgers-Lee *et al.*, 2021). Intense irradiation and sputtering could also take place in interstellar clouds where refractory dust can be irradiated and eventually destroyed (Field *et al.*, 1997; Jäger *et al.*, 2016; May *et al.*, 2000). The presence of GEMS (glass with embedded metals and sulfides) in cometary IDPs (interplanetary dust particles) characterized by amorphous silicate glass has been interpreted as being the remnant of such dust grains (Bradley, 1994) but others have interpreted them as being condensed in the early Solar System (Keller *et al.*, 2005). Deciphering between a pre-solar and solar system origin of these grains is thus a topic of great interest.

The experimental irradiation of olivine with He^+ ions has demonstrated that this process could cause substantial chemical modification of the olivine with a lowering of the Mg/Si and O/Si ratios (Carrez *et al.*, 2001, 2002) or loss of oxygen in the case of fayalite (Davoisne and Leroux, 2006). It was shown that irradiation leads to amorphization of the olivine e.g. (Brucato *et al.*, 2004). Similarly, the irradiation of olivine by 1.43 MeV deuteron (Shilobreeva and Kuzmin, 2004) also demonstrated large losses of Mg and Fe, together with a destruction of the olivine. It was never investigated whether irradiation at these energies would cause any isotope modification of the remaining olivine and whether such changes would be mass dependent. For example, (Esat, 1988) suggested that sputtering of Mg with 5 keV electron could cause isotope fractionation and even mass independent effects. There is abundant literature documenting the isotope effect of sputtering in secondary ion mass spectrometers (e.g. Sigmund 1987). However, most studies have focused on low energy beam (<100 keV) where the main

process involved in sputtering is due to direct knock-on reaction or linear cascades. For these energy ranges, the observations (Russell *et al.*, 1980) and theoretical predictions (Shulga and Sigmund, 1995; Sigmund, 1987; Watson and Haff, 1980) are that the light isotopes are preferentially removed by sputtering with a decreasing magnitude of the effect as energy increases in the tens of keV ranges. While there are numerous studies investigating irradiation with higher energy ions (in the MeV range), these studies have not focused on the isotope effects of irradiation.

In this study, we have focused on the irradiation of olivine using 200 keV and 6 MeV He ions using fluences relevant to the early Solar System as an attempt to explore the possible effect on the Si isotope composition of irradiation.

2. Samples and analytical procedure

2.1. Sample description

Isotope analysis were performed on 12 synthetic olivine samples deposited on an ultra-pure copper foil and consisted in 9 irradiated samples and 3 standard samples, i.e. not irradiated. The synthetized olivine was analysed by electron microscopy and share perfect stoichiometry with the San Carlos Olivine, ensuring the quality of the sputter deposition device (Table 1). The synthetic olivine samples were deposited on a thin layer sized 0.5 mm x 0.5 mm of ultra-pure copper (99.9999 wt%) using a PIPS (GatanTM) deposition chamber before being used as support material for the irradiation. The pressure inside the PIPS chamber was 10^{-7} bar and the energy of Ar^{+} ions was 5keV for a total ion current of 250µA. The rate of deposition (0.2-0.3 Å/s) was slow enough to avoid any temperature elevation of the olivine deposit. Targets were then irradiated with $1.57.10^{17}$ He^{2+} ions with 200 keV for 5 samples labelled “1” and with 6 MeV for the 4 samples labelled “2”. The thickness of targets “1” and “2” was measured respectively to 370 nm and 380 nm by an AFM (atomic force microscope) with an uncertainty of 10%. Copper was initially radioactive after the irradiation process due to the activation of the Cu and samples were left to decay away. The colour of the samples was slightly modified as a

result of irradiation. All the targets were then stored carefully in a box and fixed to the bottom of the box with a strong adhesive tape. This black adhesive tape sticking to the targets subsequently caused analytical difficulties for silicon isotope measurements and this aspect will be discussed later in this paper.

Table 1 : Microanalysis of prepared olivine targets and San Carlos olivine by electron microscopy.

Element (%)	Target	San Carlos olivine
Mg	26.58	25.55
O	56.24	57.16
Si	13.55	14.31
Cr	0.03	0.02
Al	0.39	0.02
Fe	2.94	2.81
Ni	0.14	0.1
Zn	0.12	0
Total (%)	100	99.97

2.2. Alkali fusion technique

The standard bracketing standard NBS28 and the two secondary standards Diatomite and BHVO-2 (a well-characterized Hawaiian basalt) were prepared using a modified alkaline fusion technique described in previous studies (Fitoussi *et al.*, 2009). A mass of ≈ 4 mg for standard NBS28 and ≈ 1 mg for both Diatomite and BHVO-2 were introduced in a silver crucible with a ≈ 200 mg NaOH pellet. The mixture was heated for 7 min 30 at 730 °C in a furnace. The fusion cake was initially left to cool down at room temperature and introduced in a 30 mL Teflon Savillex Vial filled with approximately 25 mL of MilliQ deionized water. An ultrasonic tip was introduced in each vial for 4 minutes and the solutions were left to equilibrate overnight on a hotplate at 120 °C. The sample solutions were then transferred carefully in Teflon bottles. Each vial was rinsed several times with MilliQ water to allow the recovery of all the silicon after the fusion step. MilliQ water was added to reach a silicon concentration of ≈ 6 mg/L in the solutions. The resulting very basic solutions were acidified to a pH value between 2 and 3

with HCl 6 M. This acidification step was reported to avoid precipitation of metallic hydroxides and polymerization of silica species which can lead to silicon isotope fractionation (Fitoussi *et al.*, 2009).

2.3. Dissolution procedure

A dissolution preparation technique was preferred to the usual alkaline fusion technique used for silicon isotope measurements because of the potential hazardous formation of silver-copper alloy during the fusion procedure. Analytical tests were performed on copper foil prior to the analysis of the irradiated targets to demonstrate the reliability of the chemical procedure. Copper was dissolved easily by either nitric or hydrochloric acid at various concentrations (Table 2). Considering that the analytical procedure used for silicon isotope measurements was for an HCl-based matrix, hydrochloric acid was preferred. The lower molarity was chosen to reduce the volume of sodium hydroxide used to adjust the pH of solutions prior to ion-chromatography. To optimize silicon blank value, two times distilled hydrochloric acid was used at a concentration of 0.5 M for sample dissolution. After the dissolution step, solutions were acidic (pH≈1) rather than usually basic after the alkaline fusion procedure (pH>14). Thus, two very clean solutions of 0.5 M and 0.25 M NaOH and were prepared and added to the sample solutions to reach a pH value between 2 and 3 to ensure accuracy of isotope measurements (Fitoussi *et al.*, 2009).

Table 2: Dissolution tests performed with nitric and hydrochloric acid at different molarities.

Acid	Molarity	Temperature (°C)	Dissolution time
HNO_3	15 M (concentrated)	Ambient	< 1 min
HNO_3	7.5 M	80 °C	≈ 8 h
HCl	10 M (concentrated)	80 °C	≈ 8 h
HCl	2 M	80 °C	≈ 18 h
HCl	1 M	80 °C	≈ 18 h
HCl	0.5 M	80 °C	≈ 24 h

2.4. Column chromatography

After the dissolution step, sample solutions were loaded on BioRad poly-prep columns filled with 1 mL bed volume of Bio Rad cationic resin (H^+) 50W-X8, 200-400 mesh for sample purification. The cleaning and loading procedure followed the steps described in Table 3. A blue layer was observed on the top of the resin after loading the sample solution. The purification procedure produced a full recovery of silicon with a yield close to 100 %. In slightly acidic solution, copper is in the form of Cu^+ with a majority of Cu^{2+}, as suggested by the blue colour of the dissolved solutions and can also form various complexes such as CuCl and $Cu(OH)_2$ (Charlot, 1983). A significant amount of copper not sticking to the resin would lead to matrix effects and inaccurate isotope measurements. Therefore, the concentration of copper after the column chromatography purification step was checked with an ICAP-Q mass spectrometer prior to isotope analysis. The results showed no residual copper in the purified solution and then ensure the validity of the dissolution and separation protocol.

Table 3: Column chromatography procedure for silicon separation

Separation Stage	Solution	Volume
Pre-cleaning resin	3 N HCl	Column reservoir
Pre-cleaning resin	6 N HCl	Column reservoir
Pre-cleaning resin	15 N HNO_3	200 µl
Pre-cleaning resin	6 N HCl	Column reservoir
Pre-cleaning resin	3 N HCl	Column reservoir
Pre-cleaning resin	Milli-Q	4 column reservoirs
Sample load	Acidified sample solution to pH 2-3	1.5 µg Si
Elution	Milli-Q	2 ml
Dilution to running concentration	Milli-Q	Added to reach ≈ 0.5 ppm

2.5. Mass spectrometry

Isotope measurements were carried out with a Neptune Plus MC-ICP-MS in medium resolution mode with a resolving power of ≈ 7500 allowing partial resolution of Si from its major isobaric interferences. Samples were injected into the argon plasma source with a DSN-100 desolvating system equipped with a PFA nebulization chamber (heated to 100°C to ensure solvent vaporization) and a PFA nebulizer with a 76 µL/min flow rate. After plasma ignition, a period of at least 4h was allowed for the mass spectrometer and the blank signal to stabilize prior to making any isotope measurements. Table 4 shows the characteristic mass spectrometer configuration for high precision Si isotope measurements. Each sample was measured in one block of 36 cycles with an integration time of 8.389 s and an uptake time of 3 s to allow signal stabilization. The washing procedure between two samples lasted 75 s and included two different 0.002 M HCl solutions. The instrumental blank was measured in the cleanest 0.002 M HCl wash solution prior and after each isotope measurement and subtracted from the sample signal by taking an average on-peak-zero (OPZ). The instrumental mass fractionation was corrected with the sample-standard bracketing technique. Isotope ratios $^{29}Si/^{28}Si$ and $^{30}Si/^{28}Si$ in samples were expressed relative to the ratios of the standard NBS28 as follows, with exponent x corresponding to either mass 29 or 30:

$$\delta^x Si = \left[\frac{\left(\frac{\delta^x Si}{\delta^{28} Si}\right)_{sample}}{\left(\frac{\delta^x Si}{\delta^{28} Si}\right)_{NBS-28}} - 1 \right] \times 1000 \quad (1)$$

A typical measurement session included 6 measurements of 3 different targets with approximately 10 measurements of the secondary standard Diatomite in order to check for mass dependence and mass bias stability during the sequence. The two secondary standards, Diatomite and the well-characterized hawaïan basalt BHVO-2, were analysed in this study leading to respectively $\delta^{30}Si$ = 1.27 ± 0.08 (2SD, n=122) and $\delta^{30}Si$ = -0.28 ± 0.07 (2SD, n=101) well within the range of previously reported data, and the data are shown in Figure 1 (Armytage *et al.*, 2011, 2012; Dauphas *et al.*, 2015; Fitoussi *et al.*, 2009;

Fitoussi and Bourdon, 2012; Pringle *et al.*, 2013, 2014; Savage *et al.*, 2011; Savage and Moynier, 2013; Zambardi *et al.*, 2013; Zambardi and Poitrasson, 2011).

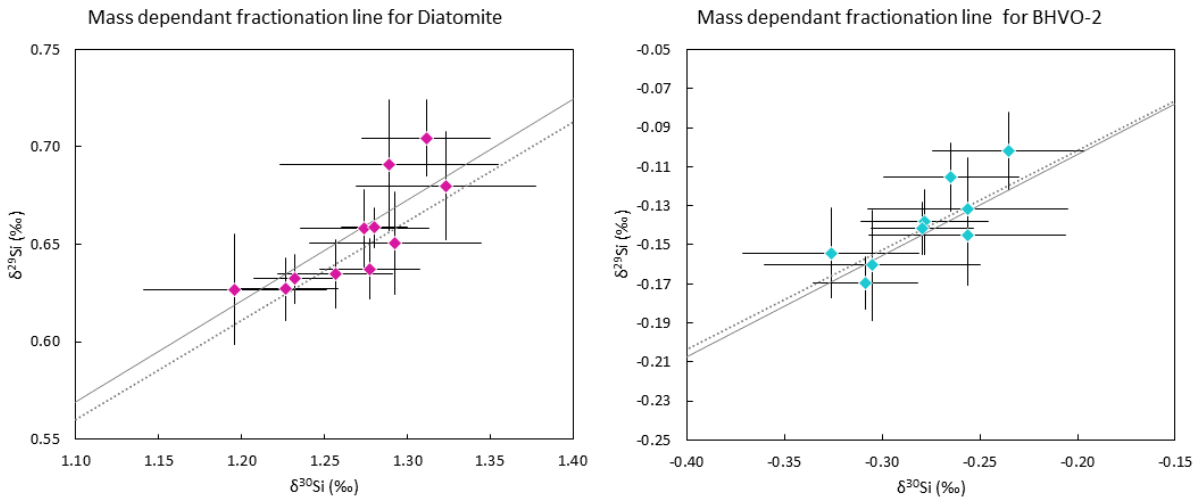

Figure 1: $\delta^{30}Si$ and $\delta^{29}Si$ (± 2SE) of the two secondary standards Diatomite and BHVO-2 measured in this study. The two lines represent equilibrium (solid line) and kinetic (dotted line) mass-dependent fractionation.

Table 4: Mass spectrometer and desolvator settings for silicon isotope analysis.

Parameter	Neptune Plus
Rf power	1200
Sampler cone	Standard "H"-type, Nickel
Skimmer cone	Jet "X"-type, Nickel
Coolant gas (Ar) flow	16 l/min
Auxiliary gas (Ar) flow	1.23 l/min
Z torch position	2.5 mm
Nebulizer uptake rate	76 µl/min
Cup configuration	H3: ^{30}Si; C: ^{29}Si; L3: ^{28}Si
Si runing concentration	0.5 ppm
Sensitivity on ^{28}Si beam	≈ 15 V
Instrumental blank	≈ 200 mV
Desolvating device	DSN-100
DSN nebulizer pressure	30 PSI
DSN hot gas flow	0.2 l/min
DSN membrane gas (Ar) flow	≈ 4 - 5 l/min

2.6. Sensitivity and blanks

Particular attention was paid to lower instrumental and analytical blanks. For example, the quartz torch as well as the desolvating system contained significant amount of undesired silica. Parameters such as the axial torch position, gas fluxes and cone choice were optimized in order to maximize the sensitivity and the signal over noise ratio without generating isobaric interferences. A higher signal/noise ratio, limited the random fluctuations in the blank signal that ultimately affects the isotopic signal, resulting in more accurate and reproducible measurements. The sensitivity of isotope measurements reached ≈ 15 V for the primary standard NBS28 on mass 28, which corresponded to a sensitivity to ≈ 30 V/ppm. The optimized instrumental blank signal achieved ≈ 0.2 V and then led to a signal to noise ratio of 75. The analytical blank was measured for the various reagents used in this procedure. The blank signal was shown to vary from 0 V to 2.6 V depending on the NaOH solution used for pH adjustment. The use of double-distilled acids for the column procedure did not improve significantly the blank level, therefore single-distilled acid was used for the ion-chromatography step. The residual blank signal was generated by the copper foil, as the level of blank signal was directly correlated with the amount of copper dissolved in the solutions loaded on the column. To test silicon environment pollution, copper foil was cleaned in MilliQ deionized water and left for a few minutes in ultrasonic bath prior to the dissolution procedure. The surprising Si blank level at ≈ 4 V highlighted the necessity of developing reliable analytical procedures.

To conclude, the analytical procedure used the following steps: (1) dissolution with 3.6 ml of double distilled 0.5 M HCl in a 7 ml clean Teflon beaker (2) adjustment of pH using NaOH solution from ultra-pure pellets and (3) ion-chromatography using distilled HCl and HNO_3 acids. This analytical procedure yielded a blank level of 60 mV for a target-type sample, corresponding to a signal to noise ratio of 250, which is well suited for silicon isotope measurements.

2.7. Adhesive tape management

The mechanical removal of the glue from the Cu targets was highly challenging, regarding the mm-sized of the samples and the sticking strength of the glue. Therefore, a chemical separation procedure was preferred. Separation of the glue from the target consisted in selective dissolution by HCl since the glue was not dissolved by this acid. Nevertheless, some small black particles were floating in the solution after complete dissolution of the copper foil. The solutions were then left for settling for a few hours. A large number of tests were performed by adding a small piece of glue with a piece of copper to determine if the clean supernatant had to be removed or centrifugated and if the addition of NaOH solution had to be done prior or after the removal of the supernatant. The addition of NBS28 at the dissolution step made it possible to quantify isotope fractionation induced by the possible adsorption of silicon on the adhesive. Then four different test samples were prepared and labelled “Cu blank” for a copper solution sample; “Cu blank + glue” for a copper solution sample with a piece of glue; “Cu NBS” for a copper solution sample with an added volume of NBS28 standard solution; “Cu NBS + glue” for a copper solution sample with a piece of glue and an added volume of NBS28 standard solution. The results of the analytical tests are described in Table 5. In Table 5, the blank level attached to each procedure is indicated, as well as the isotopic fractionation of the test samples “Cu NBS” and “Cu NBS + glue” with respect to the standard solution NBS28. Each procedure was performed with and without adding a volume of 200 µl of a Prefilter resin at the bottom of the chromatography column to add a supplementary parameter for the analytical procedure optimization. Figure 2 shows the Si isotope fractionation of the two tested samples “Cu NBS” and “Cu NBS + glue” relative to standard NBS28. The purpose of these tests was to optimize the analytical procedure by obtaining the lowest blank signal without generating Si isotope fractionation. One of the procedures could thus be validated and consists in introducing NaOH directly in the beaker after the dissolution step without any additional concern for the residual glue left in suspension in the solution. Then, the operator had to avoid pipetting suspended particles prior to loading the solution on the separation column. A volume of 0.8 to 0.9 ml corresponding to ≈ 1.5 µg of silicon was then loaded on the column, as the silicon content of each

olivine target was ≈ 6 µg. MilliQ water was added after the column procedure to match Si concentration of the bracketing standard NBS28 prior to mass spectrometer measurement.

Table 5: Results on blank levels and isotope fractionation relative to NBS28 of the two standards "Cu NBS" and "Cu NBS + glue"

(a)	**NaOH added prior to 20 min ultrasonic bath**				**NaOH added after 20 min ultrasonic bath**			
Blank value on ^{28}Si for	without Prefilter		with Prefilter		without Prefilter		with Prefilter	
Cu blank	36 mV		37 mV		23 mV		27 mV	
Cu blank + glue	175 mV		174 mV		/		/	
Isotope ratios	**δ^{29}Si (‰)**	**δ^{30}Si (‰)**	**δ^{29}Si (‰)**	**δ^{30}Si (‰)**	**δ^{29}Si (‰)**	**δ^{30}Si (‰)**	**δ^{29}Si (‰)**	**δ^{30}Si (‰)**
Cu NBS	0.07	0.16	0.06	0.12	0.05	0.13	-0.01	-0.03
Cu NBS + glue	0.06	0.15	0.1	0.2	0.15	0.31	0.12	0.26

(b)	**NaOH added prior to 4 min ultrasonic tip**				**NaOH added after 3 min 30 ultrasonic tip**			
Blank value on ^{28}Si for	without Prefilter		with Prefilter		without Prefilter		with Prefilter	
Cu blank	690 mV		655 mV		209 mV		196 mV	
Cu blank + glue	269 mV		267 mV		367 mV		402 mV	
Isotope ratios	**δ^{29}Si (‰)**	**δ^{30}Si (‰)**	**δ^{29}Si (‰)**	**δ^{30}Si (‰)**	**δ^{29}Si (‰)**	**δ^{30}Si (‰)**	**δ^{29}Si (‰)**	**δ^{30}Si (‰)**
Cu NBS	0.02	0.08	0.01	0.1	-0.03	-0.1	0.05	0.07
Cu NBS + glue	0.09	0.16	-0.03	0.02	-0.03	0.01	-0.01	-0.07

(c)	**NaOH added to the supernatant solution**	**NaOH directly added in the 7 mL teflon beaker**
Blank value on ^{28}Si for	without Prefilter / With Prefilter	without Prefilter / with Prefilter
Cu blank	52 mV / /	33 mV 52 mV[1] / /
Cu blank + glue	77 mV / /	/ 51 mV 81 mV[1]

Isotope ratios	$\delta^{29}Si$ (‰)	$\delta^{30}Si$ (‰)	$\delta^{29}Si$ (‰)	$\delta^{30}Si$ (‰)	$\delta^{29}Si$ (‰)	$\delta^{30}Si$ (‰)	$\delta^{29}Si$ (‰)	$\delta^{30}Si$ (‰)
Cu NBS			-0.01	-0.02			0.05 0.03[1]	0.03 0.02[1]
Cu NBS + glue			0.03	0.30			-0.01 0.02[1]	0.01 0.05[1]

[1] Data generated two weeks later to ensure reproducibility of the method.

Note: The tables (a) and (b) consider respectively the addition of an extra ultrasonic bath step and an extra ultrasonic tip step; table (c) summarizes the results with and without collecting the supernatant. Adding directly the NaOH solution into the beaker containing the glue seems to generate the lower blank level and isotope fractionation of the two tested standards.

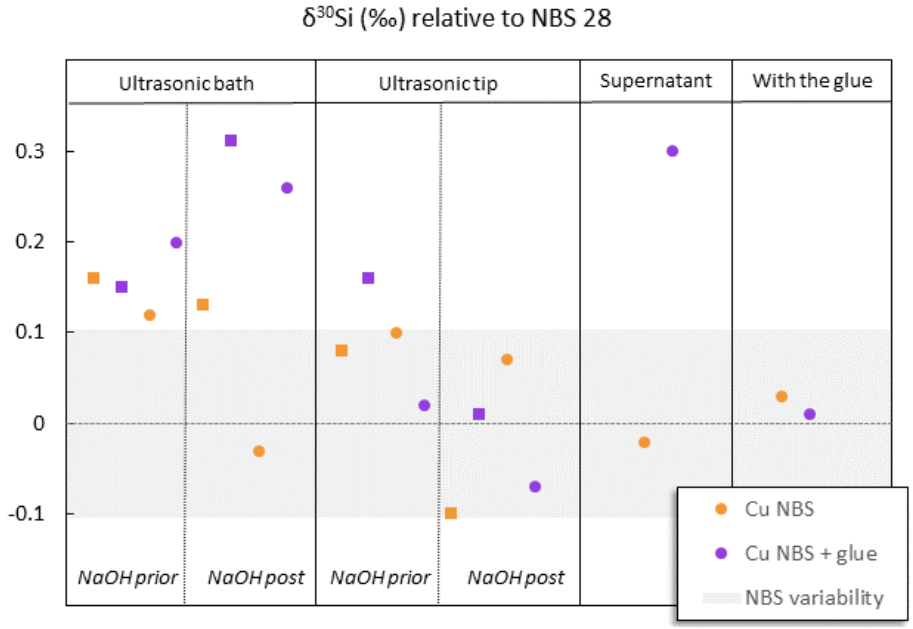

Figure 2: Results of the tests performed on the samples "Cu NBS" and "Cu NBS + glue" according to different analytical procedures described in the main text. The circle symbol show data for samples that passed through a column equipped with a prefilter layer. The shaded area corresponds to intra NBS28 standard variability during a running sequence (≈ 0.1 ‰). The purpose of these tests was to establish the analytical procedure which will cause the smallest Si isotope fractionation for the two samples, i.e. orange and purple circles should be as close as possible to zero. This configuration was obtained with direct addition of the NaOH solution into the beaker without any concern about the suspended glue particles (corresponding to the last configuration "With the glue"). Data are from Table 5.

3. Results

The isotope composition of the different targets is reported in Table 6. Each datapoint represents the average on 4 running sequences where each sample was measured 6 times. The Si isotope composition of targets shows a large range of isotope variation with δ^{30}Si ranging from 6 to 13.2 ‰ (Figure 3). The Si isotope data are mass dependent in a δ^{29}Si versus δ^{30}Si diagram (Figure 4). The slope value of 0.505 is closer to the theoretical kinetic fractionation line (slope 0.5092) than equilibrium fractionation line (slope 0.5178). The 3 targets labelled "Standard" show the largest δ^{30}Si with an average equal to 12.6 ‰. The 200 keV irradiated targets show a lighter isotope composition with a δ^{30}Si of 10.8 ‰ relative to the standard targets. The 6MeV irradiated targets are even lighter with an average δ^{30}Si of 8.2 ‰. Data dispersion within target of the same type is probably due to the sample preparation procedure, as the δ^{30}Si variability of a target during a running sequence do not excess 0.5 ‰ which is smaller than the observed δ^{30}Si variability among a given type of target. The four targets irradiated with 6 MeV He display significant isotope values from 6 to 10.2 ‰.

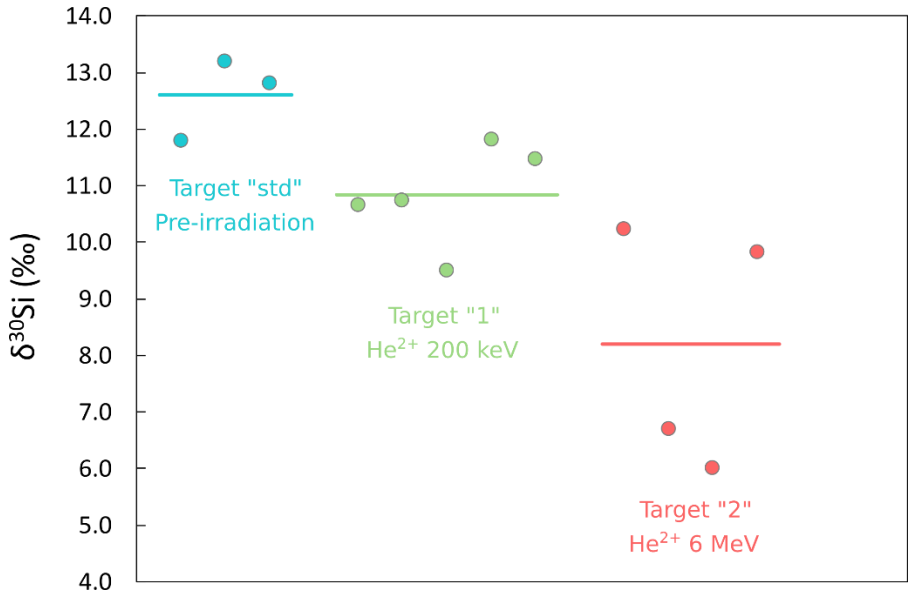

Figure 3: Silicon isotope composition of the 3 different types of targets. The 3 targets labelled "standard" were not irradiated, the 5 targets "1" were irradiated with a flux of 1.57 10^{17} He^{2+} ions at 200 keV and the 4 targets "2" were irradiated with the same procedure with a 6 MeV He flux. Coloured lines represent the mean δ^{30}Si of each target type. Error bars are smaller than data points.

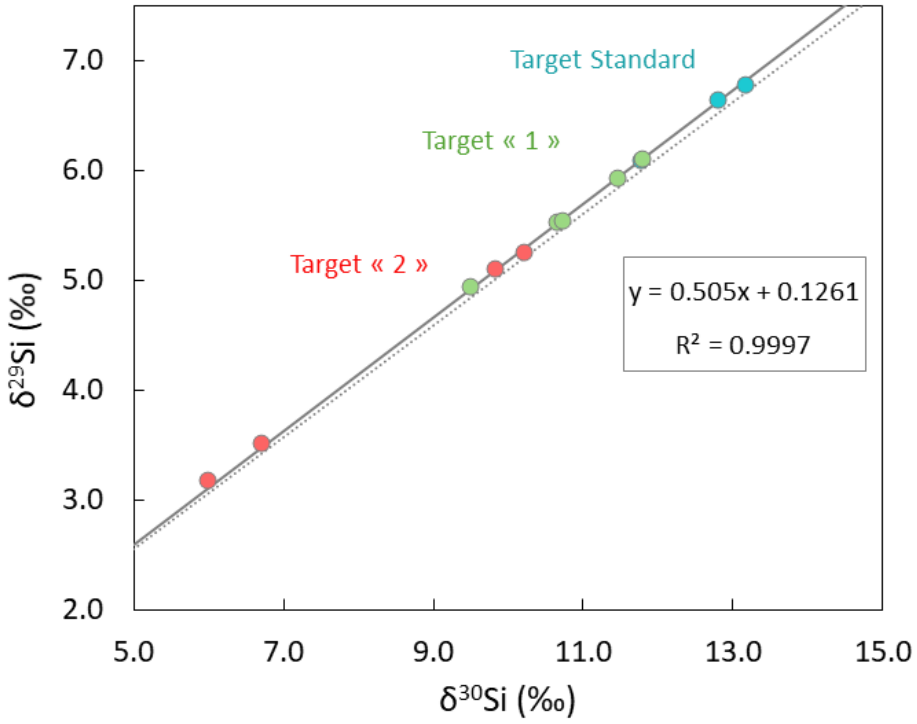

Figure 4: The Si isotope composition of the targets are mass-dependent. The grey line represents equilibrium fractionation (slope 0.5178) and the dashed line kinetic fractionation (slope 0.5092).

Table 6: Isotope composition of the 3 different targets analysed in this study.

	Sample number	**δ^{29}Si (‰)**	2SD	**δ^{30}Si (‰)**	2SD	n[1]
Target Std	1	**6.1**	0.06	**11.8**	0.12	4
Target Std	2	**6.8**	0.05	**13.2**	0.01	4
Target Std	3	**6.6**	0.05	**12.8**	0.08	4
Average target Std		**6.5**	0.72	**12.6**	1.45	N = 3
Target 1	1	**5.5**	0.06	**10.7**	0.15	4
Target 1	2	**5.5**	0.02	**10.7**	0.05	4
Target 1	3	**4.9**	0.06	**9.5**	0.08	4
Target 1	4	**6.1**	0.08	**11.8**	0.08	4
Average target 1		**5.6**	0.90	**10.8**	1.77	N = 5
Target 2	1	**5.2**	0.08	**10.2**	0.11	4
Target 2	2	**3.5**	0.03	**6.7**	0.02	4
Target 2	3	**3.2**	0.05	**6.0**	0.05	4
Target 2	4	**5.1**	0.09	**9.8**	0.12	4
Average target 2		**4.3**	2.13	**8.2**	4.29	N = 4

[1] n is the number of running sequence in which the target was measured (with approximately two times 3 consecutives measurements per sequence of the same sample).

4. Discussion

The results presented in the previous sections indicate that there is a resolvable Si isotope fractionation associated both with the sputter deposition of olivine on the copper foil and with the He^{2+} irradiation. In what follows, we shall discuss successively both sets of observations.

4.1. Sputtering and deposition of olivine

The deposition of olivine is preceeded by an efficient sputtering of olivine powder by a 5 keV Ar^{+} beam. One key observation for understanding the respective role of sputtering followed by deposition is the fact that the stoichiometry of the re-deposited olivine is that of the San Carlos olivine (Table 1). If there were a substantial elemental (and isotope) fractionation associated with the sputtering, then one would not expect to find a different stoichiometric composition for the re-deposited olivine. In fact, one would expect that there should be a fractionation in major element and an enrichment in light isotopes in the deposited olivine. Indeed, for a 5keV energy, theoretical work, simulations and observations predict an enrichment in light isotopes or light elements in the sputtered material (Russell *et al.*, 1980; Shulga and Sigmund, 1995; Sigmund, 1987). If the sputtering takes places over sufficient time, reservoir effects should result in no isotope fractionation as the residual material will get enriched in the heavy isotopes. Thus, once a steady state is reached, then there should be no further fractionation. Any fractionation (if there is any) should in fact, be in the reverse direction in this energy regime. Thus, our interpretation is that the Si isotope fractionation did not take place (except perhaps transiently) during the olivine sputtering.

With an incident energy of 5 keV, it is possible to calculate an estimate of the energy imparted to the sputtered Si atoms, assuming elastic collisions. According to (Murakami and Shingyoji, 1990), the energy transfer coefficient i.e. the ratio of the energy of the Si sputtered atom (m_2) to the energy of the incoming Ar ion with mass m_1 is:

$$\varepsilon = \frac{4m_1m_2}{(m_1+m_2)^2}cos^2\theta \qquad (2)$$

where θ is the angle between the colliding atoms. Thus for an argon atom colliding with Si, the value of ε is equal to 0.97 assuming θ=0. The energy of sputtered atoms is thus much greater than the thermal energy of gas molecules at the temperature of the chamber (room temperature). Since the distance between the olivine target and the copper plate is only of a few centimetres, one may wonder whether this distance is long enough to thermalize the kinetic energies of sputtered Si vapor species, i.e. elastic collisions should ultimately redistribute kinetic energy to the mean kinetic energy of the system. The parameter that will tell how many collisions are likely to take place in a gas is the mean free path. For a silicon atom at a pressure of 10^{-6} Torr with a temperature of at most 300 K (room temperature), the mean free path is:

$$l = \frac{1}{n\pi\sigma^2} = 205\ m \qquad (3)$$

where n is the number density and σ is the cross section of silicon atoms (220 pm). This means that the sputtered atoms will not be greatly affected by collisional exchange of kinetic energy as they move from the sputtered source to the copper foil.

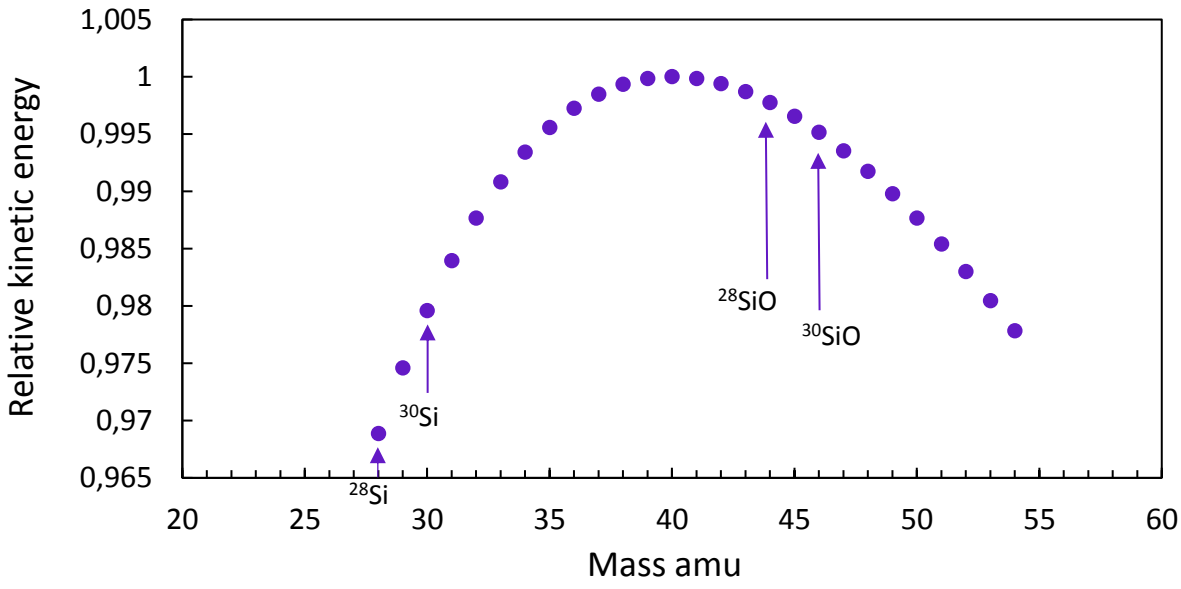

Figure 5: Relative kinetic energy of sputtered atoms or molecules scaled to ^{40}Ar primary ion kinetic energy.

The Si atoms will be deposited on the copper surface with a relatively high kinetic energy and they may or may not stick to the surface at every collision. The parameter that describes the efficiency of sticking is the sticking coefficient which has been characterized in studies of vapor deposition following sputtering. It turns out that the sticking coefficient decreases with increasing kinetic energy (Kneitz *et al.*, 1999; Matar *et al.*, 2010; Zhou and Wadley, 1999), meaning that reflection of atoms or molecules is greater if they have higher velocities. In principle, the stable species of olivine during evaporation is SiO(g) while the commonly reported Si species during sputtering is Si(g). If there is a small amount of O in the chamber, then one can observe that SiO will be present (e.g. Santamaría *et al.*, 1986). Interestingly, this has a strong impact on the energetics of sputtered particles. If the sputtered species or the species in the vapor is Si dominantly, then the kinetic energy of ^{30}Si will be greater than that of ^{28}Si. If on the other hand it is SiO, then the kinetic energy of ^{30}SiO will be smaller than that of ^{28}SiO (Figure 5). As the sticking coefficient decreases with greater energy this should result in an enrichment in heavy Si isotope in the olivine deposit, which would be in agreement with the observations.

Thus, one possible interpretation of our results is that there is kinetic isotope fractionation, that combines the effect of sputtering and deposition and a role for the sticking coefficient dependence on kinetic energy is suggested.

4.2. Isotope fractionation associated with irradiation of He

Based on the data presented in Figure 3, the effect of irradiation of olivine by a He beam is to enrich the target in light Si isotopes by 1.8 to 4.4 ‰. In principle, for an irradiation with a 200 keV or 6 MeV He beam, there are two main mechanisms that will result in energy loss of the incident ions. At lower energy, the principal mechanism of ion-matter interaction is via knock-on reactions or linear cascade (this corresponds to nuclear stopping) while at energies higher than 1 keV the main mechanism is by electronic interactions (Figure 6). In this case, the main interaction occurs via ionization of the target atoms and this will ultimately release some energy that can locally heat up the target.

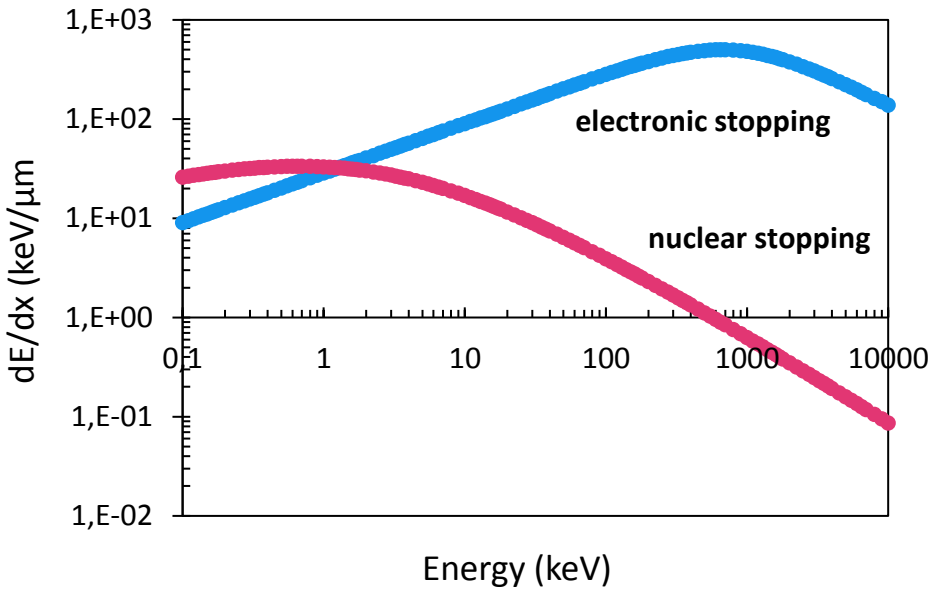

Figure 6: Energy loss in keV/µm for He irradiation of forsteristic olivine showing the relative importance of nuclear and electronic stopping.

An important difference in the two irradiation conditions is also that the distance over which energy is deposited is different between 200 keV and 6 MeV. As shown by the results of SRIM simulations in Figure 7 (Ziegler *et al.*, 1985), the ion trajectories are rather different for the two cases, with far less interaction per unit of distance in the 6 MeV case. The simulations were run using the energy parameters for olivine as given in May et al. (2000). The corresponding damage is also different with 3.6 vacancies/ion created with 200 keV and 0.1 vacancies/ion created with 6 MeV.

At low energies, the interaction of a heavy ion such as He^{2+} is to directly knock the target atoms either by direct sputtering from the surface or by producing a cascade of collisions where kinetic energy will be transmitted to other atoms in the target. It is then called a linear cascade as long as the chains of collisions are independent. As mentioned above, for low energy of the incident ion, the theoretical prediction is that the light isotopes with mass M_1 will be preferentially sputtered compared with the heavier isotope with mass M_2:

$$\frac{Y_1}{Y_2} = \frac{n_1}{n_2}\left(\frac{M_2}{M_1}\right)^m \left(\frac{U_2}{U_1}\right)^{1-2m} \quad (4)$$

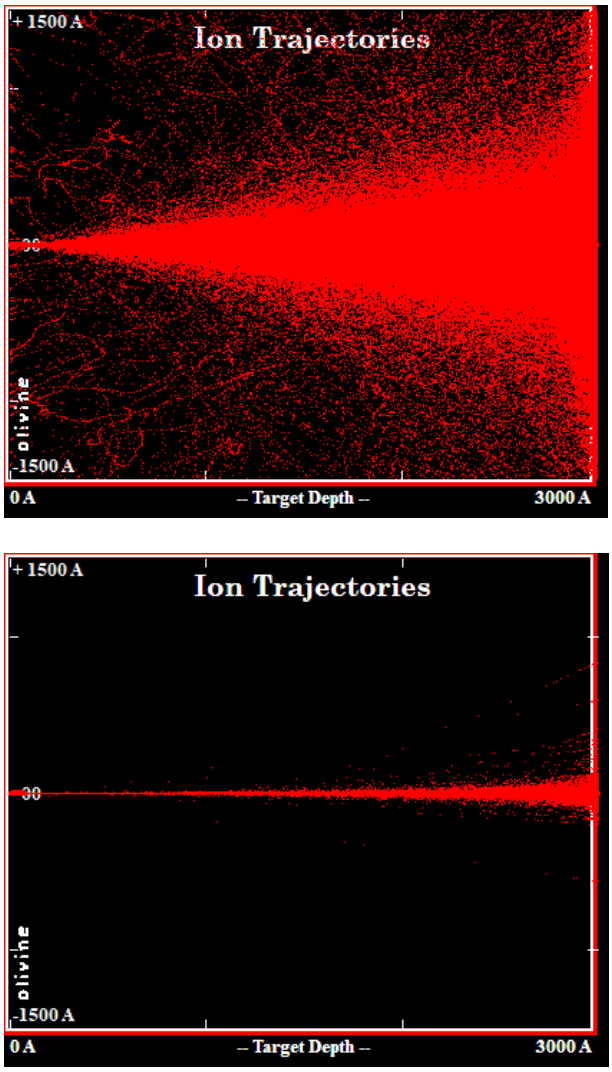

Figure 7: SRIM simulations of olivine irradiation by He^{2+} ions for (a) 200 keV and (b) 6MeV energy of incident particles. The total number of He ions is here 300000 in both cases.

with m being a parameter depending on the interatomic potentials of the target atoms and U_i represents the surface binding energy of isotope i (Sigmund 1987). Since the value of m is rather small (typically 0.055), there is in fact a stronger dependence on a second term which is the surface binding energy. However, more complete treatment of preferential sputtering including the effect of incident ion energy has shown that additional terms could play a role. In a refined theory, one needs to consider two additional terms that were developed by (Sckerl *et al.*, 1996a):

$$\frac{Y_1}{Y_2} = \frac{n_1}{n_2}\left(\frac{M_1}{M_2}\right)^{\frac{1}{2}-2m} + \frac{n_1}{n_2}\left(\frac{M_2}{M_1}\right)^{m}\left(1 + \frac{M_2 - M_1}{M}Z(m)\right) \quad (5)$$

The first term in this equation favor the heavy isotope indicating that heavy isotope should be sputtered preferentially. The second term in this equation favors also the heavy isotopes since the function Z(m) is always positive (see details in Sckerl and Sigmund 1996). However, these authors concluded that these terms should be small compared with that expressed in the previous equation.

When the incident particle has higher energies (>1keV), the incident He^{2+} ions will produce large amounts of ionization in the olivine and it is thought that this will produce a thermal spike at a temperature depending on the amount of energy deposited per unit of length (Kelly, 1977; Sigmund and Szymonski, 1984; Toulemonde *et al.*, 2011). The elevation of temperature will result in evaporation from the surface of the irradiation olivine. The flux of evaporated Si isotopes i can be described with the following equation:

$$\phi_i = \frac{P_{i,sat}(T)\gamma_i}{\sqrt{2\pi M_i kT}} \quad (6)$$

T represents here is local temperature spike linked with irradiation, this temperature can reach several thousands of degrees. The coefficient γ_i represents the efficiency of evaporation and will depend on the activation energy of condensation for isotope (e.g. Bourdon and Fitoussi, 2020). In any case, if one examines the ratio of isotope flux using this equation:

$$\frac{\phi_i}{\phi_j} = \frac{P_{i,sat}}{P_{j,sat}}\frac{\gamma_i}{\gamma_j}\left(\frac{M_j}{M_i}\right)^{\frac{1}{2}} \quad (7)$$

In this equation, the dominant effect will be the mass difference, predicting a higher flux of the light isotope relative to the heavy isotope, the reverse of what is observed for our irradiated targets. This means that the thermal spike model alone cannot explain our observations.

One can hypothesize that other secondary processes linked to the input of energy associated with irradiation could modify the chemical properties of the irradiated olivine (e.g. Lam and Wiedersich, 1981, 1986; Sckerl *et al.*, 1996b)and produced a locally different Si isotope composition. Several mechanisms could play a role: the difference in the surface properties of the irradiated layer could modify the chemical or isotope affinities due for example to radiation damage or differences in diffusion coefficients of isotopes could lead to surfacial segregation and this effect would build up as

irradiation proceeds (Lam and Wiedersich, 1986). In the case of irradiated silicate, it has been shown that the elevation of temperatures to several thousands of degrees would modify the silicate structure by producing 2 or 3- coordinated Si (Chowdhury *et al.*, 2016). A tentative explanation could be that this low coordinated Si would be enriched in ^{30}Si, since low coordinated Si should be enriched in heavy isotopes (Schauble, 2004). It has been highlighted in several studies that the irradiation itself would create defects that could speed up the rates of diffusion (Lam and Wiedersich, 1986), thereby favouring the redistribution and segregation of elements and isotopes. In this case, as ^{28}Si is lighter it would more rapidly diffuse out more rapidly than ^{30}Si. Altogether, these processes could produce local enrichment in ^{30}Si in the 'heated tube' located in the subsurface of the olivine; this will lead to an enhancement of ^{30}Si loss by vaporization (Figure 8). If this material is then quantitatively vaporized this will produce a net enrichment in light isotopes in the irradiated olivine. This sequence of events would require a better knowledge of the timescale associated with each process, notably a good quantification of the relative timescales of diffusion and vaporization.

This scenario is consistent with a dependence on energy, since it is expected that the radiation damage should be distributed differently depending on the value of the parameter dE/dx, the amount of dissipated energy per unit of length (Figure 6). A complete quantitative treatment is clearly beyond the scope of this study and would require knowledge of the parameters involved in these redistribution processes. However, our results clearly show that the classical explanation of thermal spike is not sufficient to explain our results and the role of secondary surficial processes give a qualitatively satisfactory interpretation.

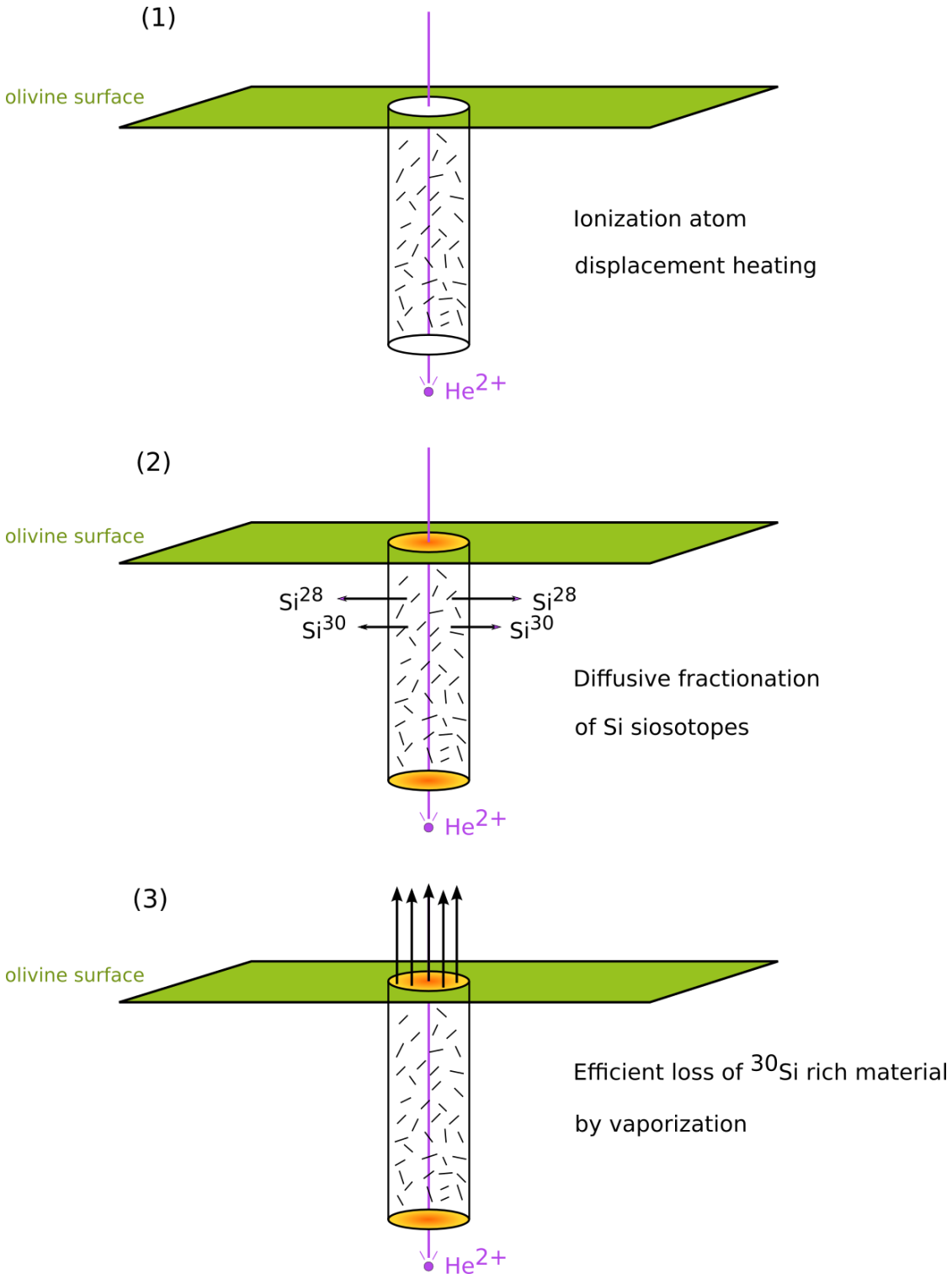

Figure 8: Schematic diagram illustrating a scenario for interpreting the Si isotope in irradiated olivine. (1) energetic He particle produces a hot track following ionization and atom displacement (2) this modifies the structure of olivine (e.g. loss of SiO_4 structure) and enhances diffusion within the track (3) material enriched in ^{30}Si is efficiently vaporization leading to an enrichment in light Si isotope in the bulk material.

5. Conclusions

Our study has demonstrated the existence of new processes leading to unusual Si isotope fractionation that have some relevance for cosmochemistry, astrophysics and material sciences.

First, we have shown that the sputter deposition of forsteritic olivine leads to a strong enrichment in heavy silicon isotopes in the re-deposited olivine by approximately 12‰. This enrichment is interpreted by the coupling of two effects: first there is a difference in energy distribution between isotopologues of the vapor species SiO, this difference may explain differences in the sticking coefficients of ^{30}SiO and ^{28}SiO upon deposition. This study thus provides new insights into an isotope fractionation mechanism associated with condensation in highly energetic environments.

Second, the analyses of irradiated olivine by 200 keV and 6 MeV He^{2+} ions also show mass dependent Si isotope fractionation with an enrichment in light isotopes of the sputtered target by 1.8 to 4.4 ‰, with an increasing fractionation at higher energies of the incident particles. This is the reverse of the expected isotope fractionation associated with a thermal spike or linear cascade reactions. This suggests that other secondary processes must play a role. This could include structural changes in Si coordination that are known to take place during irradiation or diffusive redistribution of Si isotopes following irradiation.

This study demonstrates that Si isotope signatures could be a useful tracer for deciphering the history of irradiation in astrophysical environments; this approach could be used to study the effect of protracted irradiation in presolar grains, in GEMS or in meteoritic materials. More work is needed to understand the kinetic aspects of element and isotope distribution that may affect the isotope composition of sputtered material.

References

Armytage, R.M.G., Georg, R.B., Savage, P.S., Williams, H.M., Halliday, A.N. (2011) Silicon isotopes in meteorites and planetary core formation. *Geochimica et Cosmochimica Acta* 75, 3662–3676.

Armytage, R.M.G., Georg, R.B., Williams, H.M., Halliday, A.N. (2012) Silicon isotopes in lunar rocks: Implications for the Moon's formation and the early history of the Earth. *Geochimica et Cosmochimica Acta* 77, 504–514.

Bourdon, B., Fitoussi, C. (2020) Isotope Fractionation during Condensation and Evaporation during Planet Formation Processes. *ACS Earth and Space Chemistry*. American Chemical Society 4, 1408–1423.

Bradley, J.P. (1994) Chemically Anomalous, Preaccretionally Irradiated Grains in Interplanetary Dust from Comets. *Science*. American Association for the Advancement of Science 265, 925–929.

Brucato, J.R., Strazzulla, G., Baratta, G., Colangeli, L. (2004) Forsterite amorphisation by ion irradiation: Monitoring by infrared spectroscopy. *Astronomy & Astrophysics*. EDP Sciences 413, 395–401.

Carrez, P., Demyk, K., Cordier, P., Gengembre, L., Grimblot, J., D'hendecourt, L., Jones, A.P., Leroux, H. (2002) Low-energy helium ion irradiation-induced amorphization and chemical changes in olivine: Insights for silicate dust evolution in the interstellar medium. *Meteoritics & Planetary Science* 37, 1599–1614.

Carrez, P., Leroux, H., Cordier, P., Guyot, F. (2001) Electron-irradiation-induced phase transformation and fractional volatilization in $(Mg,Fe)_2SiO_4$ olivine thin films. *Philosophical Magazine A* 81, 2823–2840.

Charlot, G. (1983) *Les réactions chimiques en solution aqueuse: et caractérisation des ions*. Paris, France.

Chowdhury, S.C., Haque, B.Z. (Gama), Gillespie, J.W. (2016) Molecular dynamics simulations of the structure and mechanical properties of silica glass using ReaxFF. *Journal of Materials Science* 51, 10139–10159.

Dauphas, N., Poitrasson, F., Burkhardt, C., Kobayashi, H., Kurosawa, K. (2015) Planetary and meteoritic Mg/Si and δ30Si variations inherited from solar nebula chemistry. *Earth and Planetary Science Letters* 427, 236–248.

Davoisne, C., Leroux, H. (2006) Structural and compositional modifications of fayalite Fe_2SiO_4 under electron irradiation. *Nuclear Instruments and Methods in Physics Research Section B: Beam Interactions with Materials and Atoms* 243, 371–376.

Esat, T.M. (1988) Physicochemical Isotope anomalies. *Geochimica et Cosmochimica Acta* 52, 1409–1424.

Feigelson, E.D., Montmerle, T. (1999) High-Energy Processes in Young Stellar Objects. *Annual Review of Astronomy and Astrophysics* 37, 363–408.

Field, D., May, P.W., Pineau des Forêts, G., Flower, D.R. (1997) Sputtering of the refractory cores of interstellar grains. *Monthly Notices of the Royal Astronomical Society* 285, 839–846.

Fitoussi, C., Bourdon, B. (2012) Silicon Isotope Evidence Against an Enstatite Chondrite Earth. *Science* 335, 1477–1480.

Fitoussi, C., Bourdon, B., Kleine, T., Oberli, F., Reynolds, B.C. (2009) Si isotope systematics of meteorites and terrestrial peridotites: implications for Mg/Si fractionation in the solar nebula and for Si in the Earth's core. *Earth and Planetary Science Letters* 287, 77–85.

Güdel, M. (2004) X-ray astronomy of stellar coronae. *The Astronomy and Astrophysics Review* 12.

Jäger, C., Sabri, T., Wendler, E., Henning, T. (2016) Ion-induced processing of cosmic silicates: a possible formation pathway to gems. American Astronomical Society 831, 66.

Keller, L.P., Messenger, S., Christoffersen, R. (2005) Gems revealed: spectrum imaging of aggregate grains in interplanetary dust. 2.

Kelly, R. (1977) Theory of thermal sputtering. *Radiation Effects*. Taylor & Francis 32, 91–100.

Kneitz, S., Gemeinhardt, J., Koschel, H., Held, G., Steinrück, H.-P. (1999) Energy and temperature dependent sticking coefficients of CO on ultrathin copper layers on Ru(001). *Surface Science* 433–435, 27–31.

Lam, N.Q., Wiedersich, H. (1981) Modifications of subsurface alloy composition during high-temperature sputtering. *Journal of Nuclear Materials* 103, 433–437.

Lam, N.Q., Wiedersich, H. (1986) Bombardment-induced segregation and redistribution. *Nuclear Instruments and Methods in Physics Research Section B: Beam Interactions with Materials and Atoms* 18, 471–485.

Matar, E., Bergeron, H., Dulieu, F., Chaabouni, H., Accolla, M., Lemaire, J.L. (2010) Gas temperature dependent sticking of hydrogen on cold amorphous water ice surfaces of interstellar interest. *The Journal of Chemical Physics*. American Institute of Physics 133, 104507.

May, P.W., Pineau des Forêts, G., Flower, D.R., Field, D., Allan, N.L., Purton, J.A. (2000) Sputtering of grains in C-type shocks. *Monthly Notices of the Royal Astronomical Society* 318, 809–816.

Murakami, Y., Shingyoji, T. (1990) Compositional difference between films and targets in sputtering of refractory metal silicides. *Journal of Vacuum Science & Technology A: Vacuum, Surfaces, and Films* 8, 851–854.

Pringle, E.A., Moynier, F., Savage, P.S., Badro, J., Barrat, J.-A. (2014) Silicon isotopes in angrites and volatile loss in planetesimals. *Proceedings of the National Academy of Sciences* 111, 17029–17032.

Pringle, E.A., Savage, P.S., Badro, J., Barrat, J.-A., Moynier, F. (2013) Redox state during core formation on asteroid 4-Vesta. *Earth and Planetary Science Letters* 373, 75–82.

Rab, C., Güdel, M., Padovani, M., Kamp, I., Thi, W.-F., Woitke, P., Aresu, G. (2017) Stellar energetic particle ionization in protoplanetary disks around T Tauri stars. *Astronomy & Astrophysics* 603, A96.

Rodgers-Lee, D., Vidotto, A.A., Taylor, A.M., Rimmer, P.B., Downes, T.P. (2021) Stellar versus Galactic: The intensity of energetic particles at the evolving Earth and young exoplanets. *arXiv:2108.05739 [astro-ph]*.

Russell, W.A., Papanastassiou, D.A., Tombrello, T.A. (1980) The fractionation of Ca isotopes by sputtering. *Radiation Effects*. Taylor & Francis 52, 41–52.

Santamaría, J., Iborra, E., Sánchez Quesada, F., González Díaz, G., Rodríguez Vidal, M. (1986) Sputtering of SiO_2 in O_2-Ar atmospheres. *Thin Solid Films* 139, 201–208.

Savage, P.S., Georg, R.B., Williams, H.M., Burton, K.W., Halliday, A.N. (2011) Silicon isotope fractionation during magmatic differentiation. *Geochimica et Cosmochimica Acta* 75, 6124–6139.

Savage, P.S., Moynier, F. (2013) Silicon isotopic variation in enstatite meteorites: Clues to their origin and Earth-forming material. *Earth and Planetary Science Letters* 361, 487–496.

Schauble, E.A. (2004) Applying Stable Isotope Fractionation Theory to New Systems. *Reviews in Mineralogy and Geochemistry* 55, 65–111.

Sckerl, M.W., Sigmund, P., Lam, N.Q. (1996a) Ion-beam induced compositional changes in alloys at elevated temperatures. *Nuclear Instruments and Methods in Physics Research Section B: Beam Interactions with Materials and Atoms* 120, 221–225.

Sckerl, M.W., Sigmund, P., Vicanek, M. (1996b) Particle fluxes in atomic collision cascades. *Mat. Fys. Medd. Dan. Vid. Selsk.* 44.

Shilobreeva, S.N., Kuzmin, L.E. (2004) Simulation of the Ion Modification Processes in the Silicate Dust of Protoplanetary Disks. *Solar System Research* 38, 59–65.

Shulga, V.I., Sigmund, P. (1995) Simulation of energy-dependent isotope sputtering. *Nuclear Instruments and Methods in Physics Research Section B: Beam Interactions with Materials and Atoms* 103, 383–386.

Sigmund, P. (1987) Mechanisms and theory of physical sputtering by particle impact. *Nuclear Instruments and Methods in Physics Research Section B: Beam Interactions with Materials and Atoms* 27, 1–20.

Sigmund, P., Szymonski, M. (1984) Temperature-dependent sputtering of metals and insulators. *Applied Physics A* 33, 141–152.

Toulemonde, M., Weber, W.J., Li, G., Shutthanandan, V., Kluth, P., Yang, T., Wang, Y., Zhang, Y. (2011) Synergy of nuclear and electronic energy losses in ion-irradiation processes: The case of vitreous silicon dioxide. *Physical Review B* 83, 054106.

Watson, C.C., Haff, P.K. (1980) Sputter-induced isotopic fractionation at solid surfaces. *Journal of Applied Physics*. American Institute of Physics 51, 691–699.

Zambardi, T., Poitrasson, F. (2011) Precise Determination of Silicon Isotopes in Silicate Rock Reference Materials by MC-ICP-MS. *Geostandards and Geoanalytical Research* 35, 89–99.

Zambardi, T., Poitrasson, F., Corgne, A., Méheut, M., Quitté, G., Anand, M. (2013) Silicon isotope variations in the inner solar system: Implications for planetary formation, differentiation and composition. *Geochimica et Cosmochimica Acta* 121, 67–83.

Zhou, X.W., Wadley, H.N.G. (1999) Hyperthermal vapor deposition of copper: athermal and biased diffusion effects. *Surface Science* 431, 42–57.

Ziegler, J.F., Littmark, U., Biersack, J.P. (1985) *The stopping and range of ions in solids*. Pergamon, New York.

Chapter 6

Conclusions and perspectives

Conclusions and Perspectives

The purpose of this doctoral thesis was first to develop a reliable and sensitive method for the analysis of silicon isotopes by multiple collector inductively coupled plasma mass spectrometry. Although there had been great improvements in the methods for analysing silicon isotopes over the past fifteen years, its application to cosmochemistry has been slowed down by discrepancies in existing data set for meteorites of various groups and by analytical difficulties that have not been really sorted out.

This was clearly the case for angrites which had been analysed in two previous studies showing mean values that were significantly different from each other outside of errors. Our results also show a restricted range, thereby allowing a more confident interpretation of the origin of the unusual Si isotope record in angrites. We have shown that by combining detailed thermodynamical modeling of both condensation and partial melting, we can explain in general terms the genesis of the angrite parent body. In principle, there could have been a wide range of temperatures and redox conditions for condensation that would match the Si isotopes. However, if one takes into account the major element chemistry, the redox state of the APB, our modeling shows that condensation with a high dust to gas ratio is more consistent with the data. By adding this constraint, one can specify better the condensation temperature. Our results are of broader significance than simply understanding the genesis of angrites, it could be that bodies similar to angrites were important constituents of the Earth.

The study of martian meteorites has also illustrated that, despite that the mean values of our data set is identical within error with previous data, the range of our data set is narrower. Our modeling of the SNC meteorite data could in the end be explained by the crystallization of a magma ocean that has left tenuous variations in Si isotopes that correlate with Sm/Nd ratios of the SNC mantle source. Unlike the Earth where subsequent magmatic activity and convective motions has gradually erased magma ocean signatures, there was indeed hope that the Martian mantle could have preserved an early signature. This indicates that efficient mixing of the mantle has been incomplete. As the total range of Si isotope variations is in fact small the reliability data needs to be reemphasized. One could hope that in the future, one could gain further confidence in the reliability of Si isotope data but how this could be achieved remains an open question.

If there indeed such magma ocean signature in the Martian mantle, one would ultimately like to know how these signatures correspond to various depths/mineralogies in the mantle and whether these reservoirs have been affected by a giant overturn, as has been described in the literature. A more comprehensive data set where one would have Hf-W, Sm-Nd, Lu-Hf and Si isotopes on the same SNC samples would certainly be helpful. It is certain that having a broader range of compositions could demonstrate our result more clearly, as our modeling suggests that there should actually be an even broader range of Si isotope compositions. This may await Mars sample return that is expected to come in the next ten years.

The last section of this doctoral thesis dealt with experiments attempting to show the effect of irradiation on the isotope composition of minerals. These experiments are difficult because the amount of material used in the irradiation is small and this is a limiting factor for the analytical method. However, thanks to a good control of blanks and of the sample treatment, it was possible to demonstrate the presence of a significant Si isotope effect due to irradiation. It was not possible to fully understand the origin of this fractionation, partly because it was not fractionated in the expected direction. It would have been necessary to test many more experimental conditions to understand the role of the energy of incident He particles, of the composition of the target or of the particle fluence. In order to have a more quantitative interpretation of our data, one would need to get a better grip on the relative timescales of the various processes that could have played a role in controlling Si isotopes in the olivine target. First, the rate of heat diffusion relative to chemical diffusion and how the creation of defects could modify diffusion coefficients. If Si is then lost by an evaporative process, one would need to know how fast material is evaporated in conditions that are far from chemical equilibrium relative to the rate of diffusion.

It would certainly have been interesting to analyse also Mg and Fe isotopes in the olivine as both elements are expected to get sputtered off the olivine. One could then hope that by having a better understanding of how these isotope signature arise, one could use this tool to understand how irradiation of dust grains could have affected their stable isotope signature and then use this to reconstruct their history. One could expect for example that if the irradiation takes place in the early Solar System, it could produce a different signature compared with that of the interstellar medium. In this respect, our study shows that there are many open questions regarding the fate of fine grain materials in the Solar System that stable isotopes such as silicon could help resolve.

Résumé

Le travail effectué au cours cette thèse porte sur l'utilisation des isotopes du silicium pour étudier des processus ayant eu lieu dans le disque protoplanétaire qui a donné naissance au Système Solaire. Les différents objets du Système Solaire présentent des compositions isotopiques en silicium variables qui sont directement reliées à l'histoire de leur formation. Une des difficultés dans l'utilisation des isotopes du silicium comme traceurs des processus de formation planétaire réside dans la faible amplitude des variations isotopiques observées et le manque de répétabilité des mesures isotopiques publiées dans la littérature, rendant les interprétations parfois hasardeuses. La première partie de ce travail de thèse s'est ainsi concentrée sur la mise en place d'une méthode d'analyse des isotopes du silicium juste, précise et reproductible avec un spectromètre de masse à couplage inductif à plasma en multi-collection. Grâce à cette méthode analytique, des météorites martiennes ont été mesurées et on y observe des traces de la cristallisation de l'océan de magma qui a existé juste après l'accrétion de Mars. L'étude des angrites, une catégorie très rare de météorites différentiées et riches en éléments réfractaires comme la Terre, a permis de mieux comprendre le rôle des processus de condensation au sein du disque protoplanétaire pour expliquer l'enrichissement en éléments réfractaires. Enfin, l'analyse des isotopes du Si dans des échantillons synthétiques irradiés a permis la première quantification des effets isotopiques de l'irradiation au début du Système Solaire.

Abstract

The work undertaken as part of this doctoral thesis addresses the use of silicon isotopes as a means to study processes that have occurred within the Solar System protoplanetary disk. Different objects in the Solar System display distinct silicon isotopic compositions that vary in direct correlation with their formation history. One of the difficulties when using silicon isotopes as tracers for planetary formation processes resides in the small magnitudes of the observed isotopic variations, and in the lack of repeatability of published isotopic measurements in the literature, sometimes making interpretations rather haphazard. The first part of this doctoral work focused, thus, on establishing a method for silicon isotopic analysis that is exact, precise, and reproducible with a multi-collector inductively coupled plasma mass spectrometer. By using this analytical method, martian meteorites were measured and we could observe traces of the crystallization of the magma ocean which formed right after the Martian accretion. The study of angrites, a very rare category of differentiated meteorites with high levels of refractory elements, like the Earth, allowed to better understand the role of condensation processes within the protoplanetary disk in explaining the enrichment in refractory elements. Finally, Si isotopic analysis on synthetic irradiated samples led to the first quantification of the isotopic effects of irradiation during the early stages of the Solar System.